MATHEMATICAL MODELLING OF AN EXOTHERMIC PRESSURE LEACHING PROCESS

by

Vladimiros G. Papangelakis

Department of Mining and Metallurgical Engineering
McGill University
Montreal, Quebec, Canada
September 1990

A Thesis submitted to the Faculty of Graduate
Studies and Research in partial fulfillment
of the requirements for the degree of
Doctor of Philosophy

ISBN 0-315-67851-8

To Elli and George

for their sensibility

To Nota

for her exuberance

Abstract

The object of the present thesis was the development of a mathematical model suitable for computer simulation of hydrometallurgical processes. The model formulation was made for a strongly exothermic three-phase reaction system, namely the pressure oxidation process as applied to the treatment of refractory gold ores and concentrates. The steps followed during the course of this work involved first, the experimental identification of the intrinsic kinetics of the two principal refractory gold minerals, arsenopyrite and pyrite, and second, the development of reactor models describing the isothermal and non-isothermal behaviour of batch and multi-stage continuous reactors at steady state. Emphasis was given to the identification of feed conditions for autothermal operation.

The key features of the developed model are the coupling of both mass and heat balance equations, the description of the non-isothermal performance of a multi-stage continuous reactor, and the treatment of a two-mineral mixture concentrate. In addition, continuous functions are used to describe the size distribution of reacting particles and gas–liquid mass transfer rate limitations are assessed.

The model predictions were in good agreement with pilot-plant scale industrial data. Simulation runs of alternative reactor configurations and feed compositions elucidated the impact of the size of the first reactor stage, the rate limiting regime, and the sulphur content of the feed on the attainment of autogenous performance.

Résumé

Le but de cette étude était de developper un modèle mathématique pour la simulation par ordinateur des processus hydrométallurgiques. La formulation du modèle a été faite pour un système de réaction de trois phases fortement exothermique, le processus d'oxidation sous pression appliqué au traitement des minerais et des concentrés réfractaires d'or. Les étapes suivies au cours de cette étude nécessitaient premièrement l'identification expérimentale de la cinétique intrinsèque des deux principaux minéraux d'or, l'arsenopyrite et la pyrite, et par la suite, le développement de modèles de réacteurs décrivant le comportement isothermique et non-isothermique de réacteurs en discontinu et de réacteurs en série continus à l'état d'équilibre. L'emphase a été donnée à l'identification des conditions d'alimentation pouvant produire une opération autothermique.

Les principales caractéristiques du modèle développé sont: la combinaison de deux équations d'équilibre de la masse et de la chaleur, la description de la performance non-isothermique de réacteurs en série continus, le traitement d'un concentré d'un mélange des deux minéraux, l'emploi de fonctions continues décrivant la distribution de la grandométrique des particules réactives, et l'estimation des limitations du transfert de masse de la phase gazeuse à la phase aqueuse.

Les prédictions du modèle étaient en accord avec les données industrielles d'échelle pilote disponibles. La simulation des diverses configurations de réacteurs et de diverses compositions d'alimentation ont élucidé l'impact du volume du premier réacteur, de la cinetique de réaction et de transfert gaz–eau, et du contenu en souffre de l'alimentation sur la performance autogène.

Acknowledgements

First, and foremost, I would like to express my sincere gratitude to Professor G.P. Demopoulos, my supervisor, for his contagious inspiration and invaluable guidance throughout the course of this study. Professor D. Berk, of the Department of Chemical Engineering, is also gratefully acknowledged for providing the starting tools from which this work has evolved.

Thanks are due to Dr. G. Carayannis for his "consultation" on various software and hardware problems, as well as to Mr. J. Hamamjoglou for enlightening me on several aspects of computer operation.

McGill University and the Natural Sciences and Engineering Research Council of Canada (NSERC) are acknowledged for providing financial support.

Ms. E. Mourelatos and Mr. E. Cheluget are also acknowledged for proofreading the first and second half of the manuscript respectively.

Thanks are also due to Professors A.R. Laplante and R. Montpetit for their assistance in the translation of the abstract into French.

Last, but not least, I would like to thank Mr. I. Mihaylov for the endless and fruitful discussions on mutual hydrometallurgical (and non-) topics during the period of sharing the WM258.

Contents

List of Figures

List of Tables

Nomenclature

Symbols

A, B	chemical formulae of compounds
a	gas–liquid specific area [$(\text{length})^{-1}$]
$\mathcal{A}$	pre-exponential Arrhenious factor
$\vec{a}_c, \vec{a}_a$	transfer coefficients for cathodic and anodic reaction
$\bar{B}$	particle “birth” rate [$(\text{time})^{-1}(\text{length})^{-3}$]
b	stoichiometric coefficient
c	spread
c_p	heat capacity [$(\text{energy})(\text{temperature})^{-1}(\text{mass})^{-1}$]
C	concentration [$(\text{mol})(\text{length})^{-3}$]
C_f	reactor configuration number
$\underline{C}_p$	molar heat capacity [$(\text{energy})(\text{temperature})^{-1}(\text{mol})^{-1}$]
$\overline{C}_p$	average molar heat capacity [$(\text{energy})(\text{temperature})^{-1}(\text{mol})^{-1}$]
d	particle diameter [length]
d'	“dummy” variable in particle size density function [length]
$\mathcal{D}_e$	effective diffusivity [$(\text{length})^2(\text{time})^{-1}$]
$\mathcal{D}$	diffusion coefficient [$(\text{length})^2(\text{time})^{-1}$]
$\bar{D}$	particle “death” rate [$(\text{time})^{-1}(\text{length})^{-3}$]
E_A	activation energy [$(\text{energy})(\text{mol})^{-1}$]
$\mathcal{E}$	effective reactor surface area [$(\text{length})^2$]
$E(t)$	residence time distribution function
$\hat{E}(t)$	residence time distribution function for a reactor series
$\hat{f}$	friction factor
$f(d), f^{\star}(d)$	particle size density function
$f_{\mathrm{m}}(d)$	particle size density function based on particle mass
$f_{\mathrm{n}}(d)$	particle size density function based on particle number
$F(d)$	cumulative particle size function
F	molar flow rate [$(\text{mol})(\text{time})^{-1}$]
F_s	mass flow rate of concentrate [$(\text{mass})(\text{time})^{-1}$]
F_{w}	molar flow rate of water [$(\text{mol})(\text{time})^{-1}$]
$\overline{F}$	total molar flow rate [$(\text{mol})(\text{time})^{-1}$]
$\mathcal{F}$	Faraday’s constant [electric charge]
g	acceleration of gravity [$(\text{length})(\text{time})^{-2}$]
$G(T)$	rate of heat generation function [$(\text{energy})(\text{time})^{-1}$]
ΔG°	standard free energy change [$(\text{energy})(\text{mol})^{-1}$], [energy]
h	heat transfer coefficient [$(\text{energy})(\text{time})^{-1}(\text{length})^{-2}(\text{temperature})^{-1}$]
$\hat{h}$	overall heat transfer coefficient [$(\text{energy})(\text{time})^{-1}(\text{length})^{-2}(\text{temperature})^{-1}$]
ΔH°	standard enthalpy change [$(\text{energy})(\text{mol})^{-1}$], [energy]
i_c, i_a	cathodic and anodic current density [$(\text{electric charge})(\text{time})^{-1}(\text{length})^{-2}$]

k	intrinsic rate constant
k'	intrinsic rate constant incorporating k_H
$\hat{k}$	thermal conductivity [(energy)(time)$^{-1}$(length)$^{-1}$(temperature)$^{-1}$]
$\vec{k}_2, \vec{k}_a$	rate constants for cathodic and anodic reaction
k_D	apparent rate constant for diffusion control [(time)$^{-1}$]
k_F	Freundlich-isotherm constant [(pressure)$^{-2}$]
k_G	apparent rate constant for gas transfer control [(time)$^{-1}$]
k_H	Henry's constant based on concentration [(pressure)(length)^3(mol)$^{-1}$]
$k_{H,y}$	Henry's constant based on mole fraction [pressure]
k_L	liquid side mass transfer coefficient [(length)(time)$^{-1}$]
k_M	apparent rate constant for mixed control [(time)$^{-1}$]
k_S	apparent rate constant for surface reaction control [(time)$^{-1}$]
$\mathcal{K}$	equilibrium constant
$\mathcal{K}_{\mathbf{sp}}$	solubility product
L	total number of continuous reactors in a series
m	total number of reactions
m	mass
$\bar{m}$	specific mass of particles [(mass)(length)$^{-3}$]
M	g-molar weight
$\mathcal{M}$	total mass of iron withdrawn with sampling
n	number of reactor division
N	number of moles
$\overline{N}$	total number of moles
$\dot{O}_2$	oxygen consumption rate [(mol)(time)$^{-1}$]
$\bar{\dot{O}}_2$	specific oxygen consumption rate [(mol)(time)$^{-1}$(length)$^{-3}$]
p	reaction order
P	pressure
Q	heat transferred
$\dot{Q}$	rate of heat transferred [(energy)(time)$^{-1}$]
$\mathcal{Q}$	volumetric flow rate [(length)^3(time)$^{-1}$]
r	particle radius [length]
$\bar{r}$	geometric mean particle radius [length]
r	component rate [(mol)(time)$^{-1}$(length)$^{-2}$], [(mol)(time)$^{-1}$(length)$^{-3}$]
$\overline{r}$	reaction rate [(mol)(time)$^{-1}$(length)$^{-2}$], [(mol)(time)$^{-1}$(length)$^{-3}$]
R_R	recycle ratio
$\mathcal{R}$	ideal gas constant [(energy)(mol)$^{-1}$(temperature)$^{-1}$]
$R(T)$	rate of heat removal function [(energy)(time)$^{-1}$]
$\bar{s}$	specific particle surface area [(length)$^{-1}$]
S	particle surface area [(length)^2]
S°	standard absolute entropy [(energy)(temperature)$^{-1}$(mol)$^{-1}$]
t	time
$\bar{t}$	mean residence time
T	absolute temperature

u_∞	water velocity relative to particle $[(\text{length})(\text{time})^{-1}]$
v	rate of change of particle property
v_S	rate of change of particle size for surface reaction control $[(\text{length})(\text{time})^{-1}]$
v_G	rate of change of particle size for gas transfer control $[(\text{length})(\text{time})^{-1}]$
$\bar{v}$	specific volume of particles
V	volume $[(\text{length})^3]$
w	weight fraction
$\hat{w}$	weight fraction of blend solids
W_R	water addition ratio
ΔW	weight fraction
x	conversion
$\langle x\rangle$	average conversion of monosize fraction
$\bar{x}$	overall conversion of wide size feed
$\hat{x}$	overall conversion in reactor series
y	mole fraction
Z	particle property
z	Pilling-Bedwarth ratio

Greek Symbols

α	minimum size in particle size density function [length]
β	constant in particle size density function
ϵ	reaction extent in batch reactor [mol]
$\dot{\epsilon}$	reaction extent in CSTR $[(\text{mol})(\text{time})^{-1}]$
ζ	particle property value
η	number of particles
$\bar{\eta}$	number of particles per unit volume $[(\text{length})^{-3}]$
$\bar{\theta}$	surface coverage
θ	temperature
ι	index
κ	size fraction
λ	"dummy" variable in convolution integral
μ	median or average particle size [length]
$\hat{\mu}$	mean particle size of a sample [length]
$\tilde{\mu}$	viscosity $[(\text{mass})(\text{length})^{-1}(\text{time})^{-1}]$
ν	stoichiometric coefficient in reaction
ρ	density $[(\text{mass})(\text{length})^{-3}]$
σ	standard deviation
$\hat{\sigma}$	standard deviation of a sample
$\Delta\phi_c$	cathodic potential
$\Delta\phi_a$	anodic potential
$\Delta\phi_m$	mixed potential
φ	ratio of first over unit reactor volume

$\bar{\psi}(d)$	particle number distribution function [(length)$^{-3}$]
$\bar{\omega}(d)$	particle mass distribution function [(mass)(length)$^{-3}$]

Subscripts

b	bulk
f	formation
f	particle film condition
i	reaction component
j	reaction
i	time index
ℓ	intermediate reactor stage
s	sample
s	surface, or concentrate
u	unit reactor
0	initial
in	inlet conditions
out	outlet conditions
inj	injected
ox	oxidized solids

Superscripts

$\star$	equilibrium
$*$	arithmetic mean approximation

Chapter 1

Introduction

Many hydrometallurgical processes involve complex three phase (gas–liquid–solid) reaction systems where a series of parallel and/or consecutive reactions occur. In this type of systems the heterogenous reactions are often highly exothermic and the process requires a specific (high) temperature range for efficient operation. A typical example is the pressure oxidation of refractory gold ores and concentrates [1.1]. The preferred industrial practice calls almost invariably for the utilization of Continuous Stirred Tank Reactors (CSTRs) to carry out these complex and exothermic reaction processes. Furthermore, autothermal operation of such exothermic processes is desired in order to make full utilization of the energy released. Optimization of the reactor design and performance can be greatly facilitated with the aid of mathematical models suitable for computer simulation.

In the past 15 years or so significant advances have been made in developing descriptive models for process simulation in high-temperature extraction metallurgy and mineral processing [1.2]. However, the modelling and simulation efforts have not been equally intensive in hydrometallurgy. On the other hand, there has been a vast amount of fundamental studies, and a plethora of kinetic data that have been published in the field of hydrometallurgy. However, all these data have been hardly used for reactor engineering purposes [1.3]. There exists therefore a significant gap between the generation of fundamental rate data by bench scale batch experimentation and the utilization of these data for optimum design and operation of continuous industrial reactors. The present work constitutes an effort towards bridging this gap. More specifically, a mathematical model that takes into account both kinetic and thermal effects for an exothermic pressure leaching process, namely the pressure oxidation of refractory gold ores and concentrates is developed. Despite the fact that the model is built around the "pressure oxidation process", it is, nevertheless, equally applicable to other hydrometallurgical processes as well. With the aid of the model, the performance of industrial pressure reactors is analyzed and ultimately the optimum reactor configuration and feed conditions for autogenous operation are identified.

The work that is described in this thesis is executed in a series of evolutionary stages. First the intrinsic kinetics of the two principal refractory gold minerals, namely arsenopyrite, and pyrite, are experimentally identified (Chapter 3). Then a preliminary model is built to simulate the performance of single stage reactors (batch or continuous) (Chapter 4). At this stage of model development, possible gas to liquid transfer limitations are neglected and the size distribution of the solid particles is described with a discrete function. The batch model predictions are verified by comparison with laboratory data (Chapter 4).

Next, the model is improved to account for multi-mineral feeds processed in multi-stage continuous pressure reactors (autoclaves). The particles are described using a continuous (rather than discrete) size distribution function, and the case of gas transfer control is addressed by linking the reactor mass transfer capacity with the individual particle kinetics (Chapter 5). The impact of autogenous reactor performance with particle kinetics limited by pure surface reaction or by pure gas-liquid mass transfer is also examined.

Finally, the reactor model is further refined to account for the case of <u>simultaneous</u> surface reaction and mass transfer limited kinetics (Chapter 6). With the latter version of the model various simulation runs are performed and the predictive power of the model is assessed by comparing its predictions with industrial data.

References

[1.1] D.R. Weir and R.M.G.S. Berezowsky, *Intl Symposium on Gold Metallurgy* (ed. by R.S Salter, D.M. Wyslowzyl and G.N. McDonald), 26-th Ann. Conf. Metall., p. 247, CIM, Winnipeg, Manitoba (1987).

[1.2] J. Szekely, L.B. Hales, H. Henein, N. Jarrett, K. Rajamani and I. Samarsekera, *The Mathematical Modelling of Metal Processing Operations*, TMS-AIME, Warrendale PA (1987).

[1.3] M.E. Wadsworth, *Proc. Copper Symposium '84*, vol. 1, no. 1, Met. Soc. CIM (1984).

Chapter 2

Literature Survey

2.1 Introduction

In this chapter a general survey of the literature written on the subject is presented. The chapter is divided into three sections. In the first, the processing of refractory gold ores and concentrates is briefly reviewed. In the second, previous work relative to the chemistry and kinetics of the two principal refractory gold mineral carriers (arsenopyrite and pyrite) is discussed. Finally, modelling concepts and previous studies of relevance to hydrometallurgical process engineering are presented in the third section.

2.2 Processing of Refractory Gold Ores

Over the years the term "refractory" has been applied to gold ore processing to denote situations in which straightforward cyanidation fails to yield high gold recovery. A number of mineralogical and chemical factors may be responsible for this "refractoriness" problem. A systematic classification of the different processing options available for the treatment of this type of gold ores has been discussed in recent review papers [2.1, 2.2]. In this section, the pre-treatment of the submicroscopic gold encapsulated within the matrix of pyrite and arsenopyrite minerals is considered. This type of gold is the ultimate refractory material because complete breakdown of the host mineral structure by oxidation is required.

The method which has been traditionally applied for the treatment of pyritic-type refractory gold ores is an oxidation roast (single-stage or double-stage depending on the As content) of a flo$\overset{a}{}$tation concentrate to produce a porous calcine, the latter being more amenable to cyanidation. With today's standards for high product recovery and clean environment, oxidation roasting is not considered particularly attractive, despite its established practice. Roasting is known to be very sensitive to heating parameters and feed composition, and deviation from optimum conditions can result in reduction in permeability, which is translated into incomplete gold liberation [2.1].

Thus, hydrometallurgical methods are the overall preferred refractory gold extraction routes and attract most of the current R&D activity. There are basically three aqueous oxidation approaches available:

- Hydrochemical oxidation
- Biochemical oxidation and
- Pressure oxidation

The aqueous oxidation methods can be applied equally to ores and concentrates alike. In hydrochemical oxidation, strong oxidants, such as chlorine gas, or nitric acid, are used to decompose the refractory minerals (80 to 100 °C). In biochemical oxidation, autotrophic bacteria are used to "catalyze" the oxidation of minerals by air and $Fe(III)$ (30 to 40 °C). Finally in pressure oxidation, oxygen and autoclaves are used at high temperatures (180 to 200 °C) and pressures (1 to 3 MPa) to increase the oxidation kinetics and suppress the formation of elemental sulphur.

Presently, pressure oxidation appears to be the best established approach to oxidation of refractory ores. It would appear to offer a number of advantages over roasting, both from the processing and environmental points of view. Strict control is not a critical factor in the operation of a pressure leach plant, as it is in the case of a roasting facility. Pressure leaching almost always renders the refractory material amenable to cyanidation and consistently high gold recoveries are usually realized. Finally, pressure oxidation is not associated with air pollution by SO_2, or arsenic emissions but immobilization management of As-laden waste solids requires careful consideration.

Pressure oxidation can be conducted in either alkaline or acidic media, but it is only the latter approach that has been promoted to the level of commercial operation. This route has been vigorously pursued by Sherritt Gordon Ltd. [2.3, 2.4, 2.5, 2.6]. Temperatures above the melting point of S^0 (119 °C) and preferably above 170 °C are employed to obtain complete oxidation of FeS_2 and $FeAsS$ with minimal S^0 formation. The latter is undesirable because it results in occlusion of gold and unreacted sulphides during pressure oxidation and increased consumption of reagents during subsequent cyanidation. The chemistry of conventional acid pressure oxidation of pyrite and arsenopyrite is being discussed in detail in the next section. Pressure oxidation of these two minerals involves a number of reactions yielding ferrous ion, ferric ion, sulphate ion, elemental sulphur and arsenic acid as products. In industrial practice most of the ferric ion produced precipitates as hematite, basic ferric sulphates, jarosite, scorodite and/or basic ferric arsenates due to the high slurry densities and temperatures which are employed.

A typical pressure oxidation flowsheet developed for the treatment of the Olympias concentrate (METBA Ltd., Greece) is shown in Figure 2.1. Following pressure oxidation, the oxidized solids which contain the precious metals are subjected to several stages of thickening, washing and neutralization prior to cyanidation while the generated acid is neutralized and the precipitated solids are disposed of in tailings areas where sub-aerial deposition is practised [2.7]. A portion of the acid might be recycled to the pressure oxidation and the preceding feed preparation stages, the latter when carbonates are present in the feed. Provided that elemental sulphur formation is limited and no significant slimes are generated during neutralization, very high (>95%)

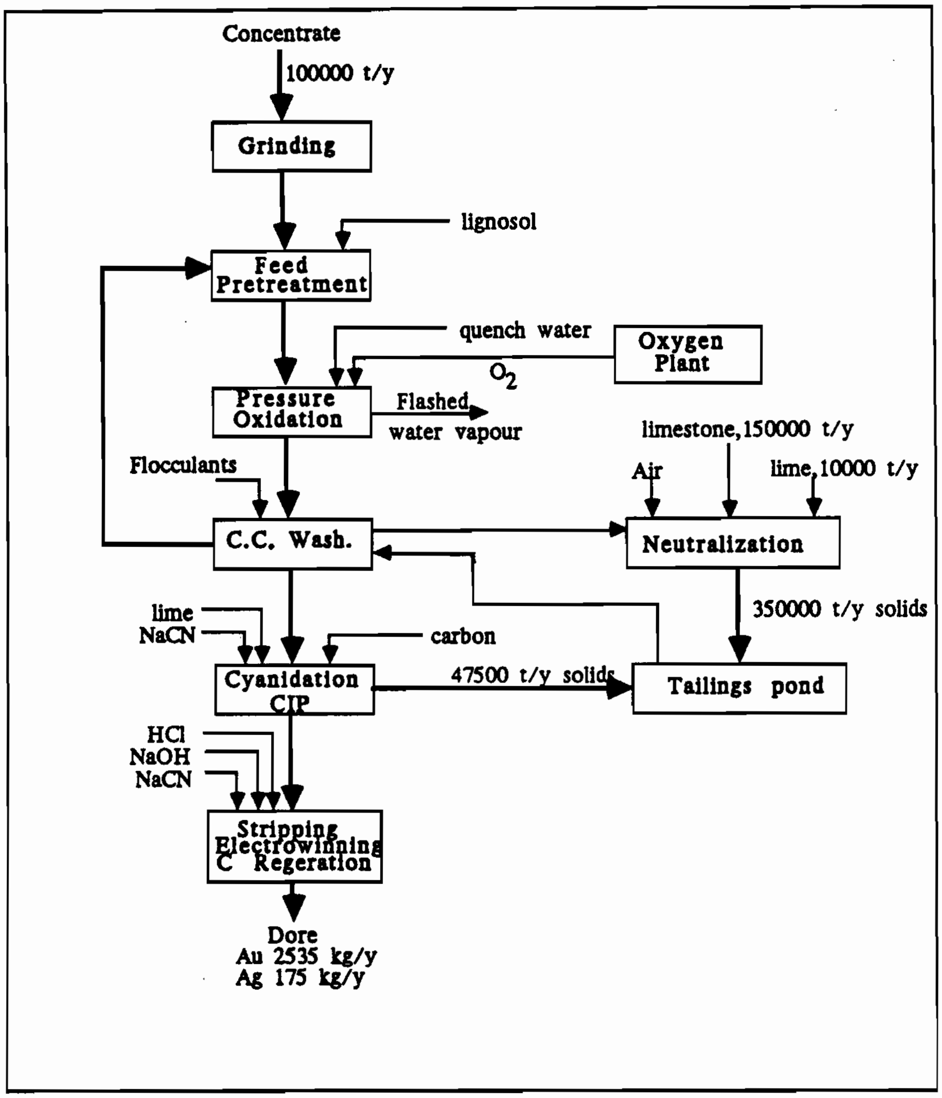

Figure 2.1: The METBA-Sherritt Gordon pressure oxidation process flowsheet (from ref. [2.8])

gold recoveries are realized with very fast cyanidation rates. Recycling of oxidized solids and lignosol additions is practised in the case of sulphur-rich concentrates as it is for example in the Olympias concentrate, in order to disperse the liquid elemental sulphur and avoid catastrophic agglomeration and gold encapsulation [2.6, 2.8].

Among the advantages of pressure oxidation are: it is not sensitive to deleterious elements like Sb and Pb; it yields consistently high Au recoveries; it can operate equally well with ores (5 to 7% S is adequate for autogenous oxidation) and concentrates. The costs of oxygen gas consumption (~60%) and neutralization (~25%) are the most important direct operating costs of the pressure oxidation process. Homestake's McLaughlin gold plant [2.9] was the first example of industrial application of pressure oxidation to the treatment of refractory gold (direct ore oxidation) while the operation of a second pressure oxidation plant (concentrate oxidation) started in Brazil in late 1986 [2.10, 2.11]. Very recently pressure oxidation was chosen by METBA Ltd. for the treatment of the Olympias arsenical pyrite concentrate in northern Greece. The decision was taken after extensive evaluation of a number of alternatives [2.8]. Design of the above pressure oxidation installations has been performed by Sherritt Gordon Ltd. Very recently, Wright Engineers Ltd. designed two additional pressure oxidation plants, one at Barrick Mercur Gold Mine in Utah (750 t ore/day; start-up early 1988), and the second at Getchell, Nevada (3000 t ore/day; start-up early 1989) [2.12, 2.13]. For the Mercur and Getchell ores, which are mixed sulphide/carbonaceous in composition, treatment at 200 to 220 °C and pH 7–8 (the natural pH of the slurry) is practised.

Autoclave design and operation are critical features of the process development and optimization work. Multi-compartment horizontal autoclaves lined with acid bricks are presently used in all pressure oxidation plants in operation, or under construction. A typical horizontal autoclave is shown in Figure 2.2. Due to the exothermic nature of the process, autogenous operation is desirable. Ores with low sulphur content might require preheating to assist the operation, while high grade

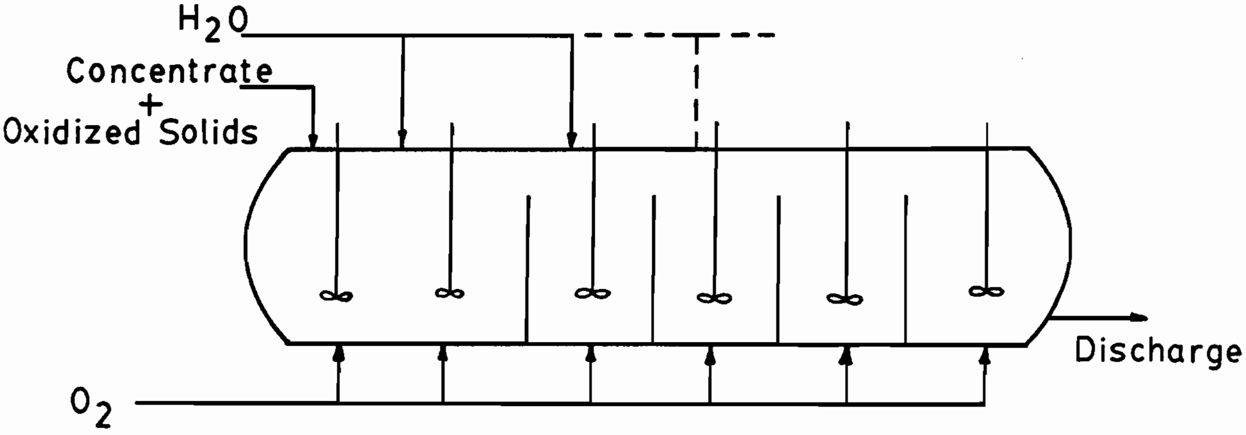

Figure 2.2: Multi-compartment horizontal autoclave

concentrates, on the other hand, might necessitate cooling by water injection. Critical questions, such as what should be the number and size of compartments, what should be the feed temperature, how much water or steam will have to be injected, what slurry density and ratio of solids (concentrate to oxidized) will have to be chosen, and so on, have to be answered for optimum design and operation. Development of descriptive process models suitable for computer simulation can greatly aid the design and optimization tasks. It is indeed the objective of this thesis to develop and demonstrate the use of a such model.

2.3 Pressure Oxidation of Refractory Gold Minerals

Pyrite, along with arsenopyrite, are principal refractory gold mineral carriers [2.14]. In the past only incidental information has been reported on the chemistry of aqueous oxidation of arsenopyrite, most of it based on information derived from the literature on the oxidation of pyrite and qualitative observations made during process

Table 2.I: Summary of pyrite pressure oxidation studies

Material	Conditions		Order	Activation Energy kJ mol^{-1}	Mechanism	Reference
	H_2SO_4	T/P_{O_2}				
Natural pyrite	0 M	130–210 °C 2.7–14.0 atm	0.5	83.7	Surface controlled–Chemisorption	[2.17]
Upgraded pyrite concentrate	0 M	130–165 °C 6.1–23.8 atm	0.5	70.3–77.4	Chemical control	[2.18]
Upgraded pyrite concentrate	0.075 M	100–130 °C 0–4 atm	1.0	55.7	Surface controlled–Chemisorption	[2.19]
Natural pyrite	0.2 M	60–160 °C 0–15.5 atm	1.0	54.8	Surface controlled–Chemisorption	[2.20]
Natural pyrite	1 M	85–130 °C 0–20 atm	1.0	51.1	Surface controlled–Electrochemical	[2.21]
		20–66.4 atm	0.5			

development studies involving complex concentrates [2.3, 2.7]. However, the aqueous oxidation of pyrite has been studied extensively.

From the large body of experimental data reported and reviewed in literature concerning pyrite oxidation studies [2.15, 2.16], only data from investigations conducted at temperatures and pressures approaching those employed in the industrial practice of acid pressure oxidation are considered here. These data are summarized in Table 2.I. The oxidation of pyrite is postulated to follow two parallel and competing reaction paths [2.21], the first yielding sulphate sulphur (eq. 2.1) and the second yielding elemental sulphur (eq. 2.2)

$$FeS_2 + \frac{7}{2}O_2 + H_2O \longrightarrow FeSO_4 + H_2SO_4 \tag{2.1}$$

$$FeS_2 + 2O_2 \longrightarrow FeSO_4 + S^0 \tag{2.2}$$

Reaction 2.1 is the dominant one at all temperatures below and above the melting point of sulphur [2.20, 2.21]. Bailey and Peters [2.21] suggest that the relative velocities of the two competing reactions depend on the potential which upon increasing favours the sulphate forming reaction. One of the earlier suggestions [2.19] that S^0 can be an intermediate to sulphate production does not seem to be the dominant mechanism in view of the kinetic stability of S^0, especially at temperatures below 160 °C [2.22, 2.23, 2.24]. Increased acidities on the other hand are known [2.19, 2.21] to favour the formation of S^0.

The pressure oxidation of pyrite has been found [2.19, 2.20, 2.21] to be chemically controlled, exhibiting predominantly first order dependence [2.19, 2.20] at the lower O_2 pressure region (< 20 atm) and half order dependence at higher pressures [2.21]. Activation energies in the order of 50 to 55 kJ mol^{-1} have been reported for temperatures below 160 °C [2.19, 2.20, 2.21]. H_2SO_4 was found by Bailey and Peters [2.21] to have a beneficial effect on pyrite leaching kinetics while McKay and Halpern [2.19], and Gerlach and coworkers [2.20] failed to detect a similar effect in their respective studies. Apart from the principal research papers quoted above, others have also reported on the kinetics of pyrite oxidation [2.17, 2.18, 2.25, 2.26]. Their results, however, are not directly comparable to the present study since temperatures below the melting point of S^0 were employed, or pyrite specimens which were not well characterized were used. The experimental kinetic results have been interpreted by early investigators on the grounds of an oxygen chemisorption mechanism followed by a slow chemical reaction [2.17, 2.18, 2.19, 2.20]. However, Bailey and Peters [2.21], in a radical departure from previous investigators, have convincingly demonstrated the mechanism of pressure oxidation of pyrite to be electrochemical, involving coupled anodic (pyrite oxidation) and cathodic (oxygen reduction) reactions.

Bailey and Peters also showed that at temperatures approaching and exceeding the melting point of S^0 (115 to 130 °C), pyrite oxidation ceases after about 65% conversion due to the apparent formation of an enveloping liquid sulphur layer (25% S^0 yield at 1 M H_2SO_4). Preliminary analysis by the two investigators of their rate data suggested the surface reaction—shrinking core model to fit the initial reaction kinetics. The reaction curves reported by Gerlach and coworkers (in the temperature range 60–160 °C and up to 85% conversion) did not seem to suggest inhibition as a result of surface coverage with sulphur (7% S^0 yield at 0.2 M H_2SO_4).

In pressure oxidation investigations [2.17, 2.18, 2.19, 2.20, 2.21] it is accepted that iron reports in solution as ferrous ion, which is subsequently oxidized to ferric ion by the following reaction

$$2FeSO_4 + \frac{1}{2}O_2 + H_2SO_4 \longrightarrow Fe_2(SO_4)_3 + H_2O \tag{2.3}$$

On the other hand, in electrochemical investigations [2.27, 2.28, 2.29, 2.30] pyrite is reported to yield ferric iron directly, regardless of the oxidation path followed (reaction 2.1, or 2.2). The potential role of ferric ion in catalyzing the kinetics of pyrite decomposition during pressure oxidation does not seem to have been clearly determined. For example, Warren [2.17], McKay and Halpern [2.19], and Gerlach *et al* [2.20] report practically no effect, while Bailey and Peters [2.21], and King and Lewis [2.26] present evidence of a ferric ion accelerating effect. Weir and Berezowsky [2.6] claim that high ferric ion concentrations during the early stages of autoclaving accelerate the oxidation process. The kinetics of low temperature leaching (≤ 100 °C) of pyrite by ferric chloride [2.31, 2.32], or ferric sulphate salts [2.33] have been established in relation to coal desulphurization processes. However, due to differences in the two mineralogical varieties of pyrite, no extrapolation to the refractory gold pressure oxidation systems can be made.

Upon formation, iron(III) undergoes hydrolysis reactions, the extent of which depend on the prevailing solution conditions. At temperatures above 150 °C the following two principal hydrolysis reactions occur [2.34]:

$$Fe_2(SO_4)_3 + 3H_2O \longrightarrow Fe_2O_3 + 3H_2SO_4 \qquad \text{at lower acidity} \tag{2.4}$$

$$Fe_2(SO_4)_3 + 2H_2O \longrightarrow 2FeOHSO_4 + H_2SO_4 \qquad \text{at higher acidity} \tag{2.5}$$

Precipitation of jarosite type compounds is also known to occur in industrial pressure oxidation systems [2.5]. During arsenopyrite pressure leaching, ferric ion is postulated [2.3] to combine with $H_3AsO_4(aq)$ to form ferric arsenate precipitates:

$$Fe^{3+}(aq) + H_3AsO_4(aq) \longrightarrow FeAsO_4(s) + 3H^+(aq) \tag{2.6}$$

Despite the extensive investigations performed by several researchers, no reliable rate equation representing the pressure oxidation of pyrite has been developed. The rate equations reported by Warren [2.17], McKay and Halpern [2.19], and Gerlach *et al* [2.20] are not in a form that can effectively be utilized in process modelling. This is due to the fact that the surface area term (or equivalently the particle size effect) has not been correctly determined. Moreover, almost all of the previous investigations were limited to temperatures much below those applied in pressure oxidation of refractory gold (Table 2.I). Thus, it was decided to determine the governing rate law of the high temperature pressure oxidation of pyrite and arsenopyrite using topochemical models.

2.4 Process Modelling of Continuous Leaching Systems

One of the principal goals of a kinetic study is the determination of the governing rate law so the latter can be used as the basis of developing a model suitable for design and performance optimization of large-scale industrial process reactors. Although during the past two decades numerous laboratory kinetic studies of mineral leaching systems have been reported, very limited application of these results in designing and optimizing hydrometallurgical process reactors has been undertaken. Laboratory determination of the intrinsic heterogeneous kinetics involves the execution of a series of batch tests using very dilute and monosize particle slurries under iso-thermal and iso-concentration conditions. However, industrial operation of hydrometallurgical processes calls almost invariably for the use of continuous reactors operating with concentrated slurries of wide size distribution mineral feeds. Under these conditions secondary reactions (homogeneous and/or heterogeneous), such as hydrolytic precipitation, are very likely to occur, the extent of which will have to be taken into account. Moreover, the flow pattern of the continuous reactor has to be coupled with the rate equations of the principal and secondary reactions to allow for the development of a mathematical model for the process.

An additional complication in coupling the heterogeneous reaction kinetics with the industrial reactor performance arises when the process is exothermic, as is the case for oxidative leaching of sulphidic concentrates. In such a system, which is very common in hydrometallurgy, the heat released by the leaching reaction must be accounted for since it would affect the design and operation of the reactor.

It appears, therefore, that an integrated modelling approach which takes simultaneously into account the rate and equilibrium properties of the chemical reaction system, and the mass/heat balance characteristics of the reactor itself, is mostly needed for effective process design and optimization. Before the previous modelling attempts in hydrometallurgy are reviewed, some basic elements and concepts of reactor modelling which constitute the foundation upon which the present work is based are briefly outlined.

2.4.1 Elements and Concepts of Reaction and Reactor Modelling

Multiple Reactions and Reaction Extent

For the general case where m chemical reactions occur simultaneously among n chemical components (reactants and products) we can write [2.35, 2.36]

$$\sum_{i=1}^{n} \nu_{ij} A_i = 0 \qquad \text{for } j = 1, 2, \cdots, m \tag{2.7}$$

where i refers to species and j to reactions, ν_{ij} is the stoichiometric coefficient of the i-th species in the j-th reaction (negative for reactants and positive for products) and A_i is the i-th species. If the reaction rate for the j-th stoichiometric equation is denoted by $\overline{r}_j$ (expressed in units of mol/time/surface area for heterogeneous, or mol/time/volume for homogeneous reactions), then the rate of production of species i by the j-th reaction is given by

$$r_{ij} = \nu_{ij} \overline{r}_j \tag{2.8}$$

Note that if i is a reactant, the rate of production is negative. If species i participates in all m reactions, then the overall rate is given by

$$r_i = \sum_{j=1}^{m} r_{ij} = \sum_{j=1}^{m} \nu_{ij} \bar{r}_j \tag{2.9}$$

In setting up conservation equations the rate is multiplied by S (reaction surface area), or V (solution volume) for heterogeneous or homogeneous reactions, respectively.

In a system where multiple reactions occur in a batch reactor, the number of moles of species i is given by

$$N_i = N_{i0} + \sum_{j=1}^{m} \nu_{ij} \epsilon_j \tag{2.10}$$

where N_i is the number of moles of species i at time t, N_{i0} is the initial number of moles, and ϵ_j is the extent of the j-th reaction. The concept of the extent ϵ, which is an extensive variable, has its origins in the thermodynamic literature dating back to the work of de Donder [2.37]. It is a convenient variable to measure the progress of a reaction since it does not depend on any particular species. Instead, it is unique for each reaction. By writing equation 2.10 for each species the stoichiometric table can be prepared. Therefore, the task of reactor modelling is to calculate ϵ, for each reaction and then with the aid of eq. 2.10 to obtain the abundance of each component.

Rates of Heterogeneous Reactions — Shrinking Core Models

In leaching systems the solid phase which consists of discrete entities (particles), often with different reactivity (primarily due to size distribution), takes part in the reaction. This generally results in the surface area of the particles changing with reaction time. Therefore, any rate study of a solid–liquid or solid–liquid–gas reaction system must take into account the change in surface area in order to come up with a heterogeneous rate law. Several so called "topochemical" models, initially developed for gas–solid reactions, have been advanced to deal with the changing surface area of various types of reacting particles under different rate-limiting regimes [2.38, 2.39, 2.40, 2.41].

The application of these models, most commonly known as "shrinking core models", to describe and interpret the batch leaching kinetics of monosize particles is well documented in extractive metallurgical literature [2.42, 2.43]. In the case that spherical (or, more precisely, equiaxed) particles of a non-porous solid phase B react according to:

$$A(aq) + bB(s) \longrightarrow \text{soluble products}$$

the following shrinking core models are available to relate the conversion x with reaction time t (or vice versa) for a single particle and constant solution concentration [2.41]

$$1 - (1-x)^{\frac{1}{3}} = k_S t \tag{2.11}$$

for surface reaction control,

$$1 - \frac{2}{3}x - (1-x)^{\frac{2}{3}} = k_D t \tag{2.12}$$

for product layer diffusion control, and

$$[1 - (1-x)^{\frac{1}{3}}](1 + \frac{y}{6}[(1-x)^{\frac{1}{3}} + 1 - 2(1-x)^{\frac{2}{3}}]) = k_M t \tag{2.13}$$

for mixed control. The conversion x is often termed as "fraction extracted", and k_S, k_D and k_M are the "apparent" rate constants. These constants are given in equations 2.14, 2.15 and 2.16.

$$k_S = \frac{bkMC_A^p}{\rho r_0} \tag{2.14}$$

$$k_D = \frac{2b\mathcal{D}_e MC_A}{\rho r_0^2} \tag{2.15}$$

$$k_M = \frac{bkMC_A}{\rho r_0} \tag{2.16}$$

Moreover,

$$y = \frac{kr_0}{\mathcal{D}_e}$$

where:

b, is the stoichiometric coefficient,

M, is the molecular weight of B

ρ, is the density of B,

r_0, is the initial particle radius,

k, is the intrinsic rate constant,

$\mathcal{D}_e$, is the effective diffusivity of A through the product layer,

C_A, is the bulk concentration of A,

p, is the reaction order in terms of aqueous reactant concentration.

The shrinking core model equations can be applied to a heterogeneous reaction system provided that some basic assumptions are met. These are: (a) the particle retains its equiaxed shape, (b) the product layer is porous, (c) the concentration in the bulk of the solution remains constant, (d) the temperature is uniform throughout the heterogeneous reaction zone. In addition, the mixed-control model equation 2.13 is applicable provided the reaction is of first order and the pseudo-steady state assumption holds [2.41, 2.45].

These models can also be extended to describe the leaching kinetics of widely sized particle feeds, as has been demonstrated for both batch [2.44] and continuous process systems [2.46, 2.47]. The linkage of the particle kinetics to the performance of a continuous reactor is made possible via the "segregated flow" model.

Residence Time Distribution — Segregated Flow Model

The concept of "residence time distribution" (RTD) was introduced for the first time by Danckwerts [2.48, 2.49] and Zwietering [2.50] in an effort to describe mixing effects in homogeneous systems in continuous reactors. According to this concept, the usual space-time-velocity coordinates are abandoned and the elements of fluid within the reactor are considered to be ordered according to their "age", or "life expectancy". States of mixing are then classified according to their residence time distribution [2.51]. More specifically, the fraction of the exit fluid stream, which has spent a time (or alternatively has an "age") between t and $t + \mathrm{d}t$ in the continuous reactor, is given by $E(t)\,\mathrm{d}t$ [2.35, 2.40], where $E(t)$ is the RTD function. This is equivalent to the probability a particular fluid element has to stay in the reactor for a time between t and $t + \mathrm{d}t$. The RTD function has the properties of a probability density function [2.40]. That is, the integration of $E(t)$ over all possible t values (i.e. from zero to infinity) yields one

$$\int_0^\infty E(t)\,\mathrm{d}t = 1 \tag{2.17}$$

For a completely backmixed reactor (continuous stirred tank reactor) the form of the RTD function is [2.35, 2.40]

$$E(t) = \frac{1}{\bar{t}} e^{-t/\bar{t}} \tag{2.18}$$

where $\bar{t}$ is the mean residence time which is defined as the ratio of the reactor volume over the volumetric flow rate of the fluid.

If the mixing state of the fluid is so that different fluid elements are moving through the reactor at different speeds and trajectories without mixing with one-another, then "segregated flow" conditions prevail. Consequently, each fluid element behaves as if it were a small batch reactor and therefore its extent of reaction depends only on the length of stay in the reactor. This is the basic premise of the segregated flow model [2.35, 2.40]. It is evident that in liquid–solid systems the population of the reacting particles constitutes a disperse phase and therefore its degree of reaction can be calculated on the basis of the segregated flow model. That is, if we consider a single reacting particle passing through a continuous reactor with $x(t)$ being the expression which evaluates its conversion versus time (i.e. shrinking core model equation), then the conversion of the particle at the exit of the reactor will be given by

$$\langle x \rangle = \int_0^\infty x(t)\,E(t)\,\mathrm{d}t \tag{2.19}$$

In other words $\langle x \rangle$ is a weighted average of $x(t)$ for all possible reaction times. Equation 2.19 is the basic equation for calculating the degree of reaction of solid particles charged in a continuous reactor.

The Population Balance Model

Twenty-five years ago, two groups of investigators, Hulburt and Katz [2.52], and Randolph and Larson [2.53, 2.54] recognized for the first time that particulate processes are unique in that the disperse phase is made up of a countable number of entities which typically possess a distribution of properties. In a radical departure from the conventional mass balance equations, they proposed the use of an equation for the continuity of particulate numbers, termed "population balance". This number balance is developed from the general equation

$$\text{input} - \text{output} + \text{net generation} = \text{accumulation} \tag{2.20}$$

applied to particles having a specified set of properties (as for example size). In this balance equation, the input and output terms represent changes in the number of particles in the specified property intervals resulting from particle flow, while the generation term accounts for particles entering and leaving the specified property intervals as a result of individual particle kinetics such as chemical reaction, particle breakage, etc. Using this innovative concept, two forms of the population balance were developed. The microscopic form, which accounts for changes in a particle population within an infinitesimal volume at any geometrical position as a function of time, and the macroscopic form which accounts for average changes in a particle population within an entire process vessel [2.53]. The latter form is applicable when the vessel is to a reasonable first approximation well mixed, or when residence time distribution is available. Mechanically-agitated leaching reactors can be assumed, in general, to behave as well mixed vessels, hence it is the macroscopic form of the population balance model (PBM) that is used later in this work. The application of the PBM to leaching processes was first contemplated and demonstrated by Herbst [2.55, 2.56]. Very recently, a number of papers have appeared in chemical engineering literature which deal with the application of the PBM to batch dissolution systems [2.57, 2.58, 2.59].

Heat Balance and Thermal Stability

The energy changes associated with chemical reaction play an extremely important role in the design and operation of commercial scale reactors. Even in those cases where the mode of isothermal operation is practiced, energy balance considerations are important in determining the heat transfer requirements and improving the overall energy economy of the process. Heat balance considerations become even more important when large enthalpy changes accompany the reaction. For reactors operating in a non-isothermal mode, some key questions that have to be answered are: 1)How can the temperature of the system be related to the degree of conversion? 2) How does this temperature influence the subsequent performance of the system? 3) What are the feed conditions for autothermal operation of the reactor? etc. To answer these questions, the material and energy balance equations have to be coupled and solved simultaneously.

The steady state thermal behaviour of continuous stirred tank reactors (CSTR) is usually analysed with the aid of the Van Heerden diagrams [2.60, 2.61] originally developed for homogeneous systems. According to these diagrams, the overall heat balance equation is broken into two parts: the heat generation part (S-shape curve $G(T)$, in Fig. 2.3) and the heat removal part (straight line $R(T)$, in Fig. 2.3), which are plotted against "possible" operating temperatures of the reactor. The intersection points (if any) define the steady state operating temperature. In case several solutions are available, decisions as to the stability of the steady state temperature should be made. For the case of Fig. 2.3 three intersection points (A, B, and C) are shown. The point where the heat removal line $R(T)$ crosses the horizontal axis ($R(T) = 0$) is the feed temperature. Solutions at points A and B are rejected since they represent low conversion and unstable operation respectively. The condition for a stable steady state is the following inequality [2.62]

$$\frac{\mathrm{d}R(T)}{\mathrm{d}T} > \frac{\mathrm{d}G(T)}{\mathrm{d}T} \tag{2.21}$$

evaluated at the steady state temperature. So it is point C which offers stable oper-

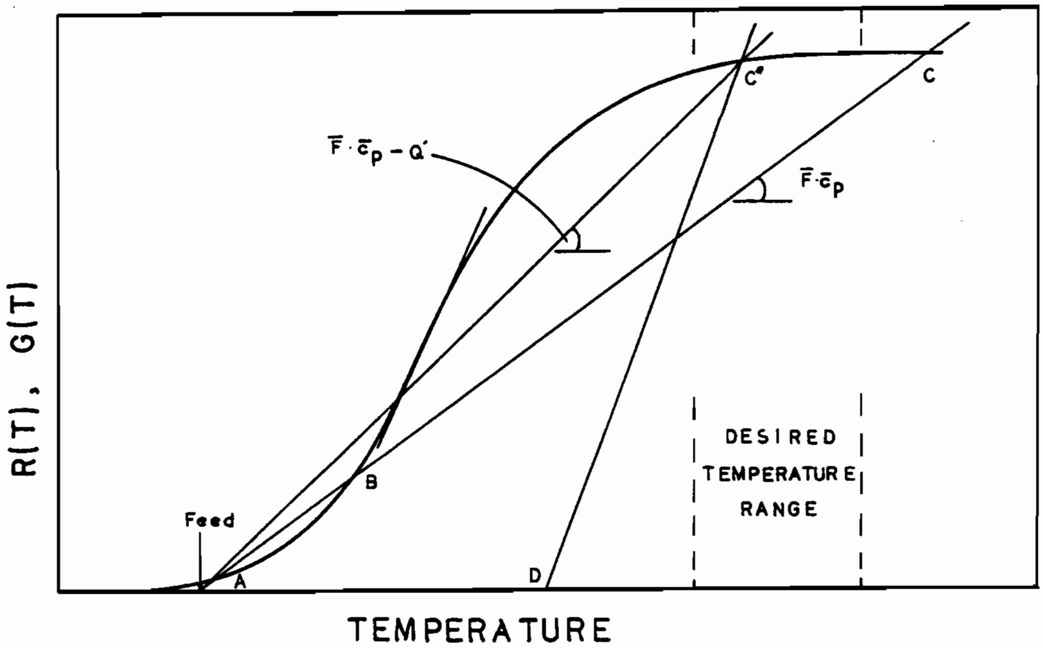

Figure 2.3: Rates of heat generation and heat removal as a function of steady state temperature in a CSTR.

ating conditions and high conversion. Line ABC represents heat removal rates due to the flow of slurry (slope $= \overline{FC_p}$). With the application of external cooling $(-\dot{Q})$ the slope of the straight line is increased and a new stable operating temperature (C*) within the targeted region is now obtained without altering the feed temperature. An alternative way to locate stable steady state points is to vary the feed temperature by moving the $R(T)$ line parallel to itself either to the left (lower feed temperature), or to the right (higher feed temperature).

2.4.2 Previous Modelling Studies in Hydrometallurgy

In the past, several modelling studies on continuous hydrometallurgical processes have been described with varying degrees of completeness. None of them, however, seems to have considered heat effects or gas transfer limited kinetic regimes. The mathematical developments by Bartlett [2.63, 2.64] and Herbst [2.55] were the first significant attempts to describe the isothermal operation of continuously agitated leaching vessels at steady state. Both authors considered the case of non-porous particles reacting in two phase (solid–liquid) systems according to first order shrinking core models. Bartlett treated the continuous flow characteristics of the vessel using a residence time distribution approach. Herbst, on the other hand, made use of the population balance framework. The practical applicability, however, of these early developments was rather limited. Bartlett had assumed some highly restrictive conditions, such as one rate-limiting step at a time, one type of feed size distribution, one heterogeneous reaction, and did not account for the depletion of the fluid reactant. Herbst, on the other hand, was able to overcome these shortcomings, with the exception of considering a single heterogeneous reaction in a single-stage process (i.e. only one stirred tank reactor was considered). In a later publication, Sepulveda and Herbst [2.56] extended the latter modelling approach to a cascade of leaching reactors.

The starting point for the development of the multi-stage reactor model was the single-stage description, based on a population balance equation for the particles, and a mass balance equation for the lixiviant. By considering the flow of solids and liquid from stage to stage for several vessels, and by the use of mathematical induction, they developed a general multi-stage model [2.56]. However, they experimentally confirmed only the single-stage model by simulating the continuous leaching of a $CuFeS_2$ concentrate with $Fe_2(SO_4)_3$ as a lixiviant. Furthermore, in order to make their model computations less system specific, they presented their model equations in non-dimensionalized form. The latter was used to perform a series of simulations examining the effect of several operating variables, such as feed size distribution, lixiviant/solid ratio and slurry mean residence time, on the single-stage leaching with various combinations of rate controlling steps (excluding mass transfer) including lixiviant recycle. It is emphasized once more though, that the reactor heat balance was not considered.

The concept of residence time distribution has also been utilized by Ruether [2.65] in the modelling of a cascade of CSTR for multi-size particles following the diffusion control—shrinking core model. The case this author considered was coal desulphurization by oxidation of pyritic sulphur with oxygen. Ruether assumed a series of equal size reactors without any inter-stage feeding or recycling, which enabled him to consider an appropriate residence time distribution for the whole cascade. More specifically, he calculated the conversion of FeS_2 on the basis of the segregated flow model

$$\langle x \rangle = \int_0^\infty x(t)\, E_L(t)\, \mathrm{d}t \tag{2.22}$$

where $E_L(t)$ is the RTD of a series of L equal size continuous reactors. For this case $E_L(t)$ is given by [2.40]

$$E_L(t) = \frac{1}{\bar{t}}(\frac{t}{\bar{t}})^{L-1}\frac{1}{(L-1)!}\exp(-t/\bar{t}) \tag{2.23}$$

rather than eq. 2.18, where $\bar{t}$ is now the mean residence time of each reactor in the series. However, his model accounted only for a single reaction under isothermal operation without oxygen transfer limitations.

A rather comprehensive modelling methodology suitable for the simulation of a continuous leaching process has been described by Hsin–Hsiung Hang [2.66]. Hang's approach was based on the RTD concept and made use of discrete particle size distributions. The system that was considered in this report was the acid leaching of chrysocolla in a series of continuously agitated vessels. The author dealt only with a single solid–liquid reaction and did not account for heat effects (i.e. isothermal operation).

Generalized model equations for topochemical reactions were presented recently by Henein and Biegler [2.67] for the purpose of reactor volume optimization in hydrometallurgical and pyrometallurgical systems. Their assumptions of maximum mixedness (i.e. no segregation of the solid phase), monosize particles, isothermal operation and only one heterogeneous reaction are too severe to allow for a realistic and a meaningful process modelling approach.

A more complex hydrometallurgical reaction system, the zinc pressure leach process [2.68], has been recently the subject of a modelling study by Dreisinger and

Peters [2.47]. Their model was formulated for a three-phase system in which multiple reactions occur in series in a multi-stage horizontal autoclave. More specifically, the following reaction scheme was considered:

1. Dissolution of $O_2(g)$

$$O_2(g) \longrightarrow O_2(aq)$$

$$r_{O_2} = k_1(C^*_{O_2} - C_{O_2})$$

2. Oxidation of divalent iron

$$4Fe^{2+}(aq) + 4H^+(aq) + O_2(aq) \longrightarrow 4Fe^{3+}(aq) + 2H_2O$$

$$r_{Fe^{2+}} = k_2 C_{Fe^{2+}} C_{O_2}$$

3. Oxidation of sphalerite by ferric ion

$$2Fe^{3+}(aq) + ZnS(s) \longrightarrow 2Fe^{2+}(aq) + Zn^{2+}(aq) + S^0(l)$$

$$r_{ZnS} = k_3 S_{ZnS} C_{Fe^{3+}}$$

The same authors made the fundamental assumption that since the reactor operates at steady state, the three consecutive reaction steps should proceed at the same rate, which in turn was expressed in terms of the oxygen transfer rate (step 1). In other words, they assumed that $r_{Fe^{2+}} = 4r_{O_2}$ and $r_{ZnS} = 2r_{O_2}$. Consequently, they attempted to explore the effect of all variables contained in the three rate equations (i.e. rate constants, steady state concentrations etc.) on the autoclave performance. The latter was achieved by fitting their model to industrial data derived from the operation of the Cominco Zinc pressure leach plant [2.68]. Dreisinger and Peters, in formulating their model, have taken into account the size and residence time distribution of the solid phase and recognized the need for calculating the particle size distribution at the exit of each reactor compartment prior to simulating the performance of the subsequent compartment. However, they did not consider heat effects.

Finally, numerous examples on modelling three phase non-catalytic chemical reaction systems can be found in the chemical engineering literature [2.69, 2.70, 2.71]. However, the implications of gas transfer controlled kinetics with multi mineral, insoluble, and reacting particles (as is the case of sulphide concentrate leaching systems) has not been treated but only in a qualitative fashion [2.72, 2.73, 2.74]. Moreover, most of these studies are not directly applicable to pressure leaching systems. The majority of them refers to sparged reactors with the CSTR being the limiting case [2.75, 2.76].

References

[2.1] G.P. Demopoulos, *Proc. 2-e Colloque sur l'Or*, pp. 273–326, CRM, Rouyn-Noranda, Que. (1987).

[2.2] G.P. Demopoulos and V.G. Papangelakis, *CIM Bulletin*, 82(931), 85 (1989).

[2.3] R.M.G.S. Berezowsky and D.R. Weir, *Minerals and Metallurgical Processing*, 1, 1 (1984).

[2.4] D.R. Weir and R.M.G.S. Berezowsky, *Leaching–Unit Operations and Processes*, Proc. 14-th Ann. Hydromet. Meeting CIM, Paper No. 12, Montreal, Que. (1984).

[2.5] D.R. Weir and R.M.G.S. Berezowski, *Gold 100*, (ed. by M.J. Lazer, J.J. Southwood and A.J. Southwood), vol. 2, pp. 275–285, SAIMM, Johannesbourg, South Africa (1986).

[2.6] D.R. Weir *U.S. Patent*, No. 4,605,439 (1986); No. 4,606,763 (1986); No. 4,571,263 (1986); No. 4,571,264 (1986).

[2.7] M.J. Collins, R.M.G.S. Berezowsky and D.R. Weir, *Arsenic Metallurgy: Fundamentals and Applications*, (ed. by R.G. Reddy, J.L. Hendrix and P.B. Queneau), pp. 115–133, TMS-AIME, Warrendale, PA (1988).

[2.8] A. Kontopoulos and M. Stefanakis, *Precious Metals '89* (ed. by M.C. Jha and S.D. Hill) pp. 179–209, TMS-AIME, Warrendale PA (1989).

[2.9] J.R. Turney, R.J. Smith and W.J.Jr. Janhanen, *Precious Metals '89* (ed. by M.C. Jha and S.D. Hill) pp. 25–45, TMS-AIME, Warrendale PA (1989).

[2.10] R.M.G.S. Berezowsky, A.K. Haines and D.R. Weir, in *Projects '88*, 18-th Ann. Hydromet. Meeting CIM, p. 24, Edmonton, Alta (1988).

[2.11] T.M. Carvalho, A.K. Haines, R.E.J. Da Silva and B.N. Doyle, *Proc. Perth Intnl. Gold Conf.*, pp. 152–156, Randol International, Golden CO (1988).

[2.12] P.G. Mason, R.B. Skeldon and R.D. Wicks, *Proc. 1-st Intl. Gold Conf.*, Vancouver, B.C. (1987).

[2.13] P.G. Mason and R.F. Nanna, *Precious Metals '89* (ed. by M.C. Jha and S.D. Hill) pp. 3–12, TMS-AIME, Warrendale PA (1989).

[2.14] G.P. Demopoulos and V.G. Papangelakis, *Proc. Int'l. Symp. on Gold Metallurgy*, (ed. by R.S. Salter, D.M. Wyslouzil and G.W. McDonald), pp. 341–357, Pergamon Press (1987).

[2.15] R.T. Lowson, *Chemical Reviews*, 82(5), 461 (1982).

[2.16] J.B. Hiskey and W.J. Schlitt, *Interfacing Technologies in Solution Mining* (ed. by W.J. Schlitt and J.B. Hiskey), pp. 55–74, SME-AIME, Littleton, CO (1982).

[2.17] I.H. Warren, *Austr. J. Appl. Sci.*, 7, 346 (1956).

[2.18] R.J. Cornelius and J.T. Woodcock, *Proc. Austr. Inst. Min. Met.*, 185, 65 (1958).

[2.19] D.R. McKay and J. Halpern, *Trans. TMS-AIME*, 6, 301 (1958).

[2.20] J. Gerlach, H. Hahne and F. Pawlek, *Erzmetall*, 19(2), 66 (1966).

[2.21] L.K. Bailey and E. Peters, *Can. Metall. Quarterly*, 15(4), 333 (1976).

[2.22] F. Habashi and E.C. Bauer, *Ind. Eng. Chem. Fund.*, 5(4), 469 (1966).

[2.23] J.P. Corriou and T. Kikindai, *J. Inorg. Nucl. Chem.*, 43, 9 (1981).

[2.24] H. Veltman and G.L. Bolton, *Erzmetall*, 33(2), 76 (1980)

[2.25] C.T. Mathews and R.G. Robins, *Austr. Chem. Eng.*, 15, 19 (1974).

[2.26] W.E. King and J.A. Lewis, *Ind. Eng. Chem. Proc.*, 19(4), 719 (1980).

[2.27] T.Biegler and D.A.Swift, *Electrochimica Acta*, 24, 415 (1979).

[2.28] R.E. Meyer, *J. Electroanal. Chem.*, 101, 59 (1979).

[2.29] F.K. Crundwell, *Hydrometallurgy*, 21, 155 (1988).

[2.30] Yin Zhou, Jianng Han, Shu Yu and Zhao Rui, *Proc. First Int'l Conf. on Hydrometallurgy (ICHM'88)* (ed. by Zheng Yulian and Xu Jiazhong), pp. 623–626, Int'l Academic Publishers-Pergamon Press, Beijing, China (1988).

[2.31] W.E. King and D.D. Perlmutter, *AIChE Journal*, 23(5), 679 (1977).

[2.32] T. Oshinowo and O. Ofi, *Can. J. Chem. Eng.*, 65, 481 (1987).

[2.33] C.Q. Zheng, C.C. Allen and R.G. Bautista, *Ind. Eng. Chem. Process Des. Dev.*, 25(1), 308 (1986).

[2.34] K. Tozawa and K. Sasaki, *Iron Control in Hydrometallurgy* (ed. by J.E. Dutrizac and A.J. Monhemius), pp. 454-476, Ellis Horwood, Chichester, U.K. (1986).

[2.35] C.G. Hill Jr., *An Introduction to Chemical Engineering Kinetics & Reactor Design*, pp. 2–3,388–417, John Wiley & Sons, New York NY (1977).

[2.36] W.R. Smith and R.W. Missen, *Chemical Reaction Equilibrium Analysis*, p. 18, John Wiley & Sons, New York NY (1982).

[2.37] T. De Donder, *Leçons de Thermodynamique et de Chemie-Physique*, Gautier-Villes, Paris (1920).

[2.38] J. Szekely, J.W. Evans and H.Y. Sohn, *Gas–Solid Reactions*, Academic Press (1976).

[2.39] P.A. Ramachandran and L.K. Doraiswamy, *AIChE Journal*, 28(6), 881 (1982).

[2.40] O. Levenspiel, *Chemical Reaction Engineering*, 2nd ed., pp. 357–377, 253–257, John Wiley & Sons, New York NY (1972).

[2.41] J.M. Smith, *Chemical Engineering Kinetics*, 3rd ed., pp. 636–648, McGraw-Hill, New York NY (1981).

[2.42] H.Y. Sohn, *Rate Processes of Extractive Metallurgy* (ed. by H.Y. Sohn and M.E. Wadsworth), pp. 1–51, Plenum Press (1979).

[2.43] M.E. Wadsworth, *Rate Processes of Extractive Metallurgy* (ed. by H.Y. Sohn and M.E. Wadsworth), pp. 133–197, Plenum Press (1979).

[2.44] C. Núñez and F. Espiell, *Metall. Trans.*, 16B, 449 (1985).

[2.45] P.R. Taylor, M. de Matos and G.P. Martins, *Metall. Trans. B*, 14B, 49 (1983).

[2.46] D. Murhammer, D. Davis and O. Levenspiel, *Chem. Eng. J.*, 32, 87 (1986).

[2.47] D.B. Dreisinger and E. Peters, *The Mathematical Modelling of Metal Processing Operations* (ed. by J. Szekely, L.B. Hales, H. Henein, N. Jarrett, K. Rajamani and I. Samarsekera), pp. 347–369, TMS-AIME, Warrendale PA (1987).

[2.48] P.V. Danckwerts, *Chem. Eng. Sci.*, 2, 1 (1953).

[2.49] P.V. Danckwerts, *Chem. Eng. Sci.*, 8, 93 (1958).

[2.50] T.N. Zwietering, *Chem. Eng. Sci.*, 11, 1 (1959).

[2.51] H. Weinstein and R.J. Adler, *Chem. Eng. Sci.*, 22, 65 (1967).

[2.52] H.M. Hulburt and S. Katz, *Chem. Eng. Sci.*, 19, 555 (1964).

[2.53] A.D. Randolph, *Can. J. Chem. Eng.*, 42, 280 (1964).

[2.54] A.D. Randolph and M. Larson, *Theory of Particulate Processes*, pp. 41–64, Academic Press (1971).

[2.55] J.A. Herbst, *Rate Processes of Extractive Metallurgy* (ed. by H.Y. Sohn and M.E. Wadsworth), pp. 53–112, Plenum Press (1979).

[2.56] J.E. Sepulveda and J.A. Herbst, *Fundamental Aspects of Hydrometallurgical Processes* (ed. by T.W. Chapman, L.L. Tavlarides, G.L. Hubred, and R.M. Wellek), AIChE Symp. Ser., 173(74), pp. 41–65, AIChE, New York (1978).

[2.57] S.E. LeBlanc and H.S. Fogler, *AIChE J.*, 33(1), 54 (1987).

[2.58] S.E. LeBlanc and H.S. Fogler, *AIChE J.*, 35(5), 865 (1989).

[2.59] A.N. Bhaskarwar, *AIChE J.*, 35(4), 658 (1989).

[2.60] C. Van Heerden, *Chem. Eng. Sci.*, 45, 1242 (1953).

[2.61] C. Van Heerden, *Chem. Eng. Sci.*, 8, 133 (1958).

[2.62] D. D. Perlmutter: *Stability of Chemical Reactors*, pp. 19–50, Prentice-Hall, Englewood Cliffs NJ (1972).

[2.63] R.W. Bartlett, *Metall. Trans.*, 2(B), 2999 (1971).

[2.64] R.W. Bartlett, *Rate Processes of Extractive Metallurgy* (ed. by H.Y. Sohn and M.E. Wadsworth), pp. 113–131, Plenum Press (1979).

[2.65] J.A. Ruether, *Can. J. Chem. Eng.*, 57, 242 (1979).

[2.66] H–H. Hang, *Computer Usage in Materials Education* (ed. by G.L. Liedl and K.S. Sree Harsa), pp. 67–87, TMS, Warrendale PA (1985).

[2.67] H. Hanein and L.T. Biegler, *Trans. Inst. Min. Metall.*, 97, C215 (1988).

[2.68] M.T. Martin and W.A. Jankola, *CIM Bulletin*, 78(876), 77 (1985).

[2.69] Y.T. Shah, *Gas–Liquid–Solid Reaction Design*, McGraw Hill, New York NY (1979).

[2.70] L.K. Doraiswamy and M.M. Sharma, *Heterogeneous Reactions*, vol. 2, John Wiley & Sons, New York NY (1986).

[2.71] J.B. Joshi, V.P. Utgikar, M.M. Sharma, and V.A. Juvekar, *Rev. Chem. Eng.*, 3(4), 281 (1985).

[2.72] G.A. L'Homme, *Mass Transfer with Chemical Reaction in Multiphase Systems* (ed. by E. Alper), vol. 2, pp. 1–18, NATO ASI Series, E(73), Martinus Nijhoff, The Hague, The Netherlands (1983).

[2.73] H. Hofman, *Mass Transfer with Chemical Reaction in Multiphase Systems* (ed. by E. Alper), vol. 2, pp. 171–198, NATO ASI Series, E(73), Martinus Nijhoff, The Hague, The Nethrlands (1983).

[2.74] E. Alper and W.D. Deckwer, *Mass Transfer with Chemical Reaction in Multiphase Systems* (ed. by E. Alper), vol. 2, pp. 199–224, NATO ASI Series, E(73), Martinus Nijhoff, The Hague, The Nethrlands (1983).

[2.75] J.B. Joshi, J.S. Abichandani, Y.T. Shah, J.A. Ruether, and H.J. Ritz, *AIChE J.*, 27(6), 937 (1981).

[2.76] P.V. Shertukde, J.B. Joshi, and M. Chidambaram, *Chem. Eng. J.*, 38, 81 (1988).

Chapter 3

Experimental Investigations

3.1 Introduction

In this chapter, the experimental work performed with the objective to establish the intrinsic kinetics of arsenopyrite and pyrite during pressure oxidation is described. Knowledge of the governing rate laws of the minerals involved in this complex chemical reaction system is absolutely essential from the stand-point of reactor design and reactor modelling. As discussed in the previous chapter, the chemistry and kinetics of arsenopyrite during pressure oxidation have not been studied previously. On the other hand all studies pertinent to the behaviour of pyrite during pressure oxidation have failed to come up with a rate law suitable for reactor modelling. It was considered, therefore, appropriate first to determine the intrinsic kinetics of the two minerals and then to proceed with the formulation of the process model.

This chapter is divided into three sections. The first section deals with the experimental procedure. In this section, the selection and characterization of the mineral specimens, the equipment used, and the methods of chemical analysis followed are described. In Section 2, the pressure oxidation studies on arsenopyrite chemistry and kinetics are discussed. This material has been published in the *Canadian Metallurgical Quarterly*[1]. Finally, in the third section the study on the pressure oxidation kinetics of pyrite is presented. This material has been accepted for publication in

---

[1] 29(1), pp. 1–12 and 13–20, 1990.

Hydrometallurgy[2].

3.2 Experimental

3.2.1 Materials

Arsenopyrite Study

High-grade arsenopyrite mineral specimens of both monoclinic and triclinic structure were used in the present study. The mineral specimens were supplied by Ward's Natural Science Establishment Inc. originating from Gold Hill, Utah (monoclinic variety) and Mexico (triclinic variety). After crushing, attrition grinding and wet sieving the massive mineral specimens were split into three narrow-sized fractions, namely –147 +104 μm, –74 +53 μm and –44 +37 μm. Wet sieving was employed to remove any dust attached to mineral particles which could interfere with the interpretation of the results.

Microscopic examination showed complete particle (arsenopyrite/silica) separation, with no signs of surface oxidation. The wettability of the ground mineral particles was good, i.e. they were not naturally floatable. Chemical analysis of the –74 +53 μm fraction showed silica to be the only major impurity. The chemical composition of the ground mineral specimens used in the present study is shown in Table 3.I. For the monoclinic specimen, the atomic ratio of arsenic to sulphur was one, while iron was present in slight excess over the stoichiometric amount. X-ray diffraction analysis identified fayalite ($FeSiO_4$) in addition to $FeAsS$ and SiO_2; the presence of the former apparently contributed to the non-stoichiometric iron excess. In Figure 3.1 typical ground mineral particle morphologies are depicted. Some quartz—totally liberated—particles are noticable in the monoclinic specimen as seen in Fig. 3.1(top).

---

[2] April 1990.

Figure 3.1: Scanning electron micrographs of the two arsenopyrite mineral specimens (-74 +53 μm fraction): monoclinic (top); triclinic (bottom).

Table 3.I: Chemical analysis of arsenopyrite material (–74 +53 μm).

Constituent	Monoclinic	Triclinic
	wt. %	
Fe	31.00	34.05
As	39.62	45.23
S	16.85	19.04
SiO_2	11.96	1.27
$FeAsS$ (based on As)	86.11	98.30

Pyrite Study

High purity pyrite cubes were supplied by Hawthorneden, Bannockburn, Ontario, originating from Navajún, La Rioja, Spain [3.1]. The mineral specimens were crushed and ground in an attrition mill prior to wet sieving to 3 narrow size fractions, namely –147 +104 μm, –74 +53 μm and –44 +37 μm. Wet chemical analysis (*aqua regia* treatment) determined 96% purity, the presence of stoichiometric amounts of Fe and S with respect to the FeS_2 formula, traces of Cu and 4% insoluble matter. X-ray diffraction confirmed the presence of cubic pyrite and quartz only.

3.2.2 Equipment and Procedure

Arsenopyrite Study

The pressure oxidation tests were conducted in a 300 mL Parr autoclave equipped with titanium internal parts. In order to avoid the possibility of dangerous exposure of reactive titanium metal to oxygen due to erosion of the protective titania layer, the stirring shaft was made of a $Ti - Al$ alloy. Also, the temperature was kept within ±0.5 °C of the desired value by using a combined heating/cooling action controller. Oxygen was supplied at constant pressure through the sampling dip tube. The leach slurry was agitated by a magnetic drive stirring unit with a single 4-pitched blade turbine impeller. Frequent leakage problems in the early stages of the work with a conventional packing gland system forced a switch to a magnetic drive system.

The experimental procedure involved preparing a leach slurry consisting of H_2SO_4 solution at specified concentrations and a pre-weighed mass of arsenopyrite. Prior to heating, the reactor was flushed with nitrogen and then heated to the desired temperature (~20 min heating period). When thermal equilibrium had been reached, a sample was collected to determine arsenic and iron concentrations at time = 0. These measurements showed marginal dissolution levels not exceeding 1% while the characteristic odour of H_2S was never detected. Oxygen was introduced at this point and the reaction was initiated. Aliquots of leach liquor were periodically withdrawn from the pressure reactor and analysed. Prior to aliquot collection, stirring was stopped for 30 sec to allow for particle settling. For the tests involving analysis of the residues, operation of the autoclave was stopped after a predetermined time, the reactor was cooled immediately (< 10 min) and the contents were filtered, washed and dried. For accurate volume correction after sample collection, the volume of each sample withdrawn (~4 mL +2 mL flush) was determined by measuring its weight and assuming a density of 1 g mL^{-1}. For the calculation of conversion, correction factors were applied to account for the volume and mass losses due to sampling. The particular correction formula used is given below:

$$x_i = \frac{(C_i V_i + \mathcal{M}_i)10^{-6} M}{m M_{Fe}} \tag{3.1}$$

with V_i and $\mathcal{M}_i$ being equal to $V_{i-1} - V_{si-1}$ and $\mathcal{M}_{i-1} + C_{i-1}V_{si-1}$ respectively, and

i, the sample number corresponding to time t_i

x_i, conversion of the mineral

C_i, iron concentration (μg mL^{-1})

V_i, volume of leaching solution prior to i-th sampling (mL)

$\mathcal{M}_i$, total mass of iron withdrawn with previous samples (μg)

V_{si}, total sampling volume (mL)

M, g-mol of the mineral

M_{Fe}, g-mol of iron

m, mass of charged solids (g)

and $t_0 = 0$, $V_0 = 180$ mL, as well as $\mathcal{M}_0 = C_0 = V_{s0} = 0$. The correction was necessary, as neglecting it could lead to errors as high as 20 percent.

Pyrite Study

The experimental-set up and procedure was similar to that described for the arsenopyrite study but with the following exceptions. The acidity was fixed at 0.5 M H_2SO_4. Pyrite dissolution was followed by iron analysis with AA spectrophotometry. To prevent iron precipitation as hematite, very dilute slurries were employed. The amount of solids charged in the autoclave was calculated so that even if pyrite dissolution was complete, the resultant solution would be unsaturated with respect to Fe_2O_3 under all experimental conditions. The hematite solubilities used in these calculations were based on those reported by Tozawa and Sasaki [3.2]. Preliminary tests with different slurry densities showed that some hematite precipitation was always taking place even if iron concentration was only half of the Fe_2O_3 solubility calculated according to the data given in ref. [3.2] (2 g L^{-1} Fe^{3+} in 50 g L^{-1} H_2SO_4 at 180 °C). Hematite was found to deposit on the walls and internal parts of the autoclave at the gas-liquid interface, most propably due to local evaporation. Digestion with warm 5 N HCl solution showed that the precipitated amounts of iron corresponded to no more than 4.5% pyrite conversion when 0.4 g FeS_2 was charged in 180 mL solution at 180 °C. At lower temperatures the extent of hematite precipitation was considerably lower. It was eventually decided, as the best overall compromise, to use 0.4 g FeS_2 per 180 mL of solution to permit the study of the oxidation kinetics under essentially precipitation-free conditions. As another precaution, the bomb and internal parts of the autoclave were soaked in warm 5 N HCl and then washed with distilled water after each experiment, in order to remove any residual iron deposits. Blank tests were followed and samples were withdrawn and analysed for iron. Only when the level of iron concentration determined from these blank tests was less than or equal to 10 ppm (corresponding to 0.1% conversion) was a new experiment performed. All glassware were thoroughly washed with distilled water to prevent any iron contamination.

3.2.3 Analysis

The chemical composition of the mineral specimens used in this work was determined by nitric acid digestion ($FeAsS$), or *aqua regia* digestion (FeS_2). Direct *aqua regia* treatment was not employed for arsenopyrite since it could result in loss of arsenic due to the possible formation of the highly volatile arsenic trichloride species. The filtrates were analysed for total dissolved arsenic and/or iron by AA spectrophotometry. Silica and total sulphur were determined gravimetrically [3.3]. Extreme care was applied during all arsenic analyses by AA since this element exhibits high instability and low absorbance values. Thus, over dilution was always avoided. The optimum concentration range was between 10 and 20 ppm. Arsenic(III) measurements were made by a method [3.4] involving arsenic separation by ion- exchange and titration with $KBrO_3$. Iron(II) was measured by potassium dichromate titration method using sodium diphenylamine sulphonate as indicator [3.5]. Arsenic(III) was found not to interfere with the titration of iron(II) at the concentration levels measured. The elemental sulphur content of the leach residues was measured by the carbon disulphide extraction method [3.5]. Analytical reagent grade CS_2 solvent was used to avoid any S^0 overestimation. Finally, chemical analysis of the precipitates produced involved a two step digestion treatment. First, the precipitates were treated with hot (70–80 °C) 4N $NaOH$ to dissolve arsenic and subsequently the remaining residues were washed with warm (50–60 °C) 5N HCl to dissolve iron. The filtrates were then analysed by AA spectrophotometry.

3.3 Pressure Oxidation of Arsenopyrite

3.3.1 Mineral and Solution Chemistry

Physicochemical Properties of Arsenopyrite

The structure of arsenopyrite has been investigated by Buerger [3.6] and Morimoto and Clark [3.7]. Buerger concluded that arsenopyrite is ideally monoclinic and commonly triclinic. Comparison of pyrite, marcasite and arsenopyrite structures [3.8] indicates arsenopyrite to be a derivative of marcasite, in which one of the two sulphur atoms is replaced by arsenic. Morimoto and Clark [3.7] found that the composition of naturally occurring arsenopyrite varies from about $FeAs_{0.9}S_{1.1}$ to $FeAs_{1.1}S_{0.9}$. By studying arsenopyrites of different compositions it was found that as the arsenic content is increased, the triclinic symmetry approaches the monoclinic. This finding is in agreement with information reported in Dana's System of Mineralogy [3.9].

Arsenopyrite, being the most abundant arsenic mineral, occurs in diverse types of deposits, the most important of which are metamorphic sulphide deposits associated with gold. The association of gold with arsenopyrite was attributed by Clark [3.10] to its high diffusivity in arsenopyrite at temperatures 660 °C and higher and also to its ability to form solid solutions. He proposed that since diffusion rates of gold in arsenopyrite are high at elevated temperatures, the gold that comes out of the solid solution during the cooling period is able to diffuse (in part) to the edges of the arsenopyrite grains. Several studies concerning the size distribution of gold in arsenopyrites from different locations of auriferous ores show that a substantial proportion of gold approaches the submicroscopic and colloidal ranges. Schwartz [3.11] found that in most of the auriferous districts, the recovered gold was found to be associated with arsenopyrite. The exact nature of the submicroscopic ("invisible") gold occurring within the structure of pyrite and arsenopyrite has yet to be unequivocally determined [3.12, 3.13].

Mineral-Solution Equilibria

The thermodynamic stability of arsenopyrite and its oxidation products can be predicted with the aid of Eh-pH diagrams. Eh-pH diagrams are usually constructed at 25 °C since thermodynamic data for many aqueous species and solid compounds are usually too limited to permit extrapolation to higher temperatures. To achieve the latter, the values of $\Delta G^\circ_{f,298}$ (or $\Delta H^\circ_{f,298}$), S°_{298} and C_p of all species involved in the system should be known. Eh-pH diagrams for the system $Fe - As - S - H_2O$ have been reported in the scientific literature only recently [3.14, 3.15, 3.16]. The latter, however, are not directly applicable to the present study since (i) they refer to 25 °C and (ii) they appear not to have included the ferric sulphate complexes and scorodite ($FeAsO_4 \cdot 2H_2O$). Arsenopyrite stability diagrams of more relevance to the current studies were constructed, using $F * A * C * T$ [3.17] and estimating a number of thermodynamic properties of species for which limited data were available. The diagrams are given in Fig. 3.2. With the aid of these diagrams, the mineral-leach solution equilibria of interest to high temperature pressure oxidation may be better understood.

A list of iron species for which some thermodynamic properties were estimated or modified, as will be described later in this section, is given in Table 3.II. For completeness, all ferric hydroxyl and sulphate complexes are shown. All the remaining thermodynamic data for the Fe, As, and S species that were considered (but not shown in Table 3.II) were taken from the data base of $F * A * C * T$, based on the references [3.18, 3.19, 3.20]. Free energy of formation values reported for scorodite and calculated from solubility data are given in Table 3.III. The variation in the reported ΔG°_f values is due, on the one hand, to the different conditions under which the solubility measurements were performed (congruent and incongruent dissolution zones) and, on the other, to the different considerations taken in analysing the data (i.e. speciation, selection of stability constants etc.). In the present work the value reported by Robins [3.28] was chosen. This value was further adjusted to –1254.7 kJ

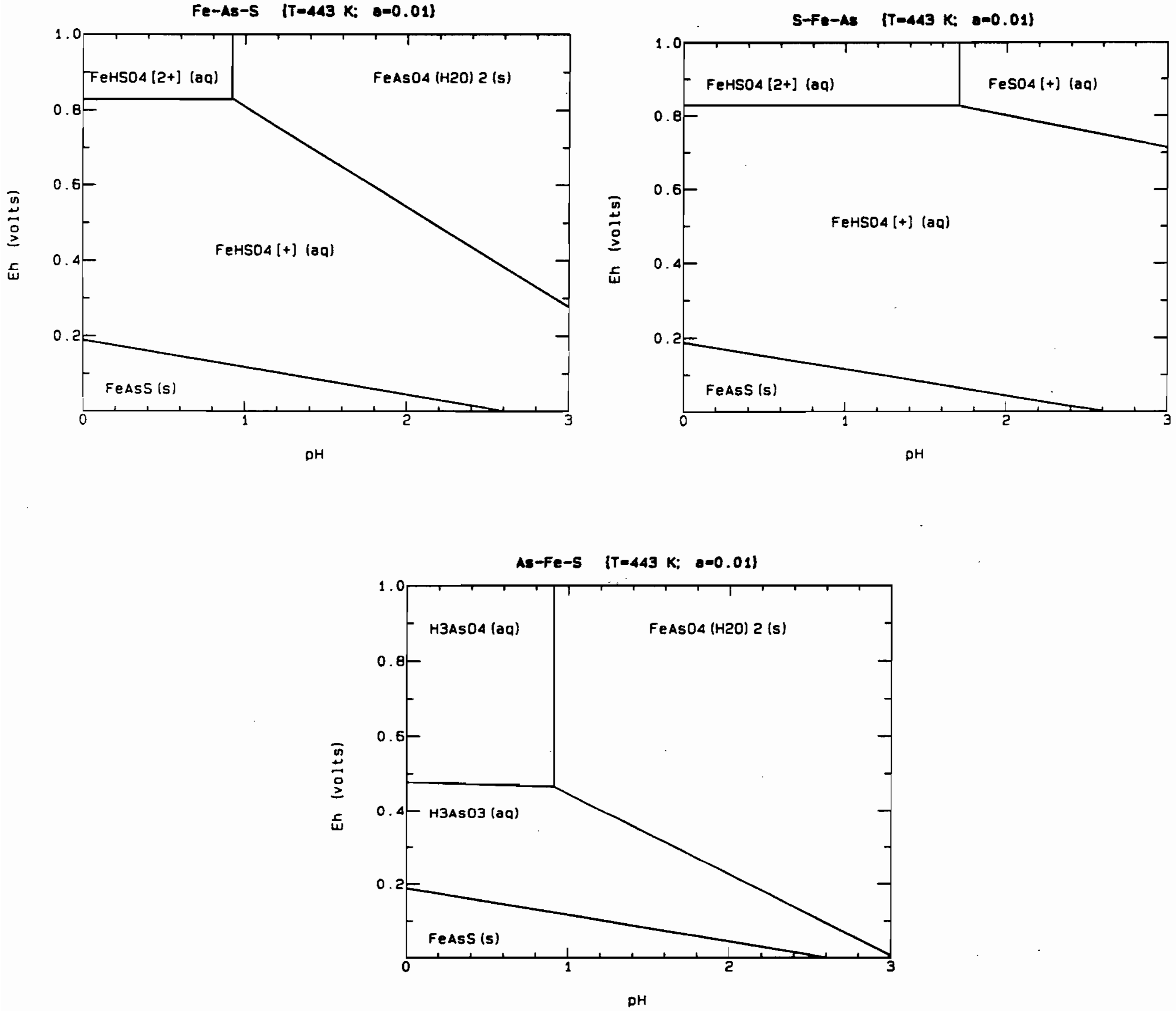

Figure 3.2: The Eh-pH diagrams for the $Fe - As - S - H_2O$ system at 170 °C; Fe (top left), S (top right), As (bottom) species; activity of all aqueous species 10^{-2}.

Table 3.II: Iron species and thermodynamic data used for the construction of the Eh-pH diagrams.

Species	$\Delta G^\circ_{f,298}$ kJ mol^{-1}	$\Delta H^\circ_{f,298}$ kJ mol^{-1}	S°_{298} J K^{-1} mol^{-1}	$C_p = A + B10^{-3}T + C10^5T^{-2}$ J K^{-1} mol^{-1}			$C_p]_{298}^{443}$ J K^{-1} mol^{-1}
				A	B	C	
$FeAsO_4 \cdot 2H_2O(s)$	−1254.70‡	−1485.19†	(171.30)	(180.54)			
$FeAsS(s)$	−49.70	−41.80	121.30	(74.82)			
$Fe^{3+}(aq)$	−4.60	−48.50	−315.90	79.09	−219.35	15.40	
$FeOH^{2+}(aq)$	−229.41	−290.80	−142.00	19.40	−21.22	29.14	
$Fe(OH)_2^+(aq)$	−446.40§	−543.80†	−29.29‖				(229.59)
$Fe(OH)_3^0(aq)$	−660.00¶	−795.73†	75.40¶	(0)			
$Fe(OH)_4^-(aq)$	−830.00§	−1050.40†	25.50¶				(−428.70)
$Fe_2(OH)_2^{4+}(aq)$	−466.97§	−611.38†	−355.64	124.68	−619.16	13.76	
$FeSO_4^+(aq)$	−772.80	−931.78	−129.70	37.70	316.78	−1.00	
$FeHSO_4^{2+}$	−768.38♮	−894.29♮	−18.68				(235.83)
$Fe_2(SO_4)_3^0(aq)$	−2243.00	−2825.04	−571.53	(0)			
$Fe(SO_4)_2^-(aq)$	−1524.65	−1828.39♯	−43.07♯				(−703.44)
$FeHSO4^+(aq)$	-838.29♮	−937.69♮	137.57♮				(128.00)

Data from ref. [3.18, 3.19, 3.20] unless otherwise stated. Values in parenthesis are estimates.
†: Calculated; ‡: Ref. [3.28]; §: Ref. [3.21]; ‖: Ref. [3.22]; ¶: Ref. [3.23]; ♮: Ref. [3.24]; ♯: Ref. [3.25].

Table 3.III: Free energy of formation of $FeAsO_4 \cdot 2H_2O$

$\Delta G^\circ_{f,298}$ (kJ mol^{-1})	Reference
−1243.0	Chukhlantsev, [3.26]
−1265.5	Dove and Rimstidt, [3.27]
−1267.1	Robins, [3.28]
−1279.2	Krause and Ettel, [3.29]

mol^{-1} since the NBS value of $\Delta G^\circ_{f,Fe^{3+}} = -4.6$ kJ mol^{-1} was used for the construction of the Eh-pH diagrams instead of –16.9 kJ mol^{-1} used by Robins in his calculations [3.28]. It should be noted that there is some ambiguity in the literature with respect to the thermodynamic data for the iron species. This has its origins in the different values of $\Delta G^\circ_{f,298}$ available for Fe^{3+}, namely –4.6 kJ mol^{-1} [3.19] and –16.9 kJ mol^{-1} [3.23]. By calculating the stability constants of the iron species listed in Table 3.II, using the two free energy values of Fe^{3+} and comparing them with the experimentally determined values [3.30], it was determined that –4.6 kJ mol^{-1} gave better agreement with most of the data. For those cases where agreement was not good with this value (but was good if –16.9 kJ mol^{-1} was used instead), the free energy of formation of the species was reduced by $n \times 12.3$ kJ mol^{-1}, where n is the number of iron g-atoms per mol. For the extrapolation to higher temperatures in the absence of directly measured data, the absolute entropy and heat capacity values of scorodite were assumed to be the same with the mineral phosphosiderite ($FePO_4 \cdot 2H_2O$). In earlier calculations the absolute entropy of $FeAsO_4$ had been estimated [3.31] by resorting to a method described by Latimer [3.32]. This approach has been abandoned in favour of the present estimation procedure, since scorodite ($FeAsO_4 \cdot 2H_2O$) rather than simple $FeAsO_4$ forms during the pressure oxidation experiments. Latimer's method [3.32] does not take into account the hydration in calculating the S°_{298} value of a compound.

The heat capacity of arsenopyrite was estimated according to Kopp's rule [3.33]. The thermodynamic data for the ferric hydroxyl and sulphate complexes were taken from various sources as shown in Table 3.II and were checked and adjusted to be consistent with experimental data [3.21]. Heat capacity values for species where no data exist were calculated according to the Criss and Cobble correspondence principle [3.34]. The latter states that the average heat capacity of an aqueous ion for the temperature range of 298 to T is a function of its absolute entropy and is given by

$$C_p]^T_{298} = a_T + b_T S^\circ_{\mathbf{absolute,298}}$$

Table 3.IV: Thermodynamic data estimated with the Criss and Cobble Correspondence Principle method

Species	$S^\circ_{\text{conv},298}$ J K^{-1} mol^{-1}	$S^\circ_{\text{abs},298}$ J K^{-1} mol^{-1}	$C_p]^{443}_{298}$ J K^{-1} mol^{-1}	Class
$Fe(OH)_2^+$	-29.29	-50.21	229.59	Simple cations
$Fe(OH)_4^-$	24.5	45.42	-428.70	Acid oxy anions
$FeHSO_4^{2+}$	-18.68	-60.52	235.83	Simple cations
$Fe(SO_4)_2^-$	-43.07	-22.15	-703.44	Acid oxy anions

where

$$S^\circ_{\text{absolute},298} = S^\circ_{\text{conventional},298} - 20.92z$$

and z is the ionic charge. The values of a_T and b_T are functions of temperature and the class of the ion.

Table 3.IV shows the species for which the heat capacity values were calculated according to the correspondence principle method, along with their respective absolute and conventional entropy values, average heat capacities and the respective class of ions that was considered for each. It should be noted, however, that there exist various complex ions which do not fall directly into any of the ion categories for which the correspondence principle was developed. For example, ions like $Fe(OH)_2^+$ or $FeHSO_4^{2+}$ should belong to the class of acid oxy cations instead of simple cations. Unfortunately, there are no correlations for such types of ions, which implies that some degree of error is unavoidable. Nevertheless, the correspondence principle method remains widely acceptable in the research community [3.25, 3.35, 3.36]. The same argument (although to a lesser extent) applies to $Fe(SO_4)_2^-$ as to whether it can safely be considered an acid oxy anion (by replacing H by Fe). Finally, since no correlation exists for neutral complex ions, the respective heat capacity for $Fe(OH)_3^0$ and $Fe_2(SO_4)_3^0$ were assumed to be zero in the present work. In Table 3.V the heat capacity parameters a_T and b_T used to estimate the $C_p]^{443}_{298}$ values of Table 3.IV are shown. Values in parentheses were calculated by linear interpolation.

Eh-pH diagrams derived for the iron, sulphur and arsenic species at 443 K are

Table 3.V: Criss and Cobble heat capacity parameters (SI units).

Temperature K	Cations a_T	Cations b_T	Acid oxy anions a_T	Acid oxy anions b_T
423	192.46	–0.59	–590.31	3.95
443	(199.16)	(–0.61)	(–613.38)	(4.07)
473	209.2	–0.63	–635.97	4.24

shown in Figure 3.2. All species were taken to have 10^{-2} activity. Moreover, the possible formation of other solid compounds such as sulphides and oxides of iron and arsenic was neglected in an effort to simulate more closely the pressure oxidation of arsenopyrite. The diagrams suggest that relatively mild oxidation potentials should be sufficient to decompose arsenopyrite. In practice, severe conditions, i.e. high temperatures and oxygen pressures, are required to bring about this decomposition in a reasonable time. In terms of products, elemental sulphur might be expected to be unstable under the applied pressure oxidation conditions. According to $F*A*C*T$ calculations, $S^0(l)$ was found to be stable only at extremely low pH (i.e. less than –2). Based on the thermodynamic diagrams, precipitation of scorodite is expected to occur at pH > 1 and at oxidizing potentials. The major species expected in solution include $FeHSO_4^{2+}$ and H_3AsO_4 at high Eh conditions and $FeHSO_4^{+}$ and H_3AsO_3 at moderate Eh conditions.

3.3.2 Results

Product Identification

Several pressure oxidation tests were performed under different experimental conditions including temperature, time, acid concentration, and slurry density. The reaction products were identified by analysing the resulting solutions and residues. Figures 3.3 to 3.6 illustrate the results. In each figure the top graph shows the effect of the operating parameter on the conversion of arsenopyrite in terms of oxidation and precipitation, and the bottom graph shows the respective product distributions,

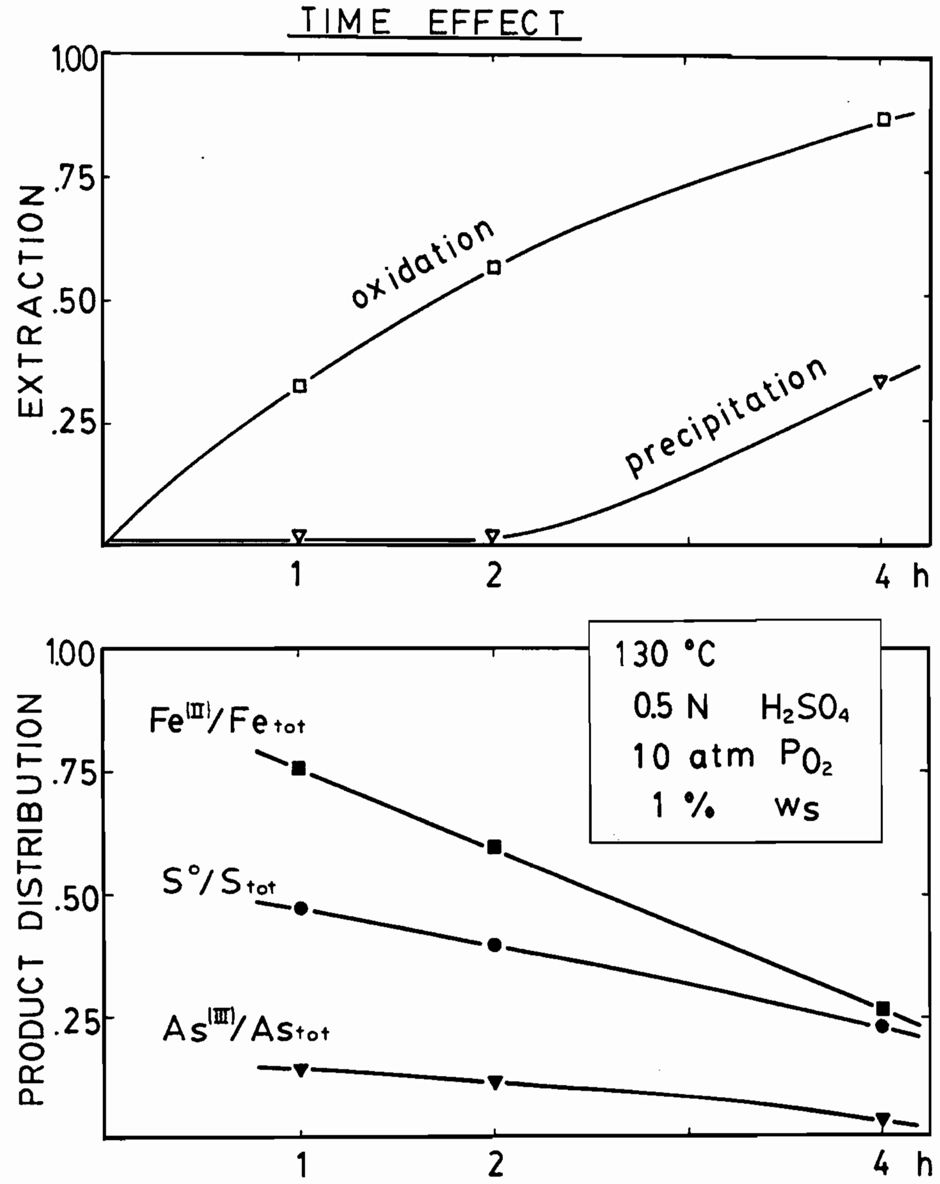

Figure 3.3: The effect of reaction time on the conversion of arsenopyrite (top) and on the distribution of products (bottom). (Exp. conditions: 130 °C; 1013 kPa O_2; 0.5 N H_2SO_4; -74 +53 μm; 1% solids.)

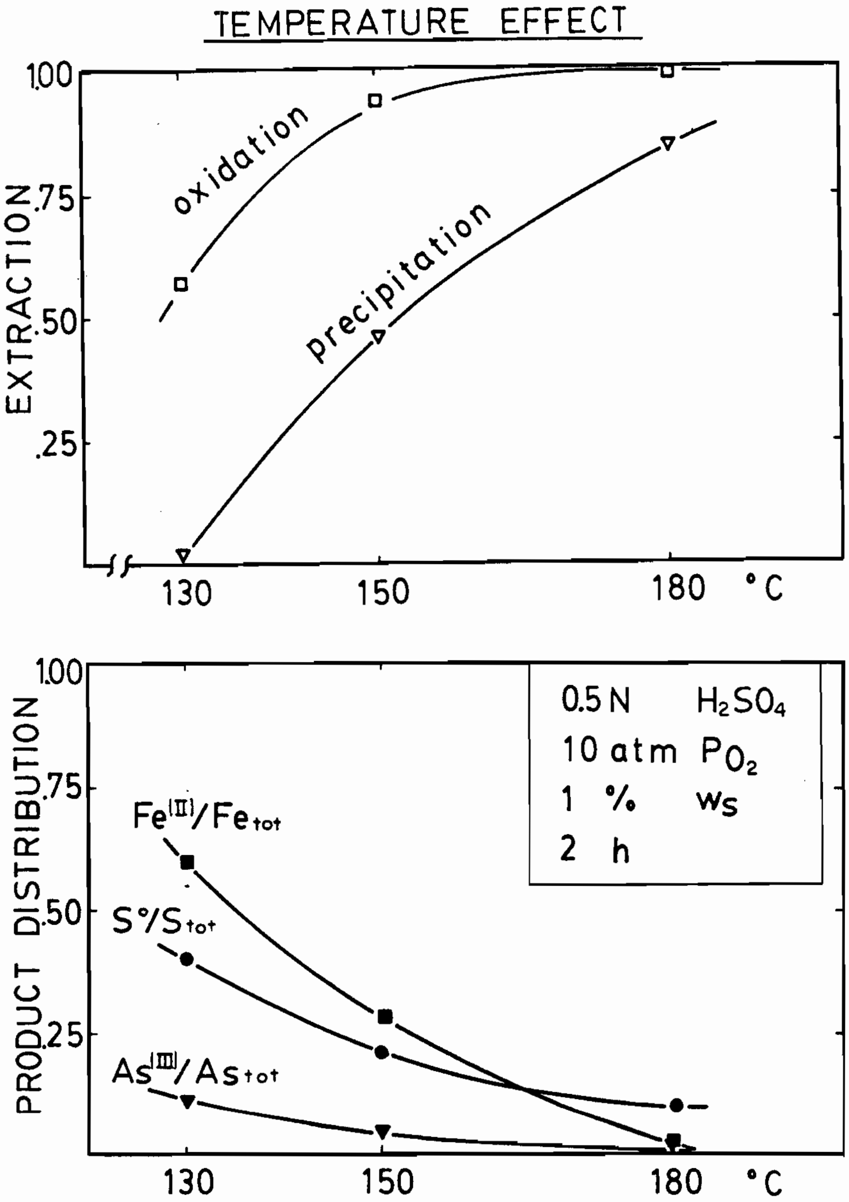

Figure 3.4: The effect of temperature on the conversion of arsenopyrite (top), and on the distribution of products (bottom). (Exp. conditions: 1013 kPa O_2, 2 hours; 0.5 N H_2SO_4; –74 +53 μm; 1% solids.)

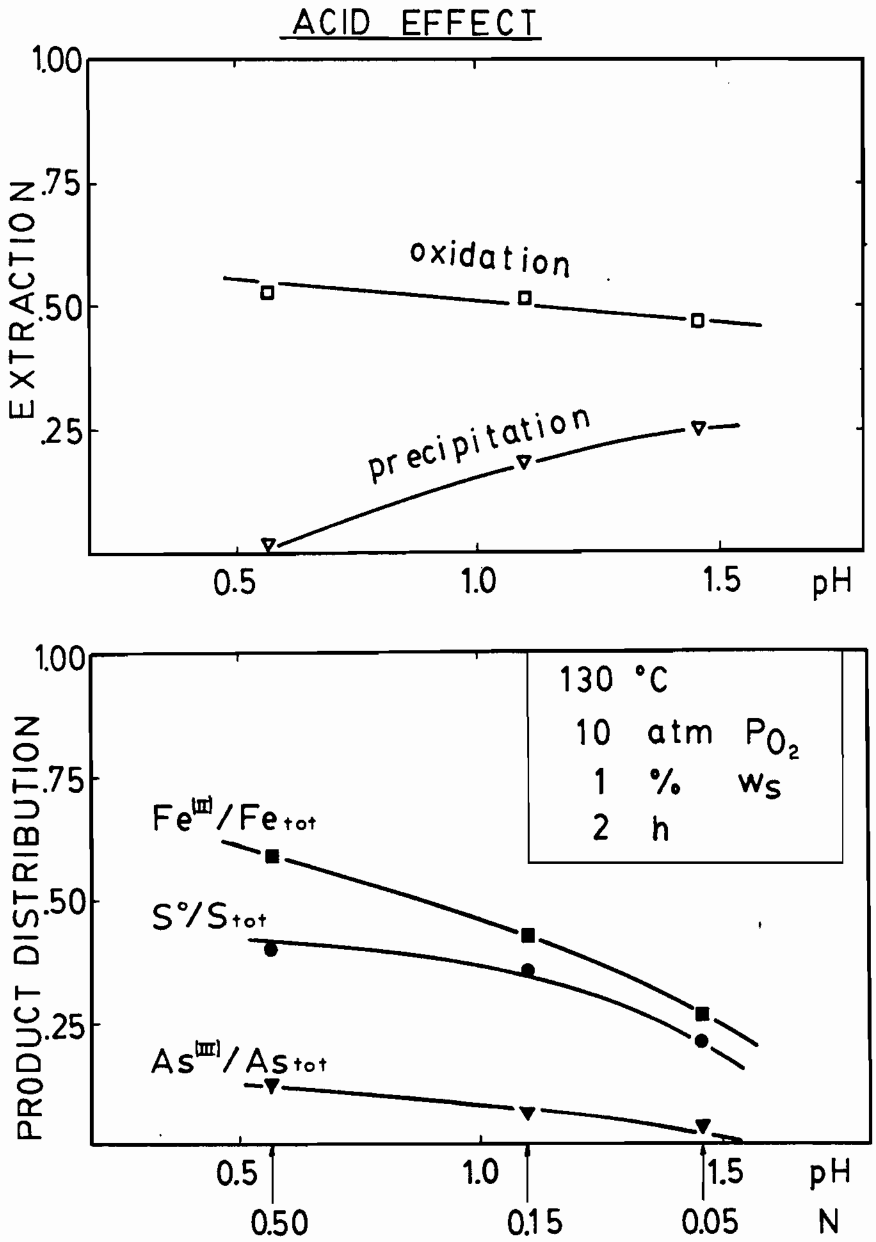

Figure 3.5: The effect of acid concentration on the conversion of arsenopyrite (top) and on the distribution of products (bottom). (Exp. conditions: 1013 kPa O_2; 2 hours; –74 +53 μm; 1% solids.)

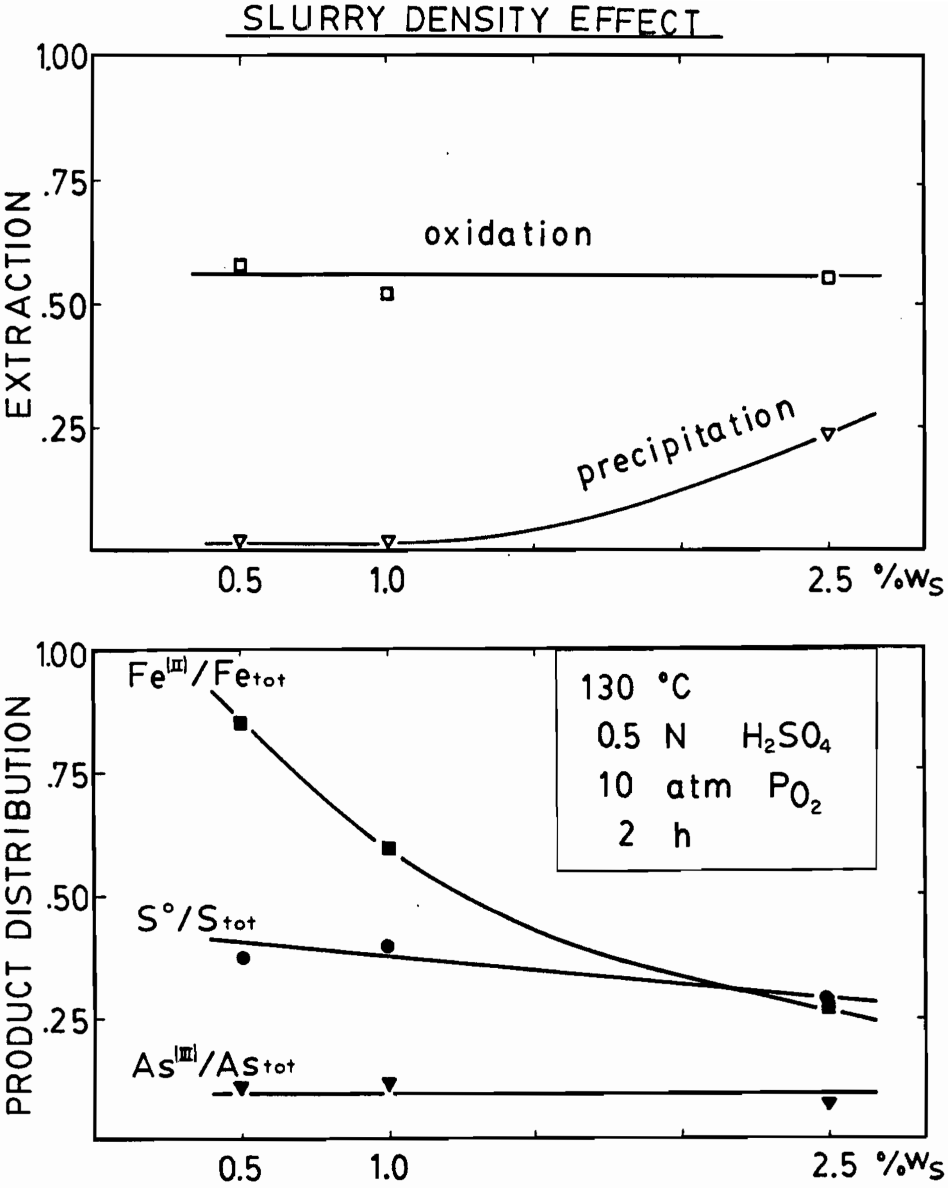

Figure 3.6: The effect of slurry density on the conversion of arsenopyrite (top) and on the distribution of products (bottom). (Exp. conditions: 1013 kPa O_2; 2 hours; 0.5 N H_2SO_4; and –74 +53 μm.)

in terms of ratios of $Fe(II)$ to total Fe extracted, S^0 to total sulphur extracted, and $As(III)$ to total arsenic extracted. The oxidation data shown on these Figures represent in each case the total fraction of initial arsenopyrite material oxidized (reporting in solution and/or precipitate). The precipitation data, on the other hand, refer only to the fraction of initial arsenopyrite material that reports in the precipitate.

Figure 3.3 shows the effect of reaction time on the extraction of arsenopyrite and on the distribution of products. The other parameters were kept constant throughout these tests, namely at 130 °C, 0.5 N H_2SO_4, 10 atm oxygen pressure and 1% slurry density, i.e. 2 g $FeAsS$/200 mL solution[3]. The extent of arsenopyrite oxidation increases with time while precipitation is observed only after 2 hours. Regarding product distributions, in the early stages of the reaction (1 h) most of the iron is in the ferrous state (75%) with elemental sulphur and sulphate sulphur present in almost equal amounts. Furthermore, most of the arsenic in solution is in the pentavalent state. As the oxidation of arsenopyrite progresses with time, the values of $Fe(II)/Fe_{\text{tot}}$ and S^0/S_{tot} decrease.

In order to establish the temperature effect, experiments were conducted at 130, 150, and 180 °C, with the other variables kept constant (i.e. 0.5 N H_2SO_4, 10 atm O_2, 1% slurry density, and 2 h reaction time). The effect of temperature is illustrated in Fig. 3.4. The oxidation of arsenopyrite is complete under the investigated conditions only at 180 °C. The most dramatic effect of temperature is on precipitation. Thus, at 180 °C, at which temperature all of the arsenopyrite has reacted, almost 80% of the oxidation products report to the leach residue. As the bottom graph of Fig. 3.4 suggests, almost all $Fe(II)$ and $As(III)$ are absent after 2 h at 180 °C while some elemental sulphur (10%) is still found even after 2 h at this high temperature.

The effects of acid concentration (over the range 0.05 to 0.5 N H_2SO_4) and slurry density (0.5 to 2.5% solids) at 130 °C were found to be marginal (Figs. 3.5 and 3.6). These variables mostly affected precipitation and product distribution. Thus,

---

[3] At that low solids concentration, slurry density values expressed in % w/w units are almost equal to % w/v units.

as seen in Fig. 3.5, the relative proportion of $Fe(II)/Fe_{\text{tot}}$ and S^0/S_{tot} decreases with increasing pH while an increase in slurry density apparently only affects the $Fe(II)/Fe_{\text{tot}}$ ratio. Of interest is the effect of pH on S^0 formation. Thus, in a test with no acid addition in the slurry (i.e. using distilled water), practically all of the oxidized sulphur was found to be in sulphate form with a final pH of 2.4. The product liquor from the latter test was cloudy due to an apparent colloidal suspension of suspected ferric arsenate. After the determination of the pH, the solution required heating and acidifying with H_2SO_4 in order to redissolve the colloidal precipitate and determine the As content. Well crystallized ferric arsenate formed in the high slurry density tests employing higher acidity was not readily soluble in hot H_2SO_4, and thus the digestion treatment described in Section 3.2.3 had to be adopted.

Several precipitates of greenish-yellow color, formed in the various tests described above, were collected and analyzed by X-ray diffractometry. In all instances, the only compound identified was crystalline hydrated ferric arsenate, $FeAsO_4{\cdot}2H_2O$, corresponding to the natural mineral scorodite (ASTM Powder Diffraction File no. 18-654). The XRD pattern of the precipitate is shown in Fig. 3.7 while in Fig. 3.8 a representative SEM picture of the same is given. These two figures confirm the excellent crystallinity of scorodite formed during pressure oxidation of $FeAsS$. Morphologically, the precipitated solids (Fig. 3.8) are well grown polycrystallite particles of more than 20 μm size.

In addition to the product identification work described above, several solution samples from a number of pressure oxidation tests conducted under conditions of no precipitate formation (0.1% solids) were analysed for As and Fe to determine the $FeAsS$ oxidation stoichiometry. The results obtained are illustrated in Fig. 3.9 in the form of conversion x, or equivalently "fraction extracted"[4] of $FeAsS$, calculated on the basis of Fe and As analyses. No deviation from stoichiometry is observed.

---

[4] In this chapter, the term "fraction extracted" is alternatively used to denote conversion.

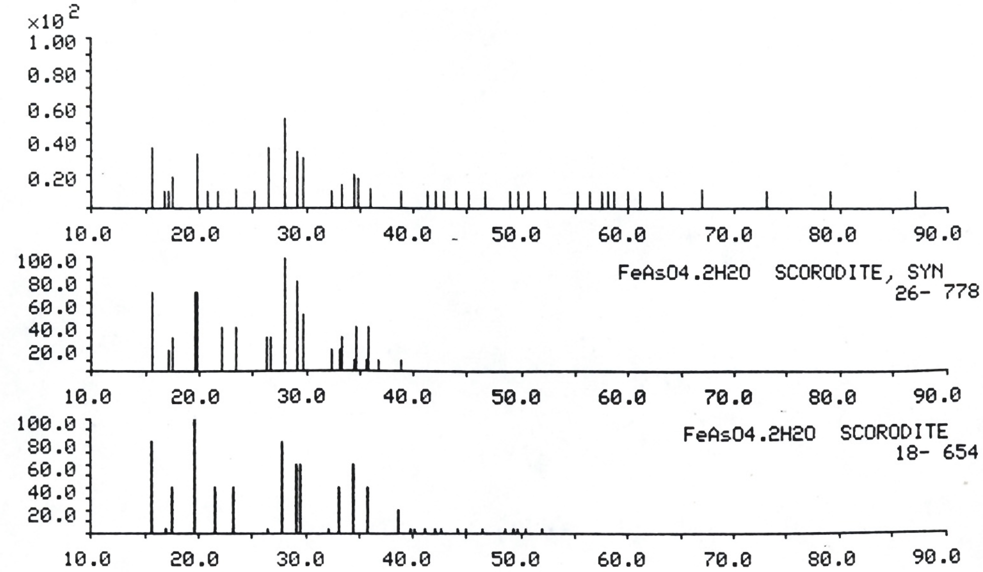

Figure 3.7: The X-ray diffraction patterns of the $Fe(III) - As(V)$ precipitate and scorodite. (Exp. conditions: 180 °C; 0.5 N H_2SO_4; 2 hours; 1013 kPa O_2; 1% solids.)

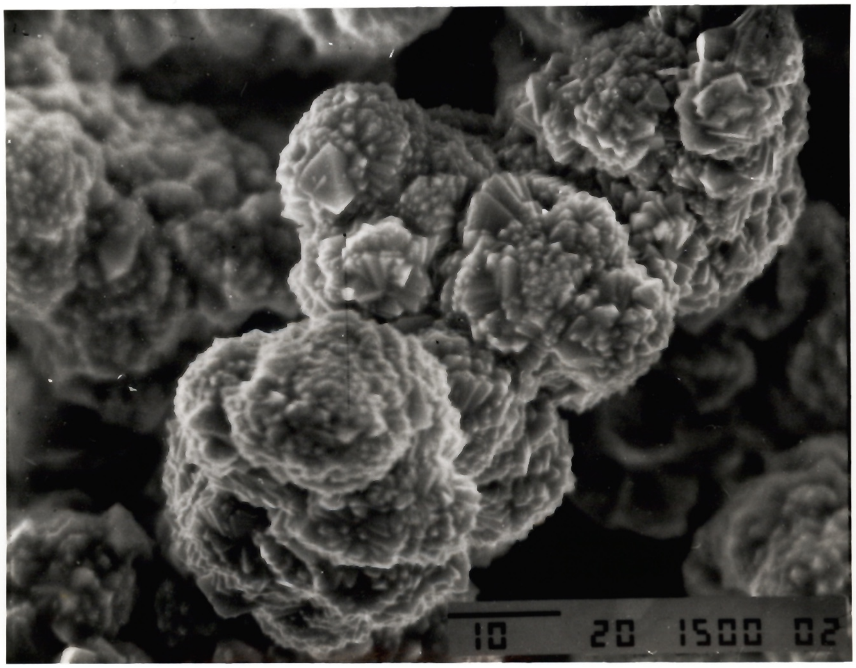

Figure 3.8: Scanning electron micrograph of the $Fe(III) - As(V)$ precipitate. (Exp. conditions: 180 °C; 2 hours; 1013 kPa O_2; 1% solids.)

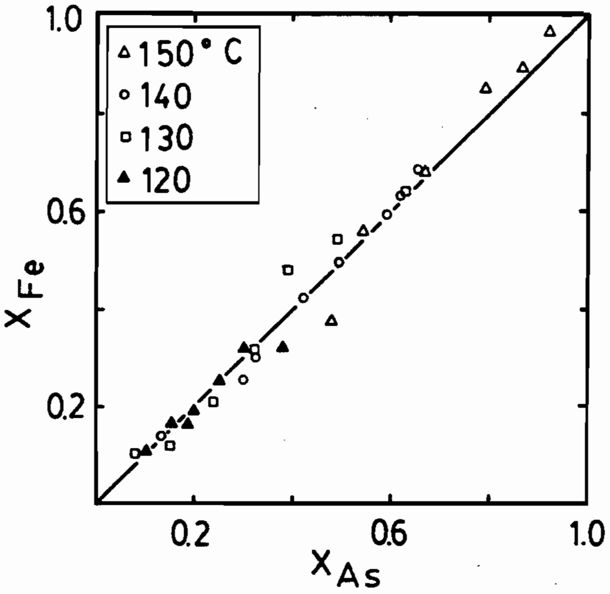

Figure 3.9: Conversion (x_{Fe}) based on *Fe* measurements versus conversion (x_{As}) based on *As* measurements at various temperatures. (Exp. conditions: 1013 kPa O_2; 0.5 N H_2SO_4; -74 +53 μm.)

Kinetic Results

As it was described in the previous subsection, during pressure oxidation of arsenopyrite, the highly insoluble scorodite compound forms. It was decided thus at the early stage of the kinetic investigation to establish a slurry density that would not be associated with precipitation. In that way the oxidation kinetics of *FeAsS* could be studied by monitoring simply the dissolved arsenic and/or iron concentrations and thus greatly facilitating the overall investigation. Furthermore, by using a low slurry density, possible O_2 mass transfer problems were effectively prevented, thus securing the unambiguous measurement of the intrinsic reaction kinetics. From a number of tests, where the amount of arsenopyrite mineral leached was varied while the other variables were kept constant at 130 °C, 10 atm O_2 and 0.5 N H_2SO_4, a slurry density of 0.1% solids was found to give precipitation-free conditions. Thus, throughout this series of experiments the slurry density was kept constant at 0.1% solids, that is 0.2 g *FeAsS*/0.2 L solution.

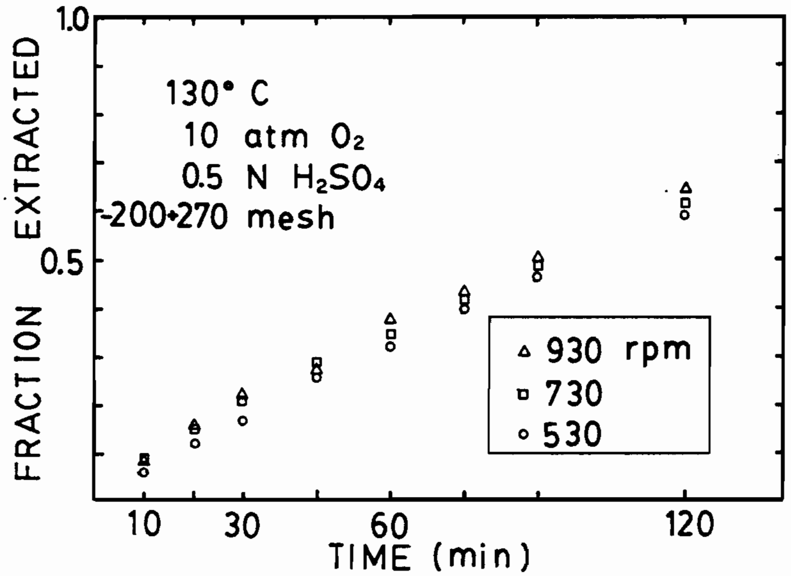

Figure 3.10: The effect of stirring speed on arsenopyrite conversion. (Exp. conditions: 130 °C; 1013 kPa O_2; -74 +53 μm)

Having thus established the slurry density for the kinetic investigations, the following variables were then studied: stirring speed, acid concentration, temperature, oxygen pressure, and particle size. Stirring speeds in the reactor were varied from 530 to 930 rpm. Lower speeds than 530 rpm were not applied since this was found to be the minimum speed to give adequate solids suspension, as it was determined by carrying out a series of agitation tests in glass liner that allowed visual observation. Results from these experiments expressed in terms of "fraction extracted", are shown in Fig. 3.10. Over this range of stirring speeds, no significant effect on the oxidation rate was found. Based on these data, the stirring speed of 730 rpm was chosen for all subsequent tests. Before the effects of the other variables are presented, it is important to clarify that As was chosen as the main element to monitor the oxidation kinetics of $FeAsS$ as a precaution against possible interference in the iron determination from corrosion of the sampling valve made of stainless steel.

All the results reported here were conducted at a constant 0.5 N H_2SO_4 concentration. The acid generated by the oxidation of $FeAsS$ itself was negligible in

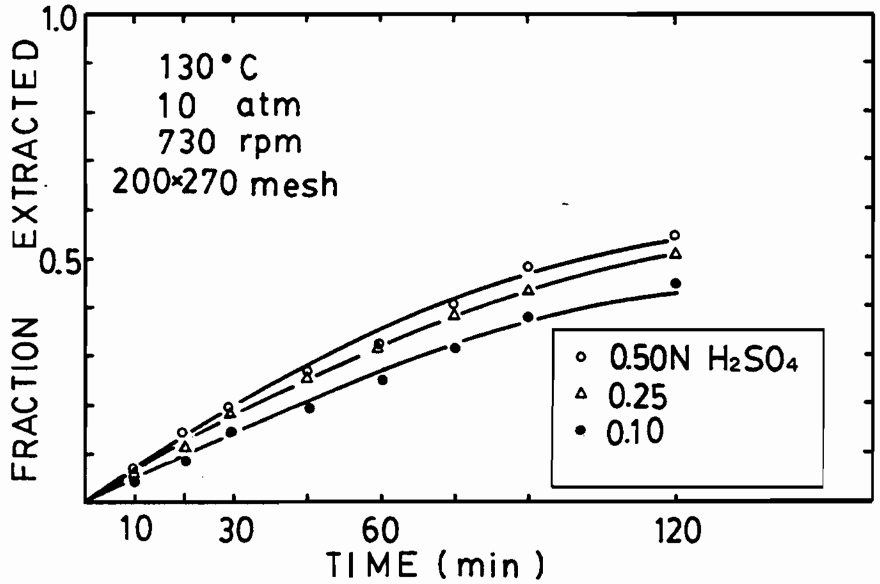

Figure 3.11: The effect of acid concentration on arsenopyrite conversion. (Exp. conditions: : 130 °C; 1013 kPa O_2; -74 +53 μm)

comparison to the 0.5 N acid level since a very small mineral quantity was used. Lower acidity levels were investigated as well and were found to result in somewhat reduced reaction rates as the results of Fig. 3.11 illustrate.

Figure 3.12 illustrates the effect of temperature at 10 atm O_2 pressure. All temperatures employed were higher than the melting point of elemental sulphur (119 °C), which forms in the present system. As it can be seen, temperatures above 150 °C are required to result in complete oxidation of arsenopyrite within the 2-hour reaction time employed. In Fig. 3.12 the test run at 130 °C was duplicated. These duplicated results along with the results of Fig. 3.10 demonstrate the degree of reproducibility of the arsenopyrite pressure oxidation tests.

The effect of partial oxygen pressure was determined for the range 203 kPa (2 atm) to 2026 kPa (20 atm) at 130 °C. The obtained results are given in Figure 3.13. It is clearly shown that an increase in oxygen pressure favours the overall oxidation kinetics. The effect of particle size is shown in Figure 3.14. All the results presented

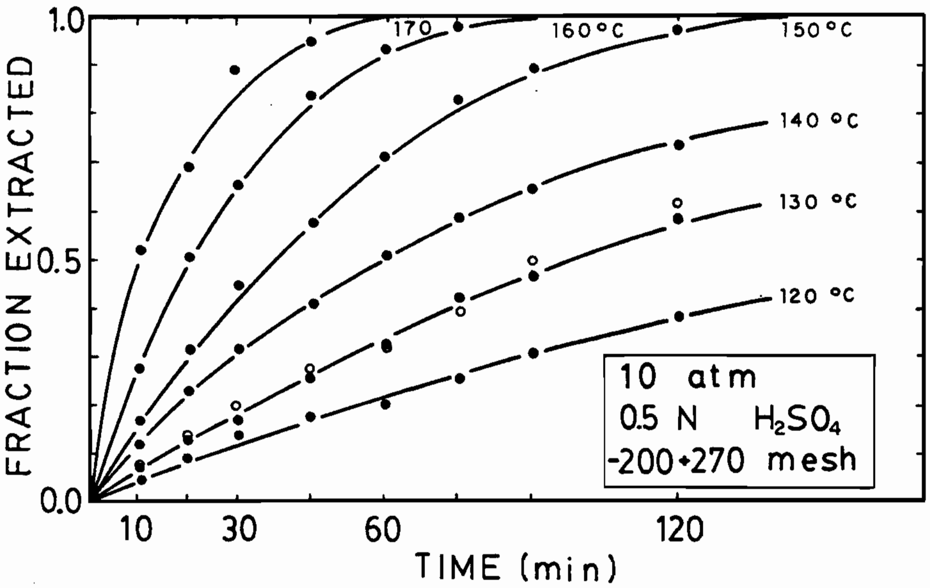

Figure 3.12: The effect of temperature on arsenopyrite conversion. (Exp. conditions: 1013 kPa O_2; 0.5 N H_2SO_4; -74 +53 μm)

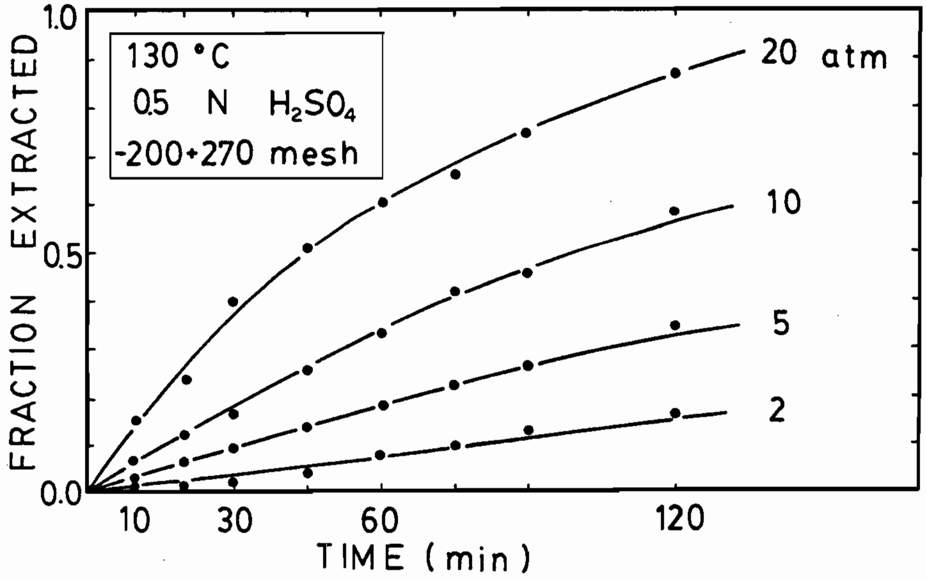

Figure 3.13: The effect of partial oxygen pressure on arsenopyrite conversion. (Exp. conditions: 130 °C; 0.5 N H_2SO_4; -74 +53 μm)

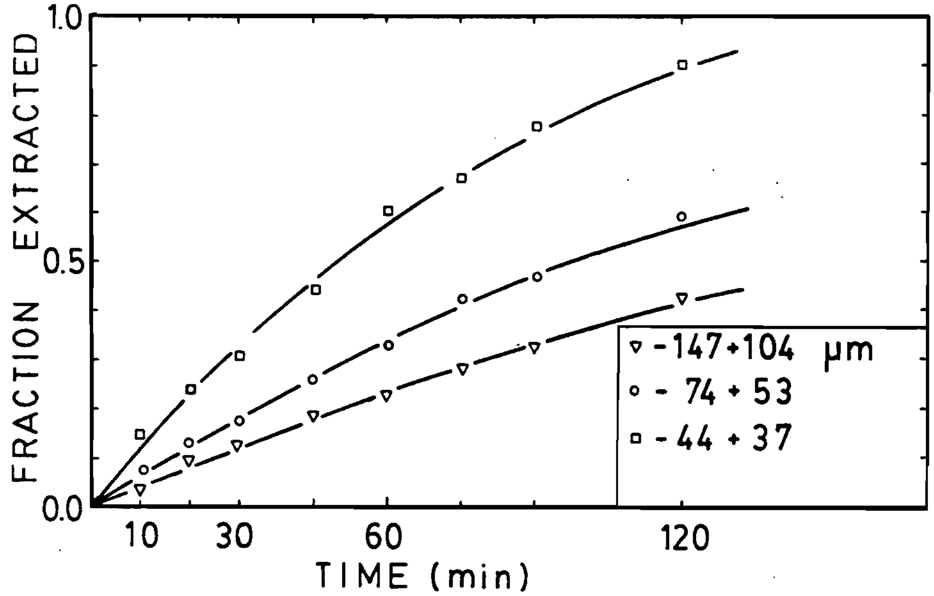

Figure 3.14: The effect of particle size on arsenopyrite conversion. (Exp. conditions: 130 °C; 1013 kPa O_2; 0.5 N H_2SO_4)

so far were established by using the monoclinic arsenopyrite mineral specimen. A number of tests were also carried out with the triclinic arsenopyrite variety. The obtained results are illustrated in Fig. 3.15.

3.3.3 Discussion

Reaction Chemistry

The results of Fig. 3.9 have indicated that the pressure leaching of arsenopyrite is stoichiometric in regard to the constituent elements of the mineral. There appears to be no formation of any intermediate sulphide containing solid phase. Phase transformation reactions have been observed in a number of sulphide mineral leaching systems such as those documented by Burkin [3.37] and Peters [3.38].

By considering the results of Figs. 3.3, 3.4, 3.12 and 3.15 it can be seen that the oxidation reaction proceeds to complete decomposition of the mineral without signs of catastrophic blockage from the produced scorodite solids or molten sul-

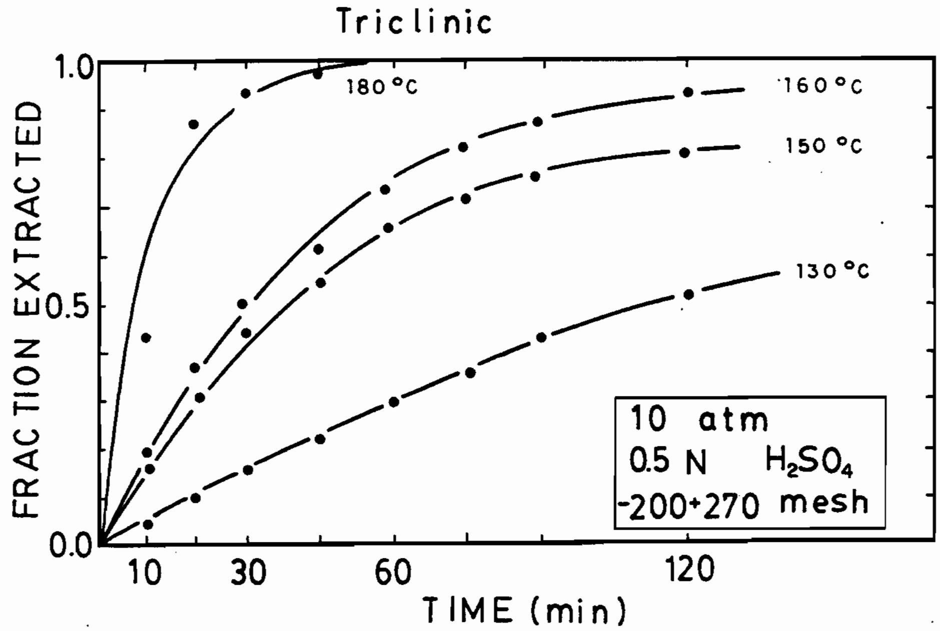

Figure 3.15: The effect of temperature on triclinic arsenopyrite conversion. (Exp. conditions: 1013 kPa O_2; 0.5 N H_2SO_4; -74 +53 μm)

phur. Examination of partially leached solids with scanning electron microscopy further strengthens the position that scorodite and $S^0(l)$ do not block the reaction. Fig. 3.16(top) shows a partially leached arsenopyrite particle (As) covered in part by assemblage of scorodite crystallites (SC) and elemental sulphur (S). The photograph shown in Fig. 3.16(bottom) was obtained by focusing on the S^0 region. Due to the intense energy of the electron beam, the elemental sulphur started evaporating upon SEM examination, thus rendering the picture somewhat unclear. Nevertheless Fig. 3.16(bottom) serves well to show that the molten sulphur has spread over regions of the partially leached particle. Moreover, Fig. 3.16(top) shows the surface of arsenopyrite after reaction to be irregular with evidence of high and low reactivity sites. The photographs of Fig. 3.16 were taken by using a residue produced at 130 °C, 10 atm O_2, 2.5% solids and 2 hours reaction time. Under these conditions 55% oxidation, 25% precipitation and 25% S^0 formation had occurred. Thus, the lack of any apparent hindering effect on the oxidation of arsenopyrite, in combination with the scorodite morphology illustrated in Fig. 3.16 leads to the conclusion that scorodite

Figure 3.16: Scanning electron micrographs of partially leached arsenopyrite particles (As: arsenopyrite; SC: scorodite; S: elemental sulphur. Exp. conditions: 130 °C; 1013 kPa O_2; 0.5 N H_2SO_4; 2 hours; 2.5% solids)

forms in the solution from dissolved iron and arsenic species rather than in the surface of the mineral by solid state transformation. This is further supported by the fact that all iron is extracted as ferrous from arsenopyrite and is subsequently oxidized to the ferric state in solution.

Evidently, ferric arsenate precipitation, in the form of scorodite, starts only after $Fe(III)$ and $As(V)$ concentrations exceed the solubility product of the compound (Fig. 3.3). It is obvious that the higher the slurry density the more extensive is the precipitation (Fig. 3.6), since more concentrated leach solutions are produced. The formation of scorodite is in agreement with the Eh-pH diagram predictions (Fig. 3.2). Furthermore, the precipitation is intensified with increasing temperature (Fig. 3.4), which suggests that scorodite formation is an endothermic process. Similar findings have been reported by Robins [3.15] for the temperature range 25 to 110 °C. In a later part of this section, the solubility product of scorodite is calculated as a function of temperature. Scorodite appears to precipitate at very fast rates considering the rather short retention time (2 h) applied in most of the tests. Mathematical modelling of the global reaction kinetics and equilibria governing the pressure oxidation of arsenopyrite which is described in Chapter 4, confirmed the notion of fast scorodite precipitation. Fast kinetics has also been reported in the parallel iron(III) phosphate precipitation system [3.39]. Dutrizac and Jambor [3.40], have also reported the formation of crystalline scorodite at elevated temperatures (160 °C) but they used nitrate rather than sulphate solutions. The precipitation of crystalline scorodite during pressure oxidation of arsenopyrite is of critical importance in view of the current controversy surrounding the environmental stability of ferric arsenates. Krause and Ettel [3.29], and Harris and Monnette [3.41] have recently demonstrated that well crystallized scorodite exhibits lower solubility by two orders of magnitude than reported previously in the literature [3.27, 3.28]. It remains to be seen, however, if scorodite forms from pressure oxidation solutions originating from concentrates where the ratio Fe/As is higher than unity. Work by Demopoulos and coworkers [3.42] on pressure chloride leaching of refractory gold concentrates ($Fe/As = 4$) has identified the presence of scorodite in the leach residue. No similar results exist from sulphate-based pressure oxidation testwork.

The ratio of ferrous iron to the total iron extracted (dissolved and precipitated) decreases with time (Fig. 3.3). Extrapolation to time $t = 0$ (i.e. at the point of oxygen introduction) shows that all iron is initially extracted as ferrous and is subsequently oxidized to ferric in the aqueous phase. Less ferrous ion is found at higher temperatures (Fig. 3.4) due to the apparent acceleration of the $Fe(II)$ to $Fe(III)$ oxidation reaction, which in turn results in more ferric arsenate precipitation. According to the Eh-pH diagram of Fig. 3.2 the actual iron species in solution are $FeHSO_4^{2+}$ and $FeHSO_4^{+}$. At 25 °C and under otherwise similar conditions the dominant species are $FeSO_4^{+}$ and Fe^{2+} respectively.

The relative proportion of $Fe(II)$ as depicted in Figs. 3.5 and 3.6 is in agreement with the well established oxidation kinetics of $Fe(II)$ to $Fe(III)$ by molecular oxygen in H_2SO_4 solution [3.43, 3.44, 3.45]. Higher acidities yield lower SO_4^{2-} or $FeSO_4^{0}$ [3.45] concentrations which have as a consequence slower overall oxidation kinetics or equivalently higher $Fe(II)/Fe_{tot}$ ratios (Fig. 3.5). On the other hand higher slurry densities result in more concentrated solutions in terms of $Fe(II)$, which in turn results in faster kinetics due to the second order dependency of the latter on $Fe(II)$ concentration. Consequently, scorodite precipitation is affected by the faster build-up of $Fe(III)$. Once more, the mathematical model described in Chapter 4, gave results in accordance with the analysis presented above.

Elemental Sulphur Formation: As it was noted with the results presented in Figs. 3.3 to 3.6, both sulphate and elemental sulphur were found always to be present in the oxidation mixture but with the former being the principal product. In an attempt to explain the production of the two oxidized sulphur species, the following analysis is offered. By representing the S^0 formation data in terms of percent yield vs. time and temperature, Figs. 3.17 and 3.18 were generated. These figures serve to show that at 130 °C the S^0 yield reaches the level of about 20% and thereafter

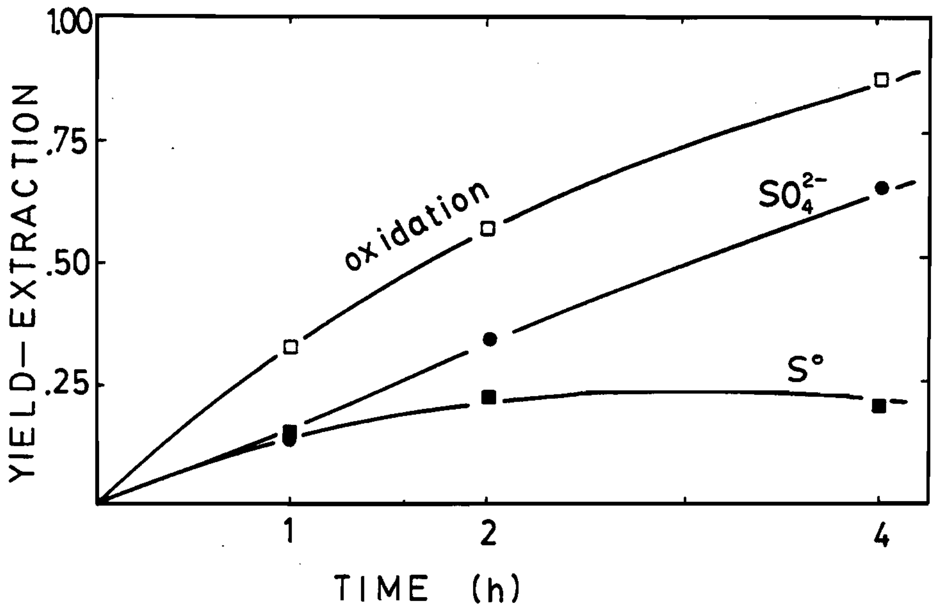

Figure 3.17: Percent yields of sulphur oxidation products and extent of arsenopyrite oxidation as a function of time at 130 °C. (Exp. conditions: 0.5 N H_2SO_4; 1013 kPa O_2.)

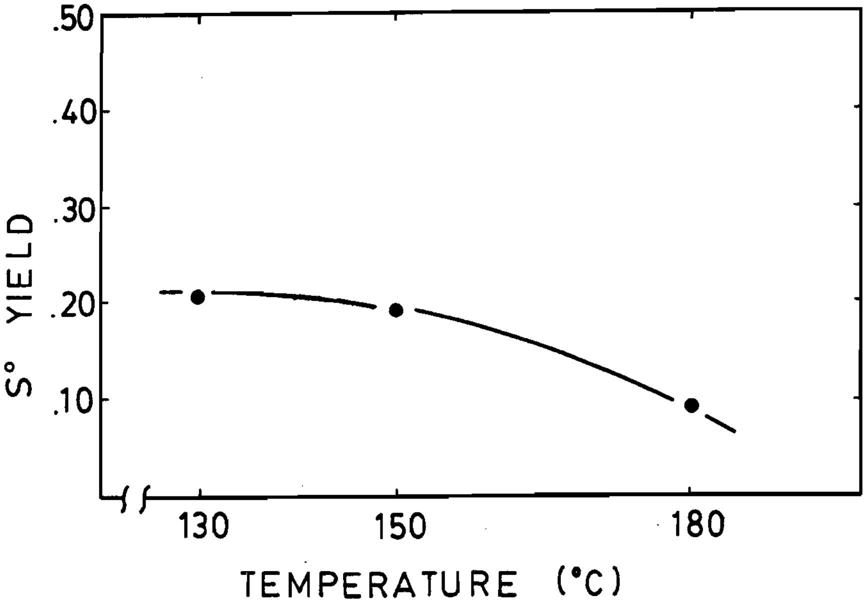

Figure 3.18: Percent yields of elemental sulphur as a function of temperature after 93 ± 6% arsenopyrite oxidation. (Exp. conditions: 0.5 N H_2SO_4; 1013 kPa O_2.)

remains constant. On the other hand, the data of Fig. 3.18 representing S^0 yields at almost complete arsenopyrite oxidation (87–99%) show the S^0 yield to remain the same (20%) between 130 and 150 °C, and to drop to 10% at 180 °C.

By analogy to the pyrite oxidation mechanism first recognized by McKay and Halpern [3.43] and later advocated by other investigators as well [3.46, 3.47, 3.48], it is postulated that the formation of elemental sulphur observed in the present arsenopyrite system is not an intermediate product but rather the result of a dual reaction mechanism. In other words, elemental sulphur and sulphate sulphur are thought to be produced via two parallel and competing reactions. The two parallel reactions are envisaged to be site specific with the sulphur forming path to be self-inhibiting. The latter view is consistent with the constant yields ($\sim$ 20% S^0) observed at 130 and 150 °C. On the other hand, the drop in the yield (10% S^0) at 180 °C may be attributed at least in part to very fast kinetics of the SO_4^{2-} forming reaction and to changes of the physical properties of liquid sulphur which are known to occur near 160 °C [3.49]. Oxidation of sulphur to sulphate may well be an additional contributing factor to the lowering of the S^0 yield. Although a common precursor species [3.50] for S^0 and SO_4^{2-} might be involved in the overall reaction scheme, nevertheless it does not seem very likely that the SO_4^{2-} is the outcome of the direct oxidation of S^0. This is particularly true for the lower temperature range (130–150 °C). Indirect support for the latter statement can be drawn from the work of Corriou and Kikindai [3.51]. Using their rate equations, it was calculated that after 6 h of pressure oxidation, only 0.7 and 9% oxidation of S^0 to SO_4^{2-} occurs at 140 and 200 °C respectively. Also on the basis of their data, the S^0 yield had to be at least 10 times less at 180 °C than that at 130 °C and not twice as was observed during the present work. Moreover, it is known that more than 90% S^0 recovery is obtained from zinc sulphide concentrates with pressure leaching at 150 °C [3.52] This is another indication of the kinetic stability of S^0 when it forms below 160 °C. Thermodynamically S^0 is unstable in the region of pressure oxidation conditions (Fig. 3.2).

It is of interest to compare the behaviour of $FeAsS$ *vis-a-vis* that determined for pyrite. Careful examination of the data published by Bailey and Peters [3.46] shows pyrite to produce approximately constant S^0 yields (25–34%) in the temperature region 100–130 °C at about 63% oxidation extent (Fig. 9 in ref. [3.46]). Similarly, the extent of reaction was not found to affect S^0 yield, this being constant at 33% between 56 and 98% pyrite oxidation (Fig. 2 in ref [3.46]). The S^0 yields are somewhat higher than those determined in this work apparently due to the difference in the acidity levels employed (i.e. 0.25 M in this work vs 1 M in ref. [3.46]). Increased acidity favours the formation of S^0 from arsenopyrite (Fig. 3.5) and pyrite [3.46, 3.43, 3.53] alike. This observation is another factor which points out the commonality of the reaction mechanism governing the pressure oxidation of the two minerals.

Arsenic Speciation: Most of the arsenic in solution is in the pentavalent state as non dissociated $H_3AsO_4(aq)$, according to the Eh-pH diagram of As-species in Fig. 3.2. $H_3AsO_3(aq)$ was never more than 10–15% of the total oxidized arsenic or more than 6% yield after 2 h oxidation at 130 °C in 0.5 N H_2SO_4. It is postulated that $H_3AsO_4(aq)$ is the direct product of the heterogeneous oxidation reaction rather than the result of a consecutive homogeneous reaction (i.e. oxidation of H_3AsO_3 to H_3AsO_4). This opinion is based on a complementary test in which $O_2/Fe(III)$ failed to oxidize a synthetically prepared H_3AsO_3 solution. The conditions of this test were: 4.9 g L^{-1} $As(III)$, 0.5 N H_2SO_4, 150 °C, 1050 kPa P_{O_2} and 0.05 M $Fe(III)$. No detectable change in the $As(III)$ concentration was found after 4 h. Undoubtedly more experimental evidence is needed to support this notion but it is interesting to see that gersdorffite ($NiAsS$), which possesses almost the same rest potential with arsenopyrite [3.4], was also found to yield $As(V)$ upon pressure leaching [3.54]. Preliminary results from an independent study on the room temperature electrochemical oxidation of $FeAsS$ also suggested the predominance of $As(V)$ [3.55].

Reactions Proposed: Based on the findings of the present work, reactions 3.2 to 3.5 are proposed to describe the pressure oxidation of $FeAsS$ in a H_2SO_4 leaching medium. These reactions are based on stoichiometric considerations rather than true speciation[5].

$$4FeAsS(s) + 13O_2(aq) + 6H_2O(l) \longrightarrow 4H_3AsO_4(aq) + 4Fe^{2+}(aq) + SO_4^{2-}(aq) \quad (3.2)$$

$$4FeAsS(s) + 7O_2(aq) + 8H^+(aq) + 2H_2O(l) \longrightarrow 4H_3AsO_4(aq) + 4Fe^{2+}(aq) + 4S^0(l) \quad (3.3)$$

$$2Fe^{2+}(aq) + \frac{1}{2}O_2(aq) + 2H^+(aq) \longrightarrow 2Fe^{3+}(aq) + H_2O(l) \quad (3.4)$$

$$Fe^{3+}(aq) + H_3AsO_4(aq) + 2H_2O(l) \longrightarrow FeAsO_4 \cdot 2H_2O(s) + 3H^+(aq) \quad (3.5)$$

Arsenopyrite is oxidized with oxygen predominantly yielding arsenic acid and sulphate sulphur according to reaction 3.2. Elemental sulphur is postulated to form through a parallel reaction path (eq. 3.3). The percent yield of the latter reaction does not exceed 20% within the temperature range of 130 to 180 °C and in the presence of 0.5 N sulphuric acid concentration. Ferrous ion produced by reactions 3.2 and 3.3 is further oxidized with oxygen to yield ferric (eq. 3.4). Finally, ferric ion combines with arsenic acid produced by equation 3.2 and 3.3 to form ferric arsenate, which precipitates as crystalline scorodite (eq. 3.5).

Furthermore, it should be noted that the acid produced during the pressure oxidation of $FeAsS$ is not the result of the oxidation reaction but the outcome of the hydrolytic precipitation of ferric arsenate (eq. 3.5). This differs from the corresponding oxidation of pyrite, which is primarily an acid generating reaction (eq. 10) in ref. [3.46]).

Reaction Thermochemistry: In designing a high temperature pressure oxidation plant for the treatment of refractory gold arsenical concentrates, the enthalpies of the

---

[5] The complexation of iron depends on total sulphate concentration, pH and temperature.

dominant reactions are required to carry out the necessary energy balance calculations. With the aid of $F*A*C*T$ [3.17], the standard enthalpy of reaction 3.2 (the dominant arsenopyrite oxidation reaction) and reaction 3.4 were calculated to be:

$$\Delta H^{\circ}_{3.2,298} = -5568.4 \text{ kJ}$$

and

$$\Delta H^{\circ}_{3.4,298} = -198.8 \text{ kJ}$$

It is thus evident that pressure oxidation of arsenopyrite is highly exothermic.

During pressure oxidation of arsenopyrite the highly insoluble scorodite compound forms and precipitates under conditions favouring build up of $As(V)$ and $Fe(III)$ in solution. Moreover the precipitation of scorodite was found to be favoured with increasing temperatures. The solubility product of scorodite $\mathcal{K}_{sp}$ is related to the free energy of the following reaction

$$Fe^{3+}(aq) + AsO_4^{3-}(aq) + 2H_2O(l) \longrightarrow FeAsO_4 \cdot 2H_2O(s)$$

through

$$\mathcal{K}_{sp} = \exp(-\frac{\Delta G^{\circ}_T}{\mathcal{R}T})$$

Using the thermodynamic data of Table 3.II and the extrapolation procedures outlined in Section 3.3.1, the solubility product was calculated at various temperatures and the results are plotted in Fig. 3.19. It can be seen that the formation of scorodite is endothermic for the whole temperature range of interest to pressure oxidation—an observation in agreement with the experimental findings of the present work (Fig. 3.4).

Reaction Kinetics

Shrinking Core Models: The object of the present kinetic study was primarily to develop a rate equation useful for reactor design and process modelling. To this end, the obtained experimental data are analysed in this section with the aid of shrinking

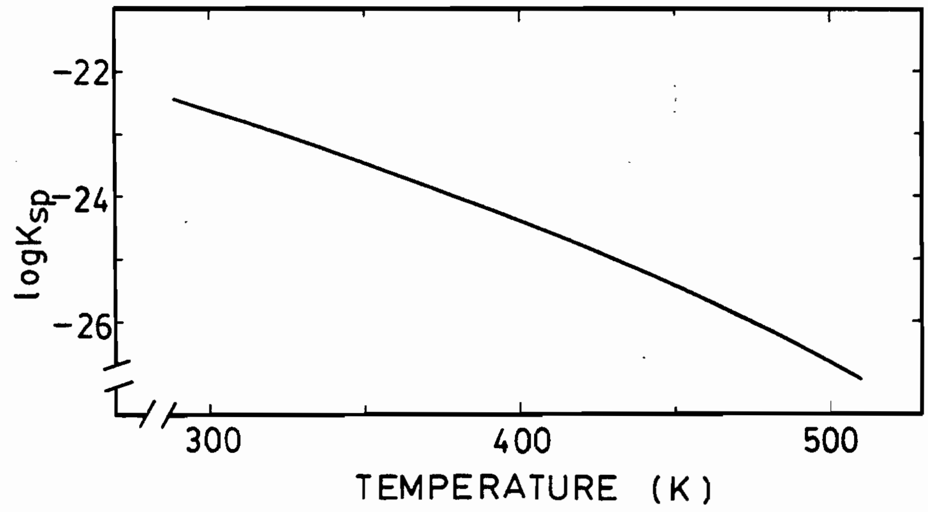

Figure 3.19: The solubility product of scorodite as a function of temperature.

core models which have been previously established (Section 2.4.1). Moreover, a mechanistic interpretation of the kinetic results is presented.

Disregarding diffusion control through the external boundary layer (see Fig. 3.10), the pressure oxidation of arsenopyrite is then expected to be controlled by either the surface reaction or the diffusion process through the product layer or combination of the two steps (i.e. mixed control). In the present system the product layer may consist of molten S^0 and scorodite particles adhering on the unreacted mineral surfaces. The basic assumptions on which the SCM is based are considered to be valid in the present system. Finally despite the high exothermic nature of the oxidation reaction 3.2 ($\Delta H^{\circ}_{3.2,298} = -5568$ kJ) assumption (d) in Section 2.4.1 is believed to be met in view of the very dilute slurry employed (see also Section 3.4.1 and Appendix A).

Initial Reaction Order: Before the shrinking core model equations are applied to the experimental kinetic data, the order of the initial reaction rate with respect to the partial pressure of oxygen will be established. The concentration of dissolved oxygen is considered to be proportional to its partial pressure according to Henry's law [3.57] i.e. $C_{O_2} = k_H^{-1} P_{O_2}$. This implies that Henry's constant is incorporated into the intrinsic rate constant.

The rate of arsenopyrite oxidation expressed as moles of oxygen disappearing per unit time, per particle is

$$-\frac{\mathrm{d}N_{O_2}}{\mathrm{d}t} = 4\pi r^2 k' P_{O_2}^p \tag{3.6}$$

where:

N_{O_2}, is the number of moles of oxygen at time t,

r, is the radius of unreacted core at time t,

k', is the apparent intrinsic rate constant ($= k_H^{-p} k$),

P_{O_2}, is the partial pressure of O_2.

From the stoichiometry of reaction 3.2

$$\frac{dN_{O_2}}{dt} = \frac{13\ \mathrm{d}N}{4\ \mathrm{d}t} \tag{3.7}$$

where N is the number of moles of $FeAsS$ present at time t. On the other hand, arsenopyrite conversion, x, is given by the following equation

$$x = \frac{N_0 - N}{N_0} \tag{3.8}$$

where N_0 is the initial number of moles of arsenopyrite. By differentiating equation 3.8 and combining with eqs. 3.6 and 3.7, equation 3.9 is obtained

$$\frac{\mathrm{d}x}{\mathrm{d}t} = \frac{16}{13N_0} r^2 k' P_{O_2}^p \tag{3.9}$$

A plot of $\ln \frac{\mathrm{d}x}{\mathrm{d}t}$ at $t = 0$ versus $\ln P_{O_2}$ would result in a straight line with slope p. The derivatives of x are taken at $t = 0$ since no elemental sulphur has yet been formed to interfere with the oxidation reaction. Second order polynomial regression was performed to fit the experimental data of Fig. 3.13. By taking the logarithms of the initial slopes ($\mathrm{S_i}$) of the regression polynomials at $t = 0$ and plotting them against the logarithms of the respective oxygen pressures, the graph of Fig. 3.20 was obtained. The resulting straight line (correlation coef. 0.997) has a slope of 1, indicating that the reaction is of first order.

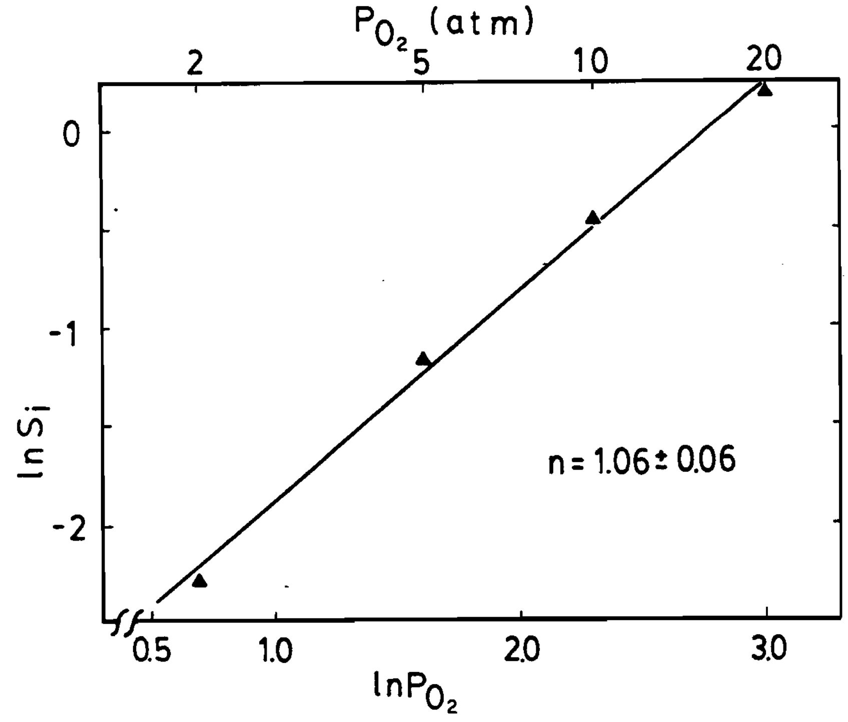

Figure 3.20: Arsenopyrite oxidation: Determination of the reaction order with respect to oxygen pressure by considering initial kinetics.

Surface Reaction Control: Analysis of the arsenopyrite pressure oxidation results (Figs. 3.10 to 3.15) indicated that all were in very good correlation with the surface reaction control SCM equation. Typically the agreement obtained is illustrated in Fig. 3.21, which represents the results of Fig. 3.12. The linearity of the "$1-(1-x)^{\frac{1}{3}}$ vs time" plots suggests that the reaction controlling step of the pressure oxidation of arsenopyrite is the chemical reaction taking place at the surface of the mineral. The SCM model equations for rate-limiting steps other than surface reaction (Section 2.4.1), failed to yield satisfactory correlation.

These findings strengthen further the notion that the minor liquid sulphur formation (10 to 20% yield), especially at the lower temperature range, does not interfere with the reaction kinetics of arsenopyrite oxidation. In other words, liquid sulphur does not form a protective impervious layer around the arsenopyrite particles. This is in contrast to the pyrite pressure oxidation system, where liquid sulphur has been found essentially to stop the reaction below the 100% oxidation level (Section 3.4.1 and ref.[3.46]). The totally different behaviour of the two minerals can be explained

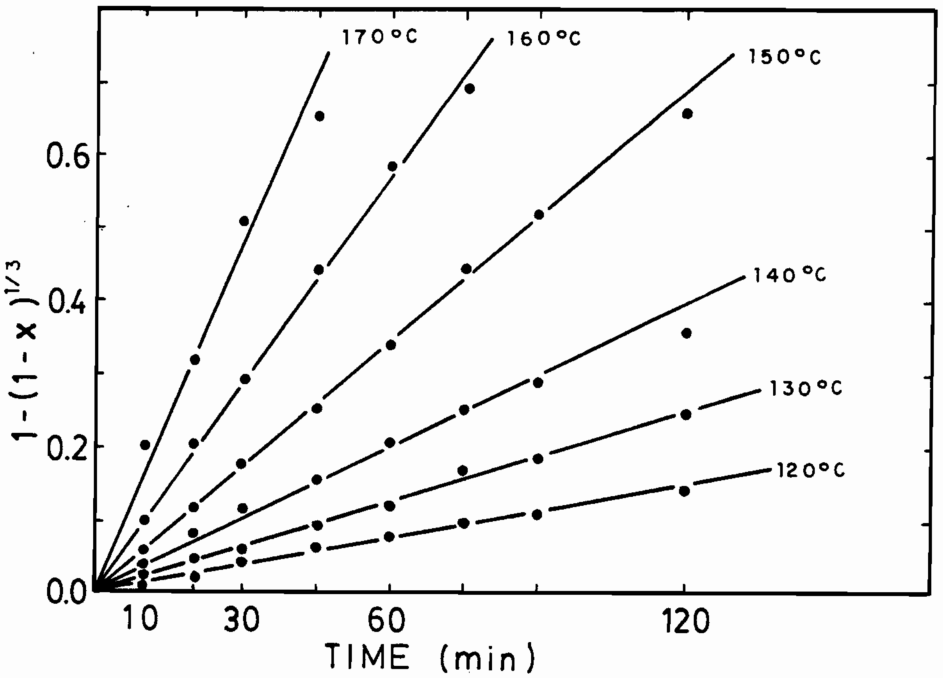

Figure 3.21: Arsenopyrite oxidation: Plots of the shrinking core surface reaction control model at different temperatures (data from Fig. 3.12).

by comparing their respective Pilling-Bedwarth ratios [3.58], z, defined as the volume of insoluble product formed per unit volume of solid reactant. Thus, the z values are:

$$z = \frac{2 \times 16.3 \text{ cm}^3 \text{ g-atom}_{S^0}^{-1}}{24 \text{ cm}^3 \text{ mol}_{FeS_2}^{-1}} = 1.36$$

for pyrite and

$$z = \frac{16.3 \text{ cm}^3 \text{ g-atom}_{S^0}^{-1}}{26.5 \text{ cm}^3 \text{ mol}_{FeAsS}^{-1}} = 0.62$$

for arsenopyrite. The molar volume values were calculated from Weast [3.59]. For sulphur, the value refers to crystalline monoclinic S_β (m.p. 119 °C). At temperatures above 119 °C the molar volume would increase but it is not expected to significantly affect the z values. It can be clearly seen that z is greater than unity in the case of FeS_2 (assuming that all sulphidic sulphur oxidizes to S^0) and this can result in a sulphur layer enveloping completely the reacting pyrite particle. However, in the case of $FeAsS$ ($z < 1$), the produced sulphur does not suffice to form a similar protective layer thus allowing the reaction to proceed to completion without any hindrance.

Apart from the elemental sulphur, of concern to the present reaction system is

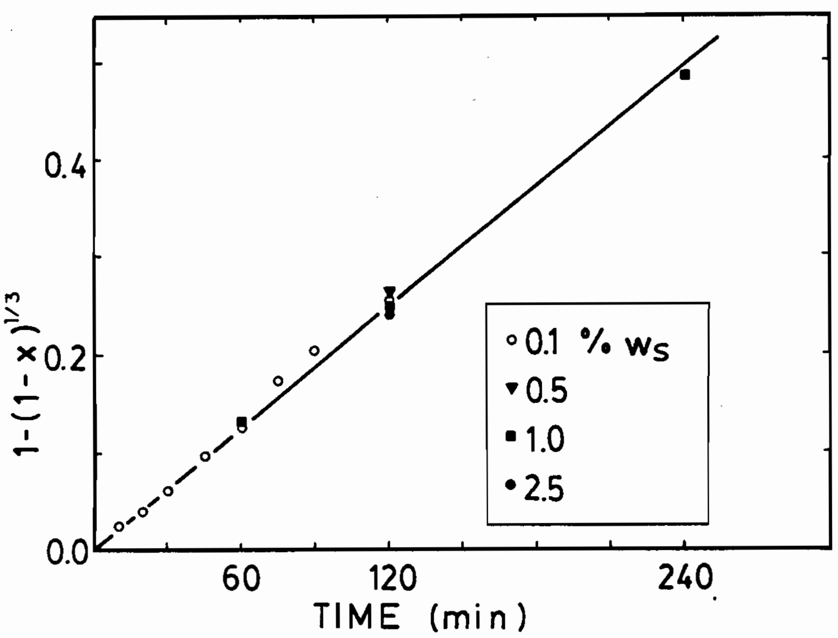

Figure 3.22: Plot of the shrinking core surface reaction control model for different slurry densities. (Exp. conditions: 130 °C; 1013 kPa O_2; 0.5 N H_2SO_4; –74 +53 μm).

also the possible effect the precipitation of ferric arsenate could have on the progress of the oxidation reaction. Application of the shrinking core surface reaction control model to the experiments represented by Figs. 3.3 and 3.6 in which precipitation had taken place, gave excellent agreement with the experimental data. The linear plot obtained is given in Fig. 3.22. In the same Figure, data from a precipitation-free (0.1% solids) experiment is plotted for the purpose of comparison. Thus, it can be seen once more that ferric arsenate precipitation does not interfere with the overall oxidation kinetics of arsenopyrite. This observation supports the fundamental assumption made in the early stages of the present investigation to monitor the kinetics of the oxidation reaction under precipitation-free conditions.

From the slopes of the "$1-(1-x)^{\frac{1}{3}}$ vs time" plots the k_S values were derived and the Arrhenius plot (Fig. 3.23) was constructed for both the monoclinic (Fig. 3.12) and triclinic (Fig. 3.15) arsenopyrite oxidation test results. Since the k_S values are directly proportional to the intrinsic rate constant (Section 2.4.1) and the data represent experimental runs of the same particle size (–74 +53 μm), the activation energy

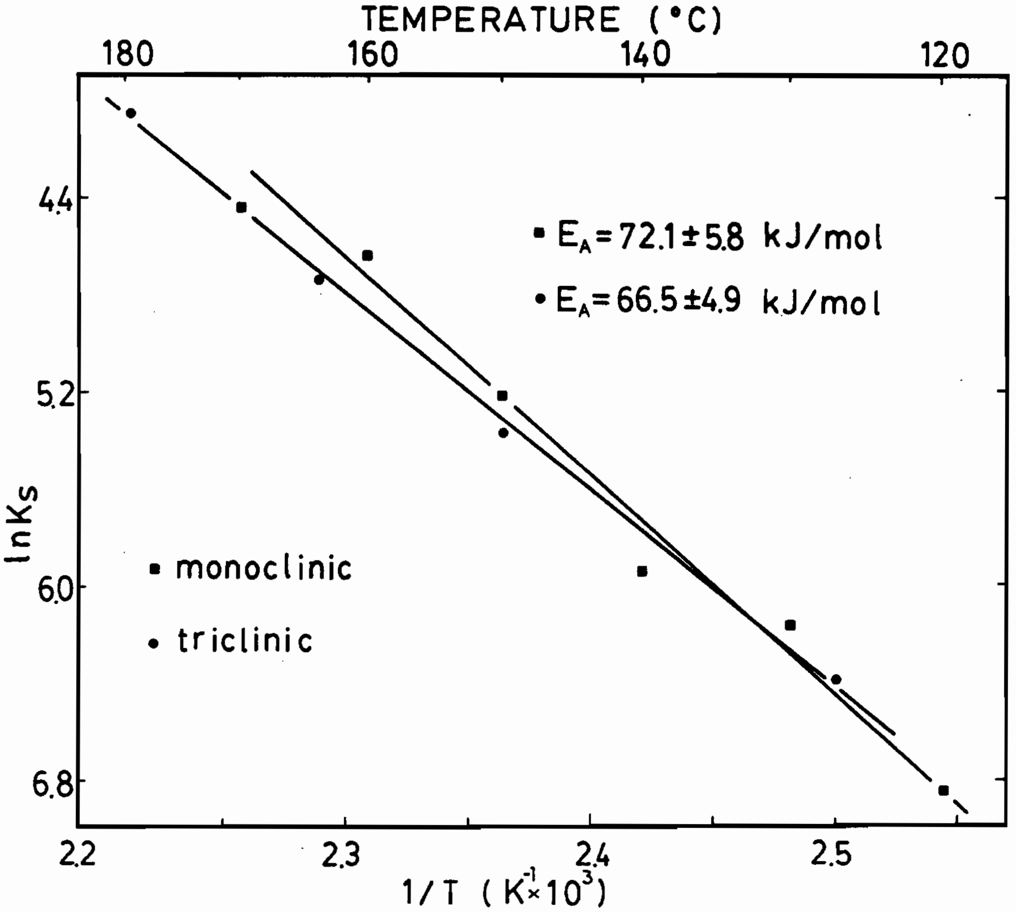

Figure 3.23: Arsenopyrite oxidation: Arrhenius plots (data from Figs. 3.12 and 3.15).

calculated is directly related to the intrinsic kinetics. The Arrhenius plot revealed an activation energy of 72.1 kJ mol^{-1} (17.2 kcal mol^{-1}) with a correlation coef. 0.988 for the tests involving the monoclinic arsenopyrite specimen and 66.0 kJ mol^{-1} (15.9 kcal mol^{-1}) with a correlation coef. 0.998 for the tests involving the triclinic mineral variety. This range of activation energy values supports the view that the pressure oxidation of arsenopyrite is controlled by the rate of the chemical reaction at the surface of the particles. Comparison of the activation energy determined for the pressure oxidation of arsenopyrite with those determined for pyrite oxidation (50–55 kJ mol^{-1} for temperatures below 160°C—see Section 3.4.1) shows stronger temperature dependence for the former mineral.

From the slope and intercept of the Arrhenius plot of Fig. 3.23 (monoclinic specimen) and SCM relations outlined in Section 2.4.1, the following SCM equation is formulated to represent the kinetics of $FeAsS$ oxidation in the temperature range 120 to 180 °C:

$$x = 1 - (1 - 1311\frac{P_{O_2}}{r_0}t\exp - \frac{8672}{T})^3 \tag{3.10}$$

In the above equation, P_{O_2} is expressed in atm and r_0 in cm. Furthermore, based on the stoichiometry of reaction 3.2 and the density value of $FeAsS$ (6.15 g mL^{-1} [3.59]), the explicit expression of the intrinsic rate constant for the pressure oxidation of $FeAsS$ (monoclinic) becomes

$$k' = 49.527\exp(-\frac{8672}{T}) \qquad \text{mol min}^{-1}\text{ cm}^{-2}\text{ atm}^{-1} \tag{3.11}$$

Consequently, the rate law of arsenopyrite oxidation becomes:

$$r_{FeAsS} = -49.527\exp(-\frac{8672}{T})P_{O_2} \qquad \text{mol min}^{-1}\text{ cm}^{-2} \tag{3.12}$$

Overall Oxygen Pressure Dependence: The linear plots of Fig. 3.24 add further support to the finding that the oxidation process is chemically controlled. Here the results of Fig. 3.13, representing experiments run at various partial oxygen pressures, are plotted in terms of the surface reaction control model (eq. 2.11). The straight lines

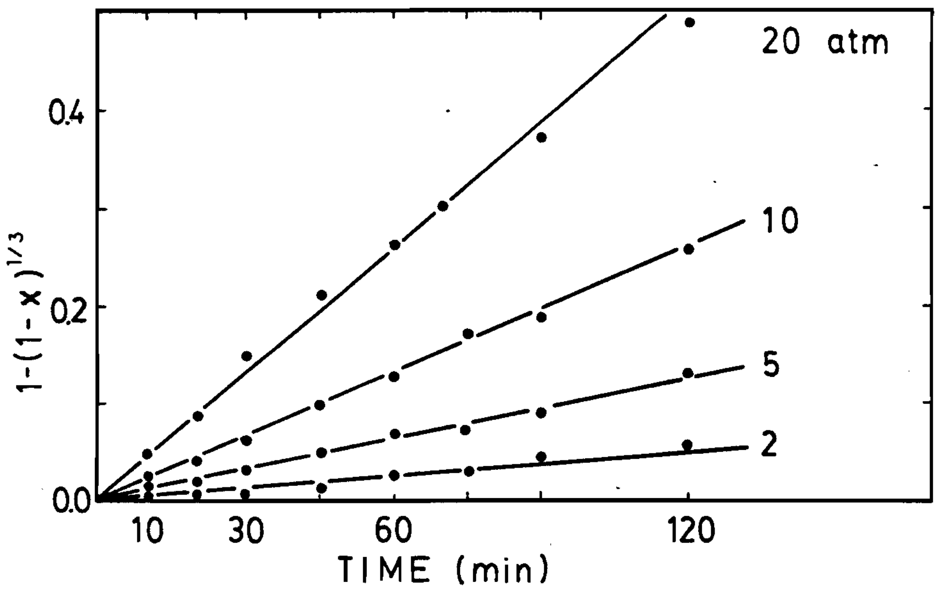

Figure 3.24: Arsenopyrite oxidation: Plots of the shrinking core surface reaction control model at different oxygen pressures (data from Fig. 3.13).

obtained indicate that the reaction mechanism does not change within the oxygen pressure range of 2 to 20 atm (203 to 2026 kPa).

The consistency of the first order dependence on pressure which was determined using initial rates (Fig. 3.20) was verified with the shrinking core model results of Fig. 3.24. Thus, by plotting the logarithm of k_S versus the logarithm of oxygen pressure (Fig. 3.25), a linear plot with slope essentially 1 (correlation coef. 0.988) was obtained. This plot confirms that pressure oxidation of arsenopyrite is first order with respect to oxygen pressure for the whole pressure range studied (2 to 20 atm). First order dependence on pressure has also been reported for pyrite oxidation at temperatures and pressures in the range of 25 to 160 °C and 0.2 to 10 atm, respectively [3.43, 3.53, 3.47]. However, for higher pressures a 0.5 order dependence has been reported for pyrite (Section 3.4.1 and ref.[3.46]). No tendency towards fractional order was detected in the present arsenopyrite oxidation system as it is testified by the plots of Figs. 3.20 and 3.25.

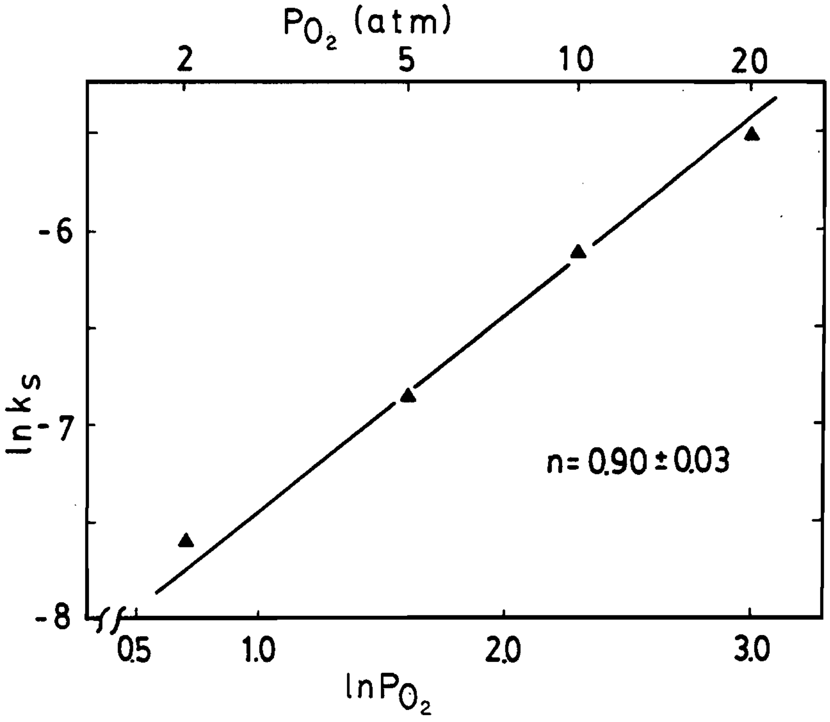

Figure 3.25: Arsenopyrite oxidation: Determination of the reaction order with respect to oxygen pressure by considering overall kinetics.

Particle Size and Acid Effects: Considering equations 2.11 and 2.14 (Section 2.4.1), and for a given temperature and oxygen pressure, plots of $\bar{r}_0[1-(1-x)^{\frac{1}{3}}]$ vs time would be expected to give a common straight line for the different particle sizes investigated. Such a "normalization" plot is shown in Figure 3.26, where $\bar{r}_0$ is the geometric mean radius of the particles corresponding to each size fraction. As it is seen, correlation of the three size fractions is very good.

The results of Fig. 3.11 were similarly analyzed with the aid of the shrinking core model and the dependence of the apparent rate constant (k_S) on H^+ concentration was found to be 0.3 (correlation coef. 0.995). The pertinent data are given in Table 3.VI. For the estimation of free H^+ concentration, H_2SO_4 was taken as being 50% dissociated, since its second dissociation constant is only 8×10^{-3} at 130 °C [3.60]. Bailey and Peters [3.46] also found that increased H_2SO_4 concentrations have a beneficial effect on pyrite pressure leaching.

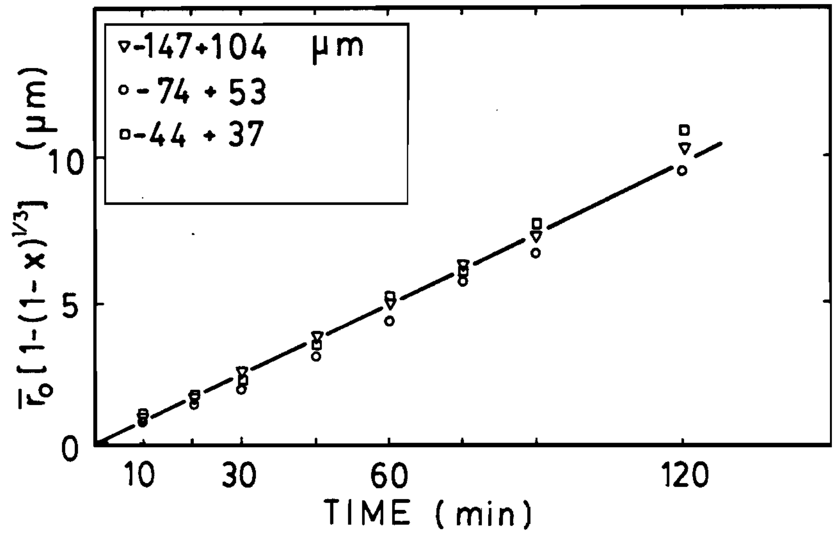

Figure 3.26: Arsenopyrite oxidation: Normalization plot of the shrinking core model (data from Fig. 3.14).

Table 3.VI: The dependence of rate constant k_S on H^+ concentration at 130 °C ($\ln k_S = 0.3 \ln C_{H^+}$).

$C_{H_2SO_4}$ (N)	C_{H^+} (M)	k_S min^{-1}
0.1	0.05	1.40×10^{-3}
0.25	0.125	1.94×10^{-3}
0.5	0.25	2.31×10^{-3}

Electrochemical Mechanism: The pressure oxidation of pyrite (rest potential 0.62 V [3.61]) has been well established to be electrochemically controlled [3.46]. Similarly the pressure leaching of chalcopyrite (rest potential 0.5 V [3.62]) has been interpreted as an electrochemically controlled process [3.63]. Arsenopyrite is also a semiconducting mineral (rest potential = 0.58 [3.16]) varying from p-type to n-type [3.64]. The behaviour of arsenopyrite as an electrocatalyst for oxygen reduction has been shown to be similar to that of other sulphide minerals such as pyrite [3.65]. It is therefore a reasonable assumption that its oxidation mechanism is of electrochemical nature in a similar fashion with that of pyrite.

The surface of arsenopyrite is envisaged to consist of anodic and cathodic sites on which the following two principal reactions[6] are believed to occur:

$$FeAsS(s) + 8H_2O(l) \longrightarrow Fe^{2+}(aq) + H_3AsO_4(aq) + SO_4^{2-}(aq) + 13H^+(aq) + 13e^- \tag{3.13}$$

$$O_2(aq) + 4H^+(aq) + 4e^- \longrightarrow 2H_2O(l) \tag{3.14}$$

The cathodic reduction of dissolved molecular oxygen at the mineral surface according to reaction 3.14 is considered the key process affecting the overall reaction kinetics. Among the several reaction paths proposed previously to account for the electrocatalytic reduction of O_2 [3.66, 3.67], the following is postulated as representing the present system:

1. Chemisorption of O_2

$$O_2(aq) + 2FeAsS(s) \longrightarrow 2FeAsS(O)_{\mathbf{ads}} \tag{3.15}$$

2. First electron-transfer

$$2(FeAsS(O)_{\mathbf{ads}} + H^+ + e^- \xrightarrow{\vec{k}_2} FeAsS(OH)_{\mathbf{ads}}) \tag{3.16}$$

3. Second electron-transfer

$$2(FeAsS(OH)_{\mathbf{ads}} + H^+ + e^- \xrightarrow{\mathbf{fast}} FeAsS + H_2O) \tag{3.17}$$

---

[6] Only the sulphate-forming anodic reaction, which dominates at high temperatures, is considered here; the possible influence of the Fe^{3+}/Fe^{2+} couple on the overall mechanism via the alternation of the mixed potential on the mineral surface is neglected.

The first electron transfer step (reaction 3.16) is taken as the rate-determining step. This is in agreement with the positive effect of H^+ concentration on the oxidation kinetics (see Table 3.VI). Alternative mechanisms call for negative or no effect at all, as has been shown in the case of low pressure (< 1 atm) pyrite systems [3.47, 3.68]. On the other hand, in high pressure leaching systems involving pyrite [3.46] and chalcopyrite [3.63], a similar effect with the present study has been found. The rate of reaction 3.16 with the aid of the Butler-Volmer equation (high field approximation) [3.67] can be expressed as follows:

$$i_c = -4\mathcal{F}\vec{k}_2\bar{\theta}C_{H^+} \exp \frac{-\vec{a}_c\mathcal{F}\Delta\phi_c}{\mathcal{R}T} \tag{3.18}$$

Similarly for the anodic oxidation of $FeAsS$ (reaction 3.13) it can be shown that

$$i_a = 13\mathcal{F}\vec{k}_a \exp \frac{\vec{a}_a\mathcal{F}\Delta\phi_a}{\mathcal{R}T} \tag{3.19}$$

where:

i_c, i_a, are the cathodic and anodic current densities,

k_2 and k_a, are the forward rate constants for cathodic (3.16) and anodic (3.13) reactions,

$\bar{\theta}$, is the fraction of arsenopyrite surface sites covered by dissolved oxygen (surface coverage by intermediates is neglected),

C_{H^+}, is the concentration of H^+,

$\vec{a}_c$, $\vec{a}_a$, are the transfer coefficients for the forward cathodic and anodic reactions respectively,

$\Delta\phi_c$, $\Delta\phi_a$, are the cathodic and anodic potentials,

$\mathcal{F}$, $\mathcal{R}$, and T, are the Faraday constant, gas constant and temperature respectively.

At the mixed potential $\Delta\phi_m$, $\Delta\phi_m = \Delta\phi_c = \Delta\phi_a$, the following equation applies (since reactions 3.13 and 3.14 do not carry the same number of electrons)

$$4i_a = -13i_c$$

which yields

$$\exp \frac{\mathcal{F}\Delta\phi_m}{\mathcal{R}T} = \left(\frac{\vec{k}_2\bar{\theta}C_{H^+}}{\vec{k}_a}\right)^{\frac{1}{\vec{a}_a+\vec{a}_c}} \tag{3.20}$$

Applying equation 3.20 to equation 3.19 gives

$$i_a = 13\mathcal{F}\vec{k}_a\Big(\frac{\vec{k}_2\bar{\theta}C_{H^+}}{\vec{k}_a}\Big)^{\frac{\vec{\alpha}_a}{\vec{\alpha}_a+\vec{\alpha}_c}} \tag{3.21}$$

Assuming $\vec{\alpha}_a = \vec{\alpha}_c$, the last equation becomes

$$i_a = 13\mathcal{F}\vec{k}_a\Big(\frac{\vec{k}_2\bar{\theta}C_{H^+}}{\vec{k}_a}\Big)^{\frac{1}{2}} \tag{3.22}$$

Equation 3.22 suggests the reaction rate to have half-order dependency on the hydrogen ion concentration and on the surface concentration of molecular oxygen ($\bar{\theta}$). The experimentally determined orders were found to be 0.3 for C_{H^+} and 0.9 for P_{O_2}. Different adsorption isotherms (Langmuir, Temkin, Freundlich) are available to describe the relationship between $\bar{\theta}$ and the applied partial oxygen pressure [3.69, 3.70]. A Freundlich type isotherm of the form $\bar{\theta} = k_F P_{O_2}^2$ which reduces to first order behaviour (eq. 3.22) may be assumed to apply. Given that no information on the exact form of this isotherm is available for the present high temperature three phase system, and that the comparison with the experiment ignores the contribution from the minor reaction path 3.3 and that a number of simplifying assumptions are inherent to the electrochemical kinetic theory, no further analysis is attempted. However, the proposed mechanism offers satisfactory explanation as to the effect of H^+ on the overall oxidation kinetics of arsenopyrite and the measured activation energies in the range of 66–72 kJ mol^{-1} further support the postulated activation control.

3.3.4 Summary

The acid (H_2SO_4) pressure (O_2) oxidation of arsenopyrite ($FeAsS$) has been studied in the temperature range 120 to 180 °C and 2 to 20 atm oxygen pressure. The pertinent reaction stoichiometries and kinetics have been determined. Arsenopyrite reacts with O_2, yielding elemental sulphur and sulphate with the latter being the dominant product. It is postulated that the oxidation process is site specific progressing via two parallel paths with the S^0 forming path being self-inhibiting. The process goes to completion without blockage due to liquid sulphur formation and/or scorodite precipitation. The formation of S^0 is favoured with increasing acidity. The presence of S^0 persists at temperatures as high as 180 °C (10% S^0). On the other hand, $H_3AsO_4(aq)$ was found to be the principal arsenic oxidation product. The latter appears to be the direct outcome of the heterogeneous oxidation process and not the result of a consecutive homogeneous reaction (i.e. $As(III)$ to $As(V)$).

Iron reports in solution as $Fe(II)$ (most likely as $FeHSO_4^+(aq)$), which is further oxidized to $Fe(III)$ ($FeHSO_4^{2+}(aq)$). Apart from higher temperatures, the oxidation of $Fe(II)$ to $Fe(III)$ is also favoured by high slurry densities and low acidities. The ferric ion produced combines with arsenic acid to form ferric arsenate, which precipitates as well grown scorodite ($FeAsO_4 \cdot 2H_2O$) crystals. The precipitation of scorodite is endothermic while the oxidation of arsenopyrite is extremely exothermic (the overall process being exothermic).

The oxidation kinetics was found to follow a shrinking core model with the surface chemical reaction as the rate-controlling step. The activation energy was determined to be in the range of 66 (triclinic arsenopyrite) to 72 (monoclinic arsenopyrite) kJ mol^{-1} for the whole temperature range investigated. The reaction order with respect to oxygen partial pressure was found to be 1 by considering both initial and overall kinetics. The acid concentration was also found to have a beneficial effect on the oxidation kinetics. Finally, normalization plots of the shrinking core model in the form of $r_0[1-(1-x)^{\frac{1}{3}}]$ vs time resulted in one straight line for various particle size fractions, thus further supporting the conclusion that the oxidation process is chemically controlled.

Having determined the activation energy and reaction order in terms of oxygen pressure, the following intrinsic rate equation was developed, based on the surface reaction control model, to represent the aqueous pressure oxidation of arsenopyrite (sulphate-forming reaction path 3.2):

$$r_{FeAsS} = -49.527 \exp(-\frac{8672}{T}) P_{O_2} \qquad \text{mol min}^{-1} \text{ cm}^{-2}$$

Finally an electrochemical reaction mechanism has been advanced involving chemisorp-

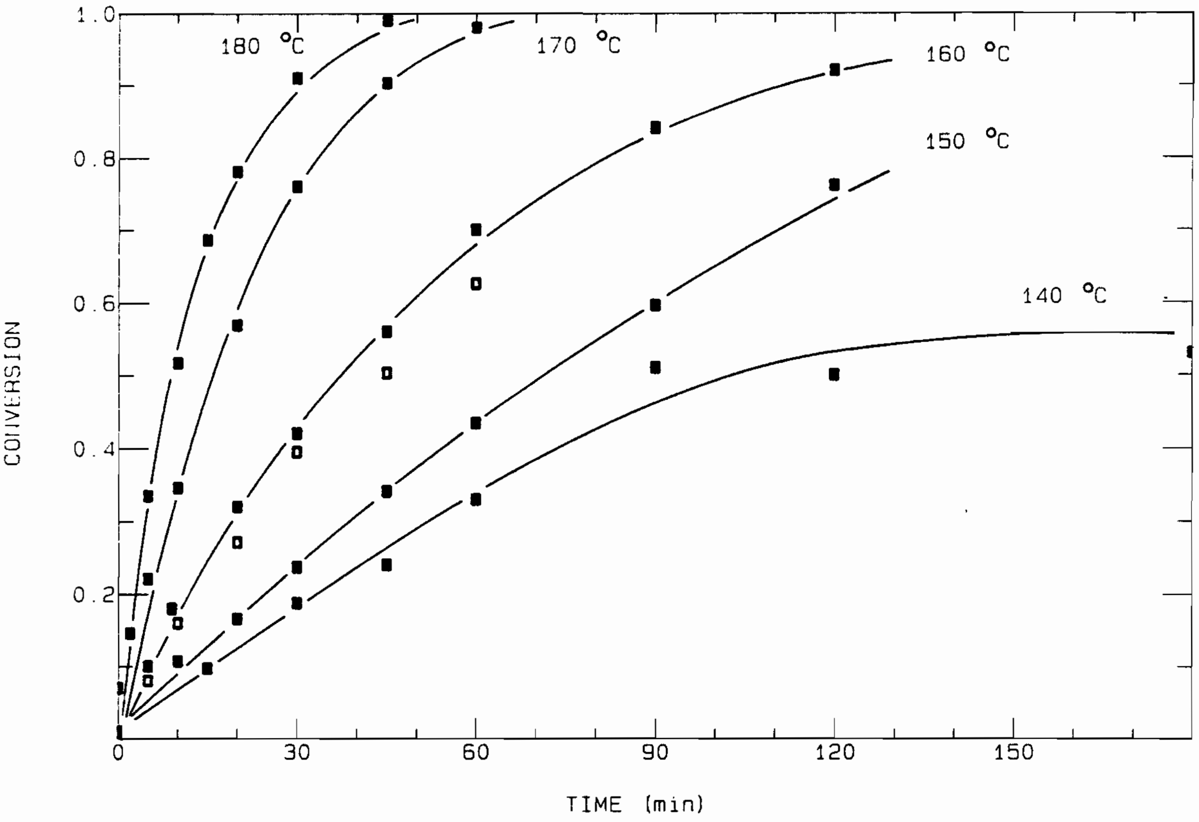

Figure 3.27: The effect of temperature on pyrite conversion. (Exp. conditions: 1013 kPa O_2, −74 + 53 μm; the hollow squares represent data from a duplicate test at 160 °C).

tion of oxygen on arsenopyrite surface followed by two single-electron transfer steps. The first electron transfer is postulated as being the rate determining step.

3.4 Pressure Oxidation of Pyrite

3.4.1 Results and Discussion

The following variables were studied: temperature (140 to 180 °C), oxygen pressure (5 to 20 atm at 150 and 170 °C), and particle size. Sulphuric acid concentration and stirring speed were kept constant throughout all tests at 0.5 M and 730 rpm respectively. The effect of temperature on pyrite oxidation at 10 atm partial pressure of oxygen is shown in Fig. 3.27. Temperatures above 160 °C are required to achieve 100% conversion within 1 h retention time. At 140 °C significant leveling off occurred

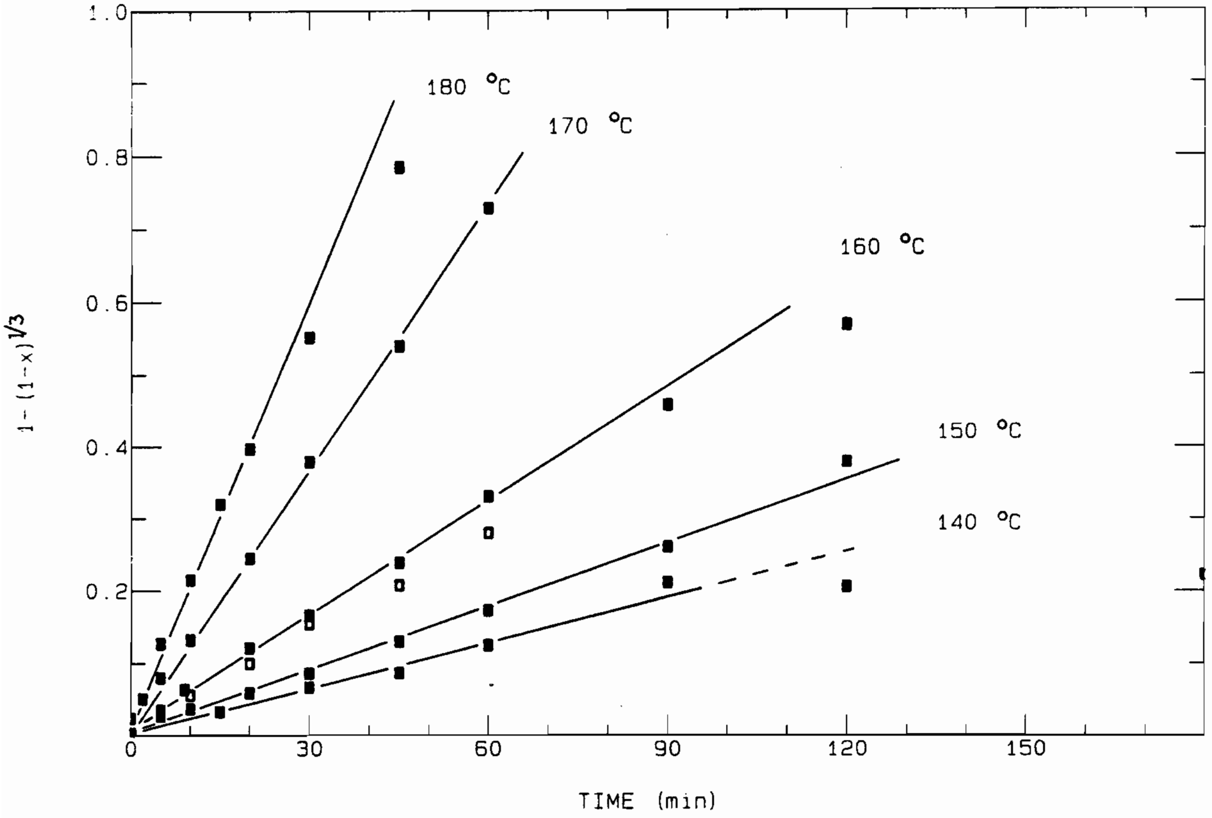

Figure 3.28: Pyrite oxidation: Plots of the shrinking core model surface reaction control for different temperatures.

which is attributed, as reported by Bailey and Peters [3.46], to the development of a kinetically inert [3.71, 3.51] liquid sulphur layer on the pyrite particles[7]. The interference of sulphur with the progress of the reaction was substantiated through visual observation made after the end of the low temperature (140–150 °C) tests where it was found that the partially reacted particles covered with the naturally hydrophobic S^0 were floating at the top of the solution. Pressure oxidation of $FeAsS$ shows only partial coverage of the grains by molten sulphur (Section 3.3.3).

The data of Fig. 3.27 were analysed with the aid of established shrinking core models (Section 2.4.1). The surface reaction control plots are shown in Fig. 3.28 while the respective diffusion through insoluble product layer plots are shown in Fig. 3.29. The linearity of the plots in Fig. 3.28 suggests that pyrite oxidation is controlled

---

[7] The melting point of monoclinic sulphur (S_β) is 119 °C

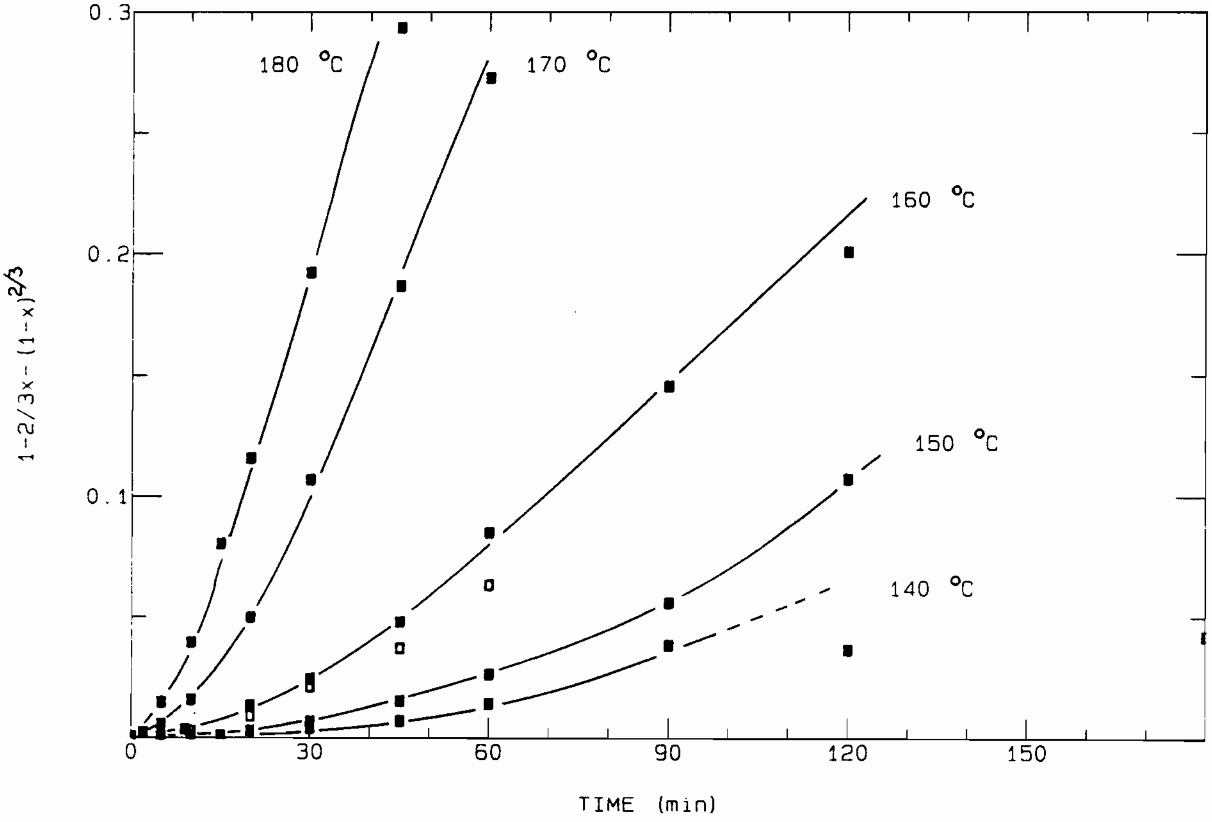

Figure 3.29: Pyrite oxidation: Plots of the shrinking core model diffusion through product layer control for different temperatures.

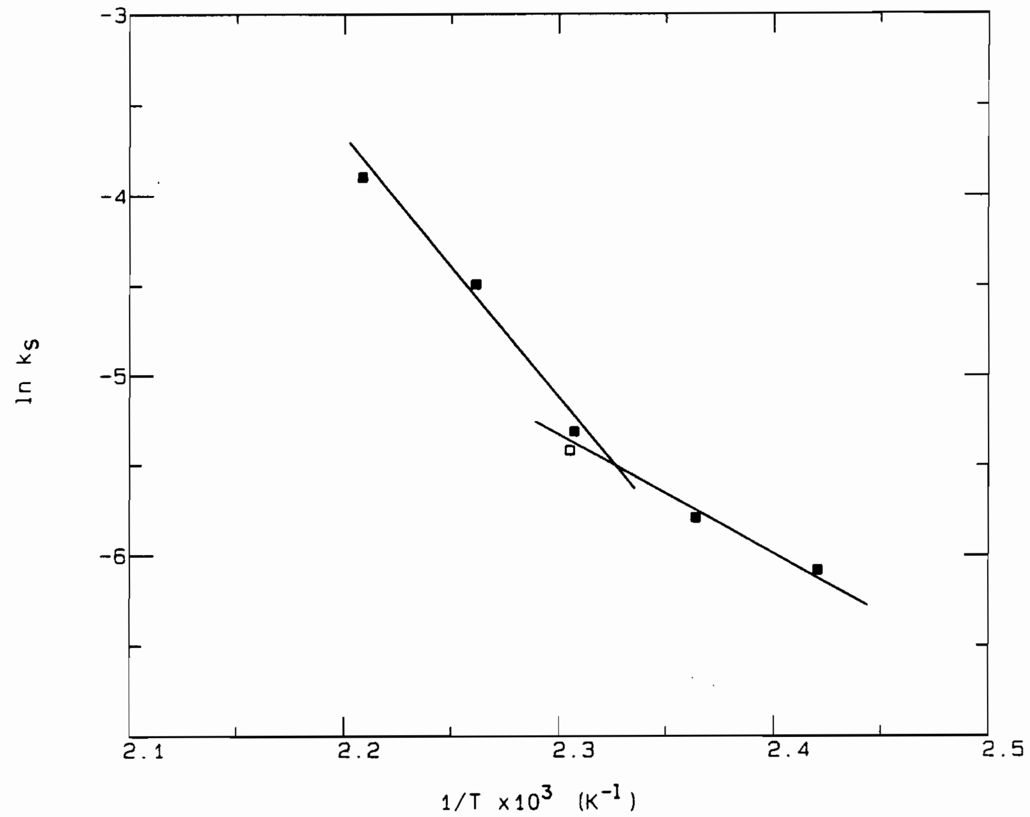

Figure 3.30: Pyrite oxidation: The Arrhenius plot.

by chemical reaction on the particle surface. Linearity is obeyed until almost 100% conversion at the higher temperature region, which is of importance to the industrial pressure oxidation practice. The apparent surface reaction control mechanism is in total agreement with the findings of other investigators (see Table 3.II).

Taking the slopes of the surface reaction control model lines $(1-(1-x)^{\frac{1}{3}} = k_S t)$, shown in Fig. 3.28, which are equal to the apparent rate constant, k_S, an Arrhenius plot was constructed which is shown in Fig. 3.30. Two distinct regions are observed. The first, between 140 and 160 °C, has an activation energy of 46.2 kJ mol^{-1} (11 kcal mol^{-1}) with a correlation coefficient of 0.998. The other region, between 160 and 180 °C, has a value of 110.5 kJ mol^{-1} (26.4 kcal mol^{-1}) with a correlation coefficient of 0.985. Once again it appears that a temperature near 160 °C is of critical importance. Among the activation energy values listed in Table 3.II, only those corresponding to temperatures less than 160 °C compare well with the 46.2 kJ mol^{-1}

found in this work. Values reported by Warren [3.72] and Cornelius and Woodcock [3.73], who investigated temperatures exceeding 160 °C, are intermediate to the low and high activation energy values reported here and apparently reflect overall values. In these early investigations ([3.72, 3.73]) no distinction between low and high activation energy regions was made.

The reason for the shift in the activation energy is not totally clear. Early on during the course of this investigation, it was thought that the observed break in the Arrhenius plot could well be due to significant difference between the true reaction temperature (particle surface temperature, T_s) and the bulk solution temperature (T_b) monitored experimentally. In other words, due to the high exothermicity of the oxidation reaction it was felt that T_s could have been considerably higher than T_b and subsequently an Arrhenius plot of $\ln k_S$ vs. $1/T_s$ rather than $1/T_b$ (as is the case of Fig. 3.30) would have given a straight line with a lower overall activation energy value. To test the hypothesis, that above 160 °C the surface temperature is higher than the bulk temperature, the heat balance around a reacting particle was considered and the calculations made are outlined in Appendix A. According to this analysis, no appreciable difference was detected which leads to the conclusion that the observed dual activation energy behaviour is not due to some uncontrolled experimental parameter but rather to the inherent nature of the heterogeneous reaction itself.

A break in the Arrhenius plot at 160 °C has also been reported by Corriou *et al* [3.74] for the pressure leaching of zinc sulphide in aqueous sulphuric acid. Corriou and coworkers explained this phenomenon by postulating the intermediate formation of H_2S which reacts with H_2SO_4, the latter acting as an oxidant only above 150 °C. However, this mechanism is not likely for the pressure oxidation of pyrite, which is known not to undergo nonoxidative dissolution (ionic model $Fe^{2+}(S_2)^{2-}$) [3.43, 3.75]. Thus, some other underlying mechanism must be held responsible for the change in the activation energy observed in the present work. It is assumed here that (in agreement with previous investigations [3.43, 3.53, 3.46]) the oxidation of pyrite yields predominantely SO_4^{2-} with some elemental sulphur forming too. For example, McKay and Halpern [3.43] determined ~10% S^0 yield at 120 °C after 50% pyrite oxidation in 0.07 M H_2SO_4 solution. Gerlach and coworkers [3.53] reported 7% S^0 yield at 160 °C after 70% pyrite conversion in 0.2 M H_2SO_4 solution, and Bailey and Peters [3.46] found 25% yield at 130 °C in 1 M H_2SO_4 solution. The variation in the percent S^0 yield is attributed mostly to the different levels of acidity employed by each group of investigators. In any case, these values serve to indicate that S^0 forms to a certain degree (although minor). It is envisaged that the oxidation of pyrite is site specific progressing via the two parallel reaction paths which are shown below (reactions 3.23 and 3.24) and have been postulated previously [3.46, 3.50]:

$$FeS_2 + \frac{7}{2}O_2 + H_2O \longrightarrow FeSO_4 + H_2SO_4 \tag{3.23}$$

$$FeS_2 + 2O_2 \longrightarrow FeSO_4 + S^0 \tag{3.24}$$

The activation energies determined here or for that matter by all previous investigators as well refer to the overall kinetics of these two parallel reactions. Intrinsic variable rates or inherent physical properties of the constituents of each reaction path may be the cause for the observed break in the Arrhenius plot.

Liquid sulphur is known to exhibit a sudden increase in viscosity at 159 °C which is due to cleavage of the S_8 rings and formation of chains (polymerization). The increase in viscosity by a factor of 10^4 reaches a maximum at 200 °C [3.76]. Corriou and Kikindai [3.51], who studied the oxidation of liquid elemental sulphur, also found 160 °C to be a significant temperature and have presented two different kinetic models accounting for the two allotropic forms of sulphur, below and above this characteristic temperature. It may well be that this change in the physical properties of molten sulphur is at least partly responsible for the two activation energy regions.

Alternatively, a shift in the electrochemical reaction controlling step due to changes in the semiconducting properties of FeS_2, or for that matter in the mode of oxygen adsorption, could be behind the observed kinetic behaviour. In view of

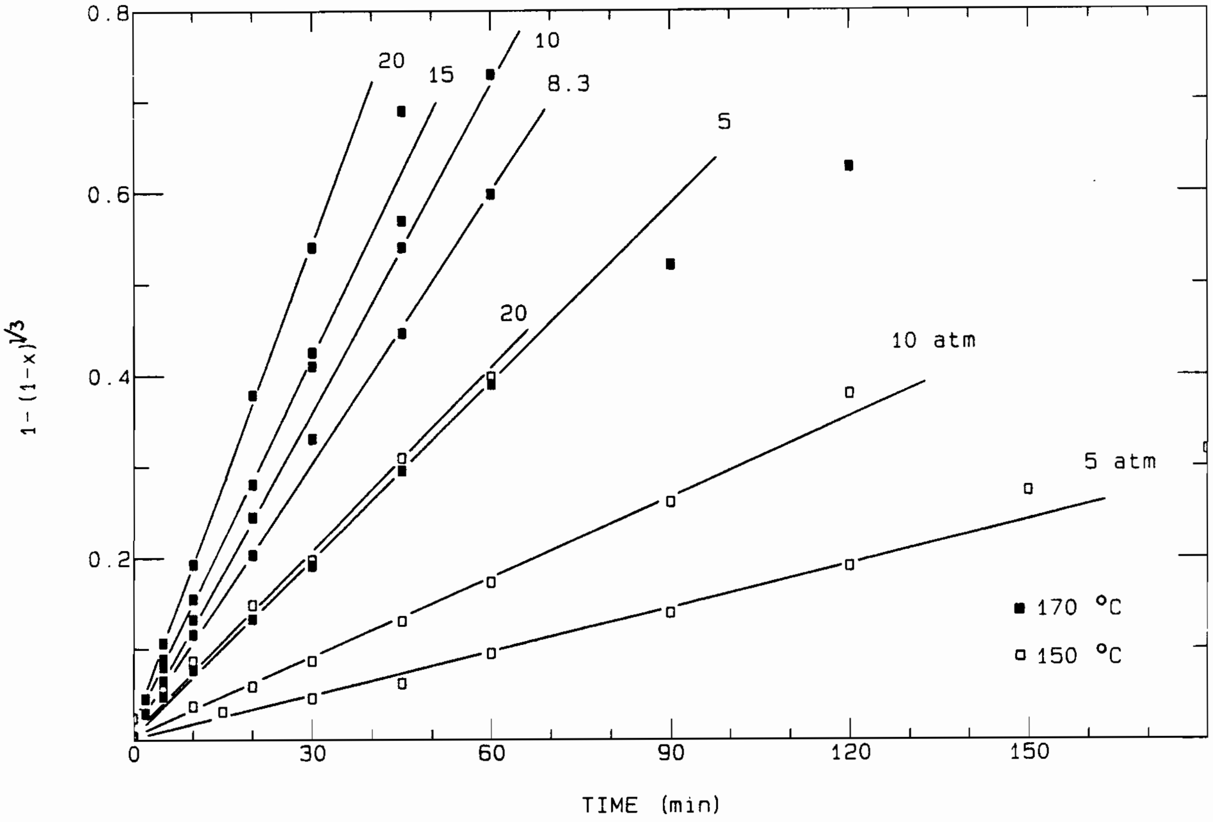

Figure 3.31: Pyrite oxidation: Plots of the shrinking core model surface reaction control for different pressures at 150 and 170 °C.

the complexity of the reaction system and the scarcity of fundamental data on the latter two properties, no further attempts at mechanistic interpretation are made. Moreover, the principal objective for the present work was the development of an overall rate equation of the high temperature pressure oxidation of pyrite, based on bulk reaction parameters suitable for process reactor modelling.

A number of kinetic tests were performed at 150 and 170 °C with partial pressures of oxygen varying between 5 and 20 atm (507–2026 kPa) in an effort to establish the order of the reaction. The obtained results were analysed with the surface reaction control shrinking core model and are plotted in Fig. 3.31. The linearity of the plots indicates that the controlling step (chemical reaction on the particle surface) does not change within the oxygen pressure range investigated. To determine the order of the reaction rate with respect to oxygen partial pressure, plots of the

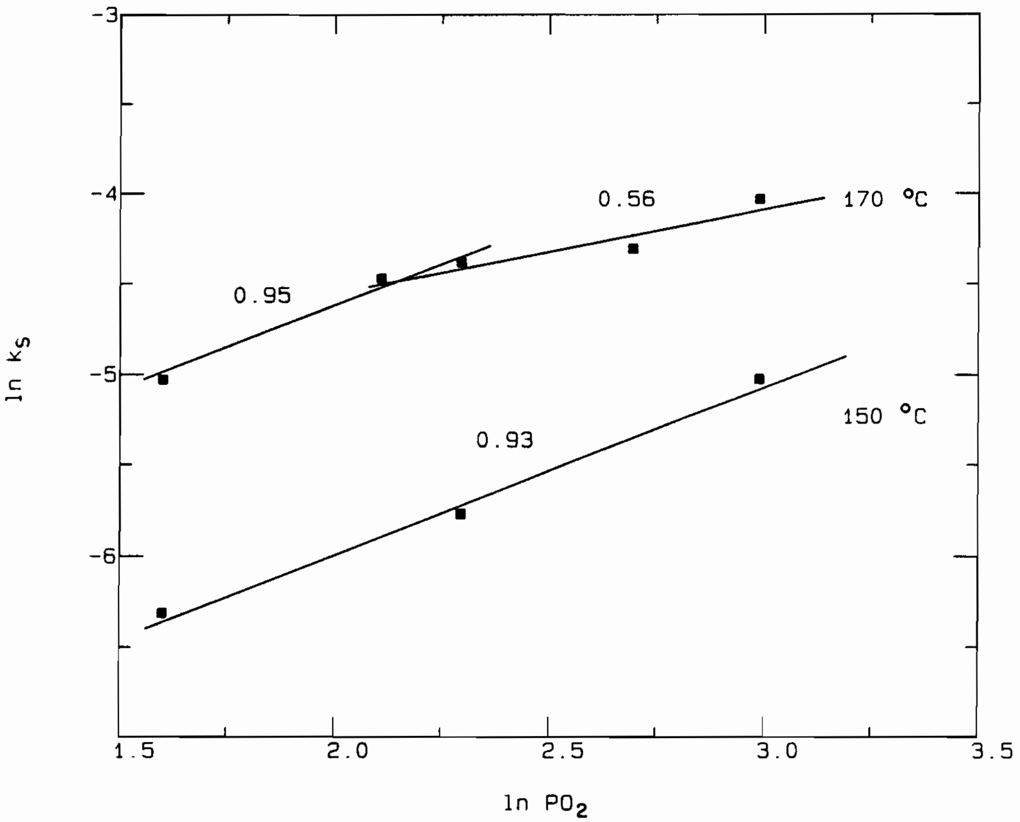

Figure 3.32: Pyrite oxidation: Determination of the reaction order with respect to oxygen pressure.

logarithm of the apparent rate constant (k_S) versus the respective logarithm of oxygen partial pressure (–74 +53 μm particle size) were made and they are shown in Fig. 3.32. Based on the best linear regression fit, two regions with slopes 0.95 (corr. coeff. 0.996) between 5 and 10 atm and 0.56 (corr. coeff. 0.998) between 10 and 20 atm are distinguished at 170 °C. An attempt to linearly fit the whole range (5–20 atm) resulted in a slope of 0.7 and a rather poor correlation coefficient of 0.978. On the other hand, a constant slope of 0.93 (corr. coeff. 0.99) is obtained at 150 °C for the whole oxygen partial pressure range. Bailey and Peters [3.46], who studied the pressure effect at 110 °C noticed departure from linearity at partial pressures exceeding 20 atm. McKay and Halpern [3.43] indicated a linear relationship at 100 °C and lower pressures (0–4 atm). Gerlach *et al* [3.53] proposed a Langmuir adsorption isotherm to account for the slight departure from linearity they observed at 100 °C and pressures between 0 and 15.5 atm. Warren [3.72] determined an order of 0.5 at 170 and 190 °C with oxygen pressures between 2.7 to 14 atm. Taking into account the findings of this work and those of previous investigations on pyrite pressure oxidation (see also Table 3.II), it can be concluded that fractional order (0.5) is observed at high temperatures (>170 °C) and pressures (>10 atm) while the order is unity at lower temperatures and partial oxygen pressures. It also appears that the transitional point (P_{O_2}) between linear and fractional order depends on temperature (i.e. lower temperatures exhibit extended first order dependence over P_{O_2} increase). This observation is in agreement with activated chemisorption behaviour [3.56].

For different particle sizes reacting according to the shrinking core model for a surface reaction controlled process, the apparent rate constant has to be linearly dependent on the reciprocal of the particle radius [3.56]. To test this hypothesis, experiments were performed with three size fractions, namely −147 +104 μm, −44 + 37 μm, and −74 +53 μm at 170 °C and 10 atm P_{O_2}. The linearity of the apparent rate constant versus $1/\bar{r}_0$ plot shown in Fig. 3.33 confirms the postulated surface reaction controlling step.

3.4.2 Rate Formulation

From a global reaction standpoint rather than a mechanistic one, the following reactions are considered to describe adequately the high temperature pressure oxidation of pyrite in acidic environment

$$2FeS_2(s) + 7O_2(aq) + 2H_2O \longrightarrow 2Fe^{2+}(aq) + 4HSO_4^-(aq) \qquad (3.25)$$

The divalent iron produced is further oxidized to trivalent iron, which undergoes a number of hydrolytic reactions depending on the prevailing conditions.

$$2Fe^{2+}(aq) + \frac{1}{2}O_2(aq) + H^+(aq) \longrightarrow 2Fe^{3+}(aq) + H_2O(l) \qquad (3.26)$$

Some elemental sulphur is expected to form, particularly at high acidities and temperatures below 160 °C. The apparent rate constant, k_S, which appears in the topochem-

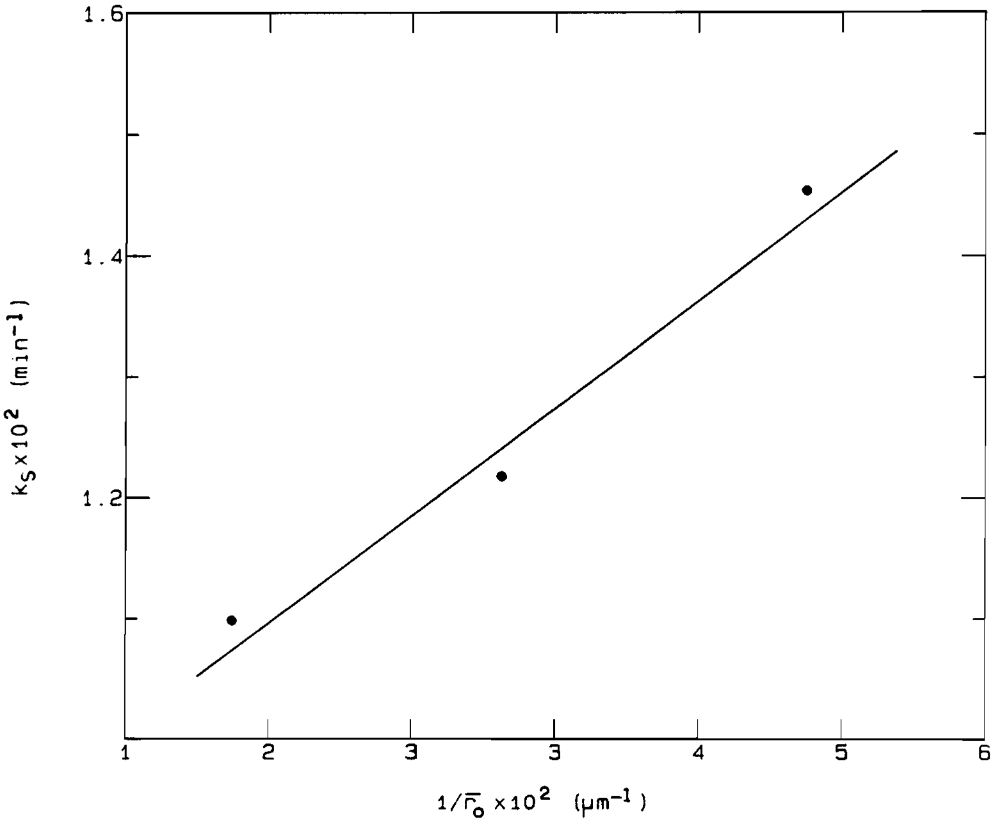

Figure 3.33: Pyrite oxidation: Plot of the apparent rate constant k_S vs the reciprocal of the geometric mean particle radius.

ical model eq. 3.27

$$1-(1-x)^{\frac{1}{3}}=k_S t \tag{3.27}$$

where:

x, is conversion and t time, is given by eq. 3.28 [3.56] for the region where first order dependence is observed. The apparent rate constant is:

$$k_S=\frac{bMk'P_{O_2}}{\rho r_0} \tag{3.28}$$

where,

b, is the stoichiometric coefficient (i.e. 2/7),

M, is the g-mol of FeS_2,

k', is the intrinsic rate constant,

ρ, is the density of FeS_2,

r_0, is the initial particle radius.

From the Arrhenius plot of Fig. 3.30 and eq. 3.27 and 3.28 the following shrinking core model equations are proposed to represent the pressure oxidation of pyrite

$$x=1-(1-36.5\cdot 10^6\frac{P_{O_2}}{r_0}t\exp\frac{-13283}{T})^3 \tag{3.29}$$

$$x=1-(1-0.5\frac{P_{O_2}}{r_0}t\exp\frac{-5559}{T})^3 \tag{3.30}$$

Equation 3.29 is valid for temperatures higher than 433 K (160 °C) and oxygen pressures less than 10 atm. Equation 3.30 applies to temperatures less than 433 K and P_{O_2} up to at least 20 atm. In the above equations time is expressed in min, r_0 in cm and P_{O_2} in atm.

Furthermore, assuming the stoichiometry of reaction 3.25 and a density of pyrite 5 g mL^{-1} [3.77], the intrinsic rate law was formulated with the aid of eq. 3.28 as

$$r_{FeS_2}=-1.52\cdot 10^6\exp(\frac{-13283}{T})P_{O_2} \qquad \text{mol min}^{-1}\text{ cm}^{-2} \tag{3.31}$$

for the same temperature and oxygen pressure levels as with eq. 3.29 and

$$r_{FeS_2}=-2.1\cdot 10^{-2}\exp(\frac{-5559}{T})P_{O_2} \qquad \text{mol min}^{-1}\text{ cm}^{-2} \tag{3.32}$$

for the same temperature and oxygen pressure levels as with eq. 3.30. For higher oxygen pressures, half order dependency has to be incorporated in the above equations.

The rate equations established constitute the basis of the mathematical models developed later in Chapters 5 and 6 to simulate the pressure oxidation of refractory gold concentrates.

3.4.3 Summary

The pressure oxidation kinetics of pyrite has been studied in the temperature range 140 to 180 °C, and 5 to 20 atm O_2 pressure. The oxidation kinetics was found to follow a shrinking core model, with chemical reaction on the surface as the rate controlling step. At temperatures lower than 160 °C, elemental sulphur formation blocks the grain surface and eventually terminates the reaction before complete conversion of pyrite is achieved. For example, at 140 °C the reaction is essentially over after two hours at 50% conversion of pyrite. At temperatures higher than 160 °C, the reaction proceeds to completion without any hindrance. This behaviour was attributed partly to the change in the physical properties of liquid elemental sulphur, which takes place at around 160 °C. The overall complex kinetic behaviour of pyrite is reflected in an activation energy shift at 160 °C with a value of 46.2 kJ mol^{-1} between 140 and 160 °C, and a value of 110.5 kJ mol^{-1} between 160 and 180 °C.

The reaction order with respect to oxygen partial pressure was found to be 1 at 150 °C and for the whole pressure range investigated (5–20 atm). At 170 °C the order becomes 0.5 for pressures beyond 10 atm. This behaviour is in agreement with an activated chemisorption process of O_2 on the surface of FeS_2. The particle size dependence of the rate was also found to be in agreement with a chemically controlled process.

Having determined the activation energy, reaction order, and particle size dependence, rate equations were developed on the basis of the shrinking core model, suitable for process modelling and reactor design.

References

[3.1] M. Calvo and E. Sevillano, *Mineralogical Record*, 20(6), 451 (1989).

[3.2] K. Tozawa and K. Sasaki, *Iron Control in Hydrometallurgy* (ed. by J.E. Dutrizac and A.J. Monhemius), pp. 454–476, Ellis Horwood, Chichester, U.K. (1986).

[3.3] E.M. Donaldson, *Methods for the Analysis of Ores, Rocks and Related Materials*, CANMET Monograph 881, 2nd ed., pp. 354–361, EMR, Ottawa, Ontario (1982).

[3.4] P.D.Kondos, *Pressure Chloride Leaching of a Complex U/Ra/Ni/As Ore: Statistical Modelling and Solution Chemistry*, pp. 146–157 and 239–241, Ph.D. Thesis, Dept. of Mining and Metallurgical Engineerig, McGill University, Montreal, Quebec (1988).

[3.5] A.I. Vogel, *A Textbook of Quantitative Inorganic Analysis*, 3rd ed. p. 309, Longmans, London, U.K., (1961).

[3.6] M.J. Buerger,*Zatschrift Kristallographie*, 95, 83 (1931).

[3.7] N. Morimoto and L.A. Clark, *Amer. Mineral.*, 46, 1448 (1961).

[3.8] C. Klein and C.S. Hurlbut Jr., *Manual of Mineralogy*, 20th ed., pp. 272–288, John Wiley and Sons, New York NY (1985).

[3.9] C. Palache, H. Berman and C. Frondel, *Dana's System of Mineralogy*, 7th ed., Vol. 1, pp. 315–321, John Wiley and Sons, New York, NY (1944).

[3.10] L.A. Clark, *Econ. Geol.*, 55, 1631, (1960).

[3.11] G.M. Schwartz, *Econ. Geol.*, 39, 371, (1944).

[3.12] S.L. Chryssoulis, L.J. Cabri and R.S. Salter, *Proc. Int'l. Symp. on Gold Metallurgy* (ed. by R. Salter, D.M. Wyslouzil and G.W. McDonald), pp. 235–244, CIM, Montreal, Quebec (1987).

[3.13] N.J. Cook and S.L. Chryssoulis, *Canadian Mineralogist*, 28, 1 (1990).

[3.14] K. Osseo-Asare, T. Xue and V.S.T. Ciminelli, *Precious Metals: Mining, Extraction and Processing* (ed. by V. Kudryk, D.A. Carrigan and W.W. Liang), pp. 173–197, TMS-AIME, Warrendale PA (1984).

[3.15] R.G. Robins, *Impurity Control and Disposal* (ed. by A. Oliver) paper No. 1, CIM, Montreal, Quebec (1985).

[3.16] M.J.V. Beattie and G.W. Poling, *Int'l. J. Mineral Processing*, 20, 87 (1987).

[3.17] C.W. Bale, A.D. Pelton and W.T. Thompson, *Facility for the Analysis of Chemical Thermodynamics (F*A*C*T)*, McGill University, Montreal, Quebec.

[3.18] D.D. Wangman et al., *Selected values of Thermodynamic Properties*, National Bureau of Standards Series 270, U.S. Dept. of Commerce, Washington DC 1968–1971.

[3.19] H.E. Barner and R.V. Scheurman, *Handbook of Thermochemical Data for Compounds and Aqueous Species*, Wiley-Interscience, New York NY (1978).

[3.20] I. Barin, O. Knacke and O. Kubaschewski, *Thermochemical Properties of Inorganic Substances*, Springer-Verlag, Berlin, (1977).

[3.21] R.M. Smith and A.E. Martell, *Critical Stability Constants*, Vol. 4, Plenum Press, NY, 1976.

[3.22] R.E. Connick and R.E. Powell, *J. Chem. Phys.*, 21(12), 2206, (1953).

[3.23] A.J. Bard, R. Parsons, J. Jordan, *Standard Potentials in Aqueous Solution*, Marcell-Dekker, NY, 1985.

[3.24] F.K. Crundwell, *Hydrometallurgy*, 19, 227, (1987).

[3.25] R.T. McAndrew, S.S. Wang and W.R. Brown, *CIM Bull.*, 101, (Jan., 1975).

[3.26] V.G. Chukhlantsev, *Zhur. Anal. Khimii*, 11, 565, (1956).

[3.27] P.M. Dove and J.D. Rimstidt, *Amer. Mineralogist*, 70, 838 (1985).

[3.28] R.G. Robins, *Amer. Mineralogist*, 72, 842 (1987).

[3.29] E. Krause and V.A. Ettel, *Amer. Mineralogist*, 73, 850 (1988).

[3.30] L.G. Sillen and A.E. Martell, *Stability Constants of Metal- Ion Complexes*, The Chemical Society special publication No. 17 (1964).

[3.31] V.G. Papangelakis, D. Berk and G.P. Demopoulos, *Hydrometallurgical Reactor Design and Kinetics*, (ed. by R.G. Bautista, R.J. Wesely and G.W. Warren), pp. 209–225, TMS-AIME, Warrendale PA (1986).

[3.32] W.M. Latimer, *Oxidation Potentials*, 2nd ed., pp. 359–365, Prentice Hall, (1952).

[3.33] D.R. Gaskell, *Introduction to Metallurgical Thermodynamics*, 2nd ed., McGraw-Hill, (1981).

[3.34] C.M. Criss and J.W. Cobble, *J. Amer. Chem. Soc.*, 86, 5385 and 5390 (1964).

[3.35] R.J. Biermat and R.G. Robins, *Electrochimica Acta*, 17, 1261, (1972).

[3.36] F.M. Doyle, *Hydrometallurgy*, 20, 65, (1988).

[3.37] A.R. Burkin, *Hydrometallurgical Process Fundamentals*, (ed. by R.G. Bautista), pp. 113–123, Plenum Press, New York NY (1984).

[3.38] E. Peters, *Trends in Electrochemistry*, (ed. by J.O'M. Bockris, D.A.J. Rand and B.J. Welch), pp. 267–290, Plenum Press, New York NY (1977).

[3.39] D.R. Dahuke, L.G. Twidnell and R.G. Robins, *Iron Control in Hydrometallurgy* (ed. by J.E. Dutrizac and A.J. Monhemius), pp. 477–503, Ellis Horwood, Chichester, U.K. (1986).

[3.40] J.E. Dutrizac and J.L. Jambor, *Hydrometallurgy*, 19, 377 (1988).

[3.41] G.B. Harris and S. Monette, *Arsenic Metallurgy Fundamentals and Applications* (ed. by R.G. Reddy, J.L. Hendrix and P.B. Queneau), pp. 469–488, TMS-AIME, Warrendale PA (1988).

[3.42] G.P.Demopoulos, V.G.Papangelakis, B.R.Buckanan and P.R.Mainwaring, *Extraction Metallurgy '89* (ed. by D.S.Flett), pp. 603–627, IMM, London U.K. (1989).

[3.43] D.R. McKay and J. Halpern, *Trans. TMS-AIME*, 6, 301 (1958).

[3.44] Y. Awakura, M. Iwai and H. Majima, *Iron Control in Hydrometallurgy* (ed. by J.E. Dutrizac and A.J. Monhemius), pp. 202–222, Ellis Horwood, Chichester, U.K. (1986).

[3.45] D.B. Dreisinger and E. Peters, *Hydrometallurgy*, 22, 101 (1989).

[3.46] L.K. Bailey and E. Peters, *Can. Metall. Quarterly*, 15(4), 333 (1976).

[3.47] T.Biegler and D.A.Swift, *Electrochimica Acta*, 24, 415, (1979).

[3.48] Yin Zhou, Jianng Han, Shu Yu and Zhao Rui, *Proc. First Int'l Conf. on Hydrometallurgy (ICHM'88)* (ed. by Zheng Yulian and Xu Jiazhong), pp. 623–626, Int'l Academic Publishers-Pergamon Press, Beijing, China (1988).

[3.49] F.A.Cotton and G.W.Wilikinson, *Advanced Inorganic Chemistry*, 4th edition, p. 508, John Wiley and Sons, New York (1980).

[3.50] R.E.Meyer, *J. Electroanal. Chemistry*, 101, 59 (1979)

[3.51] J.P. Corriou and T. Kikindai, *J. Inorg. Nucl. Chem.*, 43, 9 (1981).

[3.52] H.Veltman and G.L.Bolton, *Erzmetall*, 33(2), 76 (1980)

[3.53] J. Gerlach, H. Hahne and F. Pawlek, *Erzmetall*, 19(2), 66 (1966).

[3.54] P. Kondos and G.P. Demopoulos, *Separation Processes in Hydrometallurgy* (ed. by G.A. Davies), pp. 20–34, Ellis Horwood, Chichester, U.K. (1987).

[3.55] J.G.Dunn, P.G.Fernandez, H.C.Hughes and H.G.Linge, *Precious Metals 1989* (ed. by Bryn Harris), pp. 289–295, Allentown PA (1989)

[3.56] J.M. Smith, *Chemical Engineering Kinetics*, 3rd ed., pp. 642–645, McGraw-Hill (1981).

[3.57] H.A. Pray, C.E. Schweickert and B.H. Minnich, *Ind. Eng. Chem.*, 44(5), 1146 (1952).

[3.58] N.B. Pilling and R.E. Bedworth, *J. Inst. Metals*, 29, 529 (1923).

[3.59] R.C. Weast, *Handbook of Chemistry and Physics*, 66th ed., CRC Press, p. B-148, B-198, B-201 (1985–86).

[3.60] W.L. Marshall and E.V. Jones, *J. Phys. Chem.*, 70, 4028 (1966).

[3.61] E. Peters and H. Majima, *Can. Metall. Quarterly*, 7(3), 111 (1968).

[3.62] G.W. Warren, M.E. Wadsworth and S.M. El-Raghy, *Hydrometallurgy: Research, Development and Plant Practice* (ed. by K. Osseo-Asare and J.D. Miller), pp. 261–275, TMS-AIME, Warrendale, PA (1983).

[3.63] H.K. Lin, H.Y. Sohn and M.E. Wadsworth, *Hydrometallurgical Reactor Design and Kinetics* (ed. by R.G. Bautista, R.J. Wesely and G.W. Warren), pp. 149–168, TMS-AIME, Warrendale PA (1986).

[3.64] R.T. Shuey, *Semiconducting Ore Minerals*, p. 205, Elsevier, (1975).

[3.65] T. Biegler, D.A.J. Rand and R. Woods, *Trends in Electrochemistry* (ed. by J.O'M. Bockris, D.A.J. Rand and Welch), pp. 291–302, Plenum Press NY (1977).

[3.66] A. Damianovic, *Modern Aspects of Electrochemistry* (ed. by J.O'M. Bockris and B.E. Conway), No. 5, pp. 370–483, Plenum Press NY (1969).

[3.67] J.O'M. Bockris and A.K.N. Reddy, *Modern Electrochemistry*, pp. 991–1017 and 1251–1255, Plenum Press NY (1970).

[3.68] T. Biegler and D.A. Swift, *Electrochimica Acta*, 24, 415 (1979).

[3.69] J.J. Carberry, *Chemical and Catalytic Reaction Engineering*, pp. 378–382, McGraw-Hill NY (1976).

[3.70] E. Gileadi and B.E. Conway, *Modern Aspects of Electrochemistry* (ed. by J.O'M. Buckris and B.E. Conway), No. 3, pp. 347–442, Plenum Press NY (1964).

[3.71] F. Habashi and E.C. Bauer, *Ind. Eng. Chem. Fund.*, 5(4), 469 (1966).

[3.72] I.H. Warren, *Austr. J. Appl. Sci.*, 7, 346 (1956).

[3.73] R.J. Cornelius and J.T. Woodcock, *Proc. Austr. Inst. Min. Met.*, 185, 65 (1958).

[3.74] J-P. Corriou, R. Gély and P. Viers, *Hydrometallurgy*, 21, 85 (1988).

[3.75] F.K. Crundwell, *Hydrometallurgy*, 21, 155 (1988).

[3.76] F.A. Cotton and G. Wilkinson, *Advanced Inorganic Chemistry*, 5-th ed., pp.494–496, Wiley Interscience NY (1988).

[3.77] R.C. Weast, *Handbook of Chemistry and Physics*, 66th ed., p.F–5, E–5, F–37, CRC Press, Boca Raton FL (1985–86).

[3.78] R.B. Bird, W.E. Stewart and E.N. Lightfoot, *Transport Phenomena*, p.407, pp.180–196, John Wiley and Sons NY (1960).

[3.79] J.B. Joshi, A.B. Pandit and M.M. Sharma, *Chem. Eng. Sci.*, 37(6), 813, (1982).

Chapter 4

Reactor Models for Single Stage Pressure Oxidation: Surface Reaction Control

4.1 Introduction

Pressure oxidation of refractory gold minerals is a highly exothermic and complex reaction process. For optimal reactor design, models which couple leaching kinetics and heat effects are needed. In this chapter, the methodology of building a process model starting from the particle leaching kinetics (determined in Chapter 3) and the performance equations (mass and energy conservation) of batch and continuous stireed tank reactors is described. In particular, the single stage pressure oxidation of widely sized arsenopyrite particulates is treated here for the case of surface reaction as the rate-limiting step. Both isothermal and adiabatic modes of operation are considered. The material presented in this chapter is the subject-matter of a paper to be published in the *Metallurgical Transactions B*[1].

4.2 The Chemical Reaction System

As established in the previous chapter, when arsenopyrite is subjected to high temperature (160–200 °C) pressure oxidation in a H_2SO_4 medium, the following three

---

[1] accepted December 1989.

principal reactions occur:

$$4FeAsS(s)+13O_2(aq)+6H_2O(l) \longrightarrow 4H_3AsO_4(aq)+4Fe^{2+}(aq)+4SO_4^{2-}(aq) \quad (4.1)$$

$$2Fe^{2+}(aq)+\frac{1}{2}O_2(aq)+2H^+(aq) \longrightarrow 2Fe^{3+}(aq)+H_2O(l) \quad (4.2)$$

$$Fe^{3+}(aq)+H_3AsO_4(aq)+2H_2O(l) \longrightarrow FeAsO_4\cdot 2H_2O(s)+3H^+(aq) \quad (4.3)$$

Reaction 4.1 represents the heterogeneous oxidation of arsenopyrite particles. Reaction 4.2 represents the homogeneous oxidation of Fe^{2+} to Fe^{3+} and, finally, reaction 4.3 represents the removal of Fe^{3+} from solution by precipitation in the form of scorodite (i.e. $FeAsO_4 \cdot 2H_2O$).

Monosize particulates of arsenopyrite reacting according to the stoichiometry of reaction 4.1 were found (Section 3.3.3) to follow the shrinking core model for surface reaction control:

$$x = 1-(1-k_St)^3 \quad (4.4)$$

The heterogeneous rate constant k_S can be written as a function of partial oxygen pressure, particle diameter[2], and temperature:

$$k_S = 2622\frac{P_{O_2}}{d_0}e^{-\frac{8672}{T}}$$

where P_{O_2} is expressed in atm (1 atm = 101.3 kPa) and d_0 in cm.

The intrinsic rate law for the high temperature arsenopyrite oxidation was determined (Section 3.3.3) to be:

$$r_{FeAsS} = --49.5e^{-\frac{8672}{T}}P_{O_2} \qquad \text{mol min}^{-1}\text{ cm}^{-2} \quad (4.5)$$

For reaction 4.2, the rate equation reported by McKay and Halpern [4.1] was adopted for the present work

$$r_{Fe^{2+}} = -k_2C_{Fe^{2+}}^2P_{O_2} \qquad \text{mol min}^{-1}\text{ dm}^{-3} \quad (4.6)$$

---

[2] The equivalent equation 3.10 in Chapter 3 was written in terms of the particle radius rather than the particle diameter.

Table 4.I: Thermodynamic data for reactions 4.1, 4.2 and 4.3 (from ref. [4.2]).

Species	$\Delta H^\circ_{f,298}$ kJ mol^{-1}	$C_p = A + B10^{-3}T + C10^5T^{-2}$ J K^{-1} mol^{-1}		
		A	B	C
$O_2(aq)$	-11.715	102.32	32.125	31.614
$H_2O(l)$	-285.851	75.438	0.000	0.000
$H_3AsO_4(aq)$	-907.489	-2318.087	5145.960	903.137
$SO_4(aq)$	-909.183	874.686	-1759.698	-519.975
$Fe^{2+}(aq)$	-89.119	-1.084	1.205	39.970
$H^+(aq)$	0.000	0.000	0.000	0.000

with $k_2 = 6 \cdot 10^7 e^{-\frac{8304}{T}}$. Finally, reaction 4.3 was assumed to be very fast, attaining equilibrium instantaneously. The thermodynamic data used for the calculation of the enthalpy change of reactions 4.1 and 4.2, and for the calculation of the free energy change of reaction 4.3 at high temperatures are those listed in Tables 3.II and 4.I. Based on these data, the standard enthalpy changes at 298 K of reactions 4.1, 4.2 and 4.3 respectively were calculated to be:

$$\Delta H^\circ_{4.1,298} = -5568.4 \quad \text{kJ}$$

$$\Delta H^\circ_{4.2,298} = -198.8 \quad \text{kJ}$$

$$\Delta H^\circ_{4.3,298} = 69.6 \quad \text{kJ}$$

Extrapolation of the standard enthalpy change to high temperatures is performed through the following well-known equation:

$$\Delta H^\circ_T = \Delta H^\circ_{298} + \int_{298}^{T} \Delta C_p \mathrm{d}T$$

4.3 Elements of Reactor Modelling

Further to the concepts of reaction and reactor modelling introduced in Section 2.4.1, some additional basic elements are outlined before the actual model equations are developed.

4.3.1 Reaction Extent and Conversion

As outlined in Chapter 2, the number of moles of species i that participates in j reactions at any time is a function of the reaction extents:

$$N_i = N_{i0} + \sum_{j=1}^{m} \nu_{ij}\epsilon_j \tag{4.7}$$

For a reactant i that participates only in one reaction (say the j-th), the conversion x, which is another measure of the progress of a reaction, is given by

$$x_i = \frac{N_{i0} - N_i}{N_{i0}}$$

and is related to extent by

$$\epsilon_j = -\frac{N_{i0}x}{\nu_{ij}} \tag{4.8}$$

The above definitions apply equally to continuous reactors as well. For the latter, molar flow rates (F_i) are substituted for number of moles (N_i) in the previous equations and the units for the extent as of consequence become moles per unit time ($\dot{\epsilon}$).

4.3.2 Particle Behaviour

Particle Size Distribution

To calculate overall conversion for wide size distribution mineral feeds, discrete or continuous particle size distributions have to be considered. In this chapter a discrete size distribution approach is followed. Thus, for a batch reactor we have:

$$\bar{x} = \sum_{\kappa} \Delta W_\kappa x_\kappa \tag{4.9}$$

where $\bar{x}$ is the overall conversion of all size fractions and x_κ, ΔW_κ are the conversion and weight fraction of the κ monosize fraction respectively. The value of x_κ is calculated by the appropriate shrinking core model (eq. 4.4 in this case).

Surface Area

Variation of particle size or equivalent surface area with time (batch reactor) is again followed with the aid of the shrinking core model. The total surface area (S) of reacting mineral particles is given by

$$S = \sum_{\kappa} \pi d_{\kappa}^{2} \eta_{\kappa} \tag{4.10}$$

where d_κ is the geometric mean diameter of the κ "mono" size fraction at time t and η_κ is the initial number of particles present in the κ size fraction. For surface reaction control, particle diameter shrinks linearly with time according to

$$d_{\kappa}(t) = \begin{cases} d_{0,\kappa}(1 - k_{S,\kappa} t) & \text{for} \quad 0 \leq t < \frac{1}{k_{S,\kappa}} \\ 0 \text{ for} & t \geq \frac{1}{k_{S,\kappa}} \end{cases} \tag{4.11}$$

where $k_{S,\kappa}$ is the apparent rate constant for the κ size fraction (eq. 4.4). Finally η_κ which is assumed not to change with time[3], is estimated from

$$\eta_{\kappa} = \frac{6 N_{i0} M_1 \Delta W_{\kappa}}{\pi d_{0,\kappa}^{3} \rho_1}$$

Residence Time Distribution

To calculate the conversion of the solids in the continuous reactor (CSTR), the segregated flow model (Section 2.4.1) can be applied. According to this model, each particle retains its identity and behaves like a small batch reactor. The average conversion $\langle x_\kappa \rangle$ for the κ size fraction with initial diameter $d_{0,\kappa}$ is then given by:

$$\langle x_{\kappa} \rangle = \int_{0}^{\infty} x_{\kappa}(t) E(t) \mathrm{d}t \tag{4.12}$$

$E(t)$ is the residence time distribution (RTD) function which, for ideal mixing conditions, is:

$$E(t) = \frac{1}{\bar{t}} e^{-t/\bar{t}} \tag{4.13}$$

---

[3] This is true since each size fraction is taken to be monosize. In other words, all particles within a monosize particle set share the same residence time (batch reactor) and therefore shrink uniformly until they disappear. However, the total number of particles (i.e. sum over η_κ for all κ) changes with time.

where $\bar{t}$ is the mean residence time. For all κ size fractions of a wide size feed, the overall conversion is:

$$\bar{x} = \sum_{\kappa} \Delta W_{\kappa} \langle x_{\kappa} \rangle = \sum_{\kappa} \Delta W_{\kappa} \int_0^{\infty} x_{\kappa}(t) E(t) \mathrm{d}t \tag{4.14}$$

In addition, $x_{\kappa}(t)$, according to the shrinking core model eq. 4.4 is as follows

$$x_{\kappa}(t) = \begin{cases} 1 - (1 - k_{S,\kappa} t)^3 & \text{for} \quad 0 \leq t < \frac{1}{k_{S,\kappa}} \\ 1 & \text{for} \quad t \geq \frac{1}{k_{S,\kappa}} \end{cases} \tag{4.15}$$

Combination of eq. 4.12, 4.13 and 4.15 gives

$$\langle x_{\kappa} \rangle = \int_0^{\frac{1}{k_{S,\kappa}}} [1 - (1 - k_{S,\kappa} t)^3] \frac{1}{\bar{t}} e^{-t/\bar{t}} \mathrm{d}t + \int_{\frac{1}{k_{S,\kappa}}}^{\infty} \frac{1}{\bar{t}} e^{-t/\bar{t}} \mathrm{d}t \tag{4.16}$$

Finally, upon integration we obtain:

$$\langle x_{\kappa} \rangle = 6(k_{S,\kappa}\bar{t})^3 - 6(k_{S,\kappa}\bar{t})^2 + 3(k_{S,\kappa}\bar{t}) - 6(k_{S,\kappa}\bar{t})^3 e^{-1/k_{S,\kappa}\bar{t}} \tag{4.17}$$

It is evident that $\langle x_{\kappa} \rangle$ is a function of $\bar{t}$ with parameter $k_{S,\kappa}$. It can be seen by expanding to Taylor series that $\langle x_{\kappa} \rangle$ holds the mathematical properties of conversion, that is:

$$\lim \langle x_{\kappa} \rangle = 0 \qquad \text{when} \qquad \bar{t} \rightarrow 0$$

$$\lim \langle x_{\kappa} \rangle = 1 \qquad \text{when} \qquad \bar{t} \rightarrow \infty$$

4.3.3 Heat Effects

Heat effects are important in isothermal and non-isothermal modes of operation alike. By setting-up an energy balance equation for the isothermal mode of operation the heat transfer requirements to sustain constant temperature are determined. But more so, energy balance considerations are an absolute necessity in the adiabatic case of reactor operation. In the latter case, material and energy balance equations have to be solved simultaneously since reaction rates and equilibria depend on reactor temperature, which in turn depends on the amount of heat released by the reaction process.

A general form of the energy balance equation that was found to be particularly useful in this work (batch and CSTR reactors only) is the following:

$$\begin{array}{l}\text{Rate of sensible}\\ \text{heat entering}\\ \text{reactor with}\\ \text{feed stream}\end{array} - \begin{array}{l}\text{Rate of sensible}\\ \text{heat leaving}\\ \text{reactor with}\\ \text{outlet stream}\end{array} + \begin{array}{l}\text{Rate of heat}\\ \text{generation by}\\ \text{reaction}\end{array} + \begin{array}{l}\text{Rate of heat}\\ \text{transferred}\\ \text{from}\\ \text{surroundings}\end{array} = \begin{array}{l}\text{Rate of heat}\\ \text{accumulation}\\ \text{within reactor}\end{array} \tag{4.18}$$

Heat balance is made from the stand point of reactor (positive when heat is generated or enters the reactor) and with reference to the temperature of operation. For the batch reactor the first two terms of eq. 4.18 are zero, while for the continuous stirred tank reactor the right-hand side term of eq. 4.18 is zero at steady state. For exothermic reactions, like the one studied here, a special problem arises in determining the stable operating temperatures in autogenously run stirred tank reactors (Section 2.4.1). The problem is solved here by breaking eq. 4.18 into two terms, heat removed from the system and heat generated by the reaction, and searching for a steady state temperature that equates the two terms at high conversion.

4.4 Model Development

For the development of the model equations the following assumptions are made:

1. Solution density changes due to temperature increase and/or the presence of dissolved species are neglected.
2. Oxygen gas is supplied continuously to keep its partial pressure constant.
3. Water consumption/production via reactions 4.1 to 4.3 is negligible compared to the amount already present in the slurry.
4. Activities of species involved are equal to their concentrations.
5. Heat absorbed by scorodite precipitation is negligible.

6. For the calculation of heat accumulation by the reacting mixture the total number of moles is taken constant and equal to that of arsenopyrite and water. Moreover an average specific heat capacity, $\overline{C}_p$, with a value very close to that of water (76.4 J K^{-1} mol^{-1}), is assigned to the reacting mixture. This is justifiable in view of the small heat capacity of the solids (only 2.6% of that of water when 20% arsenopyrite solids are used).
7. The intrinsic rate-controlling step (surface reaction) of arsenopyrite oxidation governs the process kinetics throughout the various operating conditions simulated. Possible gas/liquid mass transfer limitations are ignored.
8. The volumetric flow rate of the slurry (CSTR) is equal to that of the liquid phase (20% w./w. arsenopyrite solids is only 4% v./v.) and is not affected by the extent of the reaction.
9. The CSTR is perfectly mixed, therefore the mean residence time of solids is equal to the mean residence time of the solution.

4.4.1 Batch Reactor

A batch reactor (autoclave) is considered first having a total volume $V_{\mathbf{Batch}}$. For the present 3-reaction system the stoichiometric table (see Section 2.4.1) shown in Table 4.II, is obtained according to eq. 4.7. It is clear that the number of moles of any species, at any time, can be determined if the initial number of moles of $FeAsS$, H_2O, H^+ and SO_4^{2-} are known and the three reaction extents (ϵ_1, ϵ_2 and ϵ_3) are calculated.

The working volume of the reactor is taken equal to the slurry volume, that is:

$$V_{\mathbf{Batch}} = V_{\mathbf{slurry}} = V_{\mathbf{solids}} + V_{\mathbf{solution}}$$

Hence,

$$V_{\mathbf{Batch}} = \frac{N_{10}M_1}{\rho_1} + \frac{N_{30}M_3}{\rho_3} \tag{4.19}$$

Table 4.II: Stoichiometric table for the pressure oxidation of arsenopyrite in a batch reactor.

1 :	$FeAsS$	$N_1 =$	N_{10}	$-4\epsilon_1$		
2 :	O_2	$N_2 =$	N_{20}	$-13\epsilon_1$	$-\frac{1}{2}\epsilon_2$	
3 :	H_2O	$N_3 =$	N_{30}	$-6\epsilon_1$	$+\epsilon_2$	$-2\epsilon_3$
4 :	H_3AsO_4	$N_4 =$		$+4\epsilon_1$		$-\epsilon_3$
5 :	Fe^{2+}	$N_5 =$		$+4\epsilon_1$	$-2\epsilon_2$	
6 :	H^+	$N_6 =$	N_{60}		$-2\epsilon_2$	$+3\epsilon_3$
7 :	Fe^{3+}	$N_7 =$			$+2\epsilon_2$	$-3\epsilon_3$
8 :	$FeAsO_4 \cdot 2H_2O$	$N_8 =$				$+\epsilon_3$
9 :	SO_4^{2-}	$N_9 =$	N_{90}	$+\epsilon_1$		

Consequently, the weight fraction of solids, which are present in the slurry is given by

$$w_s = \frac{N_{10}M_1}{N_{10}M_1 + N_{30}M_3} \tag{4.20}$$

Once V_{Batch} and w_s are given, N_{10} and N_{30} are calculated from the system of equations 4.19 and 4.20.

The extent of reaction 4.1, ϵ_1, is determined from the overall conversion of arsenopyrite, $\bar{x}$, using equations 4.8 and 4.9 and replacing x_κ with the surface reaction control shrinking core model (eq. 4.4).

$$\epsilon_1 = \frac{N_{10}}{4}\sum_\kappa \Delta W_\kappa[1-(1-2622\frac{P_{O_2}}{d_{0,\kappa}}e^{-\frac{8672}{T}}t)^3] \tag{4.21}$$

The extent of reaction 4.2, ϵ_2, is obtained from the mass-balance equation for Fe^{2+} in the batch reactor:

$$\frac{\mathrm{d}N_5}{\mathrm{d}t} = 4\overline{r}_{4.1}S - 2\overline{r}_{4.2}V \tag{4.22}$$

From Table 4.II

$$\frac{\mathrm{d}N_5}{\mathrm{d}t} = 4\frac{\mathrm{d}\epsilon_1}{\mathrm{d}t} - 2\frac{\mathrm{d}\epsilon_2}{\mathrm{d}t} \tag{4.23}$$

hence from 4.22 and 4.23

$$\frac{\mathrm{d}\epsilon_2}{\mathrm{d}t} = \frac{\mathrm{d}\epsilon_1}{\mathrm{d}t} - 2\overline{r}_{4.1}S + \overline{r}_{4.2}V \tag{4.24}$$

where V, the solution volume, and S, the surface area of the reacting mineral particles, is estimated from eq. 4.10. The reaction rates $\bar{r}_{4.1}$, $\bar{r}_{4.2}$ are determined from equations 4.5 and 4.6 and the respective stoichiometries of reactions 4.1 and 4.2 (see eq. 2.8 in Section 2.4.1).

Finally, ϵ_3 is calculated from the equilibrium constant of reaction 4.3

$$\mathcal{K}_{4.3,T} = \exp -\frac{\Delta G^\circ_{4.3,T}}{\mathcal{R}T} = \frac{C^3_{H^+}}{C_{Fe^{3+}} C_{H_3AsO_4}} \tag{4.25}$$

By rearranging and substituting from Table 4.II, eq. 4.25 yields

$$(2\epsilon_2 - \epsilon_3)(4\epsilon_1 - \epsilon_3) = \frac{(N_{60} - 2\epsilon_2 + 3\epsilon_3)^3}{V} \exp \frac{\Delta G^\circ_{4.3,T}}{\mathcal{R}T} \tag{4.26}$$

Isothermal Operation

For the isothermal case, the problem is reduced to the calculation of ϵ_1, ϵ_2 and ϵ_3 for the operating temperature of interest. Independent solution of equations 4.21, 4.24 and 4.26 gives respectively ϵ_1, ϵ_2 and ϵ_3. Differential equation 4.24 and algebraic equation 4.26 were solved numerically with initial conditions $\epsilon_1 = \epsilon_2 = 0$ at $t = 0$, using the Runge-Kutta and Newton-Raphson methods, respectively.

In order to calculate the heat released by the exothermic reaction and therefore to estimate the heat transfer (cooling) requirements of the process, the energy balance equation 4.18 is set up for the batch reactor:

$$\text{rate of heat generation} = -(\Delta H^\circ_{4.1,T}\bar{r}_{4.1}S + \Delta H^\circ_{4.2,T}\bar{r}_{4.2}V)$$

$$\text{rate of heat transferred from surroundings} = \frac{\mathrm{d}Q}{\mathrm{d}t}$$

$$\text{rate of heat accumulation} = \overline{NC}_p\frac{\mathrm{d}T}{\mathrm{d}t} = 0$$

where $\Delta H^\circ_{4.1,T}$ and $\Delta H^\circ_{4.2,T}$ are the enthalpies of reactions 4.1 and 4.2 respectively (the negative sign is used since the reactions are exothermic), $\overline{N}$ is the total number of moles of the reaction mixture ($\overline{N} = N_{10} + N_{30}$), and $\overline{C}_p$ is the average (molar) specific

Table 4.III: Stoichiometric table for the pressure oxidation of arsenopyrite in a CSTR.

1 :	$FeAsS$	$F_1 =$	F_{10}	$-4\dot{\epsilon}_1$		
2 :	O_2	$F_2 =$	F_{20}	$-13\dot{\epsilon}_1$	$-\frac{1}{2}\dot{\epsilon}_2$	
3 :	H_2O	$F_3 =$	F_{30}	$-6\dot{\epsilon}_1$	$+\dot{\epsilon}_2$	$-2\dot{\epsilon}_3$
4 :	H_3AsO_4	$F_4 =$		$+4\dot{\epsilon}_1$		$-\dot{\epsilon}_3$
5 :	Fe^{2+}	$F_5 =$		$+4\dot{\epsilon}_1$	$-2\dot{\epsilon}_2$	
6 :	H^+	$F_6 =$	F_{60}		$-2\dot{\epsilon}_2$	$+3\dot{\epsilon}_3$
7 :	Fe^{3+}	$F_7 =$			$+2\dot{\epsilon}_2$	$-3\dot{\epsilon}_3$
8 :	$FeAsO_4 \cdot 2H_2O$	$F_8 =$				$+\dot{\epsilon}_3$
9 :	SO_4^{2-}	$F_9 =$	F_{90}	$+\dot{\epsilon}_1$		

heat capacity of the reacting mixture. Therefore, the heat removal requirements of the process are given by

$$\frac{\mathrm{d}Q}{\mathrm{d}t} = \Delta H^\circ_{4.1,T}\bar{r}_{4.1}S + \Delta H^\circ_{4.2,T}\bar{r}_{4.2}V \qquad (4.27)$$

Adiabatic/Autogenous Operation

When the reactor operates adiabatically then

$$\frac{\mathrm{d}Q}{\mathrm{d}t} = 0 \text{ and } \frac{\mathrm{d}T}{\mathrm{d}t} \neq 0$$

and the energy balance equation yields

$$\overline{NC}_p\frac{\mathrm{d}T}{\mathrm{d}t} = -(\Delta H^\circ_{4.1,T}\bar{r}_{4.1}S + \Delta H^\circ_{4.2,T}\bar{r}_{4.2}V) \qquad (4.28)$$

In this case equations 4.21, 4.24, 4.26 and 4.28 are coupled and were solved simultaneously by Runge-Kutta.

4.4.2 Continuous Stirred Tank Reactor (CSTR)

Table 4.III shows the stoichiometric table for a single stage CSTR having working volume V_{CSTR} and operating at steady state. The residence time for a CSTR is defined as

$$\bar{t} = \frac{V_{\mathrm{CSTR}}}{Q_{\mathrm{out}}} \qquad (4.29)$$

where Q_{out} is the volumetric flow rate of the outlet slurry. But on the basis of assumptions 1, 3, 8 and 9, outlined in the beginning of this section, eq. 4.29 gives

$$\bar{t} = \frac{V_{\text{CSTR}}}{Q_{\text{in}}} = \frac{V}{Q_{30}} = \frac{\rho_3 V}{M_3 F_{30}} \tag{4.30}$$

As with the batch reactor, the extent of reaction 4.1, $\dot{\epsilon}_1$, is obtained from the overall conversion, $\bar{x}$,

$$\dot{\epsilon}_1 = \frac{F_{10}\bar{x}}{4} \tag{4.31}$$

Substitution of $\bar{x}$ from equations 4.14 and 4.17 yields

$$\dot{\epsilon}_1 = \frac{F_{10}}{4} \sum_{\kappa} \Delta W_{\kappa} [6(k_{S,\kappa}\bar{t})^3 - 6(k_{S,\kappa}\bar{t})^2 + 3(k_{S,\kappa}\bar{t}) - 6(k_{S,\kappa}\bar{t})^3 e^{-1/k_{S,\kappa}\bar{t}}] \tag{4.32}$$

The extent of reaction 4.2, $\dot{\epsilon}_2$, is determined via the mass balance equation of Fe^{2+} in the CSTR

$$F_{50} - F_5 + 4\bar{r}_{4.1}S - 2\bar{r}_{4.2}V = 0 \tag{4.33}$$

where $F_{50} = 0$ since no Fe^{2+} enters the reactor with the feed stream. The surface area containing term $(4\bar{r}_{4.1}S)$ can be effectively eliminated by resorting to the respective mass balance equation of $FeAsS$

$$F_{10} - F_1 - 4\bar{r}_{4.1}S = 0 \tag{4.34}$$

From eq. 4.31 and recognizing that

$$\bar{x} = \frac{F_{10} - F_1}{F_{10}}$$

we obtain

$$4\bar{r}_{4.1}S = 4\dot{\epsilon}_1 = F_{10}\bar{x} \tag{4.35}$$

Therefore, the need for a separate calculation of the total surface area, as was the case for the batch reactor, is eliminated. Equation 4.33 now reads

$$-F_5 + F_{10}\bar{x} - 2\bar{r}_{4.2}V = 0 \tag{4.36}$$

Substituting F_5 from Table 4.III, and $\bar{r}_{4.2}$ from 4.6 and taking into account the fact that for a continuous flow reactor, species concentrations are given by

$$C_i = \frac{F_i \bar{t}}{V}$$

the determining expression for $\dot{\epsilon}_2$ finally becomes

$$2\dot{\epsilon}_2 V - k_2(4\dot{\epsilon}_1 - 2\dot{\epsilon}_2)^2 P_{O_2} \bar{t}^2 = 0 \tag{4.37}$$

The extent of the third reaction, $\dot{\epsilon}_3$, is obtained from an equation similar to eq. 4.26

$$(2\dot{\epsilon}_2 - \dot{\epsilon}_3)(4\dot{\epsilon}_1 - \dot{\epsilon}_3) = (F_{60} - 2\dot{\epsilon}_2 + 3\dot{\epsilon}_3)^3 \frac{\bar{t}}{V} \exp \frac{\Delta G^{\circ}_{4.3,T}}{\mathcal{R}T} \tag{4.38}$$

Isothermal Operation

For the isothermal operation of the CSTR, the three extents are determined from the algebraic equations 4.32, 4.37 and 4.38. With the aid of Table 4.III the composition of the effluent stream is calculated at various operating conditions. Similarly to the batch reactor case, F_{10} and F_{30} are calculated from

$$V_{\mathrm{CSTR}} = \frac{F_{10} M_1}{\rho_1} + \frac{F_{30} M_3}{\rho_3}$$

and

$$w_s = \frac{F_{10} M_1}{F_{10} M_1 + F_{30} M_3}$$

Solution volume V is found from eq. 4.29.

Adiabatic/Autogenous Operation

For exothermic reactions, such as the one examined here, it is preferable to operate the reactor in an autogenous mode in order to benefit from the heat release. In this case, to assess the suitable feed and operating conditions, simultaneous solution of the energy balance equation along with equations 4.32, 4.37 and 4.38 is required.

eq. 4.18 is reduced now to eq. 4.39. In the present model the operating temperature T is taken as reference temperature.

$$\text{rate of sensible heat entering} = \overline{FC}_p(T - T_{\text{in}})$$

$$\text{rate of sensible heat leaving} = \overline{FC}_p(T - T) = 0$$

$$\text{rate of heat generation} = -(\Delta H^\circ_{4.1,T}\bar{r}_{4.1}S + \Delta H^\circ_{4.2,T}\bar{r}_{4.2}V)$$

$$\text{rate of heat transferred from surroundings} = -\dot{Q}$$

Finally, after substitution in eq.4.18 we have

$$\overline{FC}_p(T - T_{\text{in}}) - \dot{Q} = -[4\Delta H^\circ_{4.1,T}\dot{\epsilon}_1 + \frac{\Delta H^\circ_{4.2,T}}{2}k_2(4\dot{\epsilon}_1 - 2\dot{\epsilon}_2)^2 P_{O_2}\bar{t}^2 V] \qquad (4.39)$$

The left hand side of eq. 4.39 represents the heat removed from the system due to the flow and losses to the surroundings while the right hand side represents the heat generated. Both are functions of the steady state operating temperature (T) and can be written as

$$R(T) = \overline{FC}_p(T - T_{\text{in}}) - \dot{Q} \qquad (4.40)$$

$$G(T) = -[4\Delta H^\circ_{4.1,T}\dot{\epsilon}_1 + \frac{\Delta H^\circ_{4.2,T}}{2}k_2(4\dot{\epsilon}_1 - 2\dot{\epsilon}_2)^2 P_{O_2}\bar{t}^2 V] \qquad (4.41)$$

Equation 4.40 represents a straight line, provided that $\dot{Q}$ is linearly dependent on T (which is the usual case, i.e. eq. 4.42), while equation 4.41 represents an S-shape curve (since reaction 4.1 is irreversible and first order [4.3]). With graphical solution of eq. 4.39, the respective Van Heerden diagram, discussed in Section 2.4.1 (Figure 2.3) is constructed and temperatures for stable operation of the continuous reactor are then identified.

4.5 Model Application

The developed model equations were used to perform various computer-aided simulation runs of pressure oxidation of arsenopyrite in batch and single-stage continuous reactors. Before the simulation results are presented, the validity of the model is

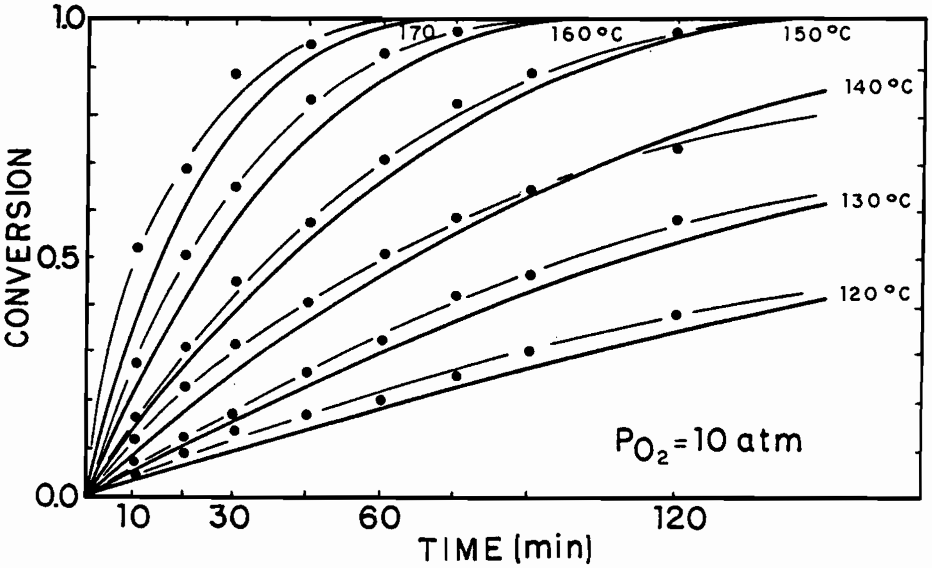

Figure 4.1: Comparison of model predictions and experimental data for the conversion of $FeAsS$ at different times and temperatures. (Conditions: 0.1% solids, –74 +53 μm)

tested comparing its predictions with small-scale experimental results that have been reported in Section 3.3.2 of the previous chapter.

4.5.1 Model Verification

In Figure 4.1 the effect of temperature on arsenopyrite conversion is shown for a number of batch tests in which very dilute (0.1% solids) slurries were used to avoid the precipitation of scorodite. The model predictions are given by the continuous lines. The model appears to give slightly lower (but not significantly different) conversions than those determined experimentally. This deviation might be attributed to two principal factors: i) the size fraction used in the leaching experiments was not a truly monosize fraction as the shrinking core model assumes[4], and ii) the arsenopyrite particles are not truly spherical but they have rather an irregular shape, thus

---

[4] The geometric mean (i.e. 62.6 μm for the –74 +53 μm fraction) was taken as the mean particle size.

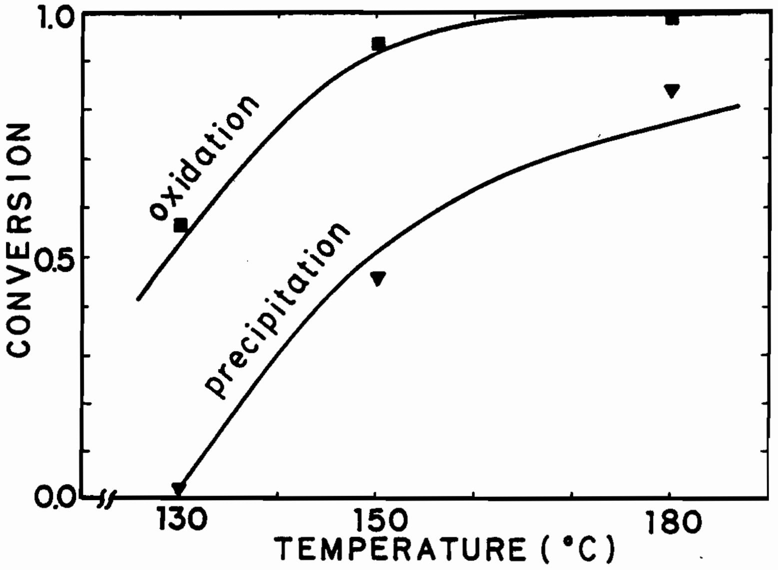

Figure 4.2: Comparison of model predictions and experimental data for the conversion of $FeAsS$ at different temperatures. (Conditions: 1% solids, 10 atm P_{O_2}, 120 min, -74 +53 μm, 0.5 N H_2SO_4)

possessing a larger surface area. Introducing a shape factor greater than one would alleviate this discrepancy. Additional experimental data (this time collected using slurry densities favouring scorodite precipitation) are compared to model predictions in Figs 4.2,4.3 and Table 4.IV. An increase in temperature promotes precipitation via the higher degree of conversion obtained and the endothermic nature of reaction 4.3 ($\Delta H^{o}_{4.3,298}$ = 69.6 kJ). Similarly, higher slurry densities increase precipitation by yielding dissolved iron(III) and arsenic(V) concentrations in excess of those predicted by the equilibrium reaction 4.3. The data of Figs 4.1 to 4.3 and Table 4.IV show reasonably good agreement between observed and calculated values. In particular, the iron distribution results are considered satisfactory with respect to the assumptions made earlier regarding the kinetics of $Fe(II)$ to $Fe(III)$ oxidation and $Fe(III)$ precipitation. This provides the necessary confidence in the model to attempt the simulation of larger scale batch and continuous reactors, which are assumed to operate under the same rate limiting step (surface reaction).

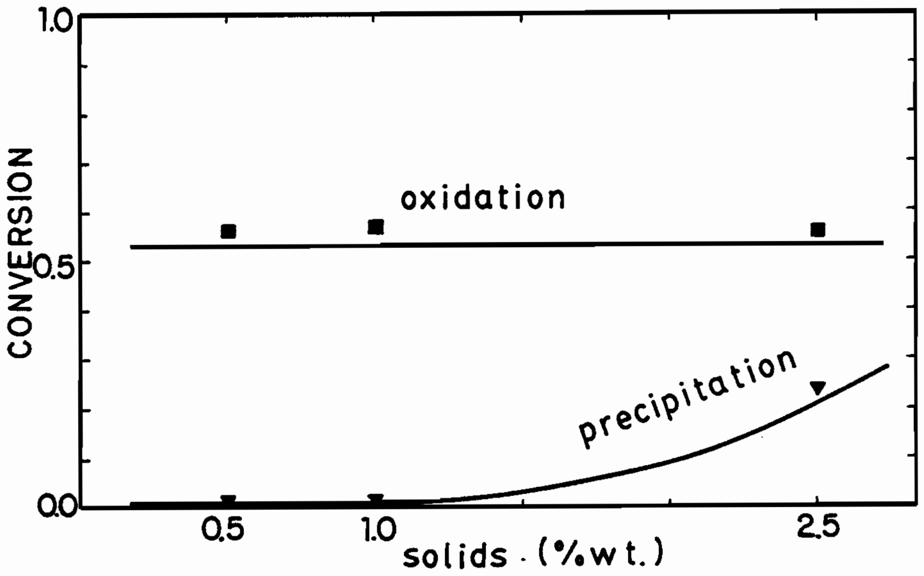

Figure 4.3: Comparison of model predictions and experimental data for the conversion of $FeAsS$ at different slurry densities. (Conditions: 130 °C, 10 atm P_{O_2}, 120 min, -74 +53 μm, 0.5 N H_2SO_4)

Table 4.IV: Comparison of model predictions and experimental data for the distribution of iron products during pressure oxidation of $FeAsS$. (Conditions: 10 atm P_{O_2}, 120 min, -74 +53 μm.)

		Iron Distribution (%)							
Conditions		Fe^{2+}(aq)		Fe^{3+}(aq)		Fe^{3+}(precip.)		Conversion (%)	
Solids (wt. %)	Temp. (°C)	Exp.	Model	Exp.	Model	Exp.	Model	Exp.	Model
1.0	130	60	54	35	36	5	10	57	54
1.0	150	28	20	22	19	50	61	96	95
1.0	180	3	3	14	17	83	80	100	100
0.5	130	84	68	16	32	0	0	56	54
2.5	130	27	34	26	19	47	47	56	54

Table 4.V: Size distribution of the arsenopyrite feed.

μm	wt. %
-74 +53	0.95
-53 +44	15.70
-44 +37	16.65
-37 +14.4	22.21
-14.4 +10.9	13.98
-10.9 +8.2	13.11
-8.2 +5.6	10.65
-5.6 +4.4	6.75

4.5.2 Batch Reactor Simulation

For the simulation runs a 100% pure arsenopyrite concentrate with the particle size distribution (PSD) given in Table 4.V is assumed to be oxidized in a single vertical autoclave with a 40 m^3 working volume.

Some simulation results (isothermal mode of operation) are shown in Figs 4.4 to 4.6. In Fig. 4.4 the effect of temperature (170–190 °C) on the oxidation of the wide size arsenopyrite feed is illustrated. For the same simulation runs (i.e. 170 to 190 °C and 20% solids), the model predicts the solution and solids compositions illustrated in Figs 4.5 and 4.6. Ferrous iron concentration initially increases rapidly followed by a gradual decay. This is typical behaviour of consecutive reactions; that is, Fe^{2+} is formed via reaction 4.1 and is consumed via reaction 4.2. Upon build-up of Fe^{3+} (via reaction 4.2), precipitation starts due to reaction 4.3 and the progress of the latter reaction can be followed in Fig. 4.6. Figure 4.6 predicts that most of the arsenopyrite ($\sim$ 90%) is completely converted to scorodite solids.

To maintain isothermal operation, the heat released by the exothermic reaction process will have to be removed continuously. With the aid of the model, the maximum rates of heat transfer are calculated and shown in Table 4.VI for various slurry densities and at 180 °C operation. These maximum rates are obtained at the initial stage of reaction 4.1 when the rate of $FeAsS$ is at its maximum. The rates are

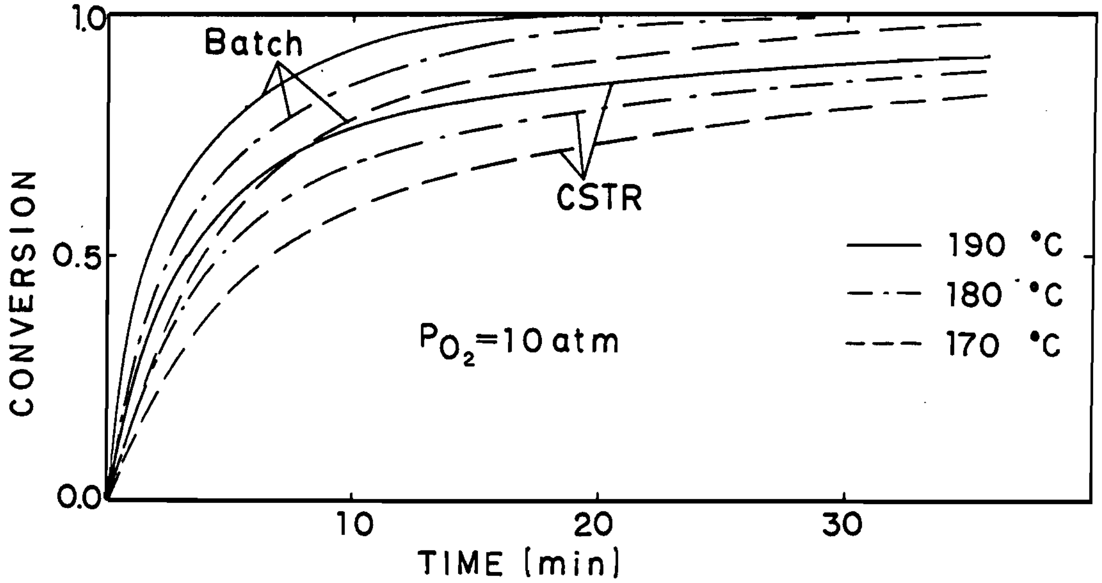

Figure 4.4: Simulation of the isothermal operation of batch reactor and CSTR: The effect of temperature on the conversion of *FeAsS*.

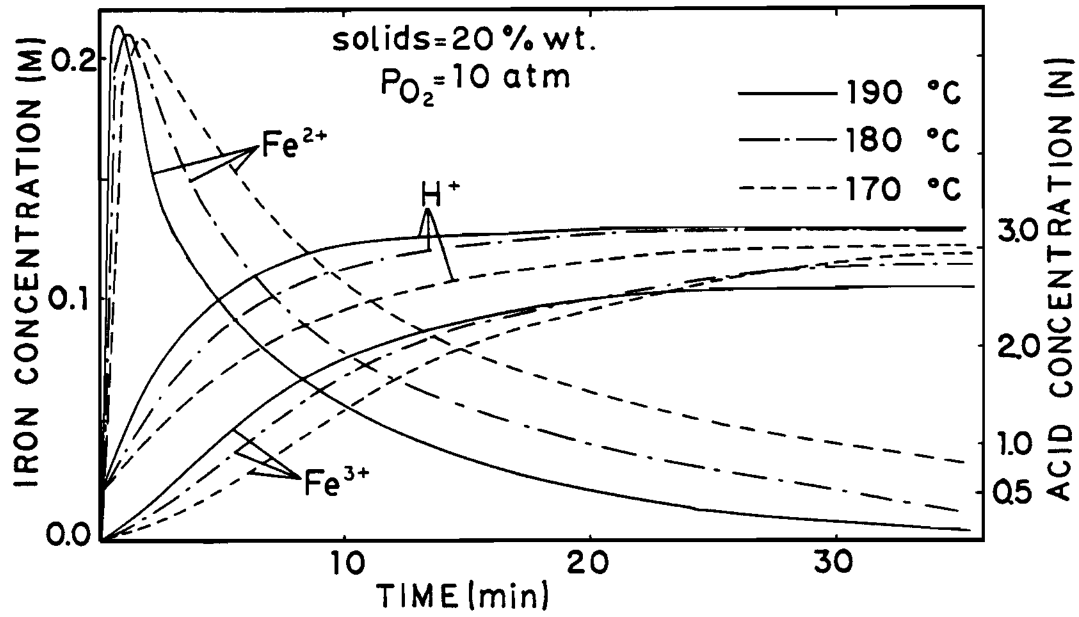

Figure 4.5: Simulation of the isothermal operation of batch reactor : Variation of the iron and acid concentrations with time.

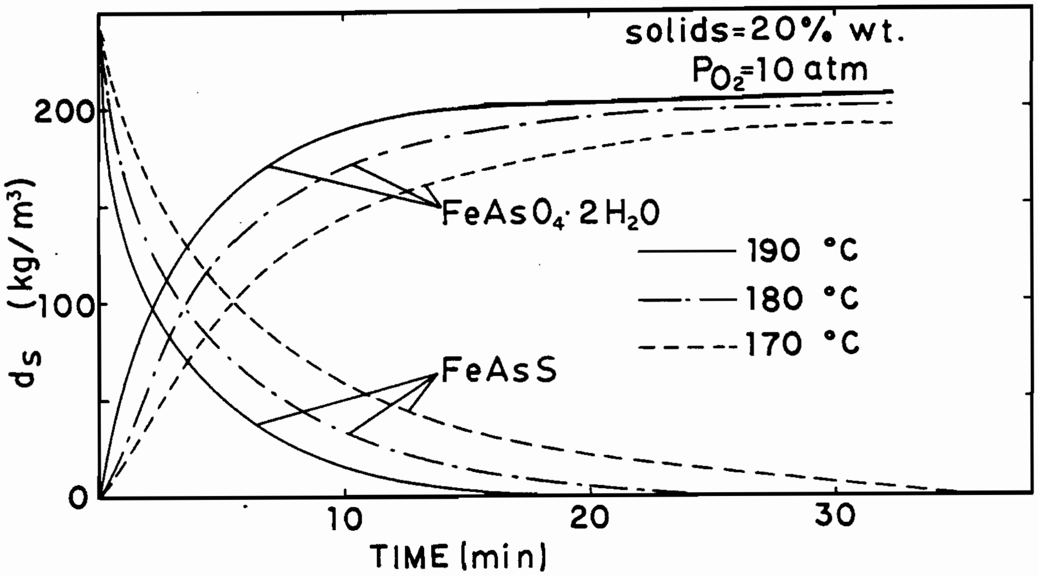

Figure 4.6: Simulation of the isothermal operation of batch reactor : The distribution of solids with time.

Table 4.VI: Isothermal operation of the batch reactor; maximum heat transfer rates. (Conditions: 180 °C; 10 atm O_2; 40 m^3 volume.)

Slurry Density (wt. %)	Heat Transfer ($kJ\ m^{-2}\ s^{-1}$)
10	27
20	60
30	100

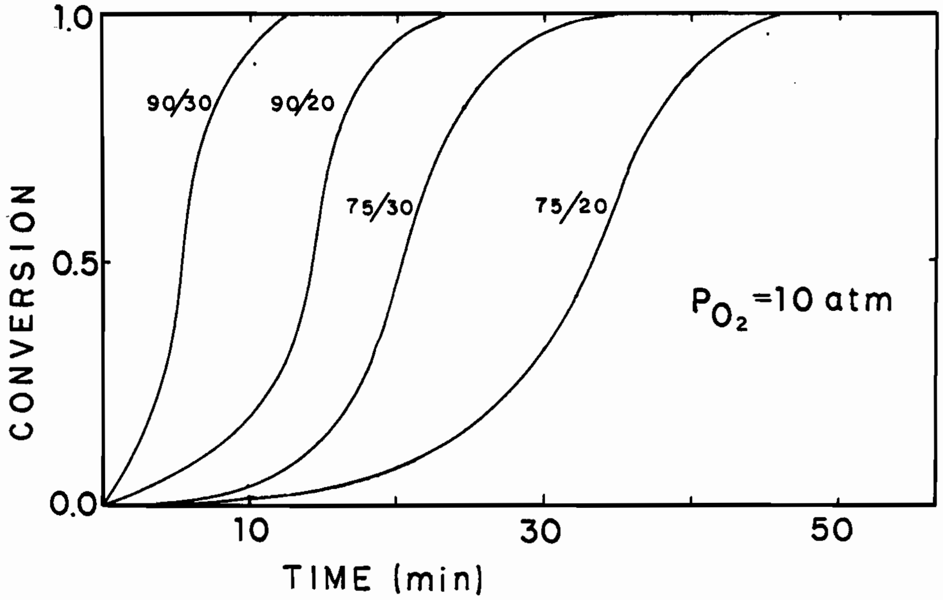

Figure 4.7: Simulation of the autogenous operation of batch reactor : The variation of conversion with time at different slurry densities and starting temperatures (temp °C/% solids).

expressed per unit area by considering heat removal affected via jacket cooling [4.4]. Heat removal through a heat exchanger can be expressed in general via the following equation:

$$-\frac{\mathrm{d}Q}{\mathrm{d}t} = \hat{h}\mathcal{E}(T - T_{\mathrm{sink}}) \tag{4.42}$$

where $\hat{h}$ is an overall heat transfer coefficient, $\mathcal{E}$ is the effective surface area (reactor walls in this case) and T_{sink} is the temperature of the cooling medium (sink). Alternative heat exchange designs [4.4] can be evaluated on the grounds of the heat removal requirements predicted by the model. However, for the present system autogenous operation is preferred.

Autogenous Operation

Typical conversion versus time curves (model results) for the case of autogenous (adiabatic) operation are shown in Fig. 4.7. These results were calculated by considering two slurry densities (20 and 30% solids) and two feed temperatures (75 and 90 °C).

It is evident that the time required for complete conversion depends now on slurry density (as opposed to the isothermal mode of operation, Fig. 4.3). This is due to the fact that the temperature rise inside the reactor depends on the amount of heat released by the reaction, i.e.

$$\text{rate of heat generation} = -(\Delta H^{\circ}_{4.1,T}\bar{r}_{4.1}S + \Delta H^{\circ}_{4.2,T}\bar{r}_{4.2}V)$$

which is proportional to the mass of charged solids.

Optimum temperatures for pressure oxidation of pyritic sulphides are in the range of 180 to 200 °C. The objective is to scan with the model various combinations of feed temperature (starting) and slurry density to obtain near 100% conversion within the target temperature region. Fig. 4.8 is a summary of the adiabatic simulation runs, where the top figure shows the final temperature (for 98% conversion) obtained at different starting temperatures and slurry densities, while the bottom figure gives the time required to achieve 98% conversion under the same operating conditions. Comparison of the isothermal run at 190 °C (Fig. 4.4) and the autogenous run at 90 °C (starting T)/190 °C (final T) (both with 20% solids) shows approximately the same total conversion time (i.e. 20 min). This comparison serves well to demonstrate the benefits of running an exothermic leaching process autogenously rather than isothermally since preheating is largely reduced (190 → 90 °C) and cooling requirements are effectively eliminated. An industrial example of a pressure leaching process operated autogenously batchwise is the Sunshine silver refinery in Kellogg, ID. A number of the operational problems experienced in this plant [4.5] could have been significantly averted if process design had been complemented with reactor modelling.

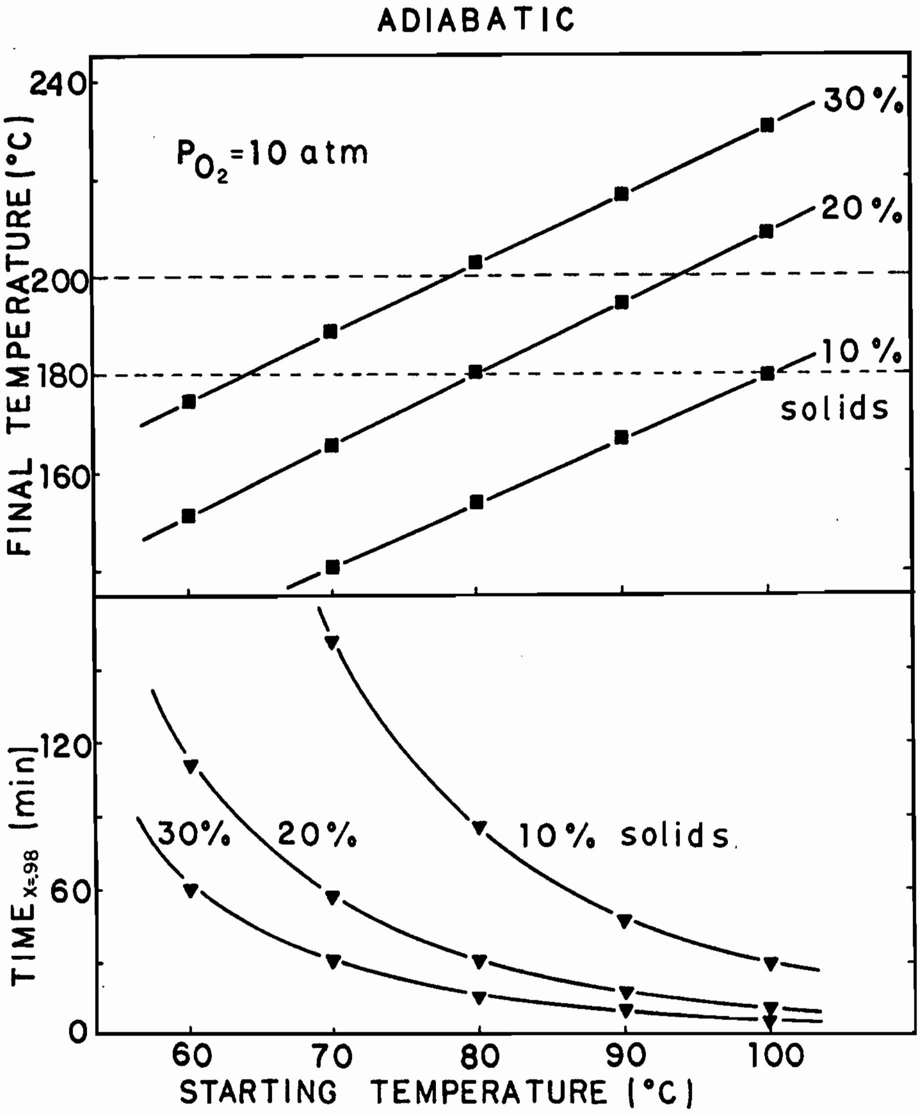

Figure 4.8: Simulation of the autogenous operation of batch reactor : The effect of starting temperature for different slurry densities on the final temperature and retention time for 98% conversion.

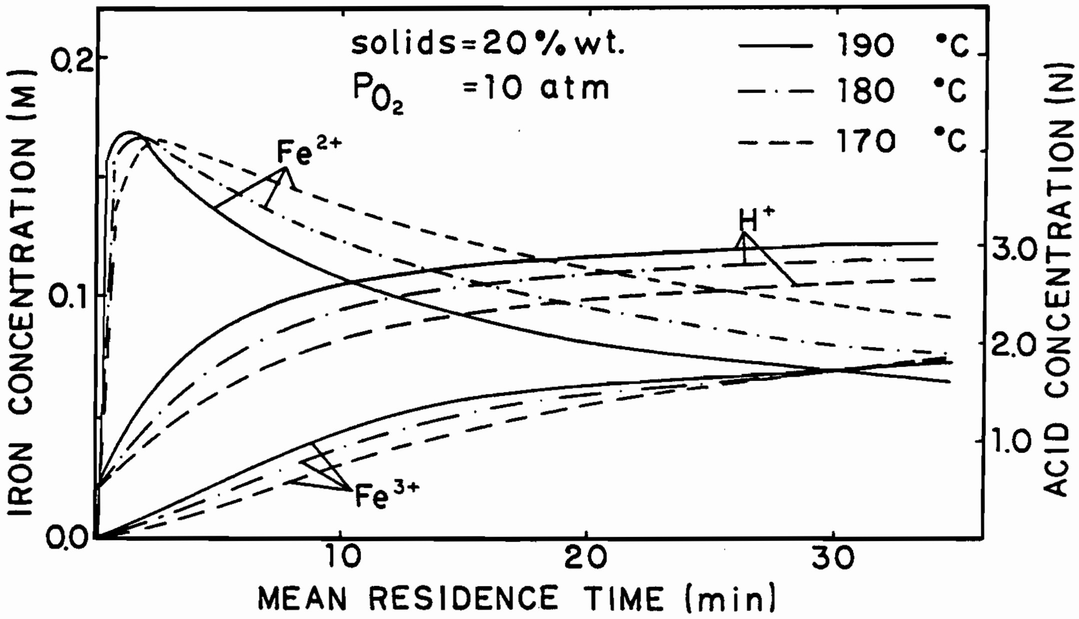

Figure 4.9: Simulation of the isothermal operation of CSTR : Variation of the iron and acid concentrations with time.

4.5.3 Continuous Reactor Simulation

Isothermal Operation

For the purpose of comparison with the batch configuration, isothermal operation is considered first. Conversion versus time curves are shown in Fig. 4.4. The lower conversions corresponding to the CSTR for the same retention time are attributed to the residence time distribution of the particles. Figs. 4.9 and 4.10 show the effects of temperature on the outlet slurry composition.

Autogenous Operation

The main objective of the model is to determine the feed temperature, slurry density and residence time (or equivalently the volumetric flow rate for a given constant volume reactor as is the case considered here) in order to obtain stable steady state operation within the targeted temperature range of 180 to 200 °C.

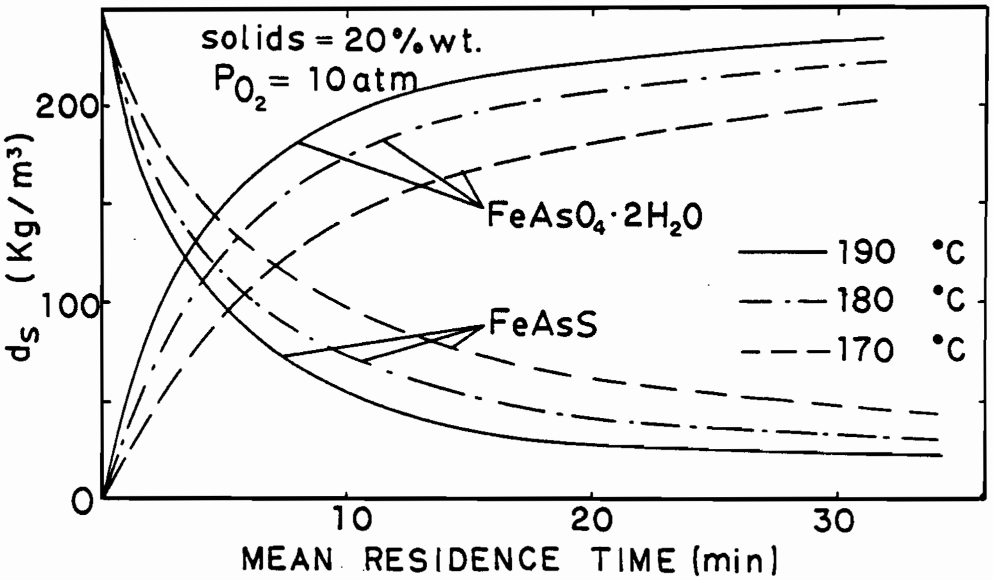

Figure 4.10: Simulation of the isothermal operation of CSTR : The distribution of solids with time.

In Figure 4.11 Van Heerden diagrams for various retention times ($\bar{t}$ =10 to 100 min) are shown for a feed temperature of 80 °C, a slurry density of 5% solids and adiabatic conditions. Arsenopyrite solids are assumed to have the particle size distribution given in Table 4.IV. Retention times 10 and 20 min represent situations where insufficient heat is generated to raise the temperature to a sufficiently high level for the process to be self sustaining (due to the very fast flow rates, the heat removal rates exceed the heat generated rates). Hence, conversion is negligible. However, for $\bar{t}$ = 30 to 100 min, enough heat is liberated to sustain stable operation within the preferred temperature region (180 to 200 °C). It is implied that for a fixed volume reactor, operation with a short (30 min) rather than a long (100 min) retention time is preferable since reactor throughput is greatly augmented without significant conversion loss (95% with 30 min versus 99% with 100 min)[5]. This important observation can lead to process intensification of existing leaching facilities. Alternatively, the same kind of process analysis can lead to reactor volume optimization for a given

---

[5] However, operating with 30 min retention time results in multiple steady states.

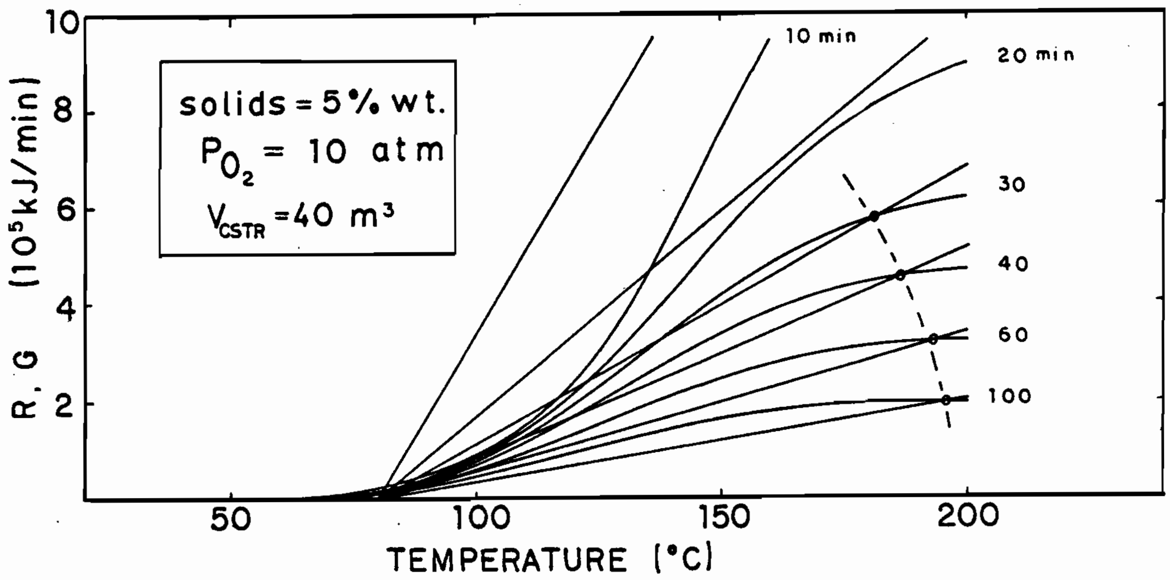

Figure 4.11: Searching for stable autogenous operating temperature : The effect of retention time ($\dot{Q} = 0$).

plant throughput with concurrent important capital savings.

Another important observation which can be made in reference to Fig. 4.11 is that it is possible to obtain a unique steady state within the target temperature region by preheating the feed at a temperature above 100 °C and applying simultaneously external cooling (in order to have a steep heat removal line). But this might not be economical since it results in a lot of energy waste (preheating and cooling). The existence of multiple solutions imposes also some problems during the start-up of the reactor, which has to be externally heated beyond the unstable steady state temperature in order to allow operation at the high conversion stable steady state temperature (points B and C in Figure 2.3, Chapter 2).

Next, the effect of feed temperature on the autogenous operation of a continuous pressure reactor (40 m^3) is examined. In Fig. 4.12 the results for 100 min retention time and two slurry densities (5 and 10%) are illustrated. According to the analysis presented above, stable steady state under autogenous operation is possible only with

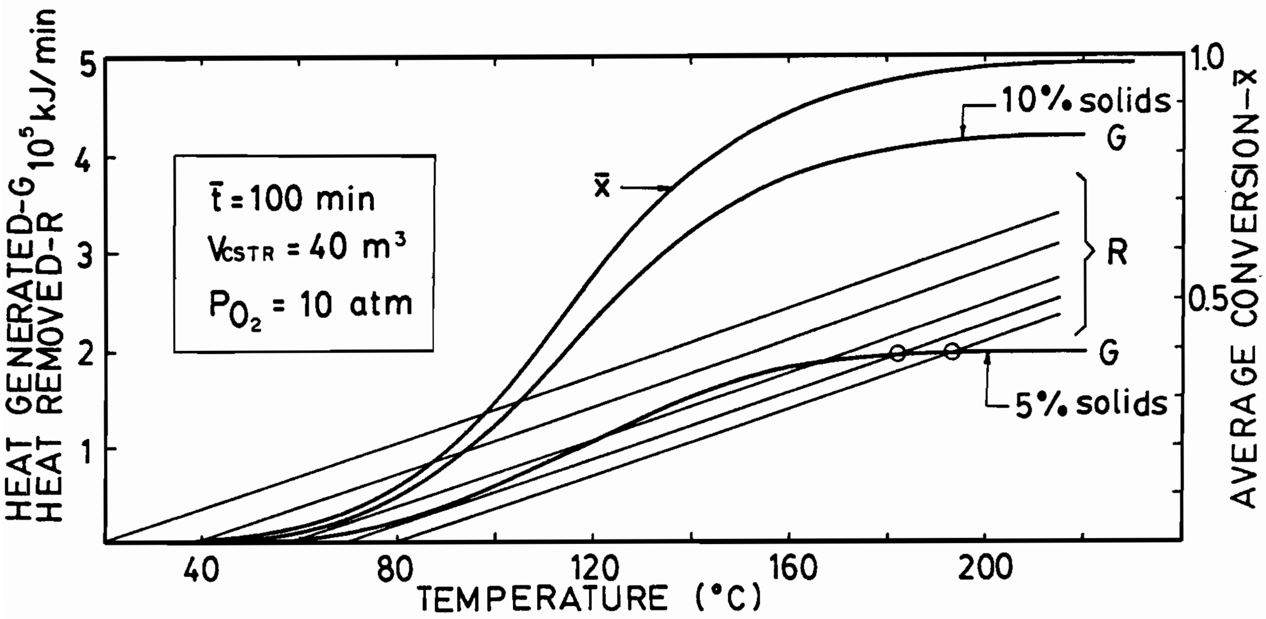

Figure 4.12: Searching for stable autogenous operating temperature : The effect of feed temperature at $\bar{t} = 100$ min ($\dot{Q} = 0$).

5% slurry density and feed temperature of 70 or 80 °C. Under these conditions the reactor operates at 180 or 190 °C yielding 95% conversion of arsenopyrite. Obviously, according to the model predictions of Fig. 4.12, provision for a cooling system is necessary if the slurry density is to be increased to 10% solids. Alternatively, if the nominal retention time is reduced to 50 min (by increasing the flow rate), then according to Fig. 4.13 autogenous operation is possible at a temperature slightly above 220 °C, with 20 °C slurry feed temperature and 10% solids. External cooling will be necessary in this case to control temperature within the target region of 180 to 200 °C.

Having identified the best conditions (i.e. feed temperature, slurry density, retention time etc.) to achieve autogenous operation of the continuous reactor, the conversion as well as solution and solids composition in the exit slurry can be obtained by referring to isothermal graphs similar to those of Fig. 4.4, 4.9 and 4.10. Thus for example, autogenous operation with 5% solids, feed temperature 80 °C and 30 min nominal retention time (Fig. 4.11) yields 180 °C steady state temperature

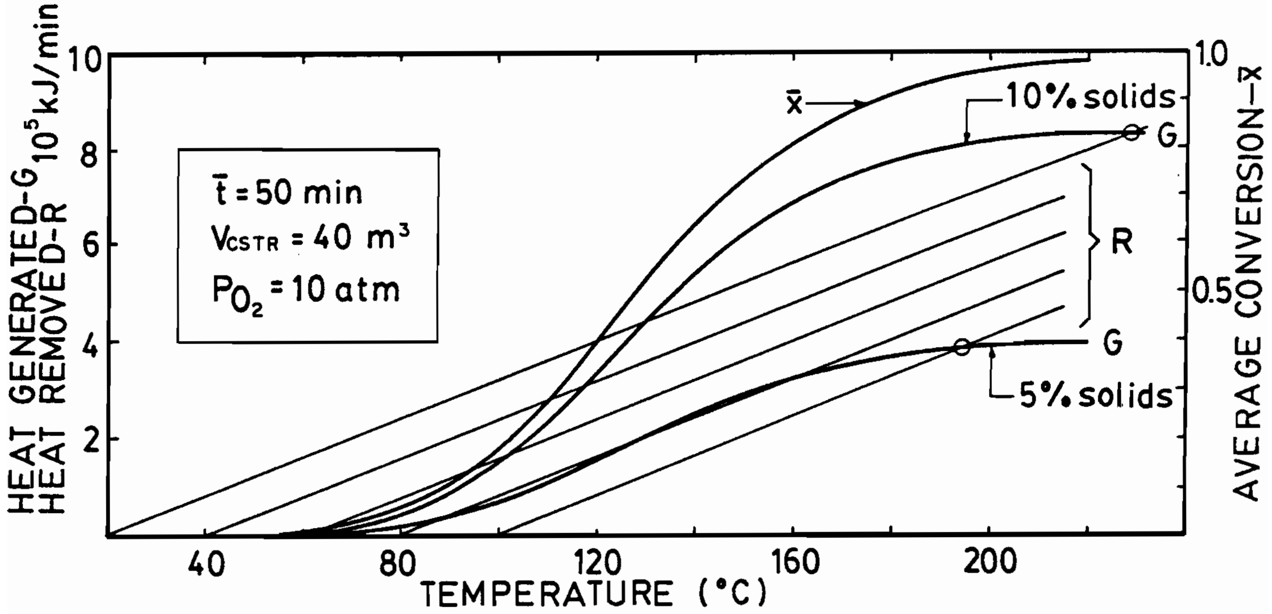

Figure 4.13: Searching for stable autogenous operating temperature : The effect of feed temperature at $\bar{t}$ = 50 min ($\dot{Q} = 0$).

and 86% arsenopyrite conversion (Fig. 4.4).

In the mathematical development presented in this chapter, it has been implicitly assumed that the same physicochemical laws govern the pressure oxidation process regardless of reactor size. Under this implicit assumption, the preceding discussion and the qualitative conclusions drawn regarding the autogenous operation of a single-stage CSTR are valid independent of reactor size. The employment of a 40 m³ reactor volume represents simply an arbitrary selection of a hypothetical industrial size reactor for the purpose of demonstrating the application of the model. A careful examination of the simulation results derived with the model, as the latter was applied to the autothermal operation of the single-stage CSTR, reveals that whenever the desired stable steady state operating temperature is in the range of 180 to 200 °C, high arsenopyrite conversions ($\geq$ 85%) are predicted (Figs 4.11, 4.12 and 4.13). The underlying cause behind this high conversion is the high activation energy value associated with the surface reaction controlling step, which results in a steep increase of the heat generation curve beyond a certain "ignition" temperature.

Since the heat removal lines (whenever no external cooling is applied) have a slope less than the slope of the heat generation curve (at the inflection point), the only intersection point which satisfies the condition for stable steady state (equation 2.21, Section 2.4.1) is the one associated with high conversion. Although stable steady state operation with high degree of conversion is highly desirable, since it can lead to reactor volume reduction, this is not what is actually observed in practice. As will be shown later in this thesis, this apparent deviation of the present predictions from industrial reactor performance data has its origins in a shift in the rate-limiting step from surface reaction to gas–liquid mass transfer.

4.6 Summary

A mathematical model which combines the intrinsic leaching kinetics of wide-size arsenopyrite particulates with the reaction extents of two secondary consecutive reactions (namely, the oxidation of Fe^{2+} to Fe^{3+} and the precipitation of scorodite) was formulated to describe the overall pressure oxidation process ($FeAsS/O_2/H_2SO_4/130-200$ °C). This model successfully predicts the outcome of laboratory-scale batch tests in terms of conversion and composition of dissolved and precipitated products.

The model was further used to simulate the performance of large scale batch and continuous reactors (single-stage CSTR) where surface reaction was assumed to be the rate-limiting step of the heterogeneous reaction. For the latter reactor configuration, the segregated flow model was applied to calculate the conversion of the mineral. An important feature of the developed model is the coupling of leaching kinetics and reactor heat balance. This is a necessary condition for modelling highly exothermic leaching systems. Examples illustrating the usefulness of the model in identifying stable steady state conditions for autogenous reactor operation were presented.

References

[4.1] D.R. McKay and J. Halpern, *Trans. TMS-AIME*, 6, 301 (1958).

[4.2] C.W. Bale, A.D. Pelton and W.T. Thomson, *"Facility for the Analysis of Chemical Thermodynamics (F*A*C*T)"*, McGill University, Montreal, Quebec.

[4.3] C.G. Hill, *An Introduction to Chemical Engineering Kinetics and Reactor Design*, , p. 2, 3, 411, 370, John Wiley and Sons, New York NY, (1977).

[4.4] K.M. Sarkar, *Trans. IMM*, 94, C184 (1985).

[4.5] J.B. Ackerman and C.S. Bucans, *Min. Metall. Proc.*, 3(1), 20 (1986).

Chapter 5

Reactor Models for Multi-Stage Continuous Pressure Oxidation: Surface Reaction or Gas Transfer Control

5.1 Introduction

In the previous chapter, the modelling of a single-stage continuous reactor for an exothermic pressure leaching process (pressure oxidation of $FeAsS$) was described. However, continuous pressure reactors used in industry have multiple stages (multi-compartment autoclaves). Operation of this type of reactor is often limited by the gas transfer rate rather than the surface reaction kinetics. It becomes necessary, therefore, that a comprehensive model dealing with the operation of a pressure reactor cascade under gas–liquid transfer limitations to be developed. In this chapter, the modelling approach employed previously (Chapter 4) is extended to address indeed this need. The following new developments and improvements to the modelling methodology presented in Chapter 4 are made:

1. The model is extended to a multi-stage continuous pressure reactor.
2. The model is further extended to deal with more than one heterogeneous reaction since industrial feeds are multi-mineral materials.

3. A continuous size distribution function (rather than discrete) is employed to describe the size of particles in the feed.

4. The macroscopic mass transfer kinetics of oxygen are coupled with the dissolution rate of a single particle.

5. The particle size distribution function at the exit of each reactor stage is derived from the size distribution of the feed, the particle kinetics, and the residence time distribution functions.

6. The powerful "Population Balance Model" is utilized to predict the size distributions and particle surface areas inside each reactor stage.

Part of the material presented in this chapter has been published in *Control '90*[1], and in *Precious Metals 1990*[2].

5.2 The Chemical Reaction System

In this chapter, a concentrate composed of pyrite and arsenopyrite (the two major host minerals of refractory gold; see Section 2.2) is considered as being the feed to a continuous multi-stage pressure reactor. Since emphasis is given to the modelling of the autothermal operation of the <u>oxidation</u> process, only the reactions associated with high enthalpy changes and significant oxygen consumption demands are considered here. Thus, the following reaction scheme represents the pressure oxidation process.

$$O_2(g) \longrightarrow O_2(aq) \tag{5.1}$$

$$2FeS_2(s) + 7O_2(aq) + 2H_2O(l) \longrightarrow 2Fe^{2+}(aq) + 4HSO_4^-(aq) \tag{5.2}$$

$$4FeAsS(s) + 13O_2(aq) + 6H_2O(l) \longrightarrow 4H_3AsO_4(aq) + 4Fe^{2+}(aq) + 4SO_4^{2-}(aq) \tag{5.3}$$

Reaction 5.1 represents the mass transfer of oxygen from the gas to the liquid phase. Reactions 5.2 and 5.3 represent the oxidation of pyrite and arsenopyrite respectively

---

[1] Ed. by R.K. Rajamani and J.A. Herbst, pp. 121–126, SME, Littleton CO (1990).

[2] Ed. by D.A. Corrigan, pp. 61–73, IPMI, Allentown PA (1990).

by oxygen. Retention of this simplified reaction scheme is justified on the following grounds. Side reactions, such as oxidation of $Fe(II)$ by $O_2(aq)$ or precipitation of $Fe(III)/As(V)$ as hematite and/or scorodite, are marginal in terms of thermal impact as established in the beginning of Chapter 4. Moreover, in terms of O_2 consumption, the oxidation of $Fe(II)$ to $Fe(III)$ is insignificant. For example, on the basis of reaction 5.2 and 5.3 stoichiometries, 3.5 and 3.25 moles of $O_2(aq)$ are consumed per g-atom of Fe respectively. On the other hand, only 0.25 moles of $O_2(aq)$ per g-atom of Fe are needed for the consecutive oxidation reaction:

$$2Fe^{2+}(aq) + \frac{1}{2}O_2(aq) + 2H^+(aq) \longrightarrow 2Fe^{3+}(aq) + H_2O \tag{5.4}$$

This corresponds to a 7.1% or 7.7% excess of $O_2(aq)$ respectively. In reality, the latter figures should be less since reaction 5.4 is not instantaneous.

The rate of oxygen dissolution in the aqueous phase (reaction 5.1) is given by [5.1]:

$$r_{O_2(aq)} = k_L a(C^\star_{O_2} - C_{O_2}) \tag{5.5}$$

where k_L is the mass transfer coefficient, a is the gas–liquid specific surface area, $C^\star_{O_2}$ the equilibrium concentration of $O_2(aq)$ corresponding to the gas phase partial oxygen pressure $P^\star_{O_2}$, and C_{O_2} the concentration of $O_2(aq)$ in the bulk. Equation 5.5 is the rate expression for the case of physical absorption (i.e. when no chemical reactions are involved in the mechanism of oxygen transfer). The use of eq. 5.5 is justified by the fact that the homogeneous reaction 5.4 is very slow and takes place in the bulk of the solution rather than at the gas–liquid interface [5.2]. Furthermore, the heterogeneous reactions 5.2 and 5.3 take place far from the gas–liquid interface. The effect of mass transfer rate enhancement due to the existence of very fine mineral particles (with sizes less than the thickness of the boundary layer), which has been qualitatively discussed elsewhere [5.3], is not considered here. Equation 5.5 can also be written in terms of oxygen pressures by using Henry's law. That is

$$r_{O_2(aq)} = k'_L a(P^\star_{O_2} - P_{O_2}) \tag{5.6}$$

Table 5.I: Thermodynamic data for reactions 5.1, and 5.2 (from ref. [5.4])

Species	$\Delta H^{\circ}_{f,298}$ kJ mol^{-1}	$C_p = A + B10^{-3}T + C10^{5}T^{-2}$ J K^{-1} mol^{-1}		
		A	B	C
$O_2(g)$	0.000	29.957	4.184	-1.674
$FeS_2(s)$	-171.544	74.764	5.577	-12.740
$HSO_4^-(aq)$	-887.008	-574.292	1342.156	266.780

where Henry's constant, k_H, is now grouped together with k_L and designated as k'_L. In equation 5.6, P_{O_2} is the hypothetical oxygen pressure which corresponds to an equilibrium concentration of C_{O_2}.

According to the findings of Chapter 3, the intrinsic kinetics of reactions 5.2 and 5.3 can be described using the shrinking core model for surface reaction control. The respective conversions as functions of oxygen pressure, particle size, and time are given by:

$$x = 1 - \left(1 - 75 \cdot 10^6 \frac{P_{O_2}}{d_0} t \exp(-\frac{13283}{T})\right)^3 \tag{5.7}$$

for FeS_2 reacting according to the stoichiometry of reaction 5.2, and by:

$$x = 1 - \left(1 - 2622 \frac{P_{O_2}}{d_0} t \exp(-\frac{8672}{T})\right)^3 \tag{5.8}$$

for $FeAsS$ reacting according to the stoichiometry of reaction 5.3. Oxygen pressure, P_{O_2}, is expressed in atm, d_0 in cm, and t in min. Strictly speaking, eq. 5.7 is valid only for temperatures higher than 160 °C and oxygen pressures less than 10 atm, as determined in Chapter 3. Nevertheless, in this study eq. 5.7 was used for lower temperatures as well, for computational simplicity. This does not influence the prediction power of the model since the target temperature range for steady state operation lies above 170 °C. For the case of gas transfer controlled kinetics a new shrinking core model equation is developed later in this chapter.

Thermodynamic data in addition to those listed in Tables 3.II and 4.I are given in Table 5.I. The inclusion of these data is necessary in view of the introduction of the two new reactions 5.1 and 5.2, for which the standard enthalpy changes at 298 K were calculated to be

$$\Delta H^{\circ}_{5.1,298} = -11.7 \quad \text{kJ}$$

$$\Delta H^{\circ}_{5.2,298} = -2729.5 \quad \text{kJ}$$

5.3 Model Development

The basic framework for modelling a continuous reactor for an exothermic leaching process was described in the previous chapter. Here, extension is made to a cascade of continuous reactors. In this section, the development of mathematical expressions is made for the general case involving the following heterogeneous reaction:

$$A(aq) + bB(s) \longrightarrow \text{soluble} \quad \text{products} \tag{5.9}$$

Application to the specific system of chemical reactions described in the previous section will be presented later. The assumptions made in Chapter 4 are also valid in this chapter, unless otherwise stated. The overall objective remains to assess the reactor performance in order to identify the feed conditions for stable steady state operation. Once the basic mathematical expressions are developed, extension to a system of multiple heterogeneous reactions is readily accomplished as demonstrated in this chapter. At this point it is useful to remember that the exothermicity of the reaction system necessitates the selection of feed conditions and reactor configurations favouring autogenous (autothermal) operation for optimum thermal energy utilization.

5.3.1 The Basic Mass and Heat Balance Equations

It is assumed that there exists a series of L continuous reactors[3], as shown in Fig. 5.1, each of arbitrary volume $V_{\text{CSTR},\ell}$ $(1 \leq \ell \leq L)$. The exit stream of each reactor constitutes the feed to the next one (no inter-stage recycling of any kind is assumed

---

[3] Or, equivalently, a multi-compartment horizontal autoclave.

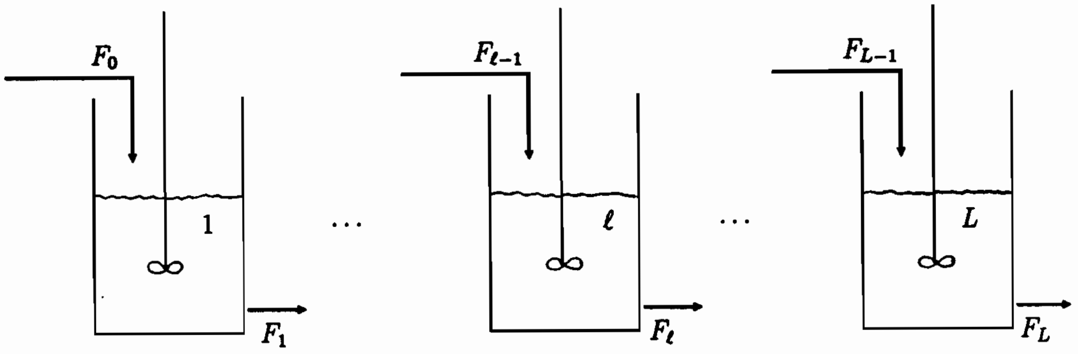

Figure 5.1: A cascade of L continuous stirred tank reactors

to take place). The following steady state mass balance equation can be written for the solid phase of reaction 5.9 in the ℓ-th reactor.

$$F_{\ell-1} - F_\ell - \bar{r}_{5.9} S_\ell = 0 \tag{5.10}$$

Similarly, the heat balance equation for the ℓ-th reactor is given by

$$(F_{\ell-1} + F_w)\bar{C}_p(T_\ell - T_{\ell-1}) - \dot{Q}_\ell = -\Delta H^\circ_{5.9,T_\ell}\bar{r}_{5.9} S_\ell \tag{5.11}$$

where the left hand side of equation 5.11 represents the rate of heat removal and the right hand side the rate of heat generation due to reaction 5.9. Both are functions of the operating temperature T_ℓ. The mean conversion of the solid phase B inside the ℓ-th reactor is defined by

$$\bar{x}_\ell = \frac{F_{\ell-1} - F_\ell}{F_{\ell-1}} \tag{5.12}$$

Combining eqs 5.10 and 5.12 the following relations are obtained

$$\bar{r}_{5.9} S_\ell = \bar{x}_\ell F_{\ell-1} \tag{5.13}$$

$$F_\ell = (1 - \bar{x}_\ell) F_{\ell-1} \tag{5.14}$$

The input molal flow rate of solids to the ℓ-th reactor ($F_{\ell-1}$) can be expressed through eq. 5.14 in terms of the initial flow rate to the first reactor (F_0 is a more convenient variable) as follows

$$F_{\ell-1} = (1-\bar{x}_{\ell-1})(1-\bar{x}_{\ell-2})\cdots(1-\bar{x}_2)(1-\bar{x}_1)F_0 \tag{5.15}$$

Substitution of eqs 5.13 and 5.15 into eq. 5.11 yields

$$[F_0\prod_{i=\ell}^{\ell-1}(1-\bar{x}_\ell)+F_{\mathrm{w}}]\bar{C}_p(T_\ell-T_{\ell-1})-\dot{Q}_\ell = -\Delta H^\circ_{5.9,T_\ell}F_0\bar{x}_\ell\prod_{\ell=1}^{\ell-1}(1-\bar{x}_\ell) \tag{5.16}$$

When j simultaneous reactions, of the same type as reaction 5.9, take place (where only one solid phase participates in each reaction, i.e. j solid phases) the j flow rates and heat of reactions have to be taken into account in eq 5.16. This results in

$$[\sum_j F_{j0}\prod_{\ell=1}^{\ell-1}(1-\bar{x}_{j,\ell})+F_{\mathrm{w}}]\bar{C}_p(T_\ell-T_{\ell-1})-\dot{Q}_\ell = -\sum_j\Delta H^\circ_{j,T_\ell}F_{j0}\bar{x}_{j,\ell}\prod_{\ell=1}^{\ell-1}(1-\bar{x}_{j,\ell}) \tag{5.17}$$

In several instances it is preferred to exercise control of the operating temperature by injecting water (at a temperature T_{H_2O}) into a reactor stage [5.5]. In this case the following term

$$F_{H_2O,\ell}C_{p,H_2O}(T_\ell-T_{H_2O})$$

must be added to the left hand side of equation 5.16 (or eq. 5.17). The addition of water changes the mean residence time $\bar{t}_\ell$, since the latter depends on the volumetric flow rate ($\bar{t}_\ell = V_\ell/\mathcal{Q}_\ell$). Thus, an appropriate adjustment is necessary to account for the increase in the volumetric flow rate ($\mathcal{Q}_\ell$). Note that due to the assumptions made in the previous chapter, the mean residence time of the aqueous phase is equal to the mean residence time of the solid phase (or to any of the j solid phases).

The mean conversion of B in the ℓ-th reactor ($\bar{x}_\ell$) is a function of the operating temperature (T_ℓ), the mean residence time ($\bar{t}_\ell$), and the particle size distribution of reacted solids at the exit of the ℓ–1-th reactor. According to the segregated flow model (see Chapter 4), the conversion is calculated from the following equation

$$\bar{x}_\ell = \int_{d_{0,\mathrm{min}}}^{d_{0,\mathrm{max}}} f_{\mathrm{m},\ell-1}(d_0)\int_0^\infty x(d_0,t)E_\ell(t)\,\mathrm{d}t\,\mathrm{d}d_0 \tag{5.18}$$

where $x(d_0, t)$ is the batch reactor conversion function (shrinking core model) for particles with initial size d_0, $E_\ell(t)$ is the residence time distribution (RTD) function of the ℓ reactor, and $f_{m,\ell-1}(d_0)$ is the particle size density (PSD) function (based on the mass of particles) at the exit of the ℓ-1-th reactor. The incorporation of $f_m(d_0)$ is what differentiates equation 5.18 from equation 4.14 employed in the previous chapter. It is evident that for the case of j multiple heterogeneous reactions equation 5.18 has to be written for each solid phase separately.

For ideal mixing conditions the RTD function for stage ℓ is

$$E_\ell(t) = \frac{1}{\bar{t}_\ell} e^{-t/\bar{t}_\ell} \tag{5.19}$$

The objective is to determine $\bar{x}_\ell$ and T_ℓ via the simultaneous solution of eqs 5.16 and 5.18 since these two variables are interdependent. To achieve this, the conversions in all previous ℓ–1 stages as well as the operating temperature of the previous stage ($T_{\ell-1}$) have to be known. The flow rate of the feed (F_0) and the rate of heat removal ($-\dot{Q}_\ell$) must also be known, and they can serve as parameters to force convergence towards a desired T_ℓ value. The graphical solution of eq. 5.16 was discussed in the previous chapter. Once $\bar{x}_\ell$ and T_ℓ are found, the overall conversion at the exit of the series of ℓ reactors ($\hat{x}_\ell$) is then calculated by

$$\hat{x}_\ell = \frac{F_0 - F_\ell}{F_0} = 1 - \prod_{\ell=1}^{\ell} (1 - \bar{x}_\ell) \tag{5.20}$$

From the preceding analysis it becomes clear that the assessment of the performance of the reactor cascade is performed on a stage by stage basis. In other words, starting from stage 1, the operating temperature, the conversion and the particle size distribution at the exit stream are calculated before going to stage 2, and so on. This procedure is mandatory only when the adiabatic mode of reactor operation is modelled. For isothermal operation, without inter-stage recycling, the whole procedure is considerably simplified by treating a reactor stage sub-sequence as a single stage. This approach is discussed in Appendix B.

5.3.2 Selection of a Particle Size Density Function for the Feed

Before dealing with the PSD of reacted particles, an appropriate PSD function for the feed has to be selected. The latter must possess the following properties:

- Have a finite value between a minimum and a maximum particle size
- Be exactly zero elsewhere

In other words, it should not tend asymptotically to zero when particle size tends to infinity, as is the case with several of the well known PSD functions (Rosin-Ramler, Normal, Log-Normal, Gamma, etc. [5.6]). This is essential in order to sustain conservation of all particles, and especially those belonging to the coarse particle fraction. These coarse particles dominate in the final stages of a reactor cascade (since finer particles react completely earlier).

The feed particle size density function chosen for the present work is the one described by Peleg *et al.* [5.7], and is given below

$$f(d_0) = \frac{\frac{\alpha d_0 - d_0^2}{\alpha d_0 - d_0^2 + \beta} \exp[-(\frac{d_0-\mu}{c})^2]}{\int_0^{\alpha} \frac{\alpha d_0 - d_0^2}{\alpha d_0 - d_0^2 + \beta} \exp[-(\frac{d_0-\mu}{c})^2] \, \mathrm{d}d_0} \tag{5.21}$$

This is a modified "normal" distribution function and has the property of being zero at $d_0 = 0$ and $d_0 = \alpha$, where 0 and α is the minimum and maximum particle size respectively. The constant β takes arbitrary values but usually $\beta = 0.1\alpha$. Furthermore, the median μ and the spread c can be varied independently which offers the ability of fitting eq. 5.21 to a wide variety of real particle populations. This particular expression was initially proposed as a PSD function, f_{n}, based on the number of particles, but its fitting flexibility allows its utilization as PSD function, f_{m}, based on the mass of particles, as well[4]. The procedure for fitting eq. 5.21 to size distribution data of a real concentrate is described in Appendix F.

---

[4] These functions will be called hereafter "number-PSD" and "mass-PSD" functions respectively.

Alternative PSD functions which might prove equally useful (but not actually tested in this work) are the Truncated Log-Normal [5.8] or the Gaudin-Meloy [5.6]. Both of them have the properties outlined in the beginning of this subsection.

5.3.3 Description of the Size Distribution of Reacted Particles

To proceed from one stage to the next, the exit mass-PSD of the previous stage must be known in order for $\bar{x}_\ell$ to be calculated via eq. 5.18. Calculation of the PSD function of reacted solids at the exit of a continuous reactor may be accomplished via two alternative approaches. The first, is to use the residence time distribution concept in order to develop the necessary expression; the second, is to use the population balance model (PBM). The latter is a powerful tool whose usefulness in the modelling of heterogeneous systems goes beyond the mere calculation of the exit PSD function. Thus, Appendix D is devoted to its description. Here the first approach, which is based on the concept of RTD, is developed for both monosize and multi-size feeds.

Monosize Feed

The size of a reacted particle at the exit of the reactor depends on its initial size (d_0), the rate of particle shrinkage (kinetics), and the time the particle spent in the reactor. If a reacting particle follows the shrinking core model for surface reaction control, then, its size decreases linearly with reaction time until it disappears according to the following function:

$$d(d_0,t) = \begin{cases} d_0(1 - k_S t) & \text{for} \quad 0 \leq t < \frac{1}{k_S} \\ 0 & \text{for} \quad \frac{1}{k_S} \leq t \end{cases} \tag{5.22}$$

Since there exists a distribution of residence times (given by eq. 5.19) it becomes evident that a monosize feed will produce a multi-size product with particle diameters d between 0 and d_0. Hence, for monosize feed, the mass-PSD function, $f_m(d)$, is given by

$$f_{\mathrm{m}}(d) = \frac{d^3 e^{-\frac{d_0-d}{\bar{t}k_S d_0}}}{\int_0^{d_0} d^3 e^{-\frac{d_0-d}{\bar{t}k_S d_0}}\,\mathrm{d}d} \tag{5.23}$$

The detailed derivation of $f_{\mathrm{m}}(d)$ is presented in Appendix C.

Multi-size Feed

The size distribution of a widely sized feed material with particle diameters varying from $d_{0,\mathrm{min}}$ to $d_{0,\mathrm{max}}$ can be described by a continuous function $f_{\mathrm{m},0}(d_0)$. The latter may be given by equation 5.21, for example. Then, the probability of a particle to have an initial size d_0 has to be taken into account as well. Hence, another variable is added, namely d_0. Again the reader is referred to Appendix C for the detailed derivation of $f_{\mathrm{m}}(d)$ for a multi-size feed, which is given by

$$f_{\mathrm{m}}(d) = \frac{d^3 \int_d^{d_{0,\mathrm{max}}} d_0^{-3} f_{\mathrm{m},0}(d_0) e^{-\frac{d_0-d}{\bar{t}k_S d_0}}\,\mathrm{d}d_0}{\int_0^{d_{0,\mathrm{max}}} d^3 \int_d^{d_{0,\mathrm{max}}} d_0^{-3} f_{\mathrm{m},0}(d_0) e^{-\frac{d_0-d}{\bar{t}k_S d_0}}\,\mathrm{d}d_0\,\mathrm{d}d} \tag{5.24}$$

Evidently, in calculating the PSD function for the ℓ-th reactor stage, $f_{\mathrm{m},0}(d_0)$ is replaced by $f_{\mathrm{m},\ell-1}(d_0)$, where d_0 is now the particle diameter in the ℓ–1 stage. The application of the PBM to the calculation of the exit size distribution of widely sized feed, results in an equation identical to eq. 5.24 (see Appendix D).

5.3.4 The Case of Gas Transfer Control

So far, the case of solid spherical particles reacting according to reaction 5.9 under chemical reaction control has been considered. However, if the reactant A is introduced into the reactor vessel as a gas, the rate of gas–liquid mass transfer might control the reaction rate. In this case, in order to calculate the conversion of the solid reactant through the segregated flow model, an appropriate shrinking core model (SCM), which accounts for gas–liquid mass transfer rate limitations is needed. Models for the three-phase systems developed in the past have not addressed the case of gas transfer rate control for multi-size particles [5.9, 5.10, 5.11]. This problem is addressed here. The approach is to link the macroscopic gas transfer capacity of the reactor with the individual particle kinetics, and to monitor the change in the size of particles with reaction time. For the development of the gas transfer control–SCM the following assumptions are made:

- Only the liquid side mass transfer resistance is significant
- The sparged gaseous reactant $A(g)$ is pure
- The transport of $A(aq)$ into the aqueous phase towards the particle surface and its diffusion through the liquid–particle boundary layer are fast
- The heterogeneous reaction(s) is so fast that there is no net accumulation of $A(aq)$

Two different routes are considered. The first one is based on the assumption that the amount of dissolved $A(aq)$ is equally distributed among particles regardless of size. The second one is based on the assumption that $A(aq)$ is distributed among particles in proportion to their individual surface area.

Equal Distribution of $A(aq)$ Among Particles

The derivation of the gas transfer control–SCM will first be developed for a <u>single</u> heterogeneous reaction in a batch reactor with <u>monosize</u> particles. We assume that the following simultaneous reactions take place in a batch reactor. The dissolution of the gaseous reactant $A(g)$ into the aqueous phase

$$A(g) \longrightarrow A(aq) \tag{5.25}$$

and the heterogeneous reaction of $A(aq)$ with the solid particles

$$A(aq) + bB(s) \longrightarrow \text{soluble} \quad \text{products} \tag{5.26}$$

The net rate of $A(aq)$ generation is equal to the algebraic sum[5] of the respective rates of generation via reactions 5.25 and 5.26. A mass balance of $A(aq)$ in the batch reactor yields

$$r_{A(aq),5.25} - r_{A(aq),5.26} = \frac{\mathrm{d}N_{A(aq)}}{V\,\mathrm{d}t} \tag{5.27}$$

Since it has been assumed that there is no net accumulation of $A(aq)$ (i.e. $\frac{\mathrm{d}N_{A(aq)}}{V\,\mathrm{d}t} = 0$), it follows that

$$r_{A(aq),5.25} = r_{A(aq),5.26} \tag{5.28}$$

The same argument implies that the concentration of $A(aq)$ in the bulk should be zero (i.e. $C_A = 0$). Hence, from the rate equation 5.5 it follows that

$$r_{A(aq),5.25} = k_L a C_A^\star \tag{5.29}$$

On the other hand, based on the stoichiometry of reaction 5.26 and the assumption that $A(aq)$ is equally distributed among particles (regardless of size) we can write for a single particle

$$\frac{r_{A(aq),5.26}}{\bar{\eta}} = -\frac{1}{b}\frac{\mathrm{d}N_B}{\mathrm{d}t} \tag{5.30}$$

or equivalently (based on eq. 5.28 and 5.29)

$$\frac{k_L a C_A^\star}{\bar{\eta}} = -\frac{1}{b}\frac{\mathrm{d}N_B}{\mathrm{d}t} \tag{5.31}$$

where $\bar{\eta}$ is the total number of particles per unit volume and N_B is the number of moles of a single particle. Recognizing that N_B is given by

$$N_B = \frac{\pi d^3 \rho_B}{6 M_B} \tag{5.32}$$

eq. 5.31 becomes

$$\frac{k_L a C_A^\star}{\bar{\eta}} = -\frac{1}{b}\frac{\pi d^2 \rho_B}{2 M_B}\frac{\mathrm{d}d}{\mathrm{d}t}$$

which is solved for the rate of particle change. That is:

$$\frac{\mathrm{d}d}{\mathrm{d}t} = -\frac{2 b M_B k_L a C_A^\star}{\bar{\eta}\pi d^2 \rho_B} \tag{5.33}$$

---

[5] A positive rate refers to generation and a negative rate to consumption.

The latter equation can be integrated to give the particle size d as a function of t. The total number of particles per unit volume ($\bar{\eta}$) remains constant with time because all particles were assumed to be monosize and they share the same residence time in a batch reactor. Assuming that $C_A^\star$ also remains constant with time, or equivalently, the partial pressure of $A(g)$ is maintained constant in the reactor (semi-batch mode), we have

$$\int_{d_0}^{d} d^2 \, \mathrm{d}d = \int_0^t \frac{2bM_B k_L a C_A^\star}{\bar{\eta}\pi\rho_B} \, \mathrm{d}t$$

which upon integration gives

$$d^3 = d_0^3 - \frac{6bM_B k_L a C_A^\star}{\bar{\eta}\pi\rho_B} t \tag{5.34}$$

Taking into account that the conversion of B is given by

$$x = 1 - (\frac{d}{d_0})^3 \tag{5.35}$$

and defining an apparent rate constant for gas transfer control k_G as

$$k_G = \frac{6bM_B k_L a C_A^\star}{\bar{\eta}\pi\rho_B d_0^3} \tag{5.36}$$

the respective shrinking core model equation for gas–liquid transfer control, which relates conversion with time becomes

$$x(d_0, t) = \begin{cases} k_G t & \text{for} \quad 0 \le t < \frac{1}{k_G} \\ 1 & \text{for} \quad t \ge \frac{1}{k_G} \end{cases} \tag{5.37}$$

and the particle size function

$$d(d_0, t) = \begin{cases} d_0(1 - k_G t)^{1/3} & \text{for} \quad 0 \le t < \frac{1}{k_G} \\ 0 & \text{for} \quad t \ge \frac{1}{k_G} \end{cases} \tag{5.38}$$

There are three terms in k_G (see eq. 5.36), namely k_L, a, and $\bar{\eta}$, which deserve further discussion. The mass transfer coefficient k_L, depends on the diffusivity ($\mathcal{D}$) of the dissolved gas in the liquid (k_L is proportional to $\mathcal{D}$ according to the Film model or to $\mathcal{D}^{1/2}$ according to Surface-Renewal model) and on the hydrodynamic conditions [5.1]. The specific gas–liquid interfacial area a, is a function of the reactor geometry, configuration and, hydrodynamic conditions. Therefore, the volumetric gas–liquid mass transfer coefficient k_La, which is the most frequent measurable quantity in gas–liquid chemical systems, should strongly depend on each individual reactor. In addition k_La is expected to exhibit the same temperature dependence as $\mathcal{D}$ since the hydrodynamic regime is not significantly affected by temperature variation. The majority of fundamental or empirical models that have been proposed for the estimation of $\mathcal{D}$ [5.12] show linear dependence on temperature and inverse proportionality with viscosity (i.e. $\mathcal{D} \propto T/\mu$). Moreover, experimental measurements of k_La in three phase systems have shown k_La to be dependent on the size of the solid particles [5.3, 5.13]. From the above, it becomes evident that an *a priori* estimation of k_La is not feasible. Previous investigations have resulted in empirical correlations which demonstrate the k_La dependence on reactor configuration (i.e. impeller design, size, speed and position etc.) [5.14, 5.15, 5.16]. However, neither temperature correlations nor measurements in three phase systems with reacting particles have been made. Therefore, k_La values for existing or emerging industrial reactors must be extracted from operating plant or pilot plant data.

Equations 5.37 and 5.38 are applicable to a batch type of operation and monosize particles. Their use in continuous reactors and/or for multi-size feed materials deserves some clarification. In a CSTR with monosize feed, the number of particles per unit volume at steady state is less than the number of particles per unit volume in the feed, since a spectrum of residence times exists (some particles exhibit longer residence time than the time required for complete conversion and, therefore, they disappear). But the calculation of $\bar{\eta}$ (through the PBM for example) depends on the value of k_G, which in turn depends on $\bar{\eta}$. A similar argument applies when a multi-size feed material is treated in a continuous or a batch reactor (a particular residence time might be long enough for some size fractions of particles to completely react). In the batch mode of operation, and with the progress of the heterogeneous reaction the fine fraction disappears fast and, therefore, integration of eq. 5.33 is not any more possible since $\bar{\eta}$ does not remain constant. However, in the case of a continuous reactor $\bar{\eta}$ can be taken to be constant at steady state. Thus, at steady state and under the assumption that the dissolving gas is equally distributed among the particles (regardless of their size), $k_L a$ and $\bar{\eta}$ can be grouped into one parameter (i.e. $k_L a/\bar{\eta}$) in eq. 5.36[6]. This lumped quantity can then be determined from continuous pilot plant, or plant operation data (at steady state). This is done by measuring the maximum total amount of gas transferred to the aqueous phase (per unit time and unit volume) for a given reactor, and then estimating $k_L a/\bar{\eta}$ by trial and error.

The assessment of the continuous reactor performance under mass transfer control is performed the same way as for the chemical reaction control case. The mean conversion in the ℓ-th reactor is calculated from eq. 5.18 but with $x(d_0, t)$ now given by eq. 5.37. The first integration in eq. 5.18, which represents the mean conversion of monosize material $\langle x_{d_0} \rangle_\ell$, can be evaluated analytically (see Chapter 4) when the RTD function for perfect mixing applies (i.e. eq. 5.19). That is

$$\langle x_{d_0} \rangle_\ell = \int_0^{1/k_G} k_G t \frac{1}{\bar{t}_\ell} e^{-t/\bar{t}_\ell}\, \mathrm{d}t + \int_{1/k_G}^{\infty} \frac{1}{\bar{t}_\ell} e^{-t/\bar{t}_\ell}\, \mathrm{d}t$$

which upon integration becomes

$$\langle x_{d_0} \rangle_\ell = k_G \bar{t}_\ell (1 - e^{-1/k_G \bar{t}_\ell}) \tag{5.39}$$

Similarly to equation 4.17 it can be seen, by expanding in a Taylor series, that $\langle x_{d_0} \rangle_\ell$ holds the mathematical properties of conversion, that is:

$$\lim \langle x_{d_0} \rangle_\ell = 0 \qquad \text{when} \qquad \bar{t} \to 0$$

$$\lim \langle x_{d_0} \rangle_\ell = 1 \qquad \text{when} \qquad \bar{t} \to \infty$$

The mass-PSD function at the exit of the first reactor stage is given by

$$f_{\mathrm{m}}(d) = \frac{d^5 \int_d^{d_{0,\max}} d_0^{-3} f_{\mathrm{m},0}(d_0) e^{-\frac{d_0^3 - d^3}{\bar{t} d_0^3 k_S}}\, \mathrm{d}d_0}{\int_0^{d_{0,\max}} d^5 \int_d^{d_{0,\max}} d_0^{-3} f_{\mathrm{m},0}(d_0) e^{-\frac{d_0^3 - d^3}{\bar{t} d_0^3 k_S}}\, \mathrm{d}d_0\, \mathrm{d}d} \tag{5.40}$$

The derivation of the latter equation was performed with the aid of the PBM as described in Appendix D.

---

[6] When $C_A^\star$ is expressed in terms of $P_A^\star$, $k_L a$ is replaced by $k_L' a$, which incorporates Henry's constant, k_H, as well.

Extension to Multiple Heterogeneous Reactions: If j heterogeneous and simultaneous reactions take place, i.e.

$$A(aq) + b_j B_j(s) \longrightarrow \text{soluble products}$$

then eq. 5.28 should read

$$r_{A(aq),5.25} = \sum_j r_{A(aq),j} \tag{5.41}$$

Since $A(aq)$ is consumed equally by all reacting particles, it is reasonable to write that the rate of $A(aq)$ consumption by all the j-type particles is equal to the number fraction of the rate of $A(aq)$ transfer, that is

$$r_{A(aq),j} = r_{A(aq),5.25} \frac{\bar{\eta}_j}{\bar{\eta}} \tag{5.42}$$

where $\bar{\eta}_j$ is the total number of particles per unit volume of the j phase alone. Hence, for a single j particle, as in eq. 5.30

$$\frac{r_{A(aq),j}}{\bar{\eta}_j} = -\frac{1}{b_j} \frac{\mathrm{d}N_{B_j}}{\mathrm{d}t} \tag{5.43}$$

It follows from eq. 5.42 and 5.43 that

$$\frac{r_{A(aq),5.25}}{\bar{\eta}} = -\frac{1}{b_j} \frac{\mathrm{d}N_{B_j}}{\mathrm{d}t} \tag{5.44}$$

or equivalently

$$\frac{k_L a C_A^\star}{\bar{\eta}} = -\frac{1}{b_j} \frac{\mathrm{d}N_{B_j}}{\mathrm{d}t} \tag{5.45}$$

The latter equation is similar to eq. 5.31, but now has to be written for every j phase. Thus the conversion and particle size functions for every j are given by expressions analogous to eq. 5.37 and 5.38 respectively. The apparent rate constant k_G has a different value for every j solid reactant. That is

$$k_{G_j} = \frac{6 b_j M_{B_j} k_L a C_A^\star}{\bar{\eta} \pi \rho_{B_j} d_{0_j}^3} \tag{5.46}$$

Distribution of $A(aq)$ Among Particles Proportionally to their Surface Area

The previous approach is improved here by taking into account the surface area of particles. Since the reaction takes place at the surface of the shrinking particle, it appears more appropriate to assume that the amount of dissolved gas available for each particle is proportional to its surface area. In this case, the procedure for calculating conversion and size distribution has to be modified as follows. The development is done directly for a system of j heterogeneous reactions.

Equation 5.42 is now written as

$$r_{A(aq),j} = r_{A(aq),5.25}\frac{\bar{s}_j}{\bar{s}} \tag{5.47}$$

where $\bar{s}_j$ is the specific surface area (area per unit solution volume) of the j-type particles, and $\bar{s}$ is the total specific area of all types of j particles. Thus for a single particle we have

$$r_{A(aq),j}\frac{\pi d_j^2}{\bar{s}_j} = -\frac{1}{b_j}\frac{\mathrm{d}N_{B_j}}{\mathrm{d}t} \tag{5.48}$$

By combining eq. 5.41, 5.47, and 5.48 we obtain

$$r_{A(aq),5.25}\frac{\pi d_j^2}{\bar{s}} = -\frac{1}{b_j}\frac{\mathrm{d}N_{B_j}}{\mathrm{d}t}$$

which reduces to

$$\frac{k_L a C_A^\star}{\bar{s}} = -\frac{1}{b_j}\frac{\rho_{B_j}}{2M_{B_j}}\frac{\mathrm{d}d_j}{\mathrm{d}t} \tag{5.49}$$

and solving for the rate of particle change

$$\frac{\mathrm{d}d_j}{\mathrm{d}t} = -\frac{2b_j M_{B_j} k_L a C_A^\star}{\bar{s}\rho_{B_j}} \tag{5.50}$$

This equation is equivalent to eq. 5.33, which was developed via the first route (assuming equal distribution of $A(aq)$ among particles). However, in contrast to eq. 5.33, eq. 5.50 is not integrated to yield the respective shrinking core model equation for the conversion (necessary for the application of the segregated flow model, as was the case previously). Here, the variation of $\bar{s}$ with time (especially when different solid phases with different size distributions exist) is retained. In a continuous reactor at steady state $\bar{s}$ possesses a unique value, which can be calculated.

The size distribution of each reacting solid phase has to be known in order to calculate $\bar{s}$. This is achieved by employing the population balance model (see Appendix D). Furthermore, if we designate the rate of particle change by v_j

$$v_j = \frac{\mathrm{d}d_j}{\mathrm{d}t} \tag{5.51}$$

then, the particle number distribution function, $\bar{\psi}(d_j)$[7], (defined in Appendices C and D) at the exit of the continuous reactor is given according to the PBM (eq. D.5) by

$$\bar{\psi}(d_j) = -\int_{d_j}^{d_{j0,\max}} \frac{\bar{\psi}_0(d_{j0})}{\bar{t}v_j} \exp \int_{d_j}^{d_{j0}} \frac{\mathrm{d}d'}{\bar{t}v_j} \,\mathrm{d}d_{j0} \tag{5.52}$$

Once $\bar{\psi}(d_j)$ is found for every j the total specific surface area $\bar{s}$ is calculated from

$$\bar{s} = \sum_j \int_0^{d_{j0}} \pi d_j^2 \bar{\psi}(d_j)\,\mathrm{d}d_j \tag{5.53}$$

Since the value of each v_j depends on $\bar{s}$, which in turn is calculated via eq. 5.53, an iterative procedure is necessary. The following sequence of steps describes the calculation of $\bar{s}$

1. Guess an initial value of total specific surface area $\bar{s}_0$. This may well be the area corresponding to unreacted particles. That is

$$\bar{s}_0 = \sum_j \int_{d_{j0,\min}}^{d_{j0,\max}} \pi d_{j0}^2 \bar{\psi}_0(d_{j0})\,\mathrm{d}d_{j0}$$

2. Calculate v_j from eq. 5.50 and 5.51.

3. Find $\bar{\psi}(d_j)$ from eq. 5.52.

4. Find $\bar{s}$ from eq. 5.53.

5. Check if $\bar{s}$ is equal to what has been assumed.

---

[7] $\bar{\psi}(d_j)$ is the number of j-type particles per unit volume that belong to the size interval $(d_j, d_j + \mathrm{d}d_j)$.

6. If not, correct $\bar{s}$ and go to step 2.

In fact, the sequence of steps 1 to 6 involves finding the root of equation 5.53. In this work, the Secant method was used in step 6. Once $\bar{s}$ is found, $\bar{\psi}(d_j)$ can be calculated. Following this the PSD function $f_{\mathrm{n}}(d_j)$ (or $f_{\mathrm{m}}(d_j)$) is determined (see Appendix C). Finally, the mean conversion $\bar{x}_j$ is calculated from (see Appendix D) the following expression

$$\bar{x}_j = \frac{\int_{d_{j0,\mathrm{min}}}^{d_{j0,\mathrm{max}}} \frac{\pi d_{j0}^3}{6} \rho_{B_j} \bar{\psi}_0(d_{j0})\, \mathrm{d}d_{j0} - \int_0^{d_{j0,\mathrm{max}}} \frac{\pi d_j^3}{6} \rho_{B_j} \bar{\psi}(d_j)\, \mathrm{d}d_j}{\int_{d_{j0,\mathrm{min}}}^{d_{j0,\mathrm{max}}} \frac{\pi d_{j0}^3}{6} \rho_{B_j} \bar{\psi}_0(d_{j0})\, \mathrm{d}d_{j0}} \tag{5.54}$$

instead of the segregated flow model expression. As discussed by Herbst [5.17], equation 5.54 can be shown to be equivalent to eq. 5.18 provided that the RTD function follows eq. 5.19.

5.4 Model Application

The model equations were used to construct appropriate computer algorithms suitable for the simulation of alternative reactor operational schemes. The application and properties of the model in describing and designing a continuous process system are demonstrated in this part.

5.4.1 Autoclave Configuration and Feed Composition

The continuous reactor is assumed to be a small size ($V_{\mathrm{CSTR}} = 26$ L, total working volume), multi-stage horizontal autoclave, similar to that used by Sherritt Gordon Ltd. [5.18, 5.19] for pilot plant testing and process development studies. A sketch of the autoclave is shown in Fig. 5.2. The size of the first compartment relative to the size of the subsequent compartments is designated as one of the system variables. Namely, three alternative autoclave configurations are considered:

1. Equal size compartments (total of 6)

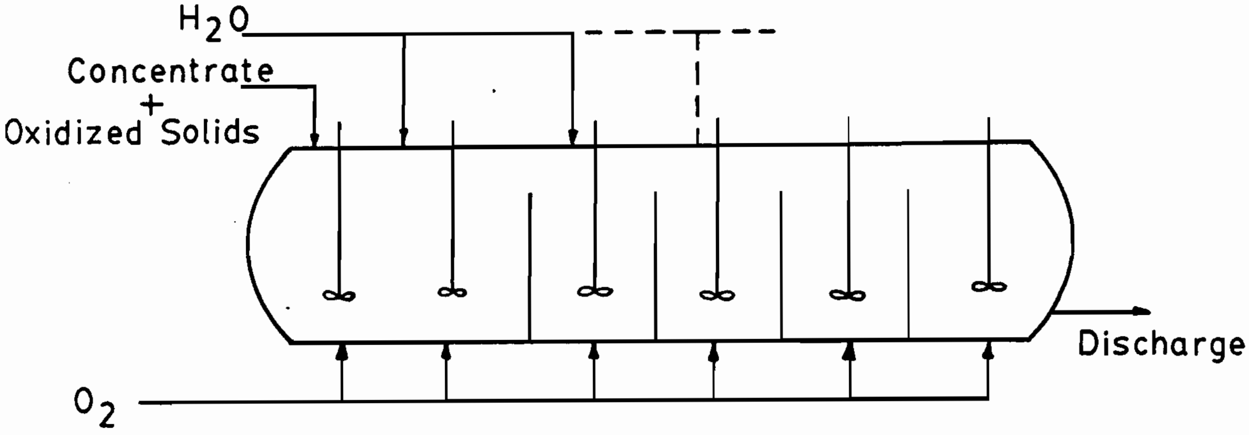

Figure 5.2: Multi-stage horizontal autoclave with double size first compartment

2. Double size first compartment (total of 5)
3. Triple size first compartment (total of 4)

The three reactor configurations are denoted respectively as $C_f = 1$, $C_f = 2$ and $C_f = 3$, where C_f is the "configuration number" defined as follows

$$C_f = \frac{\text{Volume of first compartment } (V_{\mathrm{CSTR,1}})}{\text{Unit reactor volume } (V_{\mathrm{CSTR,u}})}$$

The unit reactor volume $V_{\mathrm{CSTR,u}}$ is obtained by sub-dividing the total autoclave volume V_{CSTR} into n equal size compartments ($n = 6$ in this work). In Fig. 5.2 $C_f = 2$ is illustrated.

The feed material make-up chosen for this application resembles that of the Olympias gold concentrate [5.19, 5.20]. The selection of this particular concentrate was made because it consists primarily of pyrite and arsenopyrite for which appropriate rate equations were developed (see Chapter 3). Furthermore, in the simulations that follow the range of the main variables examined is similar to those employed by Sherritt Gordon Ltd. during the pilot plant testing of the same concentrate [5.5, 5.19]. By selecting this particular case study it was possible to evaluate the prediction power of the model against "hard" data. It is emphasized, nevertheless, that the program

Table 5.II: Composition(wt.%) and size parameters of the refractory gold concentrate

Chemical	Mineralogical	Size Parameters
41 S	66.5 FeS_2	$\mu = 21$ μm
12 As	26.1 $FeAsS$	$c = 16.5$
39 Fe	7.4 SiO_2	$d_{0,\text{max}} = 100$ μm

code developed (FORTRAN) is by no means limited to the above case study, but was prepared instead in as general as a form as possible, allowing for flexibility and adaptability during its application. The chemical/mineralogical composition [5.19] and size distribution parameters of the concentrate are given in Table 5.II. As seen in this table, the weight fraction of pyrite (w_{FeS_2}) and arsenopyrite (w_{FeAsS}) is 0.665 and 0.261 respectively. The particle size distribution parameters that were used in equation 5.21 correspond to 98% –44 μm material[8]. The parameters μ and c were calculated from discrete size distribution data of the Olympias concentrate [5.21]. Details on this calculation are given in Appendix F. It is tacitly assumed that the pyrite/arsenopyrite particles are completely liberated and that both minerals follow the same distribution function (i.e. $\mu = \mu_{FeS_2} = \mu_{FeAsS}$, and $c = c_{FeS_2} = c_{FeAsS}$).

The concentrate slurry wich originates from the grinding circuit (composed of 72 wt.% solids, or $w_s = 0.72$) is assumed to be mixed in a certain ratio with a recycle oxidized slurry (consisting of 55 wt.% solids, or $w_{ox} = 0.55$) prior to its feeding to the autoclave. The recycle ratio R_R is defined as

$$R_R = \frac{\text{mass of concentrate solids}}{\text{mass of recycled solids}}$$

Water may be added to either the slurry before entering the reactor (feed dilution) or injected directly into the autoclave (see Figure 5.2). The water addition ratio denoted by W_R is defined by

$$W_R = \frac{\text{mass of water added}}{\text{mass of water in blend slurry}}$$

---

[8] Equation 5.21 is used as a mass-PSD function, $f_m(d)$.

For the first compartment water may be either added at the same temperature with the entering feed (if feed preheating is required) or at 30 °C. For the subsequent compartments, water is injected at 30 °C. Thus, the blend solids concentration ($\hat{w}$), molar and volumetric flow rates, volume of liquid phase, and nominal residence time for the first reactor compartment depend on the values of R_R, W_R, C_f, and F_s (= flow rate of concentrate, in kg h^{-1}).

Constant density values are employed, namely, 5 g mL^{-1} for pyrite, 6.15 g mL^{-1} for arsenopyrite, and 1 g mL^{-1} for water [5.4]. A value of 2.3 g mL^{-1}, being the respective average over several polymorphic forms of SiO_2 [5.22], is used as the density of the oxidized solids. The specific heat capacity of oxidized solids is taken to be equal to that of SiO_2 (quartz), and is expressed as [5.4]

$$C_{p,SiO_2} = 46.495 + 34.309 \times 10^{-3} T - 11.279 \times 10^{5} T^{2} \quad \mathrm{J\ mol^{-1}\ K^{-1}}$$

Furthermore, Sherritt reported a total operating pressure of 1800 kPa at 190 °C [5.5] from pilot plant tests of the Olympias concentrate. Taking into account that water vapour pressure is 1254 kPa at 190 °C [5.22], a partial oxygen pressure of 546 kPa (5.4 atm) is estimated. In fact, a value of $P^{\star}_{O_2} = 5$ atm is used in all simulation runs reported in this chapter. This value is kept constant regardless of the operating temperature of each simulation. The level of all variables maintained constant (unless explicitly specified otherwise) in the simulation runs are listed in Table 5.III. It is under the set of conditions of Table 5.III and concentrate composition of Table 5.II that Sherritt Gordon Ltd. reported autogenous autoclave operation at 190 °C [5.5, 5.19], with a feed temperature of 30 °C [5.23]. Thus, the conditions of Table 5.III are labelled here as "standard" and are used as the basis for simulations hereafter. In Figure 5.3, the variables which are initialized prior to the execution of a simulation run are shown. It should be noted that all the assumptions made in the previous chapter apply in the present chapter as well, unless otherwise stated.

Table 5.III: Standard conditions employed

Variable	Level
V_{CSTR}	26 L
L	5
C_f	2
w_s	0.72
w_{ox}	0.55
F_s	2 kg h^{-1}
R_R	5
T_0	30 °C
T_{H_2O}	30 °C
$P^\star_{O_2}$	5 atm

1. Reactor: V_{CSTR}, L, C_f
2. Concentrate: w_{FeS_2}, w_{FeAsS}, $d_{0,\mathrm{max}}$, μ, c, w_s, F_s

$$\underbrace{FeS_2 \quad FeAsS \quad SiO_2}_{F_s} \quad \underbrace{H_2O}_{F_{H_2O,s}=\frac{F_s(1-w_s)}{w_s}}$$

3. Recycled solids: R_R, w_{ox}

$$\underbrace{SiO_2}_{F_{ox}=R_R\cdot F_s} \quad \underbrace{H_2O}_{F_{H_2O,ox}=\frac{F_{ox}(1-w_{ox})}{w_{ox}}}$$

4. Water addition/injection: W_R, T_{H_2O}

$$\underbrace{H_2O}_{F_{H_2O,inj}=W_R\cdot(F_{H_2O,s}+F_{H_2O,ox})}$$

5. Oxygen pressure: $P^\star_{O_2}$
6. Feed (blend) temperature: T_0
7. Min/Max operating temperature to scan: T_{min}, T_{max}

Figure 5.3: The input variables of the model

5.4.2 Estimation of the Volumetric Mass Transfer Coefficient $k_L a$

Mass Transfer Capacity of the Autoclave

The mass transfer capacity of the autoclave[9] is estimated here by using pilot plant data reported by Sherritt Gordon Ltd. [5.5, 5.24]. According to these data, the steady state value of sulphur oxidation (conversion) in the first compartment had an average value of 70±5% at 190 °C. It is reasonable to assume, therefore, that the same level of sulphur oxidation was attained for the Olympias concentrate as well (for which no specific data have been released). Furthermore, for the same concentrate, the flow rates F_s were reported as having values varying from 1.5 to 2.5 kg h^{-1} [5.5]. By taking an average value of 2 kg h^{-1} and using the data of Table 5.II, the molar flow rates of FeS_2 and $FeAsS$ are calculated as 0.185 and 0.0534 mol min^{-1} respectively. Based on the stoichiometries of reactions 5.2 and 5.3, the oxygen consumption rate, $\dot{O}_2$, at 70% sulphur conversion (assumed to be the same for sulphur in both minerals) is

$$\dot{O}_2 = (0.185 \times \frac{7}{2} + 0.0534 \times \frac{13}{4})0.7 = 0.575 \quad \text{mol}_{O_2}\,\text{min}^{-1}$$

This value[10] is rendered volume-independent by dividing by the solution volume. For $V_{\text{CSTR}} = 26$ L and $C_f = 2$, the working volume of the first compartment is 8.66 L. Under the conditions of $F_s = 2$ kg h^{-1} and the given concentrate composition (Table 5.II) the liquid phase hold-up (fraction of solution volume over working volume) is calculated to be 0.84. Hence, the specific oxygen consumption rate $\bar{\dot{O}}_2$, has a value of

$$\bar{\dot{O}}_2 = \frac{0.575}{8.66 \times 0.84} \times 10^3 = 79 \qquad \text{mol}_{O_2}\,\text{min}^{-1}\,\text{m}^{-3}$$

Assuming that the first autoclave compartment operates under O_2 starvation conditions (i.e. the steady state $O_2(aq)$ concentration is practically zero), then the

---

[9] That is, the maximum gas transfer rate for the given reactor configuration and hydrodynamic regime.

[10] In reality this O_2 consumption rate is slightly underestimated since the oxidation of Fe^{2+} to Fe^{3+} is neglected for reasons explained earlier in Section 5.2.

value of 79 $\mathrm{mol}_{O_2}\,\mathrm{min}^{-1}\,\mathrm{m}^{-3}$ corresponds to the maximum O_2 transfer capacity of the reactor. The assumption that the first autoclave compartment is under mass transfer control is justified from the results of the previous chapter. In Chapter 4, it was shown that by assuming surface reaction control governing the operation of the first compartment at least 85% sulphur conversion was obtained. The fact that Sherritt found instead a 70% conversion value (for otherwise the same conditions), is a strong indication of mass transfer limitations[11].

Finally, the value of 79 $\mathrm{mol}_{O_2}\,\mathrm{min}^{-1}\,\mathrm{m}^{-3}$ is rounded to 80 $\mathrm{mol}_{O_2}\,\mathrm{min}^{-1}\,\mathrm{m}^{-3}$ and is kept constant (at 190 °C) for every subsequent simulation run as being the upper limit of oxygen consumption rate ($\bar{\dot{O}}_{2,\mathrm{max}}$) in every reactor compartment. This is justified since the configuration of each reactor compartment (i.e. impeller design and position, sparger, agitation rate) was essentially the same for Sherritt's autoclave.

Estimation of $k'_L a$

The value of $\bar{\dot{O}}_{2,\mathrm{max}}$ is utilized in estimating the volumetric mass transfer coefficient $k'_L a/\bar{\eta}$ (or $k'_L a$). The estimation is performed at the beginning of each simulation run. More specifically, after all data have been read and molar flow rates, residence times, etc., have been calculated, an initial guess is made. For the program version that involves the assumption of "$O_2(aq)$ equally distributed among particles"[12] (Version 1), the guess is an initial value for $k'_L a/\bar{\eta}$. For the version involving the assumption "$O_2(aq)$ distributed proportionally to surface area"[13] (Version 2), the respective guess is a value for $k'_L a$. The next step is to calculate the conversions of FeS_2 and $FeAsS$ at 190 °C before estimating $\bar{\dot{O}}_2$ from the following equation:

$$\bar{\dot{O}}_2 = \frac{F_{FeS_2} \cdot \bar{x}_{FeS_2} \cdot \frac{7}{2} + F_{FeAsS} \cdot \bar{x}_{FeAsS} \cdot \frac{13}{4}}{V} \tag{5.55}$$

---

[11] It is further clarified that the modelling approach in this chapter is to consider the two kinetic regimes separately. That is, the oxidation process is controlled either by surface reaction or by oxygen mass transfer. The situation of simultaneous control by both rate-limiting regimes is considered in the following chapter.

[12] To be called Version 1 hereafter.

[13] To be called Version 2 hereafter.

If $\bar{\dot{O}}_2$ is not equal to $\bar{\dot{O}}_{2,\max}$ a new value of $k'_La/\bar{\eta}$ (or k'_La) is entered and so on. Evidently, increasing or decreasing $k'_La/\bar{\eta}$ (or k'_La) results in a respective increase or decrease of $\bar{\dot{O}}_2$. By this trial-and-error procedure, the $k'_La/\bar{\eta}$ (or k'_La) value which gives $\bar{\dot{O}}_2 = \bar{\dot{O}}_{2\max}$ is determined. However, since in Version 1 the lumped parameter $k'_La/\bar{\eta}$ depends on $\bar{\eta}$, its estimation is mandatory every time the steady state number of particles per unit solution volume changes. That is, whenever F_s or W_R change. This extra complication is avoided in Version 2 (see Appendix E).

Temperature Correlation—Version 1

The temperature dependence of $k'_La/\bar{\eta}$ is expressed in terms of an Arrhenious-type equation. That is

$$k'_La/\bar{\eta} = \mathcal{A}_1 \exp(-\frac{1500}{T}) \tag{5.56}$$

This expression corresponds to an apparent activation energy of 12.5 kJ mol^{-1}. The low "activation" energy value was selected in order to ensure moderate sensitivity to temperature (an intrinsic feature of diffusional processes, see Section 5.3.4). Moreover, consideration was given in selecting an activation energy value to satisfy the requirement of producing heat generation slopes less than the heat removal slopes at 190 °C. Once $k'_La/\bar{\eta}$ at 190 °C is selected, $\mathcal{A}_1$ is found from equation 5.56 by setting $T = 463$ K.

Temperature Correlation—Version 2

The volumetric mass transfer coefficient k'_La is estimated at 190 °C once and is kept constant for every simulation run thereafter. The estimation was performed at "standard" feed conditions (Table 5.III). The resultant k'_La value at 190 °C was found to be

$$k'_La = 1.62 \times 10^{-2} \quad \mathrm{mol\,min^{-1}\,L^{-1}\,atm^{-1}}$$

The temperature dependence of $k'_L a$ is similarly expressed in the form of

$$k'_L a = \mathcal{A}_2 \exp(-\frac{500}{T}) \tag{5.57}$$

A lower "apparent" activation energy value of 4.2 kJ mol^{-1} was selected (as opposed to 12.5 kJ mol^{-1} for Version 1) because now there is no dependence on $\bar{\eta}$. This is so because with increasing operating temperature $\bar{\eta}$ is expected to decrease (faster disappearance of particles), and consequently $k'_L a/\bar{\eta}$ is expected to increase more rapidly with temperature than $k'_L a$. $\mathcal{A}_2$ is calculated the same way as in Version 1.-

5.4.3 Simulation Results and Discussion

In actual simulation runs the decision as to whether the reactor operates under mass transfer control or surface reaction control depends on whether or not the gas supply needs under chemical reaction control exceed the maximum mass transfer capacity of the reactor (in moles of O_2/volume/time). If so, then the reactor operates under mass transfer rate control. Otherwise the reactor operates under surface reaction rate control. The program flowcharts considered for the two mass transfer mechanisms (i.e. Version 1 and 2) are shown in Appendix E.

It should be made clear at this point that the search for autogenous reactor operation is always performed for the <u>first</u> autoclave compartment since its autothermal "initialization" determines the fate of the whole process. The only means of external intervention into the subsequent compartments is by water injection, which controls the operating temperature.

The stable operating temperatures obtained from a series of simulations with Version 1 were used to prepare a number of plots depicting the effects of some key process parameters on the autogenous operation of the first compartment. To facilitate the comparison of various effects the unit flow rate of concentrate, F_{u}, is introduced. It is defined as:

$$F_{\mathrm{u}} = \frac{F_s}{C_f}$$

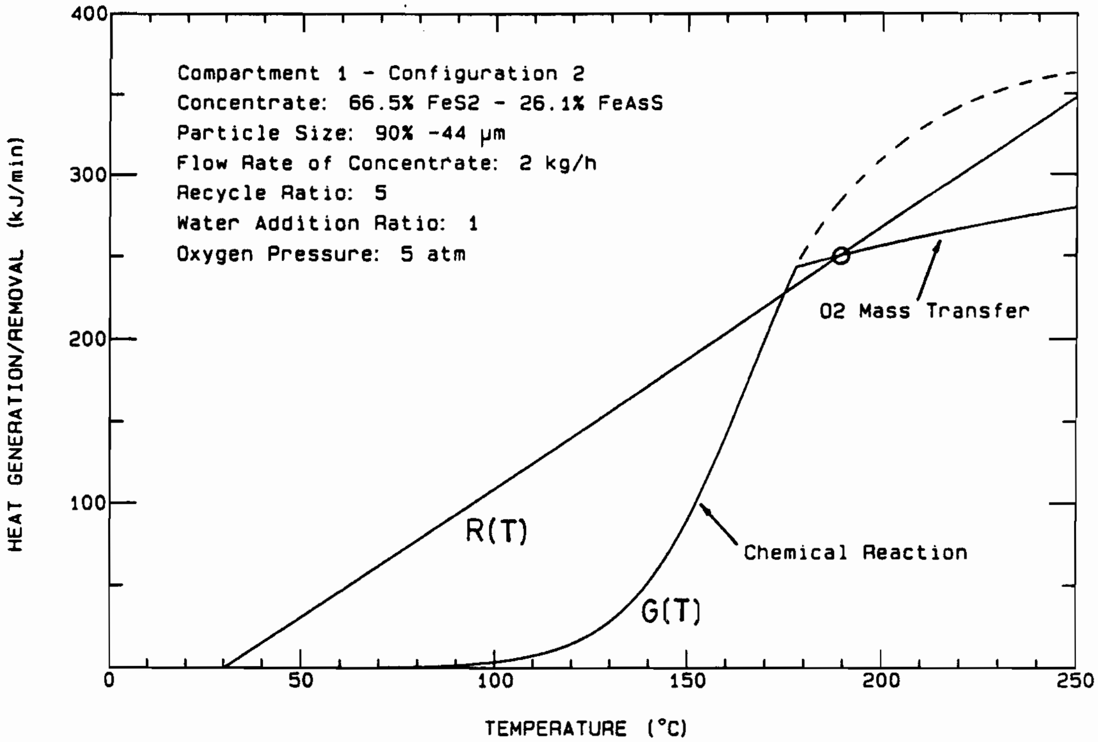

Figure 5.4: Rates of heat generation ($G(T)$) and heat removal ($R(T)$) vs steady state temperature in the first compartment. (Conditions: "standard"–Table 5.III; model Version 1.)

The result of keeping F_u constant at 1 kg h^{-1} for example, is that similar F_u values are obtained by using $C_f = 1$ and $F_s = 1$ kg h^{-1}, $C_f = 2$ and $F_s = 2$ kg h^{-1}, or $C_f = 3$ and $F_s = 3$ kg h^{-1} .

Analysis of the Performance of the First Compartment

The performance of the autoclave was simulated on a stage (compartment) by stage basis with the objective being to identify the optimum feed conditions and reactor configuration for autogenous operation. A graphical solution of the heat balance equation (for the "standard" conditions—see Table 5.III) is presented in Figure 5.4. For the specific conditions shown in Fig. 5.4, the autogenous steady state temperature in the first autoclave compartment is found to be 190 °C. This is obtained for a feed temperature of 30 °C and water dilution of the feed slurry $W_R = 1$. For the given concentrate composition and operating conditions neither feed preheating nor cooling is required. This is a truly autogenous operation since the process is self-driven by its own thermal energy. Changing feed conditions or feed composition would undoubtedly dictate a different set-up for the attainment of autogenous operation. In fact, it is this search for optimum operating conditions that is greatly facilitated by the proper use of the model.

In Figure 5.4, the rate of heat generation curve is seen to consist of two parts. The lower S-shaped part refers to operation under surface reaction control, while the upper linear part refers to O_2 transfer control. The O_2 transfer control regime results in lowering the reaction rates and, consequently, the heat generation rates. Thus, an operating temperature of 190 °C is attained, which is within the desired range (180–200 °C). According to Fig. 5.4 if no O_2 transfer limitations are encountered, the steady state operating temperature would be around 260 °C. By changing the feed temperature (i.e. shifting the $R(T)$ parallel to itself) the locus of operating temperatures (i.e. intersection points between $R(T)$ and $G(T)$) is obtained. The impact of the rate-limiting regime on reactor performance is considered below in detail.

Operation Under Surface Reaction Control: In Fig. 5.5 the stable operating temperature is plotted against feed temperature for $F_u = 0.5$ kg h^{-1}. The results of Fig. 5.5 represent operation of the autoclave under surface reaction control regime since the relatively low F_u value results in oxygen demands less than $\bar{O}_{2,\max}$. There is always a minimum operating temperature (ignition point) above which stable steady states with high conversion are obtained. According to Fig. 5.5, as the water addition ratio increases, feed preheating becomes necessary in order to achieve a particular operating temperature. This is due to the insufficient heat released by the diluted mass of reacting solids. If water is added directly into the first compartment (injection) at 30 °C, preheating at even higher temperatures is needed to allow operation at the same temperature. This is clearly not a very attractive option. On the other hand, an increase in the amount of water addition results in shortening the mean residence time in the first compartment, $\bar{t}_1$. Thus $\bar{t}_1$ decreases from 42 min to 23 min

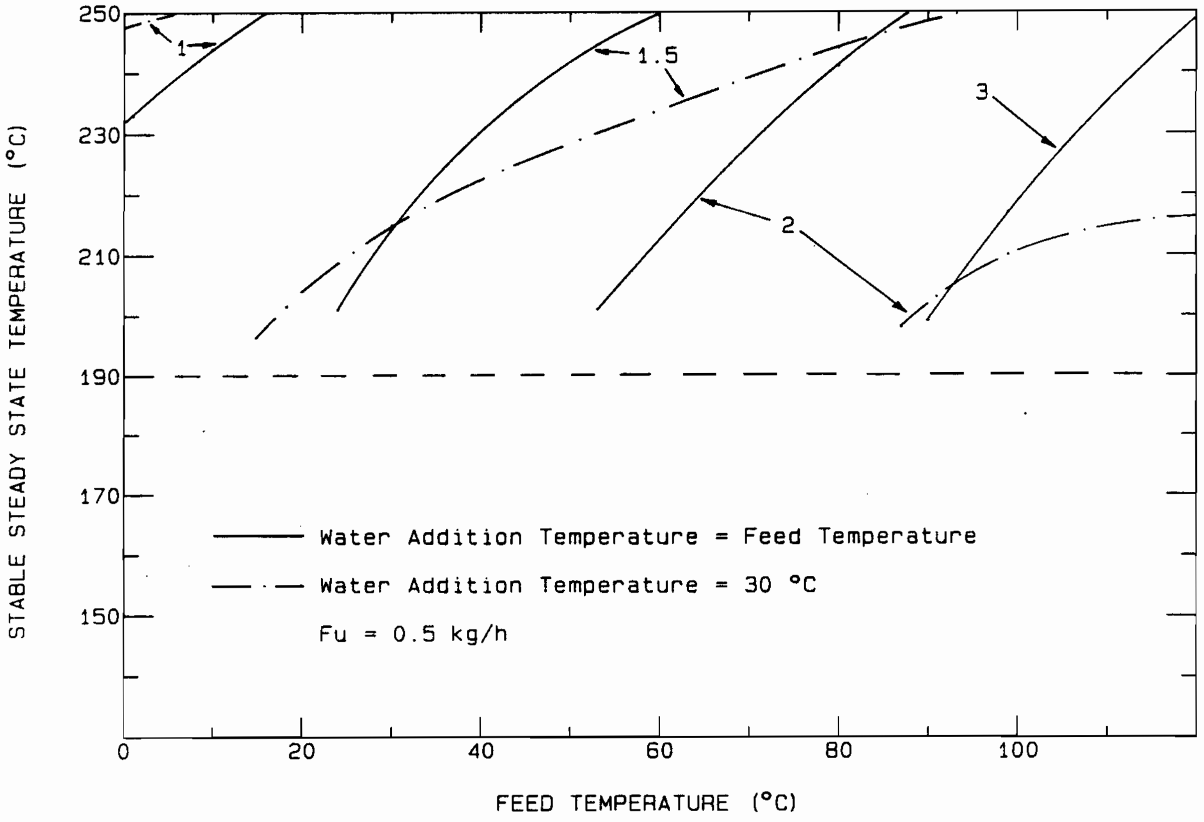

Figure 5.5: Stable operating temperature vs feed temperature in the first autoclave compartment at different water addition ratios. (Model Version 1; surface reaction control; $W_R = 1, \bar{t}_1 = 42.1$ min; $W_R = 1.5, \bar{t}_1 = 35$ min; $W_R = 2, \bar{t}_1 = 30$ min; $W_R = 3, \bar{t}_1 = 23.3$ min.)

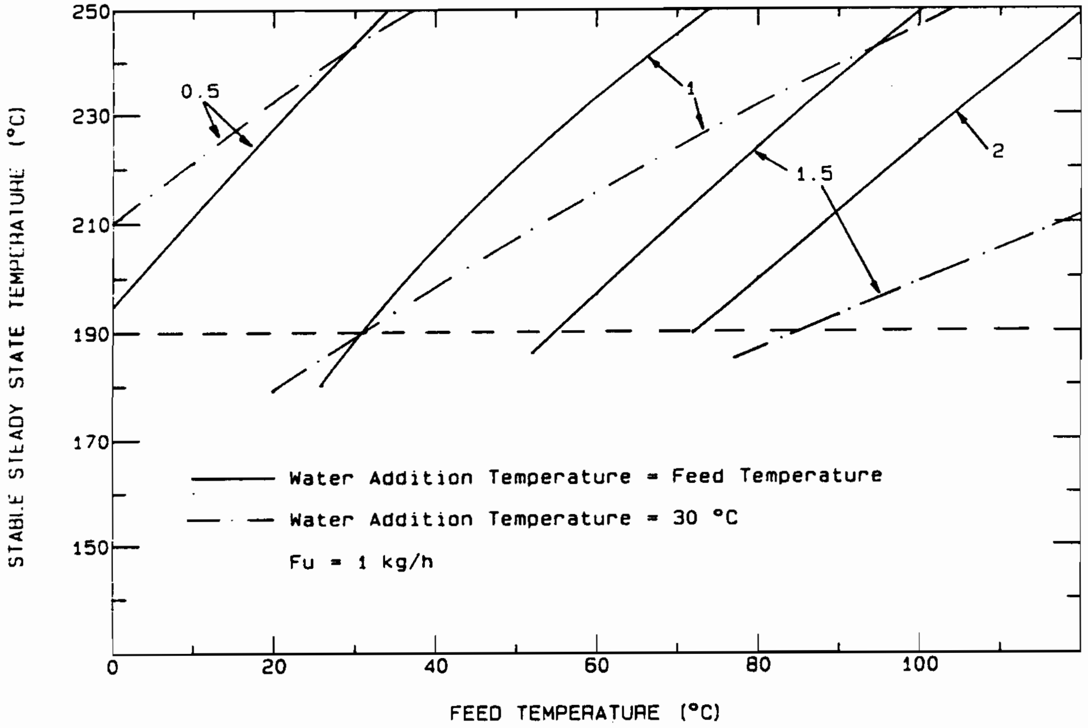

Figure 5.6: Stable operating temperature vs feed temperature in the first autoclave compartment at different water addition ratios. (Model Version 1; O_2 transfer control; $W_R = 0.5, \bar{t}_1 = 26.4$ min; $W_R = 1, \bar{t}_1 = 21$ min; $W_R = 1.5, \bar{t}_1 = 17.5$ min; $W_R = 2, \bar{t}_1 = 15$ min.)

as W_R increases from 1 to 3. At the same time sulphur conversion[14] is only slightly affected, remaining always above 0.9. Moreover, the results of Fig. 5.5 show that autogenous operation is achievable only at operating temperatures near 200 °C and higher. However, operating near 200 °C under surface reaction control is risky since the oxidation reactions may be extinguished by minor downward fluctuations of the feed temperature.

Operation Under Gas–Liquid Mass Transfer Control: An increase in the feed rate to $F_u = 1$ kg h^{-1} results in a shift from surface reaction control to O_2 mass transfer control. The results for this rate limiting regime are depicted in Fig. 5.6. The

---

[14] Sulphur conversion is the weighted average of the two individual mineral conversions, calculated by

$$\bar{x}_S = \frac{2F_{FeS_2}\bar{x}_{FeS_2} + F_{FeAsS}\bar{x}_{FeAsS}}{2F_{FeS_2} + F_{FeAsS}}$$

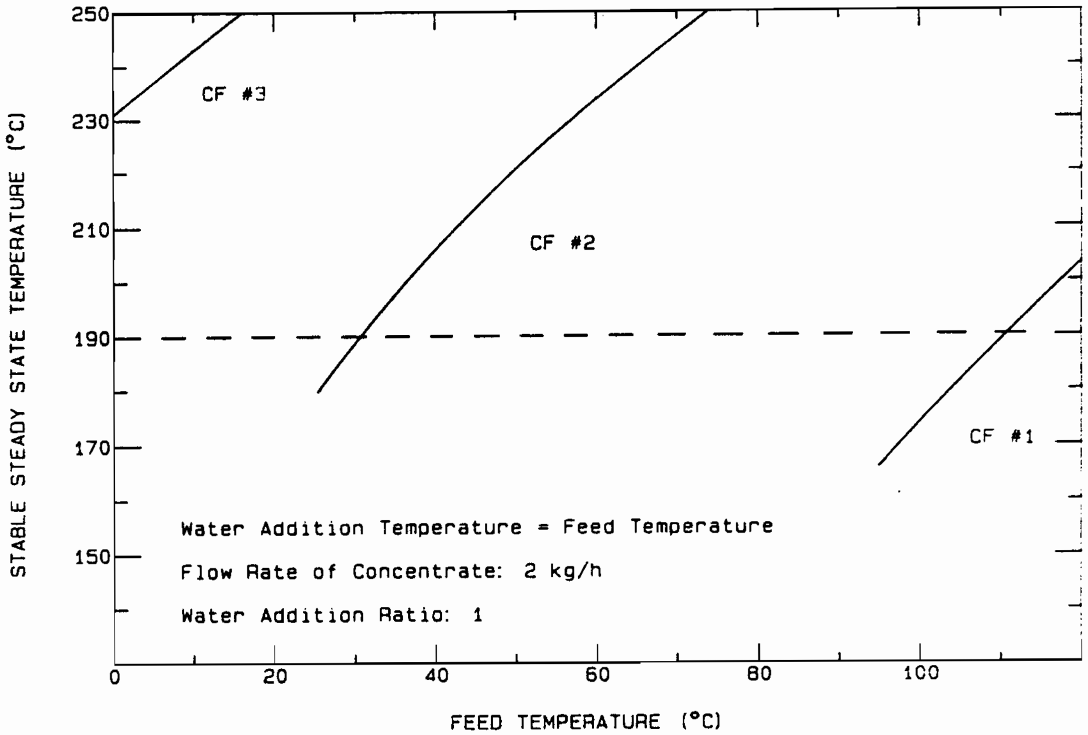

Figure 5.7: Stable operating temperature vs feed temperature in the first autoclave compartment for different reactor configurations. (Model Version 1.)

qualitative jump made by leaving the surface reaction (SR) control regime (Fig. 5.5) and entering the O_2 mass transfer (MT) control regime (Fig. 5.6) is the fact that lower stable operating temperatures in the region of 190 °C are now possible for the first compartment but with lower sulphur conversion levels ($\sim$ 0.65–0.70) than previously ($>$ 0.9). Otherwise, the same trends as before are seen to be present. According to the data of Fig. 5.6 the concentrate with a feed rate of 2 kg h^{-1} can be processed autogenously at 190 °C by using $C_f = 2$ (i.e. a double size first compartment) and $W_R = 1$. The same feed rate and reactor configuration ("standard" conditions—see Table 5.III) were employed by Sherritt Gordon Ltd. during the pilot plant testing of the Olympias concentrate [5.5, 5.19].

The impact of the size of the first compartment on the autogenous operation of the autoclave is better illustrated by Figure 5.7 and 5.8. In these figures the concentrate flow rate, the water addition temperature, and water addition ratio are kept constant at 2 kg h^{-1}, feed temperature, and 1, respectively. In Fig. 5.7 the stable operating temperature (for the first compartment) is plotted against feed tem-

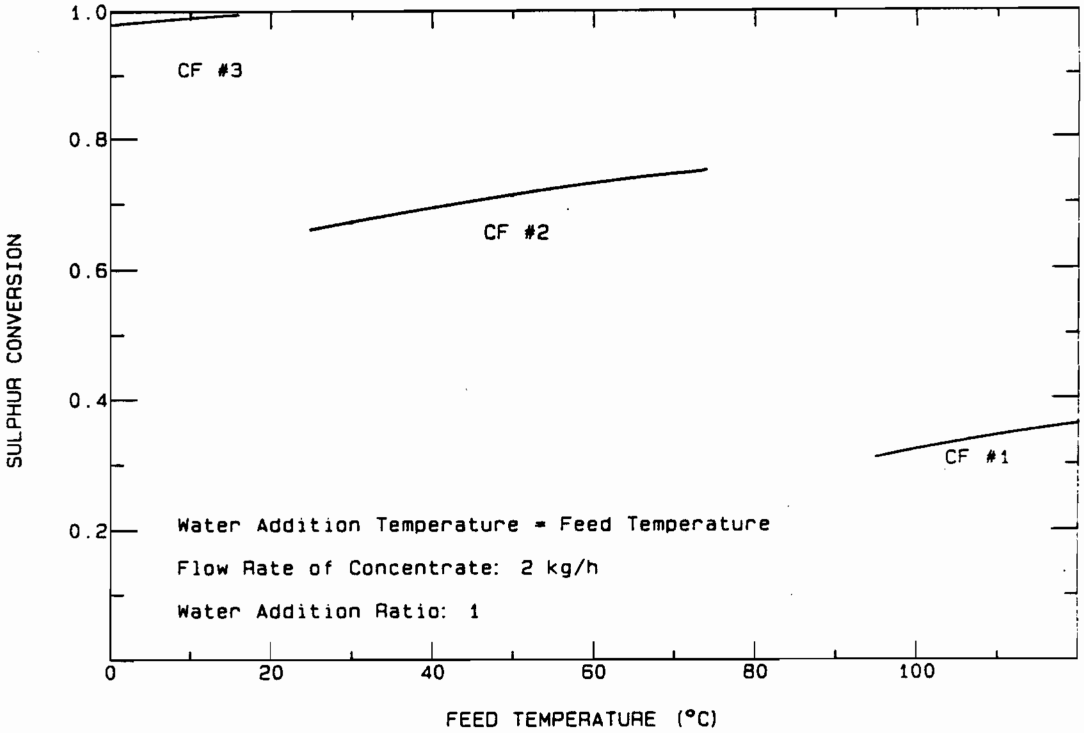

Figure 5.8: Sulphur conversion vs feed temperature in the first autoclave compartment for different reactor configurations. (Model Version 1.)

perature for three different reactor configurations, while in Fig. 5.8 the respective conversion levels for the same simulation runs are depicted. For $C_f = 1$, substantial feed preheating to 110 °C is needed in order to achieve a stable steady state at 190 °C. On the other hand, $C_f = 3$ requires cooling of the feed below room temperature (a truly impractical situation), and operating temperatures lie significantly above the target of 190 °C. However, with $C_f = 2$ autogenous operation at 190 °C with no feed preheating requirements (feed temperature of 30 °C) is now possible. Based on Figure 5.8, the sulphur conversions are: 0.30–0.35 for $C_f = 1$, 0.65–0.70 for $C_f = 2$, and 0.95–0.98 for $C_f = 3$. They correspond to residence times, $\bar{t}_1$, of 10.5 min ($C_f = 1$), 21 min ($C_f = 2$), and 31.5 min ($C_f = 3$). It is evident that the longer the residence time the higher the sulphur conversion level and consequently the higher the temperature rise due to the released heat. In the above simulations $C_f = 1$ and $C_f = 2$ are associated with O_2 transfer control while $C_f = 3$ is associated with surface reaction control. The results obtained clearly demonstrate the advantage of having the first compartment substantially bigger in size than the successive

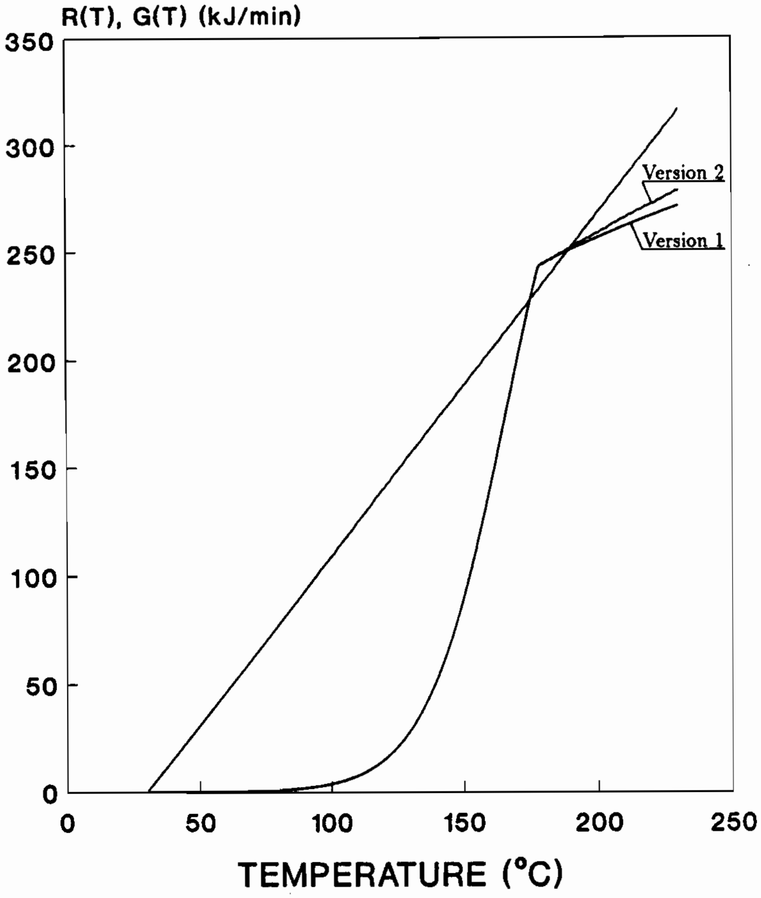

Figure 5.9: Comparison of model Version 1 and Version 2 for the first autoclave compartment. (Conditions: "standard"–Table 5.III.)

ones when autogenous operation is sought—an observation in concordance with the claims of a recent Sherritt Gordon Ltd. patent [5.25].

All the results presented so far were obtained using the model version which assumes $O_2(aq)$ to be equally distributed among particles (Version 1). The model version which assumes $O_2(aq)$ to be distributed among particles in proportion to their surface area (Version 2) was found to generate practically the same results. In Figure 5.9, the $R(T)$ and $G(T)$ vs temperature curves for both model versions are depicted for "standard" feed conditions (Table 5.III). As expected the part of the curve corresponding to surface reaction control remains unchanged, but a minor deviation is observed in the gas transfer control regime. However, the discrepancy exhibited by the two model versions has practically no effect within the target temperature

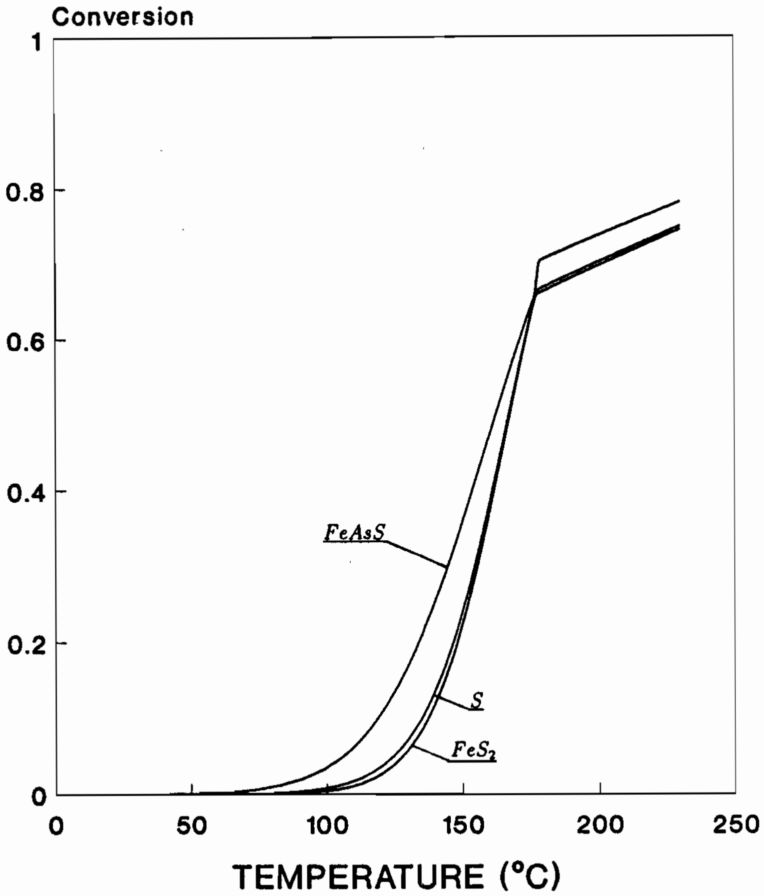

Figure 5.10: Conversions of pyrite, arsenopyrite and sulphur in the first autoclave compartment. (Conditions: "standard"–Table 5.III; model Version 1.)

region[15] of 180 to 200 °C. The good agreement between the prediction capability of the two model versions reflects the fact that in both cases $k'_L a$ was determined by processing pilot plant data collected at 190 °C. For extrapolation to temperatures beyond 200 °C, Version 2 is expected to give more accurate predictions since its formulation is more rigorous. The shape of the $G(T)$ curve is similar to the conversion curve. The rate of heat generation term accounts for the total heat generated by the two mineral oxidation reactions (plus minor amounts of heat generated by O_2 dissolution) as seen in equation 5.17, and is almost proportional to the total sulphur conversion. In Figure 5.10 the $\bar{x}_{FeS_2}$, $\bar{x}_{FeAsS}$ and $\bar{x}_S$ curves are shown for "standard" feed conditions (Table 5.III).

---

[15] This is further supported with the results of Table 5.IV and 5.V.

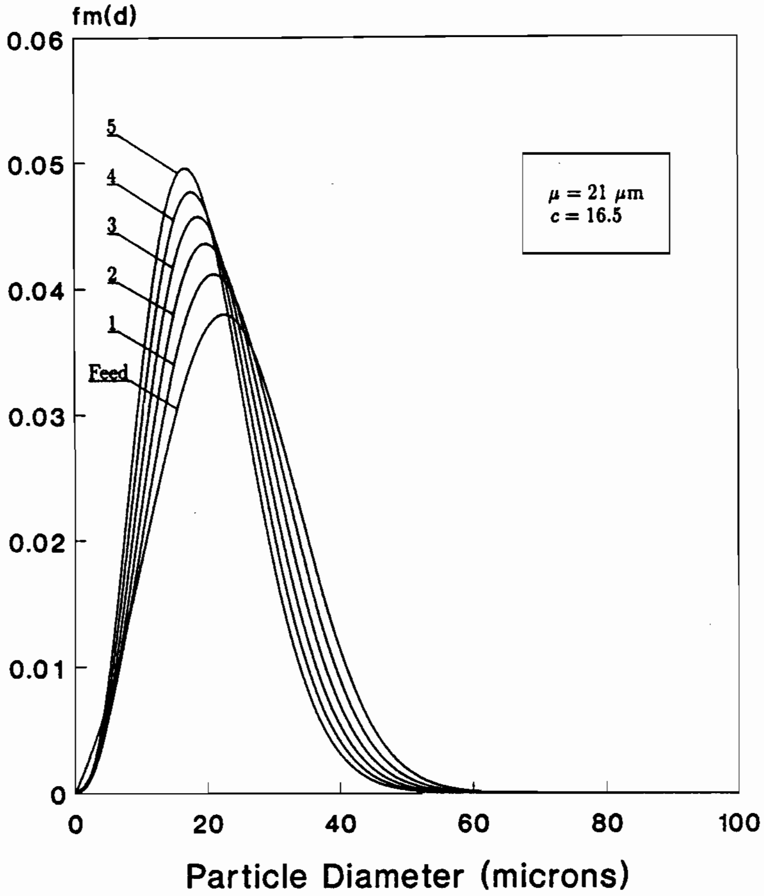

Figure 5.11: Particle size density functions (f_m) of pyrite in the feed and at the exit of each reactor compartment. (Conditions: "standard"–Table 5.III; model Version 2.)

Analysis of the Performance of the Whole Autoclave

As mentioned in Section 5.3.1, the analysis of the autoclave performance is made on a stage by stage basis. Upon determining the exit slurry composition for the first compartment (in terms of temperature, conversion and size distribution of the reacted solids), the information is used as input variables for the simulation of the second compartment, and so on. For example, the size distribution of pyrite particles calculated by the model Version 2 at the exit of each compartment is depicted in Figure 5.11. By examining Fig. 5.11 we can see that the particle size becomes gradually finer as the material moves through the autoclave compartments and the conversion approaches completion. The behaviour of arsenopyrite particles was found to be similar.

Table 5.IV: Simulation results with Version 1 at "standard" conditions (Table 5.III).

Process Parameters	Compartment 1	2	3	4	5
T (°C)	190	189	190	190	191
$\bar{x}_S$	0.683	0.859	0.940	0.975	0.990
$\bar{t}$ (min)	21	8.6	7.9	7.6	7.5
V (L)	8.7	4.3	4.3	4.3	4.3
W_R	1	0.59	0.26	0.13	0.05
$\hat{w}$ (wt.%)	35	28.7	26.5	25.5	25.1
$\dot{\bar{O}}_2$ (mol min^{-1} m^{-3})	80	38	17.4	7.6	3.4
Kinetic regime	MT	SR	SR	SR	SR

Table 5.V: Simulation results with Version 2 at "standard" conditions (Table 5.III).

Process Parameters	Compartment 1	2	3	4	5
T (°C)	190	190	190	190	190
$\bar{x}_S$	0.685	0.885	0.957	0.984	0.994
$\bar{t}$ (min)	21	8.4	7.8	7.6	7.5
V (L)	8.7	4.3	4.3	4.3	4.3
W_R	1	0.65	0.25	0.10	0.04
$\hat{w}$ (wt.%)	34.9	28.2	26.1	25.4	25.1
$\dot{\bar{O}}_2$ (mol min^{-1} m^{-3})	80	43.4	15.5	5.9	2.2
Kinetic regime	MT	SR	SR	SR	SR

Some typical results obtained by analyzing the whole autoclave performance for a given set of feed conditions are summarized in Table 5.IV. These results were generated with Version 1. The respective results generated by Version 2 are shown in Table 5.V. Comparison of Tables 5.IV and 5.V shows that both versions produce almost identical results. With the exception of the first compartment, which operates under mass transfer control (MT), all subsequent compartments operate under surface reaction control (SR). The complete simulation results of Tables 5.IV and 5.V are in good agreement with the pilot plant data reported by Sherritt [5.5, 5.19]. The simulation results given in Table 5.VI (Version 1) and Table 5.VII (Version 2) correspond to an increase in the the throughput of the reactor to $F_s = 3$ kg h^{-1}. For

Table 5.VI: Simulation results with Version 1 at F_s=3 kg h^{-1}.

Process	Compartment				
Parameters	1	2	3	4	5
T (°C)	191	190	190	190	189
$\bar{x}_S$	0.382	0.605	0.846	0.910	0.947
$\bar{t}$ (min)	23.5	7.8	5.8	5.4	5.2
V (L)	8.7	4.3	4.3	4.3	4.3
W_R	0	0.75	0.8	0.22	0.15
$\hat{w}$ (wt.%)	53	38.4	29	27.2	26
$\bar{O}_2$ (mol min^{-1} m^{-3})	80	80	80	20.3	11.8
Kinetic regime	MT	MT	MT	SR	SR

Table 5.VII: Simulation results with Version 2 at F_s=3 kg h^{-1}.

Process	Compartment				
Parameters	1	2	3	4	5
T (°C)	190	189	191	190	190
$\bar{x}_S$	0.368	0.581	0.823	0.917	0.962
$\bar{t}$ (min)	23.5	7.9	5.9	5.3	5.1
V (L)	8.7	4.3	4.3	4.3	4.3
W_R	0	0.73	0.76	0.33	0.15
$\hat{w}$ (wt.%)	53.1	38.7	29.6	26.8	25.6
$\bar{O}_2$ (mol min^{-1} m^{-3})	77.8	76.7	80	30.1	14.0
Kinetic regime	MT	MT	MT	SR	SR

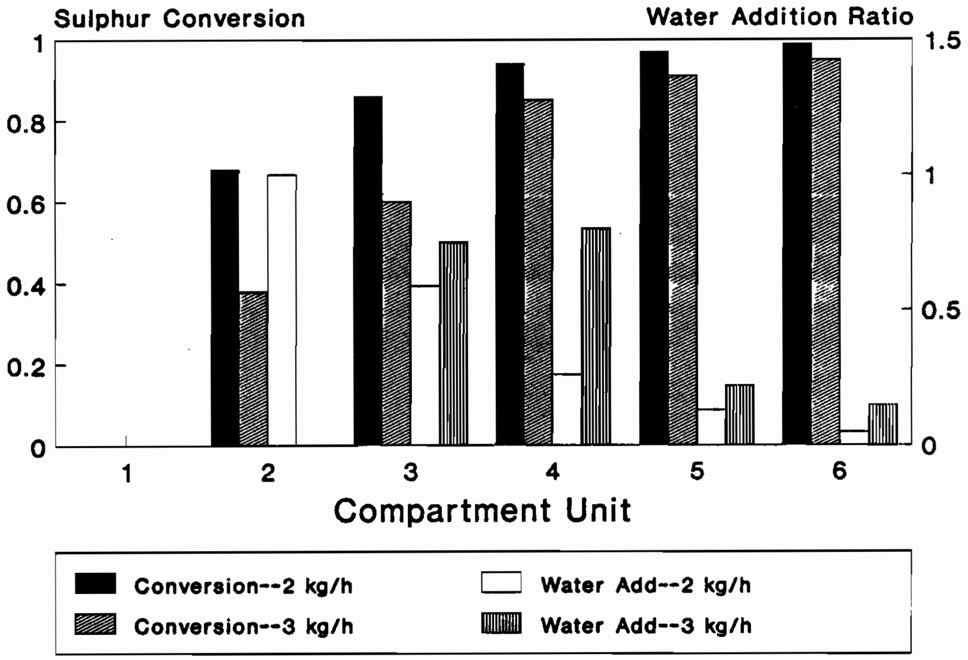

Figure 5.12: The effect of feed flow rate on sulphur conversion and water addition throughout the whole autoclave (Version 1).

this case the first three compartments operate under mass transfer control since the increased feed flow rate increases the demand for O_2. This implies that the autoclave operates near full capacity (theoretical). As a consequence, the extraction efficiency drops resulting in an overall 95% sulphur oxidation. The two feed flow rates are further compared in terms of their effect on conversion and water addition in Figure 5.12. The simulation runs at $F_s = 2$ and 3 kg h^{-1} indicate that it is possible to push more solids through the autoclave provided that some loss in sulphur conversion can be tolerated. This will obviously depend on the correlation between sulphur oxidation and gold recovery exhibited by the particular concentrate, or ore, which is determined by independent batch experimentation.

The impact of reactor configuration on sulphur conversion and water addition is examined in Figure 5.13. $C_f = 1$ (i.e. 6 equal size compartments) and $C_f = 2$ (i.e. 5 compartments with the first double in size) are compared. Autoclave operation at 190 °C with $C_f = 1$ is only possible with feed preheating to 70 °C and substantial inter-stage cooling (total $W_R = 1.55$), as opposed to no preheating ($T_0 = 30$ °C

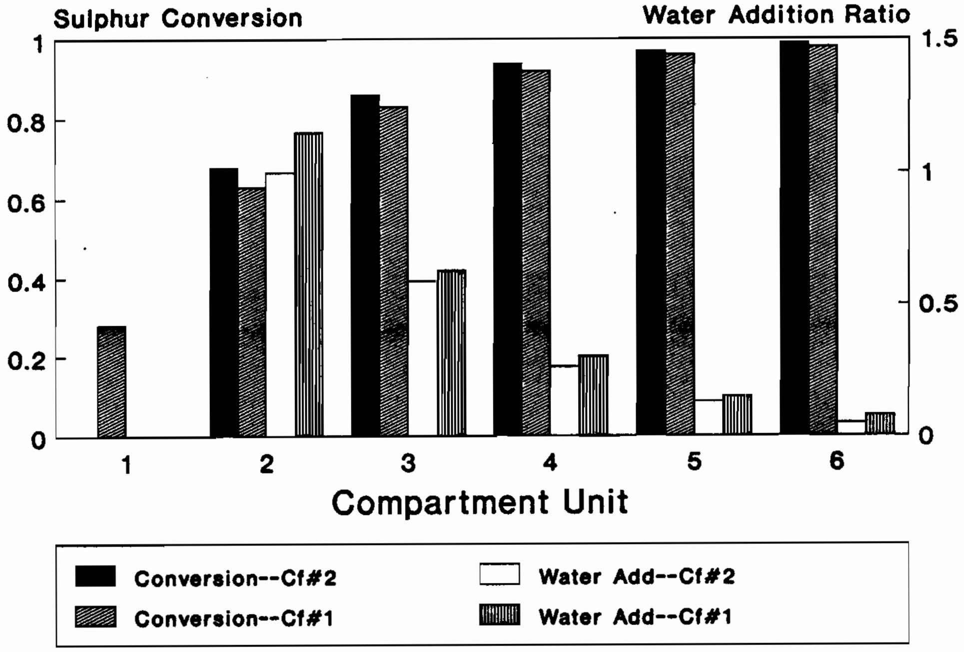

Figure 5.13: The effect of reactor configuration on sulphur conversion and water addition throughout the whole autoclave (Version 1).

and total $W_R = 1.35$) for $C_f = 2$. These results clearly demonstrate the power of computer simulation during the early stages of process design as a guide to the selection of appropriate autoclave configuration and feed conditions.

5.5 Summary

The mathematical model developed previously (in Chapter 4) has been extended to deal with a cascade of CSTRs, where multiple and strongly exothermic heterogeneous reactions occur under surface reaction, or gas transfer controlled kinetics. The model was formulated to describe the non-isothermal steady state behaviour of the reactor, in order to permit the identification of feed conditions for autothermal operation. Each reactor stage is treated separately (i.e. stage by stage analysis) by considering the exit stream of a particular reactor to be the feed to the next. A continuous particle size density function has been employed to describe the size distribution of the feed particles. Consequently, appropriate particle size density functions have been developed to describe the reacted particles under surface reaction, or gas transfer controlled kinetics. The decision whether the reactor operates under surface reaction, or gas transfer control is based on whether the gas transfer capacity of the reactor exceeds the gaseous reactant demands by the heterogeneous reactions.

Finally, it has been demonstrated that this mathematical model can greatly assist the optimization of reactor design and performance of a highly exothermic leaching process employed in the treatment of refractory gold concentrates. With the aid of the present model computer simulation of alternative operational schemes can be scanned and optimum autogenous conditions can be determined. It has been shown the rate limiting regime and reactor configuration to be of critical importance for optimal autogenous operation. Gas transfer limitations slow down the oxidation process and consequently the rate of heat release thereby permitting stable operation of the first autoclave compartment at the desired temperature range. On the other hand, having the first autoclave compartment substantially bigger in size than the successive ones permits the attainment of autogenous operation with minimal preheating and cooling requirements.

References

[5.1] J-C Charpentier, *Advances in Chemical Engineering* (ed. by T.B. Drew, G.R. Cokelet, J.W. Hoopes Jr., and T. Vermeulen), vol. 11, pp. 1–133, Academic Press, New York NY (1981).

[5.2] G. Bouboukas, A. Gaunand, and H. Renon, *Hydrometallurgy*, 19, 25 (1987).

[5.3] G.A. L'Homme, *Mass Transfer with Chemical Reaction in Multiphase Systems* (ed. by E. Alper), vol. 2, pp. 1–18, NATO ASI Series, E(73), Martinus Nijhoff, The Hague (1983).

[5.4] C.W. Bale, A.D. Pelton and W.T. Thomson, *"Facility for the Analysis of Chemical Thermodynamics (F*A*C*T)"*, McGill University, Montreal, Quebec.

[5.5] D.R. Weir and R.M.G.S. Berezowsky, *Intl Symposium on Gold Metallurgy* (ed. by R.S Salter, D.M. Wyslowzyl and G.N. McDonald), 26-th Ann. Conf. Metall., p. 247, CIM, Winnipeg, Manitoba (1987).

[5.6] R.H. Perry and C.H. Chilton, *Chemical Engineers' Handbook*, 5-th edition, p. 8–3, McGraw-Hill, New York (1973).

[5.7] M. Peleg, M.D. Normand and J.R. Rosenau, *Powder Technology*, 46, 209 (1986).

[5.8] S.E. LeBlanc and H.S. Fogler, *AIChE J.*, 33(1), 54 (1987).

[5.9] P.V. Shertukde, J.B. Joshi and M. Chidambaram, *Chem. Eng. J.*, 38, 81 (1988).

[5.10] J.B. Joshi, V.P. Utgikar, M.M. Sharma, and V.A. Juvekar, *Rev. Chem. Eng.*, 3(4), 281 (1985).

[5.11] L.K. Doraiswamy and M.M. Sharma, *Heterogeneous Reactions*, vol. 2, John Wiley & Sons, New York NY (1986).

[5.12] B.I. Morsi and J-C Charpentier, *Mass Transfer with Chemical Reaction in Multiphase Systems* (ed. by E. Alper), vol. 1, pp. 53–100, NATO ASI Series, E(73), Martinus Nijhoff, The Hague (1983).

[5.13] H. Hofman, *Mass Transfer with Chemical Reaction in Multiphase Systems* (ed. by E. Alper), vol. 2, pp. 171–198, NATO ASI Series, E(73), Martinus Nijhoff, The Hague (1983).

[5.14] K.B. DeGraaf, E. Peters and G.M. Swinkels, 24-th Ann. Conf. Metall., paper No. 44.2, CIM, Vancouver B.C. (1985).

[5.15] J.B. Joshi, A.B. Pandit and M.M. Sharma, *Chem. Eng. Sci.*, 37(6), 813 (1982).

[5.16] H. Oguz, A. Brehm and W.-D. Decker, *Chem. Eng. Sci.*, 42(7), 1815 (1987).

[5.17] J.A. Herbst, *Rate Processes of Extractive Metallurgy* (ed. by H.Y. Sohn and M.E. Wadsworth), pp. 53–112, Plenum Press (1979).

[5.18] M.E. Chalkey, I.M. Masters and D.W. Weir, *Zinc '83*, Proc. 13-th Ann. Hydromet. Meet., CIM, Edmonton, Alberta (1983).

[5.19] M.J. Collins, R.M.G.S. Berezowsky and D.R. Weir, *Arsenic Metallurgy: Fundamentals and Applications*, (ed. by R.G. Reddy, J.L. Hendrix and P.B. Queneau), pp. 115–133, TMS-AIME, Warrendale, Pa (1988).

[5.20] A. Kontopoulos and M. Stefanakis, *Precious Metals '89* (ed. by M.C. Jha and S.D. Hill) pp. 179–209, TMS-AIME, Warrendale PA (1989).

[5.21] R.M.G.S. Berezowsky, Sherritt Gordon Ltd., Fort Saskatchewan, Alberta, Personal Communication (1989).

[5.22] R.C. Weast, *Handbook of Chemistry and Physics*, 66th ed., CRC Press, p. B-138,D-190 (1985–86).

[5.23] D.R.Weir, Sherritt Gordon Ltd., Fort Saskatchewan, Alberta, Personal Communication (1989).

[5.24] R.M.G.S. Berezowsky, A.K. Haines and D.R. Weir, in *Projects '88*, 18-th Ann. Hydromet. Meeting CIM, p. 24, Edmonton, Alberta (1988).

[5.25] D.R. Weir, U.S. Patent No 4,606,763 (1986).

[5.26] C.G. Hill Jr., *An Introduction to Chemical Engineering Kinetics & Reactor Design*, p. 406, John Wiley & Sons (1977).

[5.27] O. Levenspiel, *Chemical Reaction Engineering*, 2nd ed., p. 291, John Wiley & Sons (1972).

[5.28] O. Levenspiel, *The Chemical Reactor Omnibook+*, p. 52.14, OSU Book Stores, Corvallis OR (1984).

[5.29] E.N. Beloglazov, *Solid Phase Extractors* (in Russian), p. 144, Chimia, Leningrad, USSR (1985).

[5.30] A.E. Rodrigues, *Multiphase Chemical Reactors* (ed. by A.E. Rodrigues, J.M. Calo, and N.H. Sweed), vol. 1, pp. 225–283, Sijthoff & Noordhoff, The Netherlands (1981).

[5.31] J.R. Benjamin and C.A. Cornell, *Probability, Statistics and Decision for Civil Engineers*, pp. 73–76, McGraw-Hill, New York NY (1970).

[5.32] A.D. Randolph and M. Larson, *Theory of Particulate Processes*, pp. 41–64, Academic Press (1971).

[5.33] H.M. Hulburt and S. Katz, *Chem. Eng. Sci.*, 19, 555 (1964).

Chapter 6

Reactor Models for Multi-Stage Continuous Pressure Oxidation: Simultaneous Surface Reaction and Gas Transfer Control

6.1 Introduction

The basic assumption made in the modelling approach presented in the previous chapter was that the oxidation process is controlled either by surface reaction or by gas–liquid mass transfer. In other words, a sharp shift in the rate-limiting regime was considered to take place every time the rate of oxygen consumption exceeded the maximum mass transfer capacity of the reactor. In reality, however, a transition stage between the two rate-limiting regimes is expected to exist during which the overall kinetics is governed by both surface reaction and mass transfer. Thus, it is the purpose of this chapter to expand the previous modelling approach in order to account for situations where the process kinetics is controlled simultaneously by the surface reaction and the mass transfer rate. Mathematical description of this "mixed" control regime is achieved through the mass balance of oxygen.

Table 6.I: Stoichiometric table for selected species

$$\begin{array}{llllllll}
1: & FeS_2(s) & F_1 = & F_{10} & & -2\dot{\epsilon}_2 & & \\
2: & FeAsS(s) & F_2 = & F_{20} & & & -4\dot{\epsilon}_3 & \\
3: & H_2O(l) & F_3 = & F_{30} & & -2\dot{\epsilon}_2 & -6\dot{\epsilon}_3 & +\dot{\epsilon}_4 \\
4: & O_2(aq) & F_4 = & F_{40} & +\dot{\epsilon}_1 & -7\dot{\epsilon}_2 & -13\dot{\epsilon}_3 & -\frac{1}{2}\dot{\epsilon}_4 \\
5: & Fe^{2+}(aq) & F_5 = & F_{50} & & +2\dot{\epsilon}_2 & +4\dot{\epsilon}_3 & -2\dot{\epsilon}_4 \\
6: & O_2(g) & F_6 = & F_{60} & -\dot{\epsilon}_1 & & & \\
\vdots & & & & & & &
\end{array}$$

6.2 The Chemical Reaction System

Similarly to the previous chapter, the pressure oxidation of a pyrite/arsenopyrite concentrate is again considered to be represented by the set of reactions shown below.

$$O_2(g) \longrightarrow O_2(aq) \tag{6.1}$$

$$2FeS_2(s) + 7O_2(aq) + 2H_2O(l) \longrightarrow 2Fe^{2+}(aq) + 4HSO_4^-(aq) \tag{6.2}$$

$$4FeAsS(s) + 13O_2(aq) + 6H_2O(l) \longrightarrow 4H_3AsO_4(aq) + 4Fe^{2+}(aq) + 4SO_4^{2-}(aq) \tag{6.3}$$

$$2Fe^{2+}(aq) + \frac{1}{2}O_2(aq) + 2H^+(aq) \longrightarrow 2Fe^{3+}(aq) + H_2O \tag{6.4}$$

Here, for the purpose of achieving an accurate mass balance of oxygen the oxidation of divalent iron is taken into account too (reaction 6.4). The respective rates of $O_2(aq)$, $FeS_2(s)$, $FeAsS(s)$, and $Fe^{2+}(aq)$ in reactions 6.1 through 6.4 have already been given in Chapter 3, 4, and 5, along with the thermodynamic data of all species involved.

6.3 Model Development

The stoichiometric table for the major species involved in the 4-reaction system is shown in Table 6.I. The reaction rates can be written in a general form as

$$\bar{r}_{6.1} = k_L a(C^\star_{O_2} - C_{O_2}) = k'_L a(P^\star_{O_2} - P_{O_2}) \tag{6.5}$$

$$\bar{r}_{6.2} = k_2 P_{O_2} \tag{6.6}$$

$$\bar{r}_{6.3} = k_3 P_{O_2} \tag{6.7}$$

$$\bar{r}_{6.4} = k_4 C^2_{Fe^{2+}} P_{O_2} \tag{6.8}$$

As demonstrated in Chapter 4, once the reaction extents are found, the abundance of each species in the system of chemical reactions is determined. Since we are dealing with 4 reactions, 4 independent mass balance equations must be formulated and solved for the respective reaction extents $\dot{\epsilon}_i$ ($i = 1$ to 4). Therefore, 4 species are selected, one for each reaction. These are: $O_2(aq)$, $FeS_2(s)$, $FeAsS(s)$, and $Fe^{2+}(aq)$. Their respective rates of generation are[1]:

$$r_{O_2(aq)} = r_4 = \bar{r}_{6.1} - 7\bar{r}_{6.2} - 13\bar{r}_{6.3} - \frac{1}{2}\bar{r}_{6.4} \tag{6.9}$$

$$r_{FeS_2(s)} = r_1 = -2\bar{r}_{6.2} \tag{6.10}$$

$$r_{FeAsS(s)} = r_2 = -4\bar{r}_{6.3} \tag{6.11}$$

$$r_{Fe^{2+}(aq)} = r_5 = 2\bar{r}_{6.2} + 4\bar{r}_{6.3} - 2\bar{r}_{6.4} \tag{6.12}$$

The mass balance equations for the 4 selected species in a CSTR at steady state are as follows.

Species 1, ($FeS_2(s)$):

$$F_{10} - F_1 + r_1 S_1 = 0 \tag{6.13}$$

where S_1 is the surface area of solid phase 1 (i.e. FeS_2). Substitution of r_1 from eq. 6.10 and F_1 from Table 6.I yields

$$\dot{\epsilon}_2 - \bar{r}_{6.2} S_1 = 0 \tag{6.14}$$

In Chapter 4, it was shown that the product $r_1 S_1$ can be effectively expressed in terms of the conversion. Hence, eq. 6.13 can be written as

$$r_1 S_1 = -\frac{F_{10} - F_1}{F_{10}} F_{10} = -\bar{x}_1 F_{10} \tag{6.15}$$

---

[1] Table 6.I must be consulted for index identification.

Combining equations 6.10, 6.14, and 6.15, the following important relation is obtained

$$\dot{\epsilon}_2 = \frac{\bar{x}_1}{2} F_{10} \tag{6.16}$$

where $\bar{x}_1$ is given by (see Chapter 5):

$$\bar{x}_1 = \int_{d_{1,\mathrm{min}}}^{d_{1,\mathrm{max}}} f_{\mathrm{m}}(d_1) \int_0^\infty x(d_1, t) E(t)\, \mathrm{d}t\, \mathrm{d}d_1 \tag{6.17}$$

Species 2, ($FeAsS(s)$):

$$F_{20} - F_2 + r_2 S_2 = 0 \tag{6.18}$$

where S_2 is the surface area of solid phase 2 (i.e. $FeAsS$). In a similar way, equation 6.18 yields

$$\dot{\epsilon}_3 - \overline{r}_{6.3} S_2 = 0 \tag{6.19}$$

and

$$\dot{\epsilon}_3 = \frac{\bar{x}_2}{4} F_{20} \tag{6.20}$$

where $\bar{x}_2$ is given by

$$\bar{x}_2 = \int_{d_{2,\mathrm{min}}}^{d_{2,\mathrm{max}}} f_{\mathrm{m}}(d_2) \int_0^\infty x(d_2, t) E(t)\, \mathrm{d}t\, \mathrm{d}d_2 \tag{6.21}$$

Species 5, ($Fe^{2+}(aq)$):

$$F_{50} - F_5 + r_5 V = 0 \tag{6.22}$$

Substitution of r_5 from eq. 6.12 and F_5 from Table 6.I yields

$$-2\dot{\epsilon}_2 - 4\dot{\epsilon}_3 + 2\dot{\epsilon}_4 + 2\overline{r}_{6.2} S_1 + 4\overline{r}_{6.3} S_2 - 2\overline{r}_{6.4} V = 0 \tag{6.23}$$

Simplification of eq. 6.23 with the aid of relations 6.14 and 6.19 yields

$$\dot{\epsilon}_4 - \overline{r}_{6.4} V = 0 \tag{6.24}$$

which after substitution of $\overline{r}_{6.4}$ from eq. 6.8 results in

$$\dot{\epsilon}_4 - k_4 C_5^2 P_{O_2} V = 0 \tag{6.25}$$

Furthermore, the concentration of any species C_i in the CSTR is given by

$$C_i = \frac{F_i \bar{t}}{V}$$

and thus

$$\dot{\epsilon}_4 - k_4 \frac{(F_{50} + 2\dot{\epsilon}_2 + 4\dot{\epsilon}_3 - 2\dot{\epsilon}_4)^2 \, \bar{t}^2}{V} P_{O_2} = 0 \tag{6.26}$$

Species 4, ($O_2(aq)$):

$$F_{40} - F_4 + r_4 V = 0 \tag{6.27}$$

Substitution of r_4 from eq. 6.9 and F_4 from Table 6.I yields

$$-\dot{\epsilon}_1 + 7\dot{\epsilon}_2 + 13\dot{\epsilon}_3 + \frac{1}{2}\dot{\epsilon}_4 + \bar{r}_{6.1}V - 7\bar{r}_{6.2}S_1 - 13\bar{r}_{6.3}S_2 - \frac{1}{2}\bar{r}_{6.4}V = 0 \tag{6.28}$$

which, after further simplification using equations 6.14, 6.19, and 6.24 is

$$-\dot{\epsilon}_1 + \bar{r}_{6.1}V = 0 \tag{6.29}$$

The rate of oxygen transfer, given by eq. 6.5, is substituted into eq. 6.29

$$-\dot{\epsilon}_1 + k'_L a(P^{\star}_{O_2} - P_{O_2})V = 0 \tag{6.30}$$

Thus a system of 4 algebraic equations, eqs. 6.16, 6.20, 6.26, and 6.30 is identified and solved for the 4 reaction extents. However, in the above equations there exists an additional unknown, P_{O_2}, and a fifth equation is therefore required. This is the one which relates P_{O_2} and C_{O_2} through Henry's law. More specifically, if k_H is the Henry's constant defined in concentration units, the necessary equation is:

$$\frac{P_{O_2}}{k_H} = \frac{(F_{40} + \dot{\epsilon}_1 - 7\dot{\epsilon}_2 - 13\dot{\epsilon}_3 - 1/2\,\dot{\epsilon}_4)\bar{t}}{V} \tag{6.31}$$

The 5-equation system is summarized Table 6.II.

The essence of the present approach is that the oxidations of FeS_2, $FeAsS$, and Fe^{2+} are always calculated on the basis of their intrinsic reaction kinetics for a steady state oxygen pressure P_{O_2}. The latter value is controlled by the rate of O_2 transfer given by eq. 6.5. In other words P_{O_2} assumes intermediate values between

Table 6.II: The system of 5 equations

$$\dot{\epsilon}_2 - \frac{\bar{x}_1}{2} F_{10} = 0$$

$$\dot{\epsilon}_3 - \frac{\bar{x}_2}{4} F_{20} = 0$$

$$\dot{\epsilon}_4 - k_4 \frac{(F_{50} + 2\dot{\epsilon}_2 + 4\dot{\epsilon}_3 - 2\dot{\epsilon}_4)^2\, \bar{t}^2}{V} P_{O_2} = 0$$

$$\dot{\epsilon}_1 - \frac{k_L a}{k_H}(P^{\star}_{O_2} - P_{O_2})V = 0$$

$$\frac{P_{O_2}}{k_H} - \frac{(F_{40} + \dot{\epsilon}_1 - 7\dot{\epsilon}_2 - 13\dot{\epsilon}_3 - 1/2\, \dot{\epsilon}_4)\bar{t}}{V} = 0$$

0 (extreme case 1: pure gas–liquid transfer control), and $P^{\star}_{O_2}$ (extreme case 2: pure surface reaction control without any mass transfer limitations). The two extreme cases were considered in Chapter 5.

The 5-equation system with unknowns $\dot{\epsilon}_1$, $\dot{\epsilon}_2$, $\dot{\epsilon}_3$, $\dot{\epsilon}_4$, and P_{O_2} is solved here with a multi-dimensional Newton-Raphson method. The numerical procedure is similar to that described by I and Nancollas [6.1], where the algorithm was modified to ensure positive roots. Hartley's method [6.2] is also applied to increase the convergence rate. The reactor cascade is assessed on a stage by stage basis as explained in Chapter 5. The mass-PSD function of reacted particles is calculated through equation 5.24. Finally, the general program flowchart is similar to that shown in Appendix E for model Version 2.

6.4 Model Application

The model developed is used in two distinctly different modes. First, the model is used with the assumption that the partial pressure of oxygen is constant at any temperature. We refer to this model version as Version 3. Second, the model is used with the assumption that the total pressure (water vapour and oxygen) is constant at all temperatures. We refer to this model version as Version 4. Before the simulation results generated with these two model versions are presented, the volumetric mass transfer coefficient has to be determined.

6.4.1 On the Values of k_La and k_H

In estimations in the previous chapter, the volumetric mass transfer coefficient k_La and Henry's constant k_H were grouped together as a single lumped parameter k'_La, where

$$k'_La = \frac{k_La}{k_H}$$

Here, k'_La is decoupled from k_H. To do so, recently published data by Prini and Crovetto [6.3] on the relation of Henry's constant with temperature were assessed and appropriately used. Prini and Crovetto [6.3] presented the temperature dependence of Henry's constant based on mole fraction scale, $k_{H,y}$, with the following polynomial expression:

$$\ln k_{H,y} = \sum_{\iota=0}^{3} \frac{\mathcal{P}_{\iota+1}}{T^{\iota}} (1000)^{\iota} \tag{6.32}$$

Equation 6.32 is valid for O_2 solubility in pure H_2O, in which case the respective values of $\mathcal{P}_\iota$ are:

$$\begin{aligned} \mathcal{P}_1 &= -15.9766 \\ \mathcal{P}_2 &= 15.7951 \\ \mathcal{P}_3 &= -4.3331 \\ \mathcal{P}_4 &= 0.3502 \end{aligned}$$

With the above values, $k_{H,y}$ results in GPa units. Transformation of $k_{H,y}$ into the respective k_H, which is based on concentration units (mol L^{-1}), was performed assuming constant water density as follows. According to the thermodynamic definition of Henry's constant [6.4] we have

$$P^{\star}_{O_2} = k_{H,y} y^{\star}_{O_2} \tag{6.33}$$

where y_{O_2} is the mole fraction of oxygen, i.e.

$$y^{\star}_{O_2} = \frac{N^{\star}_{O_2}}{N_{H_2O} + N^{\star}_{O_2}} \tag{6.34}$$

The definition of Henry's constant based on concentration units should read

$$P^{\star}_{O_2} = k_H C^{\star}_{O_2} \tag{6.35}$$

where $C^{\star}_{O_2}$ is:

$$C^{\star}_{O_2} = \frac{N^{\star}_{O_2}}{V_{H_2O}} \tag{6.36}$$

By proper manipulation of equations 6.33 through 6.36 and by considering that 1 Pa = 0.9869×10^{-5} atm and $N_{H_2O} = V_{H_2O}\rho_{H_2O}/M_{H_2O}$ (with $\rho_{H_2O} = 1000$ g L^{-1} and $M_{H_2O} = 18$ g mol^{-1}), the following equation is obtained

$$k_H = \frac{(k_{H,y} \cdot 10^4 \cdot 0.9869 - P^{\star}_{O_2})18}{1000} \tag{6.37}$$

The transformation equation 6.37 results in atm L mol^{-1} units when $k_{H,y}$ and $P^{\star}_{O_2}$ are expressed in GPa and atm respectively[2]. Numerical evaluation of equations 6.32 and 6.37 for $T = 463$ K (190 °C), and $P^{\star}_{O_2} = 5$ atm yields[3]:

$$k_H = 760 \quad \text{atm L mol}^{-1}$$

In the previous chapter, $k'_L a$ was estimated to have a value of

$$k'_L a = 1.62 \times 10^{-2} \quad \text{mol min}^{-1}\ \text{L}^{-1}\ \text{atm}^{-1}$$

at 190 °C. Using the k_H value given above $k_L a$ is further calculated to be

$$k_L a = 12.31 \quad \text{min}^{-1}$$

Assuming an apparent activation energy $E_A = 4.2$ kJ mol^{-1} (as in Chapter 5 for model Version 2) the following temperature dependence function for $k_L a$ is obtained

$$k_L a = 36.25 \exp(-\frac{500}{T}) \quad \text{min}^{-1} \tag{6.38}$$

---

[2] In fact, equation 6.37 is rather insensitive to $P^{\star}_{O_2}$, which renders k_H virtually independent of $P^{\star}_{O_2}$.

[3] In reality, the value of k_H is expected to be somewhat lower due to the presence of dissolved ionic species (i.e. not pure water). However, due to the lack of direct experimental measurements, this effect is neglected. The negative effect of this simplification, though, is compensated during the estimation of $k_L a$ as explained later.

On the basis of eq. 6.38, k_La at 25 °C has a value of 6.77 min^{-1}, or equivalently 0.11 s^{-1}. The latter is well within the range of values (0.24 to 12 min^{-1}) that have been measured and reported in literature lately for three-phase reactors [6.5, 6.6]. In the present work k_La is an adjustable parameter and no effort is made to correlate its value to the hydrodynamic conditions that prevail inside the reactor. In the remainder of the current chapter, k_La values refer to 190 °Cwhich is the target operating temperature.

6.4.2 Simulation Results with Constant $P^\star_{O_2}$

The present reactor model, which accounts for simultaneous surface reaction and gas transfer kinetics under constant $P^\star_{O_2}$, is named Version 3. The effect of the magnitude of k_La on the attainment of autogenous operation in the first autoclave compartment is shown in Figure 6.1. In the same figure, bulk oxygen "pressures", P_{O_2} are also shown. The feed conditions are the "standard" ones (i.e. those listed in Table 5.III).

The significance of $k_La \rightarrow \infty$ is that the mass transfer of oxygen is infinitely fast which in turn implies that the solution is always saturated with oxygen ($P_{O_2} = P^\star_{O_2} =$ 5 atm). In this case, the oxidation process takes place at the fastest possible rate. As k_La is assigned smaller values, gas transfer limitations slow down the oxidation process, which is now controlled by a "mixed" kinetic regime. As a consequence, the $G(T)$ and P_{O_2} curves, in Fig. 6.1, are shifted toward lower values. With increasing temperature, the surface reactions become increasingly fast, due to their strong temperature dependence (i.e. high activation energies), consuming oxygen faster than its rate of replacement. The net result is a depletion in terms of oxygen concentration, which inevitably drops below the equilibrium value corresponding to $P^\star_{O_2}$. Evidently, the depletion is more pronounced as k_La becomes smaller. However, it also seen in Fig. 6.1 that P_{O_2} attains a minimum in the vicinity of 200 °C (with finite k_La) before increasing again with temperature. This behaviour is attributed to the temperature dependence of k_H. Oxygen solubility (or equivalently k_H) increases drastically beyond

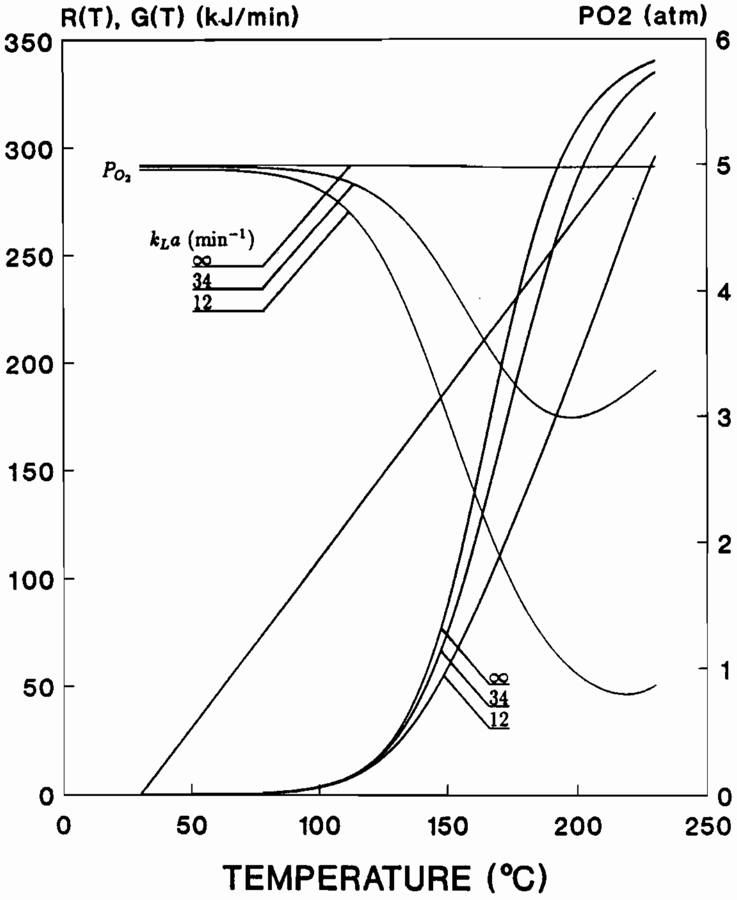

Figure 6.1: The effect of k_La on steady state operation and P_{O_2} in the first compartment. (Conditions: "standard"–Table 5.III; model Version 3.)

200 °C as can be seen from equation 6.32. Apparently, the rate by which O_2 solubility increases with temperature outweighs the respective increase in O_2 consumption by the oxidation reactions.

The Van Heerden diagram of Fig. 6.1 does not predict a stable steady state at 190 °C for any of the $k_L a$ values tested. Stable operation is predicted only at around 230 °C when $k_L a = 12$ min^{-1}. For the same $k_L a$ value, however, model Version 2 (Chapter 5) predicted stable steady state operation at 190 °C. Increasing the value of $k_L a$ to 34 min^{-1} an unstable steady state at 190 °C is obtained. Finally, further increase in $k_L a$ up to a value approaching infinity (i.e. 10^4 min^{-1}) gives essentially the same response as the pure surface reaction control based model, which was demonstrated in Chapter 4 (Figures 4.12 and 4.13).

The results presented in Fig. 6.1 are not directly comparable with the respective ones presented in the previous chapter. As a reminder, the model treated the two rate-limiting regimes separately in Chapter 5 (i.e. either surface reaction control or pure gas transfer control). As a consequence, P_{O_2} had a value of 5 atm in the former case and 0 atm in the latter. Furthermore, k_H was then lumped with $k_L a$ with an overall activation energy of 4.2 kJ. This is equivalent (from the computational point of view) to having $k_L a$ vary with the same activation energy and k_H constant. Hence, by taking $k_L a = 12$ min^{-1} (at 190 °C) and keeping k_H constant at 760 atm L mol^{-1}, the model version(s) in Chapter 5 can be compared with the current "mixed" Version 3. It is under this set of conditions that the results shown in Figure 6.2 were obtained. Recognizing that the surface reaction control and gas transfer control are the limiting cases, it is expected the $G(T)$ and P_{O_2} curves obtained by the "mixed" control approach to have as asymptotes the respective curves obtained by the former model versions (i.e. Version 1 and 2; Chapter 5). The $G(T)$ and P_{O_2} vs T curves in Fig. 6.2 do indeed exhibit this behaviour at low and high temperatures. However, the transition between the two rate-limiting regimes is greatly extended. A value of $P_{O_2} = 1.7$ atm rather than 0 atm at 190 °C is calculated, and significant levelling off

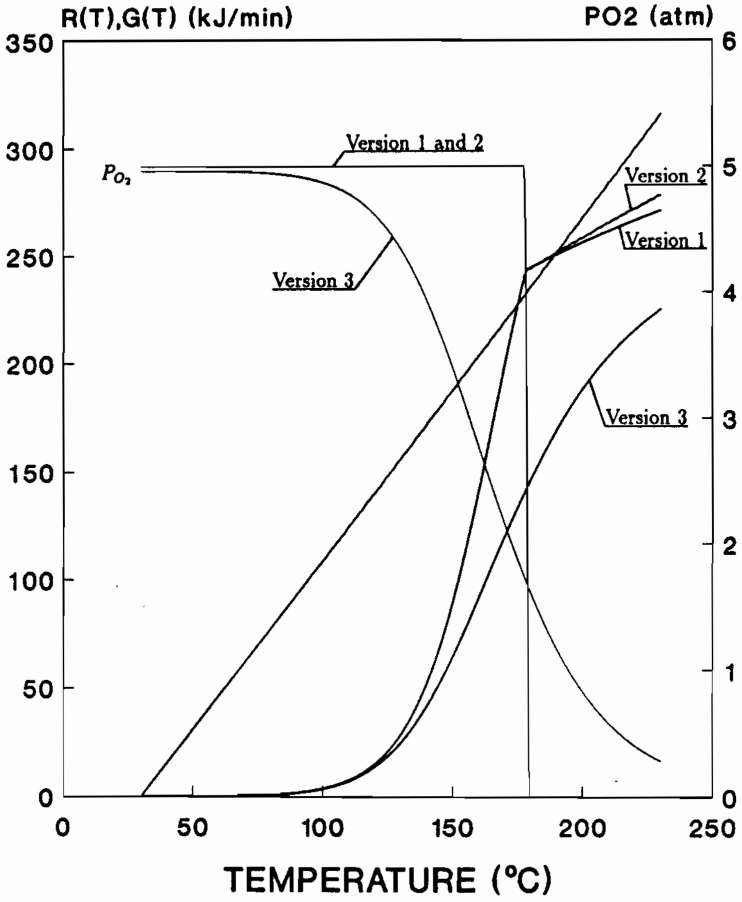

Figure 6.2: Comparison of model Version 1 and 2 with 3 for the first compartment. (Conditions: "standard"–Table 5.III; $k_La = 12\ \text{min}^{-1}$; $k_H = 760$ atm L mol^{-1}.)

of the $G(T)$ curve occurs before the latter approaches the gas transfer control straight line(s). The end result is that stable steady state at 190 °C is never obtained (i.e. no intersection between $G(T)$ and $R(T)$ at $T = 190$ °C). The latter result was further substantiated by running a series of simulations with different $k_L a$ values (ranging between 6 to 100 min^{-1}), and feed conditions (F_s between 1 and 3 kg h^{-1} and W_R between 0 to 1). At this point it was decided to tackle the problem by keeping the total pressure rather than the partial oxygen pressure constant. This approach proved to be successful and is described next.

6.4.3 Simulation Results with Constant P_{total}

Careful examination of Sherritt's description of the pressure oxidation process and pilot plant testing shows that the operating pressure is always given as total pressure (i.e. $P_{\text{total}} = P_{H_2O} + P^{\star}_{O_2}$) [6.7, 6.8, 6.9]. It is also mentioned that the vent valve of the autoclave is regulated to maintain constant total working pressure [6.9]. The sparging rate of O_2 is also kept constant [6.9]. It appears, therefore, that it is in fact the total pressure which is kept constant rather than the partial oxygen pressure. In terms of model formulation, this implies that at any temperature, $P^{\star}_{O_2}$ has to be calculated by subtracting the vapour pressure from the total pressure. The resulting model, which employs this particular feature will be hereafter labelled as model Version 4.

The vapour pressure of water at 190 °C is 12.4 atm (or equivalently 1255 kPa) according to the *Handbook of Chemistry and Physics* [6.10]. To maintain $P^{\star}_{O_2} =$ 5 atm at 190 °C the total pressure must be 17.4 atm. In order to facilitate the calculations, the vapour pressure was expressed as a function of temperature by fitting $P^{\star}_{O_2}$ data from reference [6.10] into an exponential-type function. The following function calculates the vapour pressure in atm at a given temperature θ in °C.

$$P_{H_2O} = \frac{\theta^{4.168}}{14.69} \exp(-16.665) \tag{6.39}$$

This function was obtained by linear regression of $\ln P_{H_2O}$ vs $\ln \theta$ between 160 to

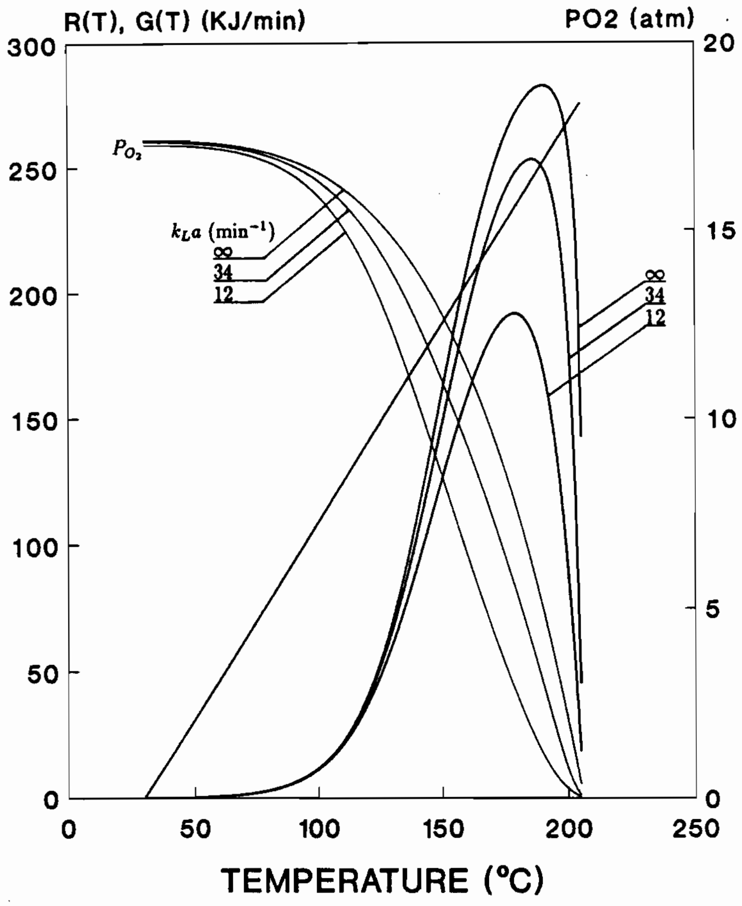

Figure 6.3: The effect of k_La on steady state operation and P_{O_2} in the first compartment at $P_{\text{total}} = 17.4$ atm. (Conditions: "standard"–Table 5.III; Version 4.)

200 °C (cor. coef. 0.999), and was extrapolated to lower temperatures as well.

Simulation runs employing "standard" feed conditions (Table 5.III) and $P_{\text{total}} = 17.4$ atm at three different k_La values, namely 12, 34 and 10^4 min^{-1} (always evaluated at 190 °C), are shown in Figure 6.3. Now, a stable steady state is indeed attained at 190 °C when $k_La = 34$ min^{-1}. In fact, both modelling approaches (i.e. keeping P_{total} constant or keeping $P^{\star}_{O_2}$ constant) yield exactly the same results at 190 °C in terms of $\bar{x}_{FeS_2}$, $\bar{x}_{FeAsS}$, $\bar{O}_2$, P_{O_2}, $C_{Fe^{2+}}$, etc., since they are both formulated to yield $P^{\star}_{O_2} = 5$ atm at 190 °C. However Version 3 predicts instability while Version 4 predicts stability, as seen by comparing Figures 6.1 and 6.3. The qualitative difference between the two figures is that the rate of $G(T)$ curves obtained by setting the total pressure constant attain a maximum and then they sharply decrease. This is due to the exponential increase of vapour pressure with temperature, which becomes equal to the total pressure (17.4 atm) at around 205 °C, thus forcing $P^{*}_{O_2}$ to drop to 0 atm. In Fig. 6.3 P_{O_2} is also plotted against the operating temperature. As expected, P_{O_2} decreases with increasing temperature since $P^{*}_{O_2}$ also decreases.

From a reactor operation stand point, keeping $P_{\mathbf{total}}$ constant acts as a self-regulating process control mechanism effectively stabilizing the steady state operating temperature of the reactor. Careful examination of the shape of the $G(T)$ curves in Fig. 6.3 reveals that stability is achieved only at operating temperatures beyond the temperature of $G(T)_{\mathbf{max}}$. This is evident from the fact that the slope of $G(T)$ is far less than the slope of $R(T)$ in this region, a necessary condition to ensure thermal stability (as discussed in Chapter 4). In fact, the slope of $G(T)$ is always negative beyond $G(T)_{\mathbf{max}}$. The additional effect of having negative $G(T)$ slope is that the stable steady state is rather insensitive to perturbations in the feed temperature (parallel move of R(T) line; see Chapter 2) offering, therefore, enhanced stability. Moreover, if we assume that the operating temperature accidentally increases beyond its current stable steady state value, $P^{*}_{O_2}$ will drop. As a consequence, the reaction rates will slow down, since they exhibit first-order dependence in P_{O_2}, and the system will acquire a tendency for self-readjustment back to the normal operating temperature. The reverse will take place if the operating temperature accidentally decrease. Thus, not only thermal but also kinetic stability is achieved, when the reactor operates under constant total pressure.

Comparison of the Model Versions

The attainment of steady state operation (stable or unstable) at 190 °C (for "standard" feed conditions; Table 5.III) is compared in Figure 6.4 for all model versions developed in this thesis. Only Versions 1,2, and 4 predict stable steady state at 190 °C. Complete simulation results[4] generated with model Version 4 are shown in

---

[4] Since according to Fig. 6.3 the value of $k_L a = 34$ min^{-1} yields stable steady state at 190 °C under "standard" feed conditions, it is retained in all subsequent simulations with Version 4.

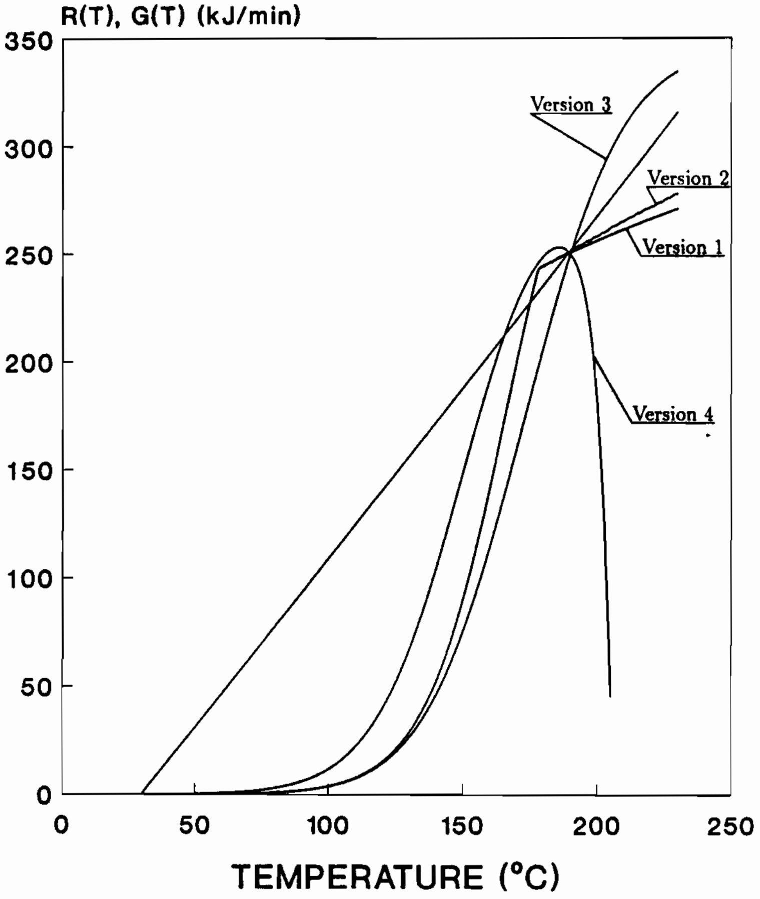

Figure 6.4: Comparison of the different model versions for the first compartment. (Conditions: "standard"–Table 5.III.)

Table 6.III: Simulation results with Version 4 at "standard" conditions (Table 5.III).

Process Parameters	Compartment				
	1	2	3	4	5
T (°C)	190	190	191	190	190
$\bar{x}_S$	0.722	0.887	0.956	0.984	0.994
$\bar{t}$ (min)	21	8.7	8.1	7.8	7.7
V (L)	8.7	4.3	4.3	4.3	4.3
W_R	1	0.55	0.23	0.10	0.05
$\hat{w}$ (wt.%)	35	28.9	27	26.1	25.7
$\bar{\dot{O}}_2$ (mol min^{-1} m^{-3})	83.7	36.9	15.4	6.2	2.4
P_{O_2} (atm)	3.1	4.1	4.3	4.8	4.9
$C_{Fe^{2+}}$ (mol L^{-1})	0.083	0.055	0.037	0.026	0.018

Table 6.IV: Simulation results with Version 4 at C_f=1; T_0=80 °C.

Process Parameters	Compartment					
	1	2	3	4	5	6
T (°C)	190	191	190	190	189	191
$\bar{x}_S$	0.498	0.766	0.896	0.955	0.981	0.992
$\bar{t}$ (min)	10.5	7.9	7.0	6.6	6.4	6.4
V (L)	4.3	4.3	4.3	4.3	4.3	4.3
W_R	1	0.85	0.45	0.22	0.12	0.12
$\hat{w}$ (wt.%)	35.8	27.2	23.9	22.6	21.9	21.9
$\bar{\dot{O}}_2$ (mol min^{-1} m^{-3})	114.9	58.4	28.3	13.0	5.7	2.5
P_{O_2} (atm)	2.4	3.4	4.3	4.7	5.1	4.6
$C_{Fe^{2+}}$ (mol L^{-1})	0.101	0.071	0.049	0.035	0.025	0.019

Table 6.III. These results are consistent with those listed in Tables 5.IV (Version 1) and 5.V (Version 2). Some differences among the various model versions developed in this work do exist, however, when other than the "standard" conditions are tested. Nevertheless, in a qualitative sense, the same trends are observed with all model versions (1, 2, and 4). Thus the results of Table 6.IV, which refer to $C_f = 1$, do indicate that with equal size compartments feed preheating is necessary. However, preheating to 80 °C rather than 110 °C is predicted (Figure 5.7).

Extensive verification of the model predictions by comparing with detailed data from continuous pilot plant and/or industrial size pressure reactors has to be performed to properly assess the validity of all these models. From the stand point of theoretical development, though, the latest model Version 4 is considered the most comprehensive and rigorous one. It is this model version that is retained in the process analysis section that follows.

6.4.4 Process Analysis

Inter-Relations of Key Variables

Before simulating alternative feed conditions and reactor configurations, the governing inter-relations of some key process variables are first analyzed at "standard" feed conditions (Table 5.III) and for the first autoclave compartment. Thus, in Figure 6.5 the variation of pyrite/arsenopyrite conversion and gas-phase/liquid-phase oxygen pressures with operating temperature is shown. The conversion curves of the two minerals have exactly the same shape as the rate of heat generation curve (Fig. 6.3). In other words, $G(T)$ is directly proportional to the degree of conversion of the two sulphides. By examining Fig. 6.5 it can be seen that the oxidation rate of arsenopyrite is higher than that of pyrite up to a temperature of 175 °C and then the relative order of velocities of the two oxidation reactions 6.2 and 6.3 is reversed. At 190 °C the conversion of $FeAsS$ and FeS_2 is 0.67 and 0.73 respectively. It should be noted that the "high temperature" rate of pyrite oxidation (> 160 °C; see Chapter 3) is employed in all simulation runs.

In terms of oxygen pressures, the ascending operating temperature causes both $P^{\star}_{O_2}$ and P_{O_2} to drop, due to vapour pressure elevation (P_{total} = constant). The driving force for O_2 transfer is always the difference between $P^{\star}_{O_2}$ and P_{O_2} at a given temperature. ΔP_{O_2} is plotted in Figure 6.6 along with the overall sulphur conversion $\bar{x}_S$. Both curves exhibit the same shape as the $G(T)$ curve. They only differ as to the temperature at which they attain their maximum. Sulphur conversion is controlled by the mass transfer rate of oxygen. This is better seen in Figure 6.7, where the

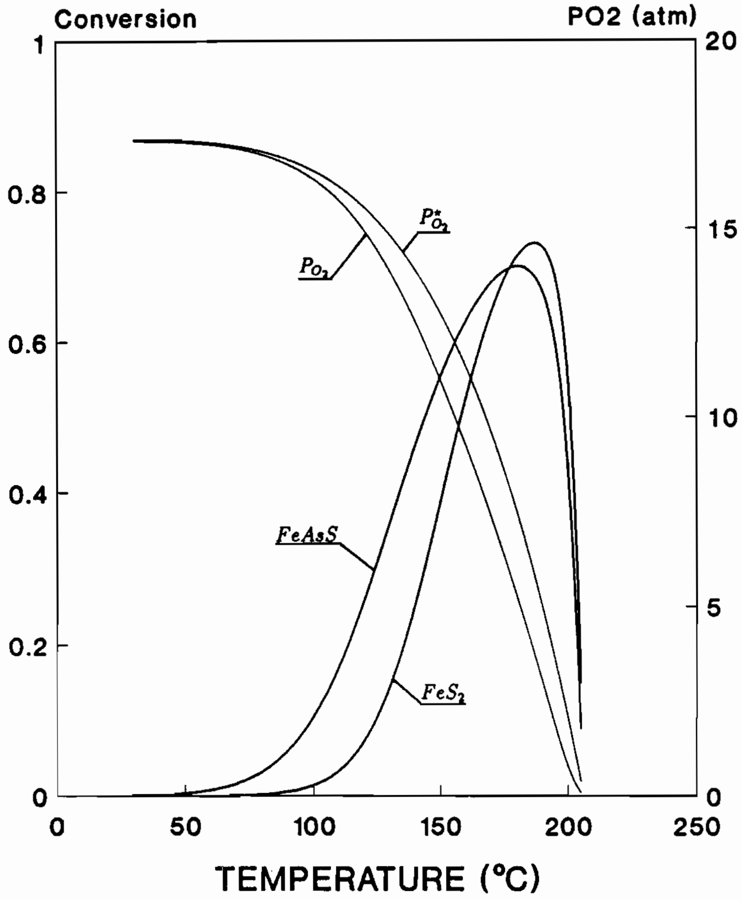

Figure 6.5: Variation of pyrite/arsenopyrite conversion and gas-phase/liquid-phase oxygen pressure with operating temperature in the first compartment. (Conditions: "standard"–Table 5.III; model Version 4.)

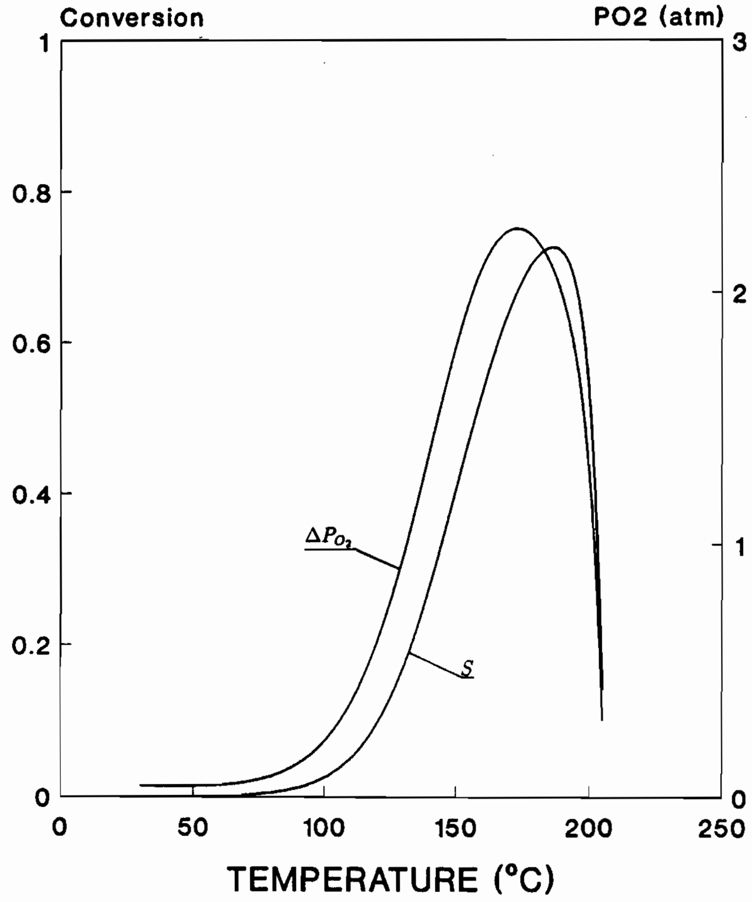

Figure 6.6: Variation of sulphur conversion and gas-phase/liquid-phase oxygen pressure difference with operating temperature in the first compartment. (Conditions: "standard"–Table 5.III; model Version 4.)

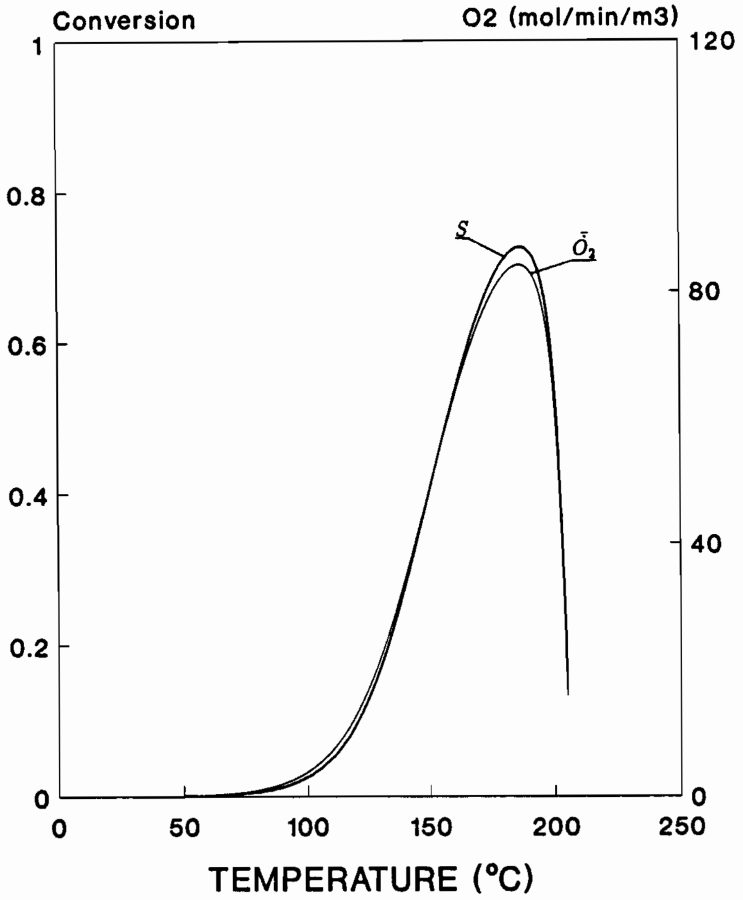

Figure 6.7: Variation of sulphur conversion and rate of oxygen consumption with operating temperature in the first compartment. (Conditions: "standard"–Table 5.III; model Version 4.)

rate of oxygen consumption, $\bar{\dot{O}}_2$, is plotted together with sulphur conversion. Here it is seen that the maximum rate occurs at the maximum $\bar{x}_S$ level. The difference between the temperature at which ΔP_{O_2} and $\bar{\dot{O}}_2$ (or $\bar{x}_S$) attain their maximum is due to the different temperature dependence of k_H and k_La. It is worthy of note that, according to Figure 6.8, $\bar{\dot{O}}_2$ is equal to 80 mol min^{-1} m^{-3} at 190 °C as expected from the published data of Sherritt Gordon Ltd. (see Chapter 5). Finally, heat generation is almost proportional to $\bar{x}_S$ as illustrated in Figure 6.8. The similarity among $G(T)$, $\bar{x}_S$ and $\bar{\dot{O}}_2$ curves in Figs 6.6 to 6.8 has its origins in the fact that most of the heat evolved and oxygen consumed is due to the sulphide mineral oxidations. In other words, reactions 6.2 and 6.3 dominate by being very exothermic in comparison to reactions 6.1 and 6.4 (reaction 6.1 is slightly endothermic; see Table 5.I), and by

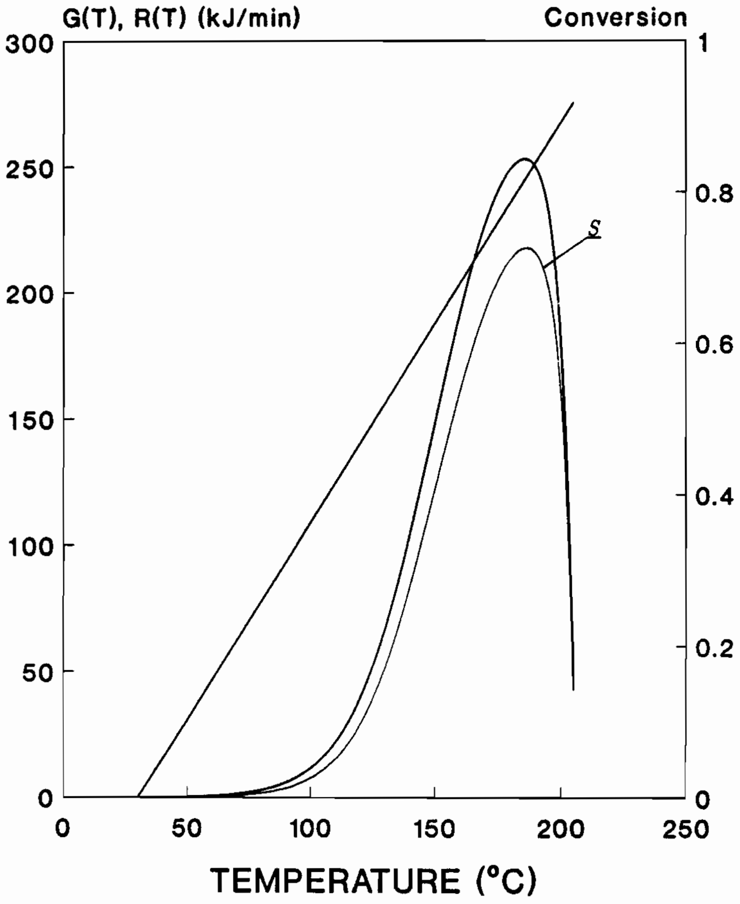

Figure 6.8: Variation of sulphur conversion and rate of heat generation with operating temperature in the first compartment. (Conditions: "standard"–Table 5.III; model Version 4.)

consuming most of the stoichiometrically needed oxygen at rates much faster than the rate of $Fe(II)$ to $Fe(III)$ oxidation.

On the Sulphur Content: From Concentrate to Ore

By examining the heat of reactions 6.2 and 6.3 on a mole of sulphide (FeS_2 or $FeAsS$) basis at 190 °C we see that their values are almost the same. That is

$$\Delta H^{\circ}_{463,6.2} = -1446.2 \quad \mathrm{J\ mol}^{-1}_{FeS_2}$$

$$\Delta H^{\circ}_{463,6.3} = -1470.7 \quad \mathrm{J\ mol}^{-1}_{FeAsS}$$

This implies that the heat evolved during sulphur oxidation is almost the same with the heat evolved during arsenic oxidation, since FeS_2 has two g-atom of S per mole and $FeAsS$ has one As and one S. Therefore, in terms of "fuel" capacity, arsenic is equivalent to sulphur. This is further supported from the fact that around 190 °C the oxidation rates of FeS_2 and $FeAsS$ are similar in magnitude, as shown in Figure 6.5. Hence, the total sulphur and arsenic content constitutes the basic parameter in determining to what extent autogenous operation is possible with a given feed material. For the Olympias concentrate, which has a ratio of $S/As = 8$ (on g-atom basis; see Table 5.II), the As content was neglected since As is only 11% of the total $S + As$. However, concentrates rich in As must be accounted for their As content as well.

As shown in the previous section, the degree of sulphur conversion has a direct impact on the attainment of autogenous operation. But the amount of heat generation depends on the sulphur content of the feed. The latter is effectively adjusted by varying the recycle ratio R_R. This approach was used here in an effort to simulate various feed conditions, varying from low grade ore to high grade concentrate. For example, model predictions for the Olympias concentrate (Table 5.II) given in Figure 6.3, and Tables 6.III and 6.IV, correspond to 6.7 wt.% sulphur content, which was adjusted by setting $R_R = 5$. The relation between sulphur content and recycle ratio (for the same concentrate of Table 5.II) is shown in Figure 6.9. For $R_R = 0$,

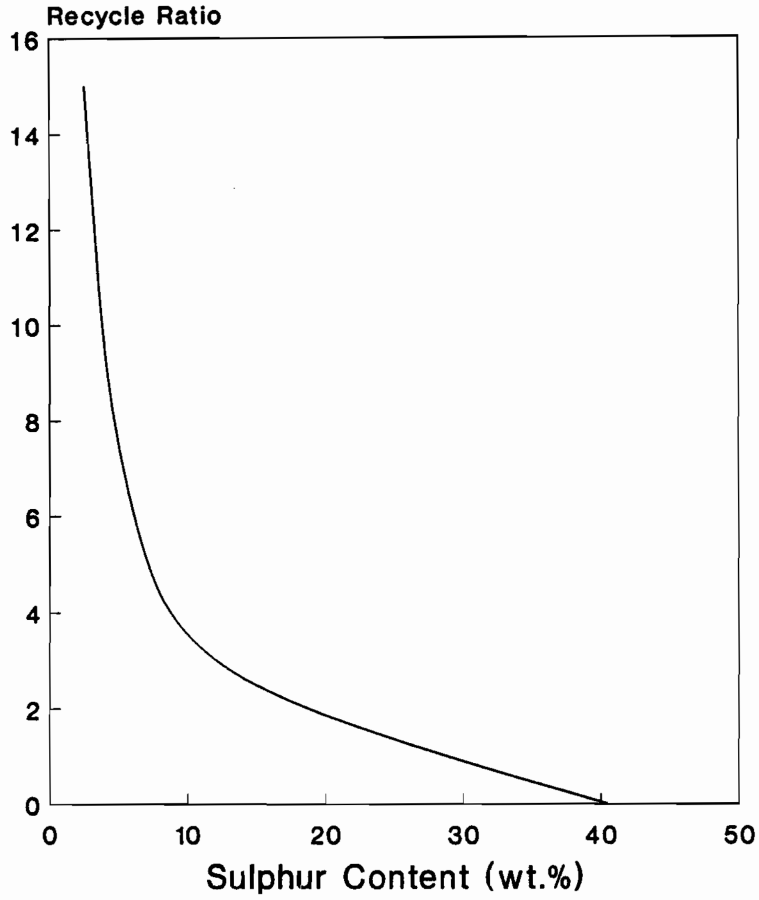

Figure 6.9: Recycle ratio R_R versus sulphur content relation for the Olympias concentrate.

the S content of the blend solids is equal to that of the original concentrate (i.e. 41 wt.%; see Table 5.II).

By conducting a series of complete simulation runs (from the first to the final compartment) at four different throughput values, namely $F_s = 1$, 2, 3, and 4 kg h^{-1}, in which the recycle ratio varied each time, the effect of sulphur content on the autogenous autoclave operation was investigated. At each run, the feed slurry density and feed temperature which would give stable steady state at 190 °C were identified. All simulations were performed with the same autoclave configuration, $C_f = 2$. In Figure 6.10, the effect of sulphur content on the feed temperature is illustrated for different flow rates of concentrate[5]. From examining Fig. 6.10, two regions can be distinguished—the truly autogenous and the pseudo-autogenous region[6]. The first corresponds to S content higher than 5 wt.% while the second corresponds to less than 5 wt.%. Magnification of the pseudo-autogenous region is shown in Figure 6.11.

According to these results, the higher the concentrate flow rate the higher the feed temperature must be at a fixed sulphur content. This is so, because as the flow rate increases the residence time decreases, having as a result lower sulphur conversion and less heat evolution, which in turn is insufficient to raise the temperature to 190 °C. The result is that feed preheating becomes necessary to compensate for the lower heat generation. It appears, therefore, that when the S content is maintained high enough ($>$ 5 wt.%) there is no problem with respect to autothermal operation. Furthermore, the higher the S content the lower the slurry density must be, and vice versa, as illustrated in Figure 6.12. By lowering the solids concentration, a larger heat sink is

---

[5] It is clarified that the F_s values refer to the concentrate of Table 5.II and not to the total flow of solids entering the reactor. Therefore, a fixed F_s value does not necessarily correspond to a fixed residence time. F_s and $\bar{t}$ can only be correlated at the same sulphur content (or equivalently at the same R_R). The flow rate of solids is always higher than F_s, depending on the recycle ratio, unless $R_R = 0$. Thus, the higher the F_s, the higher the operating capacity of the autoclave (higher throughput).

[6] The term "truly autogenous" is used here to define the situation where no feed preheating is required (i.e. $T_0 = 30$ °C) to achieve stable steady state at the target temperature (190 °C). In the same way, the term "pseudo-autogenous" is used to define the situation where feed preheating is necessary.

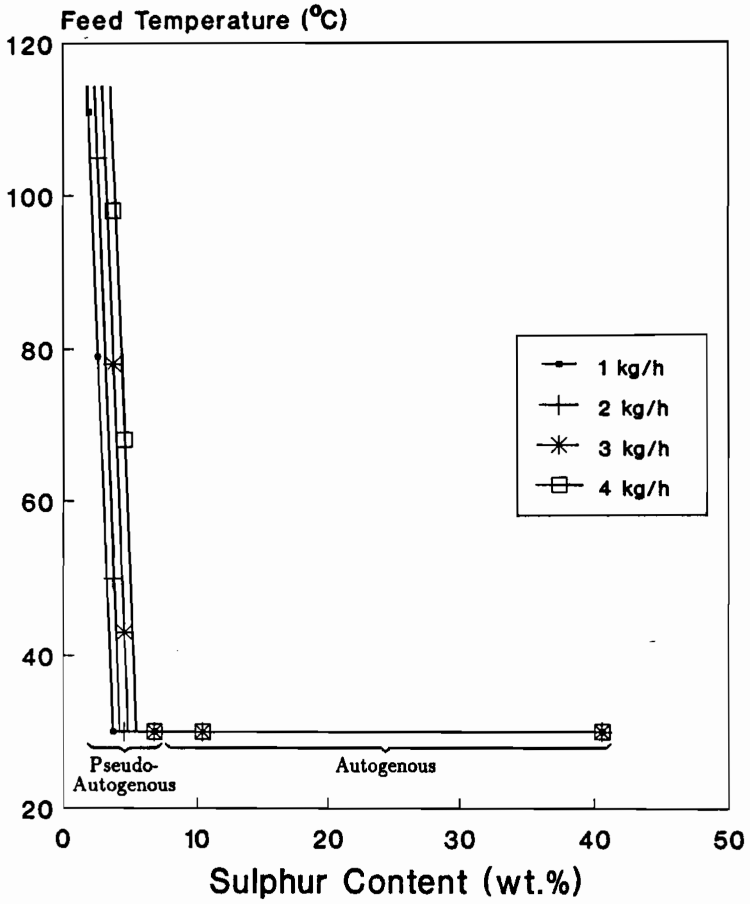

Figure 6.10: Feed temperature versus sulphur content at different concentrate flow rates for steady state operation at 190 °C.

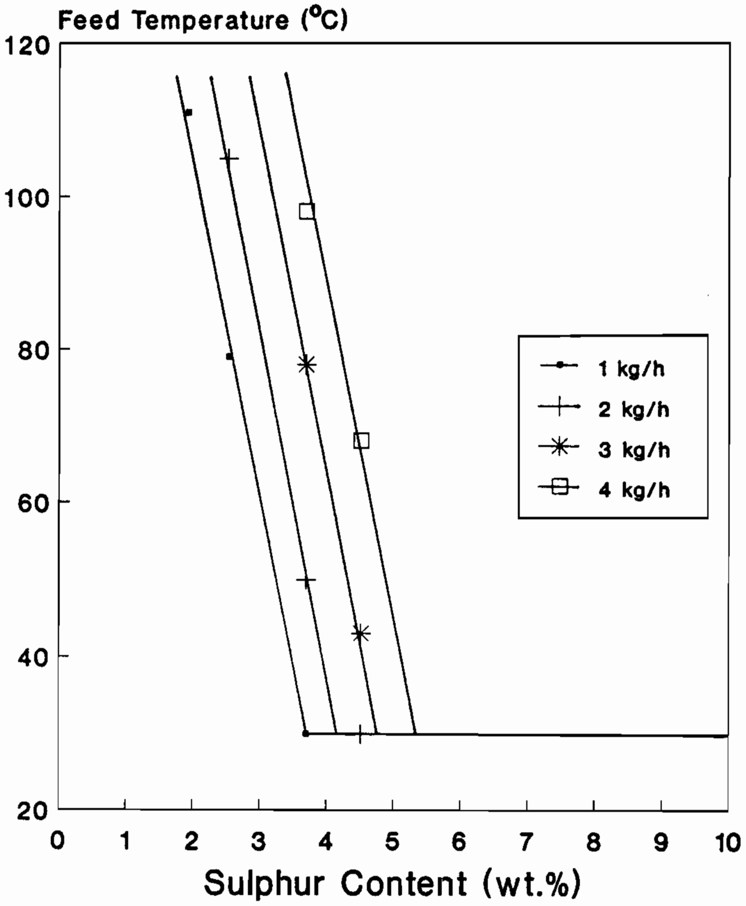

Figure 6.11: Magnification of the pseudo-autogenous region of Fig. 6.10. Feed temperature versus sulphur content for steady state operation at 190 °C.

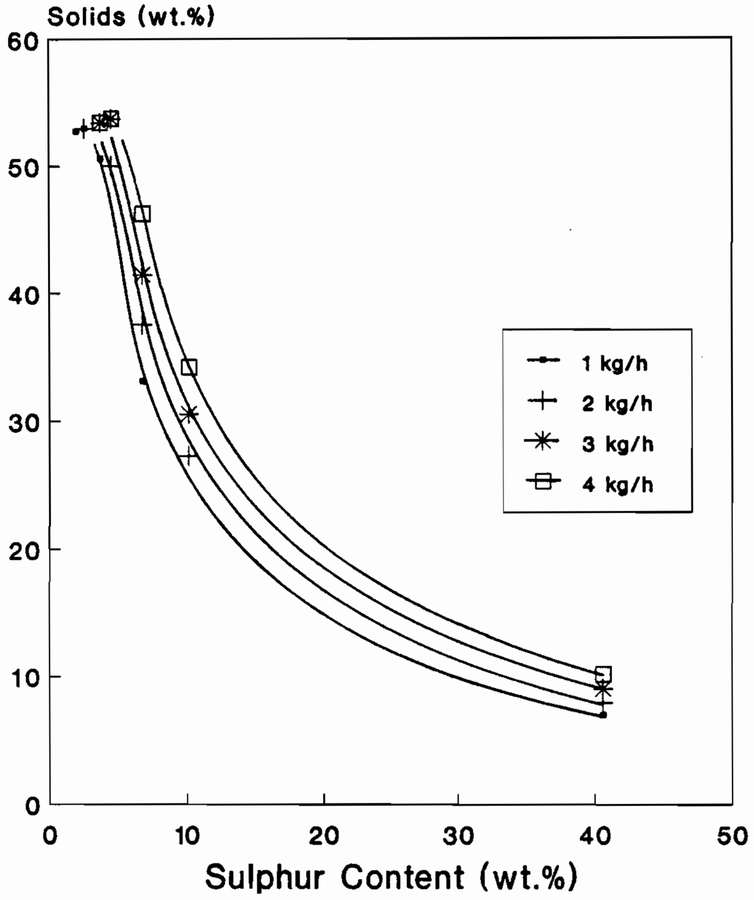

Figure 6.12: Percent solids in slurry versus sulphur content at different concentrate flow rates for steady state operation at 190 °C.

created (that of water) capable to absorb the large quantities of heat generation by the oxidation of the rich-in-sulphur feed. However, in the pseudo-autogenous region (S content $< 5\%$), the slurry density cannot be further adjusted. These poor-in-sulphur feeds require high slurry densities in order to provide the necessary sulphur (the "fuel") for sufficient heat generation, and limited cooling to allow for adequate temperature increase. The maximum slurry densities shown in the top-left corner of Fig. 6.12, correspond to those resulting from mixing the concentrate (at 73 wt.%) with inert solids (at 52 wt.%) at high R_R values without any water addition ($W_R = 0$) at all. Hence, the maximum approaches the inert solids concentration value (i.e. 52%). Since the slurry density cannot be further increased in this region, feed preheating becomes necessary. Finally, it is also shown in Fig. 6.12 that by increasing the flow rate of concentrate, higher blend solids concentration is required (at a given S content) due to the shortening of residence time.

Achieving autogenous operation with minimal preheating is not a sufficient issue by itself alone. Maximization of conversion to ensure full liberation of the locked gold values is equally important. Thus, in Figure 6.13 overall S conversion achievable at the exit of the autoclave is plotted against S content. Evidently, higher flow rates of concentrate result in lower conversion levels due to lower residence times[7]. The latter is demonstrated in Figure 6.14. At this point it is useful to remember that the total mean residence time is the sum of the mean residence times experienced by solids in each compartment. The variable water injection quantities, dictated by the cooling needs of each compartment, change the residence time of the solids from one compartment to the other. That is why residence times shown in Fig. 6.14 are not

---

[7] It appears that the particular reactor can treat autogenously concentrate at a flow rate of 3 kg h^{-1}, 50% above the average 2 kg h^{-1} level adopted by Sherritt Gordon Ltd. In this case, the sulphur content must increase to 10% (by employing $R_R = 3$) to achieve 98% sulphur conversion. However, this might not be acceptable for considerations other than the attainment of autothermal operation. For example, increasing the S content can lead to sulphur agglomeration problems and effectively seize the mineral oxidation process [6.7]. Therefore, a S content value offering the best compromise between these two opposing restrictions has ultimately to be chosen. The 5 to 7% S content recommended by Sherritt to satisfy these process requirements is in good agreement with the model predictions of this work.

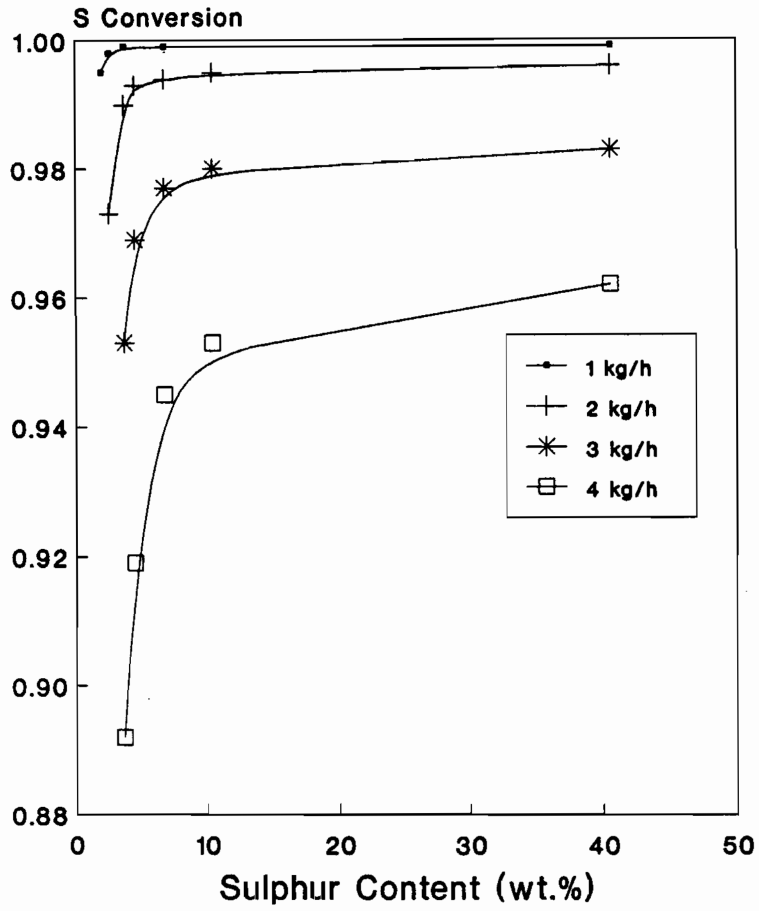

Figure 6.13: Overall sulphur conversion versus sulphur content at different concentrate flow rates for steady state operation at 190 °C.

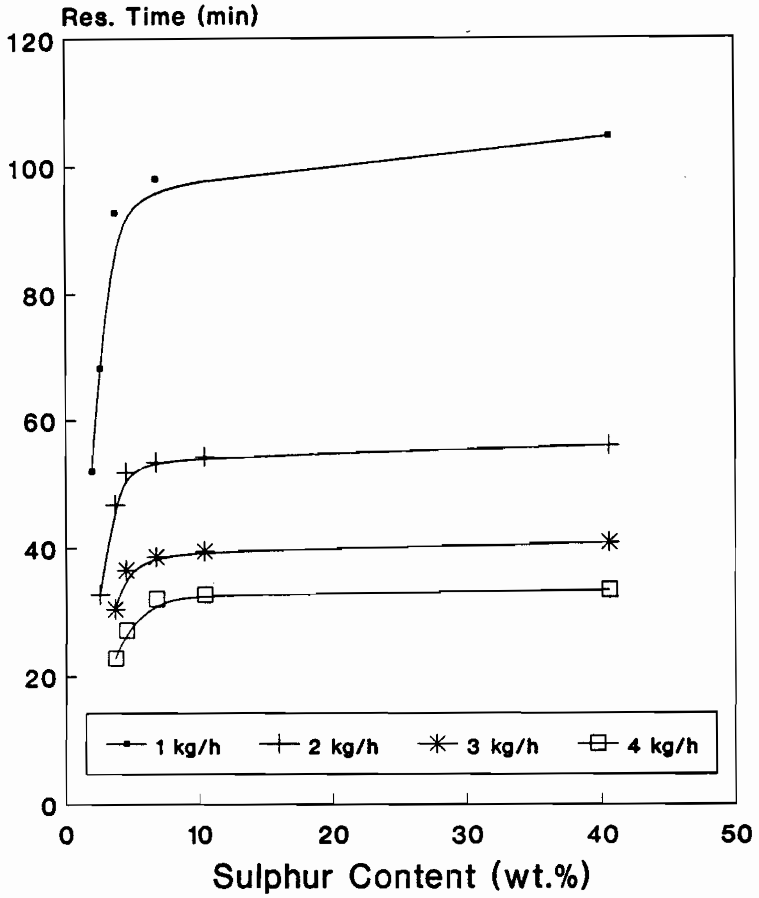

Figure 6.14: Total mean residence time versus sulphur content at different concentrate flow rates for steady state operation at 190 °C.

directly proportional to the concentrate flow rates. In the truly autogenous region $\bar{t}$ remains constant regardless of the S content. The following explanation is offered for this. Dilution of the blend solids to a particular slurry density level (see Fig. 6.12) necessary to yield autogenous operation fixes $\bar{t}$ to a constant value (for a specific F_s). That is, at constant F_s, the flow rate of blend solids increases as we move from right (high S content value) to left (low S content value) on the horizontal axis in Fig. 6.14. But the amount of water added (W_R) to fix the feed slurry density decreases so that the residence time remains almost constant in this region. As we move beyond the points of maximum permissible slurry density (see Fig. 6.12) the residence time is not maintained constant (since W_R remains constant at zero), and sharply decreases thus yielding low overall S conversion.

In conclusion, process analysis using the simulation results of Figures 6.10 to 6.14 offers a valuable means to identify *a priori* feed conditions for attaining autogenous reactor operation. Despite the fact that the above simulations were performed for a fixed reactor volume (26 L), the results are equally valid for different reactor volumes as well, as long as the concentrate flow rates follow proportionally the variation in reactor volume. It is recognized, however, that for large scale-up factors caution should be exercised since the gas–liquid transfer characteristics of the reactor change.

On the Number and Size of Autoclave Compartments

By keeping the reactor volume constant and varying the number of compartments, L, another series of simulations were executed (at otherwise "standard" feed conditions). The objective here was to assess the effect of autoclave division into several equal-size compartments, on the autogenous reactor performance. The results obtained are summarized in Table 6.V. The second and third column of Table 6.V refer to the final sulphur conversion and total residence time for the whole autoclave respectively. The fourth and fifth column refer to the feed slurry density and water addition ratio in

Table 6.V: Effect of autoclave division into equal-size compartments on the autogenous reactor performance (Model Version 4; C_f=1).

L	$\bar{x}_S$	$\bar{t}$ (min)	$\hat{w}$ (wt.%)	W_R
1	0.897	51.2	31.8	1.58
2	0.966	52.5	34.6	1.27
4	0.991	54.1	40.6	0.76
6	0.996	54.9	46.2	0.40

the first compartment respectively. In all cases, stable autogenous operation at 190 °C was attained without feed preheating. By viewing the $\bar{x}_S$ column, the well known beneficial effect of employing a multi-stage continuous reactor is immediately seen. Sulphur conversion increases with increasing L. The total residence time slightly increases with increasing L, but this is due to a parallel decrease in total inter-stage water injection, which controls the temperature at 190 °C. That is, the greater the number of compartments, the less inter-stage cooling requirements and the longer the $\bar{t}$. At the same time, with increasing autoclave division into several compartments, the mean residence time in the first compartment decreases. The latter, as has already been explained, is of crucial importance since it determines the degree of heat liberation and thus, the autothermal initialization of the process. As a consequence, more concentrated feed slurry is required (or equivalently, less water dilution factors), as seen from the last two columns of Table 6.V. The results of Table 6.V suggest that a four-stage autoclave is sufficient for complete and autogenous S oxidation. four-stage autoclaves have been employed [6.11] or proposed [6.12] in the industry for the treatment of refractory gold ores or concentrates.

The effect of autoclave division and configuration on reactor performance at increased throughput is demonstrated in Table 6.VI. Thus, an increase in F_s from 2 (Table 6.V) to 3 kg h^{-1} (Table 6.VI) results in 97% sulphur conversion (a 2% drop) in a four-stage autoclave without a need for feed preheating. On the other hand, a six-stage autoclave can only exhibit the same performance at 3 kg h^{-1} as the

Table 6.VI: Effect of autoclave division and configuration on reactor performance at increased throughput (Model Version 4; F_s=3 kg h^{-1}).

L	C_f	T_0 (°C)	$\bar{x}_S$	$\bar{t}$ (min)	$\hat{w}$ (wt.%)	W_R
4	1	30	0.970	40.1	46.8	0.37
6	1	40	0.979	41.1	54.6	0.00
5	2	30	0.977	38.6	41.6	0.70

four-stage autoclave if a moderate feed preheating to 40 °C is employed (yielding a final S conversion of 98%). This is due to the very short residence time in the first compartment of the six-stage autoclave. It is worth of note that under the conditions of Table 6.VI a six-stage autoclave operates at the limit of its truly autogenous region, as seen by viewing the zero value of water addition in the first compartment in Table 6.VI. By doubling the size of the first compartment and having a five-stage autoclave instead, increased throughput can be tolerated more easily since no preheating at all is required. It appears that the 5-compartment/C_f = 2 configuration is the best overall.

On the Size of the Reacting Particles

The final series of simulation runs is aimed at analyzing the size distribution of the reacting particles. This is demonstrated here only for FeS_2 particles. The behaviour of $FeAsS$ particles is very similar. The evolution of the size distribution (mass-PSD) of the reacting particles along the 5-compartment autoclave is illustrated in Figure 6.15 (feed particles having size parameters μ = 21 μm and c = 16.5; see Table 5.II). These results correspond to the "standard" feed conditions of Table 5.III and the operating conditions of Table 6.III. Figure 6.15 shows that the median of the distribution shifts towards smaller values when the solids pass from one compartment to the next, which implies that the material becomes increasingly fine. This behaviour was also observed in Chapter 5 when model Version 2 was employed (Figure 5.11).

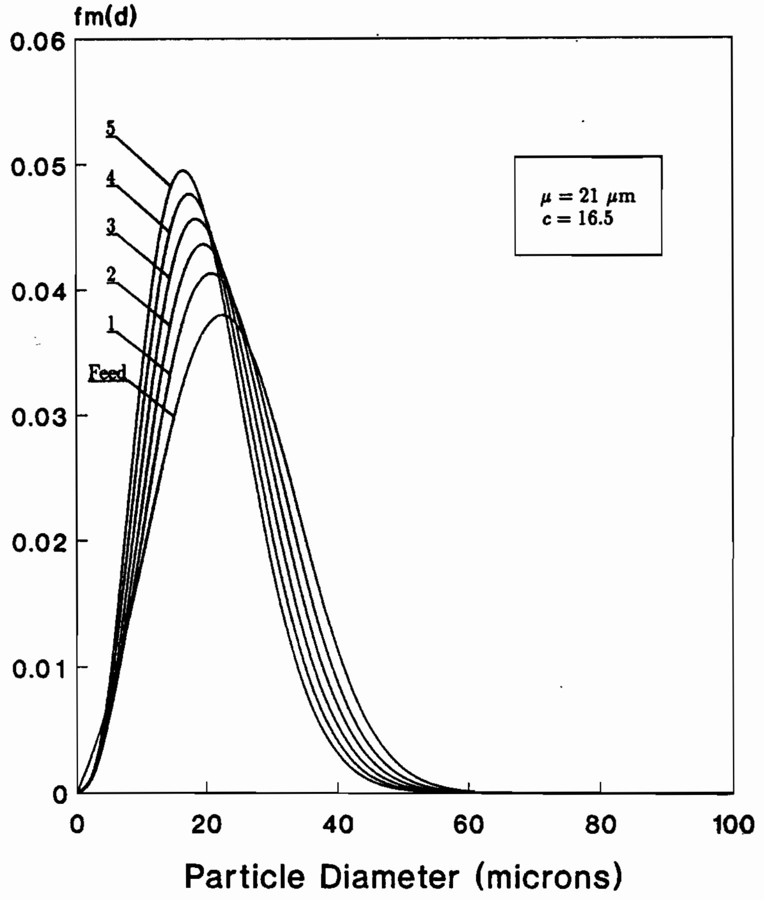

Figure 6.15: Particle size mass density functions of FeS_2 particles in the feed and at the exit of each compartment. (Conditions: Table 6.III.)

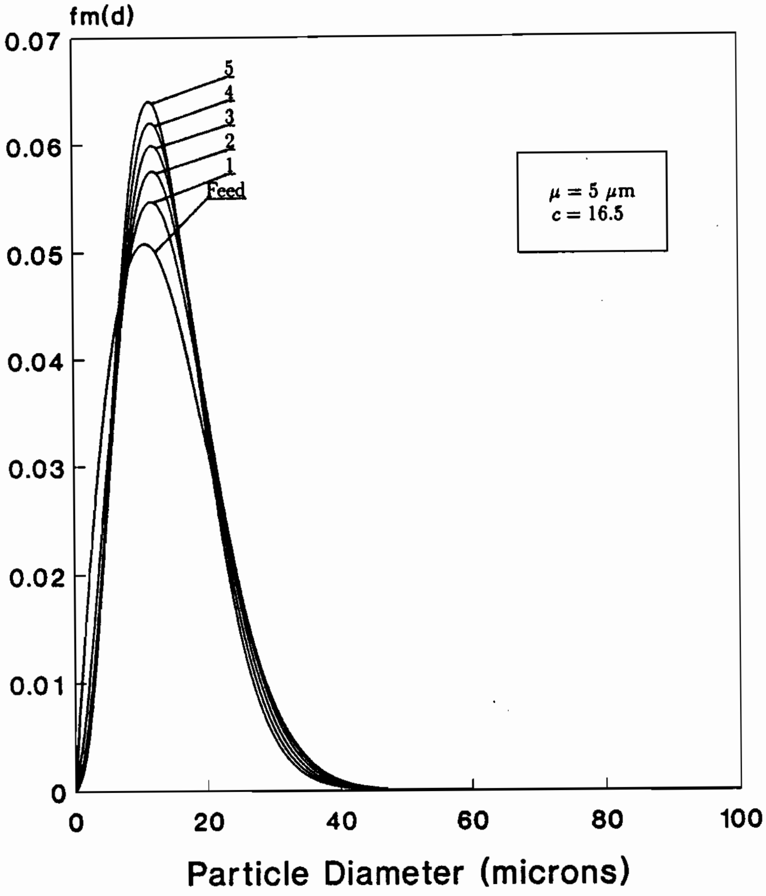

Figure 6.16: Particle size mass density functions of FeS_2 particles in the feed and at the exit of each compartment ($\mu = 5\ \mu$m).

However, this trend of obtaining increasingly fine material as we move from one compartment to the next does not hold always. The evolution of the size distribution depends on the median and the spread of the starting material. Thus, if the feed to the autoclave becomes very fine with $\mu = 5\ \mu$m (and $c = 16.5$), then the shift of the median of the distribution is reversed as shown in Figure 6.16. In this case, the average size of the reacting particles becomes coarser, due to the very fast disappearance of the fines which are now abundant. The feed distribution in Fig. 6.16 corresponds to 99.9% –44 μm, and yields a final S conversion of 99.8%. The same material necessitates a slightly less concentrated slurry in order to be processed autogenously (35 wt.% solids at $\mu = 5\ \mu$m, versus 38 wt.% at $\mu = 21\ \mu$m). With substantially coarser feed having $\mu = 50\ \mu$m (and $c = 16.5$) the mean particle size decreases in a more drastic fashion. The distributions are shown in Figure 6.17. This material requires

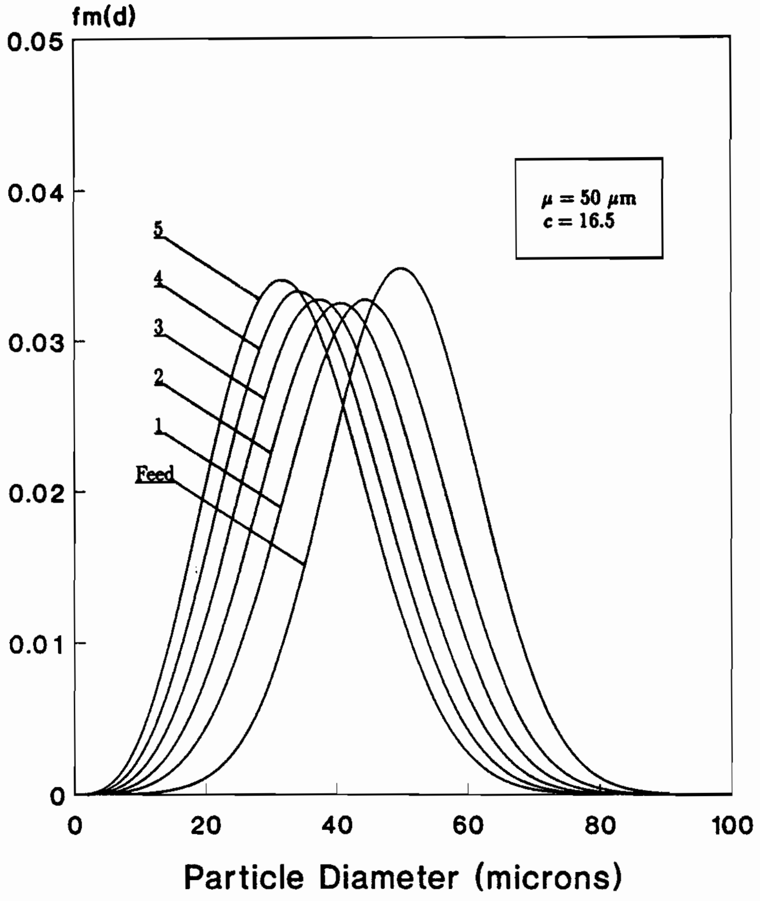

Figure 6.17: Particle size mass density functions of FeS_2 particles in the feed and at the exit of each compartment (μ = 50 μm).

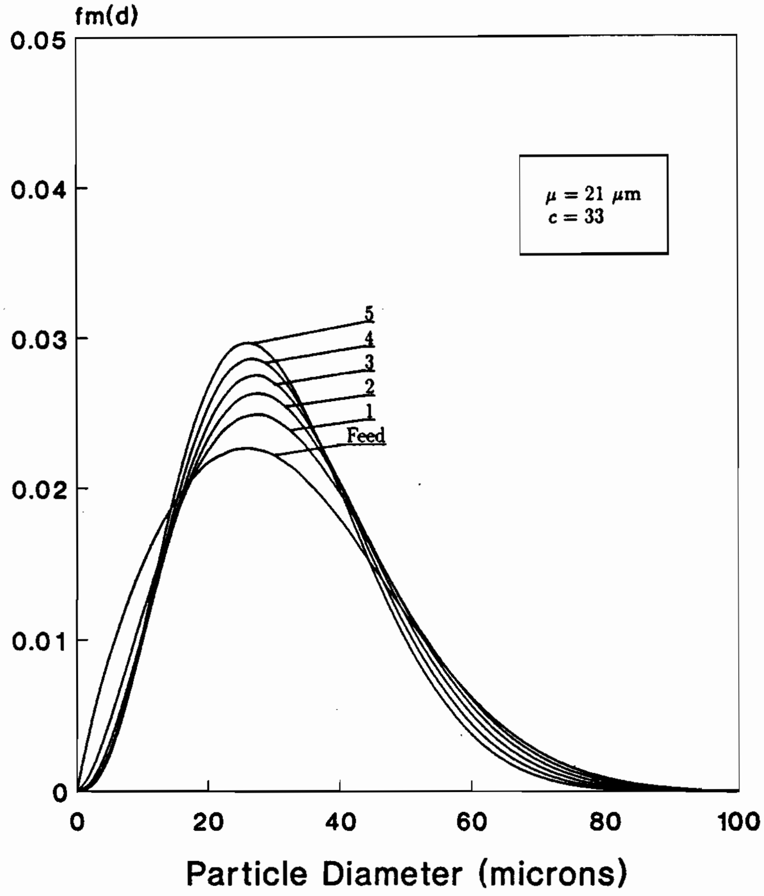

Figure 6.18: Particle size mass density functions of FeS_2 particles in the feed and at the exit of each compartment ($\mu = 21$ μm, $c = 33$).

preheating to 65 °C if it is to be processed at a slurry density 38 wt.% at which a final S conversion of 95.5% is obtained. It can be processed, though, autogenously (without preheating) if a slurry density of 42.6 wt.% is employed, in which case the final S conversion is 96.8%. The size distribution of this material corresponds to 30% –44 μm. Sherritt Gordon Ltd. suggests that the concentrate must be around 96% –44 μm to ensure rapid oxidation and to achieve high S conversion. Finally, simulation of a concentrate with a spread value of $c = 33$ is shown in Figure 6.18. This material corresponds to 76.7% –44 μm and yields 98.4 S conversion. It is interesting to observe in this case that the median initially shifts to higher and then to lower particle sizes, but on the average it remains almost constant. Fully autogenous oxidation of this material is achieved at a feed slurry density of 39%.

6.5 Summary

The mathematical description of the continuous multi-stage pressure oxidation process has been further refined by accounting for simultaneous surface reaction and gas transfer kinetics. Formulation of the "mixed" control kinetics has been achieved by performing an oxygen mass balance where the volumetric mass transfer coefficient serves as an adjustable parameter. Simulation runs at which the partial oxygen pressure was kept constant at any possible operating temperature failed to yield a stable steady state within the target temperature range of 180 to 200 °C. However, simulation runs at which the total pressure (i.e. oxygen plus water vapour pressure) was kept constant were successful in predicting stable and autogenous reactor performance. In particular, application of the model to the pilot plant test data of the Olympias concentrate that have been reported by Sherritt Gordon Ltd. showed good agreement between model predictions and plant measurements. The results indicate that the reactor operation under constant total pressure offers enhanced thermal and kinetic stability.

The inter-relations of some key process variables and their effect in attaining autogenous and complete sulphur oxidation has been investigated by scanning a range of alternative feed conditions and reactor configurations. More specifically, the effect of sulphur content, slurry density, feed rate, reactor division and compartment size, as well as particle size, on the autothermal and stable reactor performance have been quantitatively assessed. The combined sulphur/arsenic content is of critical importance in determining the feasibility of obtaining autogenous operation with a given feed material. The results have also revealed that fully autogenous operation can be achieved when the sulphur content of the feed is more than 5 wt.%. Otherwise, feed preheating is required the extent of which depends on reactor throughput. Furthermore, division of a horizontal autoclave into four rather than six compartments appears to be better from the stand point of attaining autothermal operation (although some loss in final conversion must be expected in this case). However, a five-compartment autoclave having the first compartment double in size than the rest offers overall the best performance in terms of autothermal operation, final conversion, and throughput.

References

[6.1] T-P. I and G.H. Nancollas, *Anal. Chem.*, 44(12), 1940 (1972).

[6.2] H.O. Hartley, *Technometrics*, 3(2), 269 (1961).

[6.3] R.F. Prini and R. Crovetto, *J. Phys. Chem. Ref. Data*, 18(3), 1231 (1989).

[6.4] K. Denbigh, *The Principles of Chemical Equilibrium*, 4-th ed., p. 229, Cambridge Univ. Press, Great Britain (1981).

[6.5] H. Oguz, A. Brehm and W.-D. Dechwer, *Chem. Eng. Sci.*, 42(7), 1815 (1987).

[6.6] D.B. Mills, R. Bar and D.J. Kirwan, *AIChE J.*, 33(9), 1542 (1987).

[6.7] D.R. Weir and R.M.G.S. Berezowsky, *Intl Symposium on Gold Metallurgy* (ed. by R.S Salter, D.M. Wyslowzyl and G.N. McDonald), 26-th Ann. Conf. Metall., p. 247, CIM, Winnipeg, Manitoba (1987).

[6.8] M.J. Collins, R.M.G.S. Berezowsky and D.R. Weir, *Arsenic Metallurgy: Fundamentals and Applications*, (ed. by R.G. Reddy, J.L. Hendrix and P.B. Queneau), pp. 115–133, TMS-AIME, Warrendale PA (1988).

[6.9] D.R. Weir, J.A. King and P.C. Robinson, *Min. and Metall. Proc.*, 3(4), 201 (1986).

[6.10] R.C. Weast, *Handbook of Chemistry and Physics*, 66th ed., CRC Press, p. D-190 (1985–86).

[6.11] P.G. Mason and R.F. Nanna, *Precious Metals '89* (ed. by M.C. Jha and S.D. Hill) pp. 3–12, TMS-AIME, Warrendale PA (1989).

[6.12] G.D. Hallett, W.F. Luinstra and R.W. Stanley, *Precious Metals 1990* (ed. by D.A. Corrigan), pp. 105–118, IPMI, Allentown PA (1990).

Chapter 7

Synopsis

7.1 Introduction

In this chapter conclusions, arising from a global stand point, are highlighted. In addition, original contributions made to knowledge are identified and ideas for future research are offered.

7.2 Conclusions

Foremost, it has been demonstrated how individual particle heterogenous reaction kinetics can be combined with mathematical descriptions of reactor performance in order to form reactor models suitable for process modelling. In particular, models were developed to describe strongly exothermic and complex pressure leaching reactions conducted in batch and/or continuous stirred tank reactors. The process modelled was the pressure oxidation of refractory pyritic gold materials. However, the modelling strategy followed in this work is based on fundamental concepts and thus is not simply limited to the above process system but is equally applicable to other heterogenous and exothermic leaching systems as well. For its application the individual mineral kinetics and the mass transfer characteristics of the reactor have to be known in advance.

The central goal was, first, to mathematically describe the steady state non-isothermal performance of a series of continuous reactors charged with reacting particulate minerals. This was followed by the execution of a series of computer-aided simulation runs using the model in order to identify conditions for autogenous operation. The latter mode of operation is the preferred one since it allows for the full utilization of the thermal energy of the system. "En route" towards reaching this goal several components of the work were analyzed and studied separately before being synthesized into a comprehensive model. Initially, the intrinsic pressure oxidation kinetics of arsenopyrite and pyrite (the two principal refractory gold carriers) were identified. This laboratory study revealed the following:

- Upon high temperature (130 to 180 °C) pressure oxidation (2 to 20 atm) of arsenopyrite the following major reaction products are obtained: $Fe(II)$, $Fe(III)$, $As(V)$, $S(VI)$, and $FeAsO_4 \cdot 2H_2O$ (scorodite). The reaction sequence involves first, the formation of $Fe(II)$ which is then oxidized to $Fe(III)$. Subsequently, trivalent iron combines with arsenate ions to form scorodite precipitate. A minor but important oxidation product is elemental sulphur. The latter, however, does not interfere with the progress of the heterogeneous reaction.

- The surface reaction control–shrinking core model was adequate in describing the pressure oxidation kinetics of both triclinic and monoclinic arsenopyrite. The dependence of the apparent rate constant on temperature (E_A = 66 to 72 kJ mol^{-1}), oxygen pressure (first order), and particle size (k_S vs $1/\bar{r}_0$ linear) were in agreement with the above kinetic model.

- The true rate determining step is probably electrochemical in nature involving the first electron transfer during reduction of the surface-adsorbed oxygen.

- The pressure oxidation kinetics of pyrite were also found to follow the shrinking core model with surface reaction being the rate controlling step within the temperature range of 140 to 180 °C and 5 to 20 atm partial oxygen pressure.

However the reaction proceeds to completion only at temperatures exceeding 160 °C as elemental sulphur product layers seem to form at lower temperature and effectively block the surface reaction.

- The overall complex kinetic behaviour of pyrite is reflected in an activation energy shift at 160 °C (from 46.2 to 110.5 kJ mol^{-1}) and a reaction order change (from 1 to 0.5) depending on pressure and temperature. Thus, at 150 °C first order dependence prevails in the range of 5 to 20 atm, while at 170 °C and for pressures exceeding 10 atm fractional order is observed.

Having established the pertinent rate laws which govern the pressure oxidation kinetics of arsenopyrite and pyrite, reactor models were built to simulate the isothermal, and non-isothermal performance of single-stage reactors (batch, and continuous at steady state). The heat and mass balance equations were coupled and solved simultaneously. At this stage of model development, the pressure oxidation of wide size arsenopyrite particulates was considered in a consecutive reaction scheme involving the oxidation of $FeAsS$, followed by the oxidation of $Fe(II)$ to $Fe(III)$, followed by the instantaneous precipitation of scorodite. The size distribution of the particulate mineral was described by a discrete function and the heterogeneous oxidation was assumed to be governed by surface reaction kinetics. The results showed that:

- There was very good agreement between the bench-scale experimental data and model prediction, not only in terms of mineral conversion but also in terms of product distribution.
- Unusually high mineral conversions ($> 85\%$) were obtained with the single-stage continuous reactor operating at steady state. This was attributed to the surface reaction rate limiting regime assumed to control the process.

The model was subsequently extended to describe a multi-stage continuous reactor operating under surface reaction control or gas–liquid mass transfer control in order to simulate the performance of industrial reactors. The gas–liquid dissolution rate of oxygen was taken into account in order to address possible gas transfer limitations. The process was assumed to be controlled by gas to liquid transfer kinetics whenever the predicted O_2 consumption rates exceeded the mass transfer capacity of the reactor. A mixture of two minerals, namely pyrite and arsenopyrite was considered as feed. The size distribution of the particulate minerals was described in terms of continuous functions. The system chosen for the application of the model was the continuous piloting of a rich in $FeS_2/FeAsS$ industrial concentrate, namely the Olympias concentrate. This modelling effort showed that:

- The multi-stage analysis had to be performed stage by stage. Thus, the size distribution of the reacted particles at the exit of each reactor stage was calculated each time since this material constitutes the feed to the next compartment.
- Mass transfer limitations slow down the oxidation process which in turn slows the rate of heat release thereby permitting stable operation of the first reactor stage within the desired temperature range (180 to 200 °C).
- The size of the first reactor stage is of critical importance to the thermal economy of the process. By having the first stage substantially bigger in size than the subsequent stages, autogenous operation with minimal preheating and cooling requirements is achieved.
- The conversion levels and feeding conditions predicted by the model were found to be in good agreement with pilot-plant test data published in an independent industrial study.

Further refinement of the model was achieved by considering the oxidation kinetics to be controlled simultaneously by both oxygen mass transfer and surface reaction. This model was used to simulate alternative operational schemes and to analyze the effect of some key process variables. The results showed that:

- Enhanced reactor stability is obtained when the reactor operates under constant total pressure (oxygen and water vapour) rather than constant oxygen pressure.
- To attain a truly autogenous operation (i.e. without any feed preheating requirements) a minimum level (5 wt.%) of sulphur (and arsenic) content in the feed is needed. This finding is in total agreement with industrial observations. For materials with lower $S + As$ content, feed preheating becomes inevitable.
- A four-stage equal-size reactor appears to give better performance than a six-stage reactor of equal volume, when it comes to autogenous processing of a low-in-sulphur feed at high flow rate. Nevertheless, a five-stage reactor having the first stage double in size offers the additional advantage of tolerating even higher throughput under truly autogenous operation.
- Depending on the feed size distribution, the reacting particles become coarser or finer as they advance from one stage to the other in the reactor cascade.

7.3 Claims to Originality

In the author's opinion, the following are the most important contributions made to original knowledge as a result of the experimental and theoretical work presented in this thesis.

1. The **pressure oxidation chemistry and kinetics of arsenopyrite** were experimentally studied and identified for the first time. An appropriate heterogenous rate equation was formulated.
2. The rate law which governs the **high temperature** (above 130 °C) **pressure oxidation of pyrite** was also determined for the first time.
3. The **mathematical description** of the **non-isothermal** operation of a **multi-stage three-phase continuous reactor** charged with **reacting solids** is considered original.

4. The **mathematical description** of the non-isothermal operation of a multi-stage continuous reactor charged with a **mixture of two widely sized particulate minerals** following **continuous particle size distribution functions** is original.

5. The development of mathematical expressions describing the **exit size distribution** of particles reacting under **surface reaction control** kinetics in a continuous reactor, on the basis of the **feed size distribution** and the **residence time distribution** has not been previously reported.

6. The **mathematical modelling of the pressure oxidation process** on the basis of fundamental principles was described for the first time.

7. The **linkage** of the macroscopic gas-liquid mass transfer rate with the **individual particle kinetics** to describe the dissolution of **reacting particles** is considered novel.

8. The mathematical description of the **"mixed" control** kinetic regime for a gas–liquid–solid reaction scheme with **reacting particles** in a **CSTR** is original.

7.4 Recommendations for Future Work

The following points summarize the directions and define the areas where future work can be pursued.

1. Further verification of the prediction power of the model by comparing model predictions with detailed pilot plant data. This will add to confidence in the model and at the same time will identify areas that require further improvement. The latter is essential if the model is to become a real process simulator.

2. A sensitivity analysis is recommended in order to reveal which variables and/or model components mostly affect the model predictions. This will not only

serve as a means to determine the directions of model refinement from a mathematical description point of view, but will possibly reveal the most important physicochemical variables that influence the process as well.

3. The transformation of the developed model equations into non-dimensional form is highly desirable in order to render the model less system specific. This will improve the model universality and facilitate the exploration of a wider range of conditions and alternative operational schemes.

4. Proper kinetic studies of other sulphide and arsenide minerals (i.e. pyrrhotite, realgar, orpiment, etc.) which are usually present in refractory ore deposits and concentrates will permit the reactor simulation of various types of mixed mineral materials. By "proper" it is meant that the effect of particle size must be clearly identified during the course of a such kinetic study, as well as the effects of temperature, oxygen pressure, and acid concentration.

5. Incorporating into the reaction scheme the hydrolytic precipitation of iron and iron-arsenate compounds would expand the usefulness of the model. By predicting the extent of iron and arsenic precipitation, *a priori* decisions can be made as to the direction the operating condition should be modified in order to promote as much arsenic and iron precipitation as possible into the autoclave, thus minimizing subsequent neutralization demands. This necessitates the study of precipitation kinetics and high temperature solubilities of the various precipitating compounds. Preliminary theoretical work has already been conducted by the present author (but not included in this thesis), with the object of predicting the high temperature solubilities of Fe_2O_3 and $FeAsO_4{\cdot}2H_2O$ in H_2SO_4–H_3AsO_4–$Fe_2(SO_4)_3$–$FeSO_4$ solutions.

6. The study of the transient reactor behaviour is of great interest because it will provide accurate information with respect to the "time" stability of the steady state predictions. But most important, the time dependence formulation of the

model will frame the route towards dynamic simulation and process control.

7. It is of interest to extend the model to other multi-stage systems in order to test its applicability and universality.
8. It is also interesting to utilize the model for process optimization through the "Dynamic Programming" method. The latter is mostly applicable to staged processes like the pressure oxidation process described in this thesis.

Appendix A

Calculation of Particle Surface Temperature

For the calculation of particle surface temperature, quasi-steady state is assumed where the heat generated by the reacting particle is taken to be equal to the heat removed from the particle [3.56]

$$hS(T_s - T_b) = \bar{r}S(-\Delta H) \tag{A.1}$$

where:

h is the heat transfer coefficient

S is the particle surface

$\bar{r}$ is the rate of reaction 3.25

ΔH is the enthalpy change of reaction 3.25.

The heat transfer coefficient is estimated from the empirical correlation A.2 [3.78], which is valid for heat transfer by forced convection around submerged spheres:

$$\mathrm{Nu} = 2.0 + 0.6\mathrm{Re}^{\frac{1}{2}}\mathrm{Pr}^{\frac{1}{3}} \tag{A.2}$$

where:

Nu is the Nusselt number $(= \frac{hd}{\hat{k}_f})$

Re is the Reynolds number $(= \frac{du_\infty \rho_f}{\tilde{\mu}_f})$

Pr is the Prandtl number $(= \frac{c_p\bar{\mu}}{\hat{k}})$

d is the particle diameter

$\hat{k}$ is the thermal conductivity of water

u_∞ is the velocity of water relative to particle

ρ is the density of water

$\tilde{\mu}$ is the viscosity of water

c_p is the heat capacity of water.

Subscript "f" refers to properties at the "film temperature" $T_f = \frac{T_b+T_s}{2}$.

If the break in the Arrhenius plot of Fig. 3.30 is to be attributed solely to the surface temperature difference, then at $T_b = 180$ °C it can be estimated from Fig. 3.30 that T_s should be around 210 °C assuming that E_A retains its value of 46.2 kJ mol^{-1} for the whole temperature range. Therefore T_f should have a value of 195 °C (or 468 K).

The minimum value of u_∞ necessary to have particles in suspension corresponds to the free settling velocity [3.79] which can be estimated from correlations between friction factors ($\hat{f}$) and Re values for flow around spheres [3.78]

$$\hat{f} = \frac{4}{3}\frac{gd}{u_\infty^2}(\frac{\rho_s - \rho}{\rho}) \tag{A.3}$$

where:

g is the acceleration of gravity

ρ_s is the density of the solid particle.

On the other hand, $\hat{f}$ is an empirical function of Re

$$\hat{f} = \mathcal{F}(\mathrm{Re}) \tag{A.4}$$

which is given in Fig. 6.3–1 in ref. [3.78]. Taking into account that $g = 980$ cm s^{-1}, $\rho = 0.9$ g cm^{-3} at 195 °C (estimated from [3.77]), $\rho_s = 5$ g cm^{-3} (from [3.77]), $d = 63 \cdot 10^{-4}$ cm (geometric mean particle diameter of the fraction –74 +53 μm) and solving eq. A.3 and A.4 for Re it is found that Re = 4.

Finally, taking $c_p = 1$ cal g^{-1} °C^{-1}, $\tilde{\mu} = 0.13 \cdot 10^{-2}$ p at 195 °C (estimated from [3.77]) and $\hat{k} = 1.58 \cdot 10^{-3}$ cal s^{-1} cm^{-1} °C^{-1} at 197 °C (from [3.77]), it follows that Pr = 0.823. Consequently, Nu, which is found from eq. A.2, has a value of 3.12 and from that the heat transfer coefficient h is calculated to be 0.78 cal cm^{-2} s^{-1} °C^{-1}, or equivalently 196.7 J cm^{-2} min^{-1} °C^{-1}. Furthermore, the enthalpy change of reaction 3.25 at 195 °C which was calculated with the aid of F*A*C*T [3.17], has a value of $\Delta H^\circ_{468} = -2896.2$ kJ. The rate of reaction 3.25 is given by

$$\bar{r} = -\frac{1}{2} r_{FeS_2}$$

and r_{FeS_2} is given by eq. 3.31 evaluated at 180 °C. Substitution in equation A.1 gives $T_s - T_b = 0.002$ K.

Despite the approximations and assumptions made, the outcome of this analysis suggests that the particle surface temperature is essentially the same as that of the solution and, therefore, no need for corrections in the Arrhenius plot are justified.

Appendix B

Isothermal Operation in a Series of CSTRs

B.1 Introduction

If the following conditions are met

- all reactor stages operate at the same temperature T,
- there is no feed to any intermediate stage,
- there is no water addition (injection) to any intermediate stage,

then a heat balance over the ℓ-th reactor simplifies equation 5.16 and yields:

$$-\dot{Q}_\ell = -\Delta H^\circ_{1,T} F_0 \bar{x}_\ell \prod_{i=1}^{\ell-1}(1-\bar{x}_i) \tag{B.1}$$

Furthermore, the mean conversion $\bar{x}_\ell$ can be expressed in terms of the overall conversions $\hat{x}_\ell$ and $\hat{x}_{\ell-1}$ of the series of ℓ and $\ell-1$ reactor stages respectively, as

$$\bar{x}_\ell = \frac{\hat{x}_\ell - \hat{x}_{\ell-1}}{1-\hat{x}_{\ell-1}} \tag{B.2}$$

Equation B.1 is now written with the aid of eqs 5.20 and B.2 as

$$-\dot{Q}_\ell = -\Delta H^\circ_{1,T} F_0 (\hat{x}_\ell - \hat{x}_{\ell-1}) \tag{B.3}$$

The overall conversion for the series of ℓ reactors is calculated from an equation similar to eq. 5.18, that is

$$\hat{x}_\ell = \int_{d_{0,\min}}^{d_{0,\max}} f_{\mathrm{m},0}(d_0) \int_0^\infty x(d_0, t)\hat{E}_\ell(t)\,\mathrm{d}t\,\mathrm{d}d_0 \tag{B.4}$$

In eq. B.4, the PSD of the feed replaces the PSD of the partially reacted product of the $\ell - 1$ reactor in eq. 5.18, and $\hat{E}_\ell(t)$ is the RTD for the series of ℓ stages. In other words, the cascade of ℓ reactors is considered as a single reactor with an appropriate RTD function. Simultaneous solution of eqs B.3 and B.4 for a given operating temperature, common for all stages, is now possible without having to calculate the particle size distribution at the exit of each of the preceding individual reactors. Thus, the computational effort is reduced. Assessment of the performance of the reactor cascade is, however, still made on a stage by stage basis. Each "stage" is the equivalent of all the preceding stages. At each time, the rate of heat removal $(-\dot{Q}_\ell)$ required to maintain constant temperature, as well as the overall conversion $(\hat{x}_\ell)$ of the solid phase, in the series of ℓ reactors is calculated.

Normally, the evaluation of $\hat{x}_\ell$ through the double integral of equation B.4 is performed numerically. However, depending on the complexity of the functions involved an analytical solution is also possible. An example of analytical solution for the integration of eq. B.4 with respect to time is given in the following section. The case treated involves the reaction of monosize particles under surface reaction-controlled kinetics in a cascade of L (equal volume or first stage being double in size) continuous reactors.

B.2 Analytical Solutions for the Conversion of Monosize Particles

In a cascade of L continuous reactors of equal volume, the RTD function for the ℓ stages in series $(1 \le \ell \le L)$ is given by [5.26, 5.27]

$$\hat{E}_\ell(t) = \frac{L}{(\ell-1)!}\left(\frac{Lt}{\bar{t}}\right)^{\ell-1}\frac{e^{-Lt/\bar{t}}}{\bar{t}} \tag{B.5}$$

In eq. B.5, $\bar{t}$ is the total residence time for the whole series of L reactors. The above equation is valid only if the volumetric flow rate is the same for each reactor stage i.e.

- The volume change due to reactions is negligible
- No intermediate streams are fed to the reactor series

In this case the mean residence time for each reactor is the same and equal to $\bar{t}/L$.

If monosize particles with initial size d_0 react according to the shrinking core model for surface reaction control, their conversion as a function of time (in a batch reactor) is given by

$$x(d_0, t) = \begin{cases} 1 - (1 - k_S t)^3 & \text{for} \quad 0 \le t < \frac{1}{k_S} \\ 1 & \text{for} \quad \frac{1}{k_S} \le t \end{cases} \tag{B.6}$$

where the apparent rate constant k_S is another function of d_0. According to the segregated flow model, the average conversion of a monosize feed at the exit of the ℓ-th reactor in a series of L continuous reactors is

$$\langle x_{d_0} \rangle_\ell = \int_0^\infty x(d_0, t) \hat{E}_\ell(t)\, \mathrm{d}t \tag{B.7}$$

Substituting the conversion and RTD from eqs B.6 and B.5 respectively and integrating the above equation, we obtain

$$\langle x_{d_0} \rangle_\ell = 1 - \sum_{m=0}^{\ell-1} \frac{(\ell - m + 2)!}{(\ell - m - 1)! m!} (\frac{k_S \bar{t}}{L})^{3-m} e^{-L/k_S \bar{t}} - \sum_{m=0}^{3} \frac{(\ell + m - 1)! 3!}{(\ell - 1)! m! (3 - m)!} (-\frac{k_S \bar{t}}{L})^m \tag{B.8}$$

A similar equation has been proposed by Levenspiel [5.28] and Beloglazov [5.29].

Next, a series of continuous reactors having the first stage substantially bigger in size than the rest is considered. In a cascade of L reactors, where the first has a volume φ times bigger than the rest (which are of equal volume, V_u) the RTD function is calculated as follows. The total reactor volume is given by

$$V_{\mathrm{CSTR}} = \varphi V_\mathrm{u} + (L - 1) V_\mathrm{u} \tag{B.9}$$

where V_u is the "unit" reactor volume. The total mean residence time is then

$$\bar{t} = \frac{V_{\mathrm{CSTR}}}{Q} = \frac{(L+\varphi-1)V_u}{Q} \tag{B.10}$$

Consequently, the mean residence time of the first stage is

$$\bar{t}_1 = \frac{\varphi\bar{t}}{L+\varphi-1} \tag{B.11}$$

and the mean residence time of the remaining $L-1$ stages is

$$\bar{t}_2 = \bar{t}_3 = \cdots = \bar{t}_L = \frac{\bar{t}}{L+\varphi-1} \tag{B.12}$$

The RTD function for the first stage is then

$$E_1(t) = \frac{L+\varphi-1}{\varphi\bar{t}}e^{-\frac{(L+\varphi-1)t}{\bar{t}}} \tag{B.13}$$

and for the rest $L-1$ stages

$$E_2(t) = E_3(t) = \cdots = E_L(t) = \frac{L+\varphi-1}{\bar{t}}e^{-\frac{(L+\varphi-1)t}{\bar{t}}} \tag{B.14}$$

For any intermediate stage ℓ ($1 \leq \ell \leq L$), the RTD for the series of the ℓ stages is obtained by convolution [5.30], that is

$$\hat{E}_\ell(t) = E_1 * E_2 * E_3 * \cdots * E_\ell \tag{B.15}$$

or equivalently:

$$\hat{E}_\ell(t) = \int_0^t \int_0^{\lambda_1} \int_0^{\lambda_2} \cdots \int_0^{\lambda_{\ell-2}} E_\ell(t-\lambda_1)E_{\ell-1}(\lambda_1-\lambda_2)\cdots E_1(\lambda_{\ell-1})\,\mathrm{d}\lambda_{\ell-1}\,\mathrm{d}\lambda_{\ell-2}\cdots\mathrm{d}\lambda_1 \tag{B.16}$$

Substituting eqs B.13 and B.14 in eq. B.16 and performing the integration for $\ell = 2$ we obtain

$$\hat{E}_2(t) = \frac{(L+\varphi-1)}{(\varphi-1)\bar{t}}e^{-\frac{(L+\varphi-1)t}{\bar{t}}}\left[e^{\frac{(\varphi-1)(L+\varphi-1)t}{\varphi\bar{t}}} - 1\right] \tag{B.17}$$

We can proceed in a similar manner to obtain $\hat{E}_3(t)$, $\hat{E}_4(t)$ etc. It is apparent that $\hat{E}_1(t) = E_1(t)$. If appropriate stepwise integrations are performed, the following recursive formula is obtained

$$\begin{aligned}\hat{E}_\ell(t) \quad = \quad & \frac{(L+\varphi-1)\varphi^{\ell-2}}{(\varphi-1)^{\ell-1}\bar{t}}e^{-\frac{(L+\varphi-1)t}{\bar{t}}}\Bigg\{e^{\frac{(\varphi-1)(L+\varphi-1)t}{\varphi\bar{t}}} \\ & - \sum_{m=2}^{\ell}\frac{1}{(m-2)!}\left[\frac{(L+\varphi-1)(\varphi-1)t}{\varphi\bar{t}}\right]^{m-2}\Bigg\}\end{aligned} \tag{B.18}$$

Further calculation of the exact solution for the average conversion according to eq. B.7 is tedious due to the complexity of the functions involved and numerical integration has to be employed.

Appendix C

Derivation of the Exit Particle Size Distribution for Surface Reaction Control—Shrinking Core Kinetics

C.1 Monosize Feed

C.1.1 Number-PSD Function

The size of a reacting particle decreases continuously with reaction time until the particle disappears. At that moment, the "particle" attains a size of 0 and any further increase in reaction time will not change its size. The following function, $d(d_0, t)$, gives the variation of size d with reaction time t, for a spherical particle of initial size d_0 under surface reaction control—shrinking core kinetics.

$$d(d_0, t) = \begin{cases} d_0(1 - k_S t) & \text{for} \quad 0 \le t < \frac{1}{k_S} \\ 0 & \text{for} \quad \frac{1}{k_S} \le t \end{cases} \tag{C.1}$$

The apparent heterogeneous rate constant k_S, which is inversely proportional to d_0, is given by[1]

$$k_S = \frac{b M_B k C_A}{\rho_B d_0} \tag{C.2}$$

---

[1] With reference to the general heterogeneous reaction 5.9.

The residence time distribution function[2] for a perfectly mixed continuous reactor is

$$E(t) = \frac{1}{\bar{t}} e^{-t/\bar{t}} \tag{C.3}$$

The objective here is to derive the probability density function (PDF) for the particle size, recognizing that the latter is related to residence time by the function given in eq. C.1 and the residence time has a PDF of its own, given by eq. C.3.

According to the theory of probability the PDF is the first derivative of the cumulative distribution function (CDF) [5.31]. In other words if $f(d)$ is the PDF and $F(d)$ is the CDF of the particle size, then

$$f(d) = \frac{\mathrm{d}F(d)}{\mathrm{d}d} \tag{C.4}$$

For a given particle diameter d, $F(d)$ is the probability that a particle has diameter d' less than or equal to d. If P("event") denotes the probability of a specific "event" happening, then in more rigorous terms

$$F(d) = \mathrm{P}(0 \leq d' \leq d) \tag{C.5}$$

The latter probability is further split into two components via the relation

$$\mathrm{P}(0 \leq d' \leq d) = \mathrm{P}(d' = 0) + \mathrm{P}(0 < d' \leq d) \tag{C.6}$$

Consequently, the probabilities are expressed in terms of t. To achieve this, the particle size function C.1 must be inverted. The particle diameter d' is a monotonic function of t only when $0 \leq t < 1/k_S$ (see eq. C.1), and can be inverted in this interval. It is not a monotonic function when $t \geq 1/k_S$, and cannot be inverted in $[1/k_S, \infty)$. More specifically, d' approaches 0 when t approaches $1/k_S$ (minimum reaction time required for a particle to react completely), and d' has the value of d when t has the value of $(d_0 - d)/k_S d_0$ (reaction time for a particle to attain the specified size d). Hence

$$\mathrm{P}(0 < d' \leq d) = \mathrm{P}(\frac{d_0 - d}{k_S d_0} \leq t < \frac{1}{k_S}) \tag{C.7}$$

---

[2] In pure mathematical terms, it is a probability density function.

The right hand side of eq. C.7 is equal to

$$\mathrm{P}\left(\frac{d_0-d}{k_S d_0} \le t < \frac{1}{k_S}\right) = \int_{\frac{d_0-d}{k_S d_0}}^{\frac{1}{k_S}} E(t)\,\mathrm{d}t \tag{C.8}$$

Performing the integration after substituting for $E(t)$ from eq. C.3 we obtain

$$\mathrm{P}(0 < d' \le d) = e^{-\frac{d_0-d}{\bar{t}k_S d_0}} - e^{-\frac{1}{\bar{t}k_S}} \tag{C.9}$$

Furthermore, the probability of a particle having completely reacted and, thus, having a size equal to 0, is equal to the probability of the particle staying inside the reactor vessel for a time longer or equal to $1/k_S$

$$\mathrm{P}(d' = 0) = \mathrm{P}\left(\frac{1}{k_S} \le t\right) \tag{C.10}$$

but

$$\mathrm{P}\left(\frac{1}{k_S} \le t\right) = \int_{\frac{1}{k_S}}^{\infty} E(t)\,\mathrm{d}t \tag{C.11}$$

Performing the integration

$$\mathrm{P}(d' = 0) = e^{-1/\bar{t}k_S} \tag{C.12}$$

According to relation C.6, the summation of eqs. C.9 and C.12 yields

$$\mathrm{P}(0 \le d' \le d) = e^{-\frac{d_0-d}{\bar{t}k_S d_0}} \tag{C.13}$$

Hence, from eq. C.5, the CDF of particle sizes is

$$F(d) = e^{-\frac{d_0-d}{\bar{t}k_S d_0}} \qquad \text{for} \qquad 0 \le d \le d_0 \tag{C.14}$$

It is readily evident that $F(d)$ has the property of a CDF, that is $F(d_0) = 1$.

According to eq. C.4, the PDF is obtained by taking the derivative of $F(d)$ with respect to d. In strict mathematical terms

$$f^{\star}(d) = \frac{1}{\bar{t}k_S d_0} e^{-\frac{d_0-d}{\bar{t}k_S d_0}} \qquad \text{for} \qquad 0 \le d \le d_0 \tag{C.15}$$

However, if $f^{\star}(d)$ is integrated over all d the result is not 1, but rather $1 - e^{-1/\bar{t}k_S}$.

At this point some necessary clarifications must be made in physical rather than mathematical terms. The probability of a particle, which enters a continuous reactor with size d_0, exiting with a size between d and $d + \mathrm{d}d$ is $f^\star(d)\,\mathrm{d}d$. Consequently, if $\bar{\eta}_0$ particles per unit volume[3] enter the reactor, then $\bar{\eta}_0 f^\star(d)\,\mathrm{d}d$ particles with sizes in the interval $(d, d+\mathrm{d}d)$ exit. Two conclusions can be drawn. The first is that $f^\star(d)$ is the <u>number</u>-PSD function of reacted particles in the continuous reactor, and will be further symbolized by $f_{\mathrm{n}}^\star(d)$[4]. The second is that $f_{\mathrm{n}}^\star$ refers to the total <u>initial</u> number of particles (i.e. unreacted). The total number of particles per unit volume at the exit stream with all possible sizes (between 0 and d_0) is found by integration over all particle sizes, i.e.

$$\bar{\eta} = \int_0^{d_0} \bar{\eta}_0 f_{\mathrm{n}}^\star(d)\,\mathrm{d}d \tag{C.16}$$

or

$$\bar{\eta} = \bar{\eta}_0(1 - e^{-1/\bar{t}k_S}) \tag{C.17}$$

The term $e^{-1/k_S\bar{t}}$ represents the probability of a particle reacting completely and therefore disappearing (see eq. C.12). In a population of $\bar{\eta}_0$ initial particles, the same term represents the fraction of the $\bar{\eta}_0$ particles which disappear. Consequently, $1 - e^{-1/k_S\bar{t}}$ is the fraction of $\bar{\eta}_0$ particles which are present in the exit stream of a continuous reactor. Therefore, in order to normalize $f_{\mathrm{n}}^\star(d)$ with respect to the total final number of particles we must divide by $1 - e^{-1/\bar{t}k_S}$. The final "normalized" form of PDF then becomes

$$f_{\mathrm{n}}(d) = \frac{1}{\bar{t}k_S d_0(1 - e^{-1/k_S\bar{t}})} e^{-\frac{d_0 - d}{\bar{t}k_S d_0}} \quad \text{for} \quad 0 \le d \le d_0 \tag{C.18}$$

Now, from a mathematical stand point $f_{\mathrm{n}}(d)$ <u>is</u> a PDF, that is

$$\int_0^{d_0} f_{\mathrm{n}}(d)\,\mathrm{d}d = 1 \tag{C.19}$$

The number of particles per unit volume at the exit stream with sizes between d and $d + \mathrm{d}d$ can now be written as $\bar{\eta}_0(1 - e^{-1/k_S\bar{t}}) f_{\mathrm{n}}(d)\,\mathrm{d}d$, which is exactly equal to $\bar{\eta}_0 f_{\mathrm{n}}^\star(d)\,\mathrm{d}d$.

---

[3] Unit volume may or may not include the volume of particles as long it is consistently defined. In this work the particle-free volume is considered.

[4] The subscript "n" is added to make clear the difference between the particle size density function based on the number of particles (f_{n}), with the respective function based on the mass (f_{m}).

The procedure for finding $f_n(d)$ described above applies well even when the RTD function does not have the neat form of eq. C.3 (perfectly mixed—single reactor). The only requirement is that the function be analytical (i.e. eqs B.5 or B.18). However, significant complications arise when a complex expression of $d(d_0, t)$ applies to a particular system; for example, non surface reaction control—shrinking core kinetics. For the latter case, numerical methods may (in principle) be applied for the calculation of $d(d_0, t)$ and $f_n(d)$.

C.1.2 Mass-PSD Function

The particle size density function based on the number of particles must be transformed into the respective one based on mass since the latter is needed for the calculation of conversion according to the segregated flow model. Let us further define a function that represents the net number (rather than the fraction) of particles with a specified size of d per unit volume. This function is denoted by $\bar{\psi}(d)$, and will be hereafter called the "particle number distribution" function. It then follows that the number of particles at the exit stream with sizes in the interval $(d, d + \mathrm{d}d)$ is given by

$$\bar{\psi}(d)\,\mathrm{d}d = \bar{\eta} f_n(d)\,\mathrm{d}d \tag{C.20}$$

The total number of particles (per unit volume) is found by integration

$$\bar{\eta} = \int_0^{d_0} \bar{\psi}(d)\,\mathrm{d}d \tag{C.21}$$

In similar terms, a respective "particle mass distribution" function $\bar{\omega}(d)$ is defined, so that the mass of particles per unit volume at the exit stream with sizes in the interval $(d, d + \mathrm{d}d)$ is given by

$$\bar{\omega}(d)\,\mathrm{d}d = \bar{m} f_m(d)\,\mathrm{d}d \tag{C.22}$$

and the total mass of particles (per unit volume) is given by

$$\bar{m} = \int_0^{d_0} \bar{\omega}(d)\,\mathrm{d}d \tag{C.23}$$

The following mass equality relates $\bar{\psi}(d)$ with $\bar{\omega}(d)$

$$\bar{\omega}(d)\,\mathrm{d}d = \frac{\pi d^3}{6}\rho\bar{\psi}(d)\,\mathrm{d}d \tag{C.24}$$

and equivalently, the following equation relates $f_\mathrm{n}(d)$ with $f_\mathrm{m}(d)$

$$\bar{m} f_\mathrm{m}(d)\,\mathrm{d}d = \frac{\pi d^3}{6}\rho\bar{\eta} f_\mathrm{n}(d)\,\mathrm{d}d \tag{C.25}$$

By integrating both sides of eq. C.25 over all particle sizes, and taking into account that the integral of $f_\mathrm{m}(d)\,\mathrm{d}d$ is 1, we obtain

$$\bar{m} = \int_0^{d_0} \frac{\pi d^3}{6}\rho\bar{\eta} f_\mathrm{n}(d)\,\mathrm{d}d \tag{C.26}$$

Substituting $\bar{m}$ in eq. C.25 and solving for $f_\mathrm{m}(d)$, the following relation, which transforms the particle number to particle mass density function, is obtained

$$f_\mathrm{m}(d) = \frac{d^3 f_\mathrm{n}(d)}{\displaystyle\int_0^{d_0} d^3 f_\mathrm{n}(d)\,\mathrm{d}d} \tag{C.27}$$

Combining eqs. C.18 and C.27 we finally get

$$f_\mathrm{m}(d) = \frac{d^3 e^{-\frac{d_0-d}{tk_S d_0}}}{\displaystyle\int_0^{d_0} d^3 e^{-\frac{d_0-d}{tk_S d_0}}\,\mathrm{d}d} \tag{C.28}$$

C.2 Multi-Size Feed

Let us assume that the feed material is widely ranging in size, according to a mass-PSD function $f_{\mathrm{m},0}(d_0)$. If we denote the particle number distribution function of the feed by $\bar{\psi}_0(d_0)$, then the number of particles per unit volume in the <u>feed</u> stream that belong to the size interval $(d_0, d_0 + \mathrm{d}d_0)$ is found by dividing the mass of these particles by the mass of a single particle. That is

$$\bar{\psi}_0(d_0)\,\mathrm{d}d_0 = \frac{6\bar{m}_0 f_{\mathrm{m},0}(d_0)}{\pi d_0^3 \rho}\,\mathrm{d}d_0 \tag{C.29}$$

The number of particles at the <u>exit</u> stream with sizes in $(d, d + \mathrm{d}d)$ originating from particles with initial sizes in $(d_0, d_0 + \mathrm{d}d_0)$ is equal to the total remaining particles, which had initial sizes in $(d_0, d_0 + \mathrm{d}d_0)$, multiplied by the probability that a particle belongs in the size interval $(d, d + \mathrm{d}d)$. That is

$$\bar{\psi}(d, d_0)\,\mathrm{d}d\,\mathrm{d}d_0 = \underbrace{\bar{\psi}_0(d_0)(1 - e^{-1/k_S\bar{t}})\,\mathrm{d}d_0}_{\text{remaining particles which had initial size } d_0} \cdot \underbrace{f_\mathrm{n}(d)\,\mathrm{d}d}_{\text{probability of particles having size } d}$$

Since the particles shrink from an initial size $d_0 \geq d$ down to a size d, all particles with size d ought to originate from particles with initial sizes between d and $d_{0,\mathrm{max}}$. Therefore, the number of <u>all</u> particles with sizes in the interval $(d, d + \mathrm{d}d)$ is given by equation C.30

$$\bar{\psi}(d)\,\mathrm{d}d = \underbrace{\int_d^{d_{0,\mathrm{max}}} \bar{\psi}_0(d_0)(1 - e^{-1/k_S\bar{t}})\,\mathrm{d}d_0}_{\text{remaining particles with initial size } \geq d} \cdot \underbrace{f_\mathrm{n}(d)\,\mathrm{d}d}_{\text{probability of particles having size } d} \tag{C.30}$$

Therefore, for a multi-size feed, eq. C.25 is written as

$$\bar{m} f_\mathrm{m}(d)\,\mathrm{d}d = \frac{\pi d^3}{6}\rho \int_d^{d_{0,\mathrm{max}}} \bar{\psi}_0(d_0)(1 - e^{-1/k_S\bar{t}})\,\mathrm{d}d_0 \cdot f_\mathrm{n}(d)\,\mathrm{d}d \tag{C.31}$$

By integrating both sides of eq. C.31 over all possible particle sizes d (that is from 0 to $d_{0,\mathrm{max}}$) we obtain

$$\bar{m} = \int_0^{d_{0,\mathrm{max}}} \frac{\pi d^3}{6}\rho f_\mathrm{n}(d) \int_d^{d_{0,\mathrm{max}}} \bar{\psi}_0(d_0)(1 - e^{-1/k_S\bar{t}})\,\mathrm{d}d_0\,\mathrm{d}d \tag{C.32}$$

Substitution of eq. C.32 into eq. C.31 yields

$$f_\mathrm{m}(d) = \frac{d^3 \int_d^{d_{0,\mathrm{max}}} \bar{\psi}_0(d_0)(1 - e^{-1/k_S\bar{t}}) f_\mathrm{n}(d)\,\mathrm{d}d_0}{\int_0^{d_{0,\mathrm{max}}} d^3 \int_d^{d_{0,\mathrm{max}}} \bar{\psi}_0(d_0)(1 - e^{-1/k_S\bar{t}}) f_\mathrm{n}(d)\,\mathrm{d}d_0\,\mathrm{d}d} \tag{C.33}$$

The mass-PSD must now be expressed in terms of the feed mass-PSD. Taking into account that $\bar{\psi}_0(d_0)\,\mathrm{d}d_0$ is given by eq. C.29 and that $f_\mathrm{n}(d)$ is given by eq. C.18, and performing appropriate simplifications, the following function is obtained, which calculates the mass-PSD function when the one of the feed is known

$$f_\mathrm{m}(d) = \frac{d^3 \int_d^{d_{0,\mathrm{max}}} d_0^{-3} f_{\mathrm{m},0}(d_0) e^{-\frac{d_0 - d}{\bar{t}k_S d_0}}\,\mathrm{d}d_0}{\int_0^{d_{0,\mathrm{max}}} d^3 \int_d^{d_{0,\mathrm{max}}} d_0^{-3} f_{\mathrm{m},0}(d_0) e^{-\frac{d_0 - d}{\bar{t}k_S d_0}}\,\mathrm{d}d_0\,\mathrm{d}d} \tag{C.34}$$

It is stated once more that eq. C.34 is valid only when particles shrink under surface reaction control kinetics. For other rate limiting regimes more complex expressions are expected to result requiring numerical rather than analytical solution.

Appendix D

The Population Balance Model and its Use in Describing Particulate Processes

D.1 Fundamentals

We consider a population of particles per unit volume at time t possessing Z_m properties (i.e. particle size, reactivity, content of valuable material, etc.) in an arbitrary reactor. The function describing the distribution of these properties is denoted again by $\bar{\psi}$ having the same meaning as in Appendix C. Consequently, the number of particles per unit volume with property Z_1 in the interval $(\zeta_1, \zeta_1 + \mathrm{d}\zeta_1)$, property Z_2 in the interval $(\zeta_2, \zeta_2 + \mathrm{d}\zeta_2)$ etc. at time t will be $\bar{\psi}(\zeta_1, \zeta_2, \cdots, \zeta_m; t)\mathrm{d}\zeta_1\, \mathrm{d}\zeta_2 \cdots \mathrm{d}\zeta_m$. In Appendix C, $\bar{\psi}$ was a function of only one variable (namely d) for the monosize feed case, and of two variables (namely d and d_0) for the multi-size feed case. If $\bar{\eta}(t)$ is the total number of particles at time t (per unit volume) and $f(\zeta_1, \zeta_2, \cdots, \zeta_m; t)$ is the particle number density function, then the following equation holds

$$\bar{\psi}(\zeta_1, \zeta_2, \cdots, \zeta_m; t) = \bar{\eta}(t) f(\zeta_1, \zeta_2, \cdots, \zeta_m; t) \tag{D.1}$$

By performing a particle "balance" the following equation can be written [5.17]

$$\underbrace{\mathcal{Q}_0 \bar{\psi}_0}_{\textbf{input}} - \underbrace{\mathcal{Q}_{\text{out}} \bar{\psi}_{\text{out}}}_{\textbf{output}} + \underbrace{V[(\bar{B} - \bar{D}) - \sum_{j=1}^{m} \frac{\partial}{\partial \zeta_j}(v_j \bar{\psi})]}_{\textbf{generation}} = \underbrace{\frac{\partial}{\partial t}(V \bar{\psi})}_{\textbf{accumulation}} \tag{D.2}$$

In eq. D.2, $\bar{B}$ and $\bar{D}$ is the "birth" and "death" rate of particles due to discrete changes in the specified ζ_m intervals. Alternatively, the $\frac{\partial}{\partial \zeta_j}(v_j\bar{\psi})$ terms represent the contribution to particle generation from continuous changes in particle properties, and v_j is the time rate of change (velocity) of property Z_j in the specified interval $(\zeta_j, \zeta_j + \mathrm{d}\zeta_j)$. That is

$$v_j = \frac{\mathrm{d}\zeta_j}{\mathrm{d}t}$$

In principle, the differential equation D.2 can be solved for $\bar{\psi}$ once $\bar{B}, \bar{D}, v_j$ and the relationship between $\bar{\psi}_{\mathrm{out}}$ and $\bar{\psi}$ are known.

For the case of a single stage continuous reactor, eq. D.2 can be simplified significantly. The steady state assumption implies that

$$\frac{\partial}{\partial t}(V\bar{\psi}) = 0$$

Only two particle properties are of interest. That is the size d of a reacted particle, and the initial particle size d_0. Thus

$$v_1(d, d_0) = \frac{\mathrm{d}d}{\mathrm{d}t} \qquad \text{and} \qquad v_2(d, d_0) = \frac{\mathrm{d}d_0}{\mathrm{d}t}$$

The size of the particle at feed conditions is a fixed quantity (unreacted), therefore $v_2(d, d_0) = 0$. The following assumptions are also made

- The size distribution of the solid particles does not change as a result of breakage, attrition or coalescence inside the reactor (i.e. $\bar{B} = \bar{D} = 0$)

- The flow rate of the slurry is not significantly affected by the extent of reaction (i.e. $Q_0 = Q_{\mathrm{out}} = Q$)

- The reaction vessel is well mixed (i.e. $\bar{\psi}_{\mathrm{out}} = \bar{\psi}$)

As a consequence of the above assumptions and the fact that $\bar{t} = V/Q$, eq. D.2 becomes

$$\frac{1}{\bar{t}}[\bar{\psi}_0(d, d_0) - \bar{\psi}(d, d_0)] - \frac{\partial}{\partial d}[v_1(d, d_0)\bar{\psi}(d, d_0)] = 0 \qquad \text{(D.3)}$$

Recognizing that the particles in the feed stream are completely unreacted, eq. D.3 can be integrated [5.17] to yield the joint number distribution function (of two variables, namely d and d_0)

$$\bar{\psi}(d, d_0) = -\frac{\bar{\psi}_0(d_0)}{\bar{t}v_1(d, d_0)} \exp \int_d^{d_0} \frac{\mathrm{d}d'}{\bar{t}v_1(d', d_0)} \tag{D.4}$$

where d' is a dummy variable. The marginal number distribution function (of only one variable, namely d) is obtained by integrating eq. D.4 over all permissible d_0 values

$$\bar{\psi}(d) = -\int_d^{d_{0,\max}} \frac{\bar{\psi}_0(d_0)}{\bar{t}v_1(d, d_0)} \exp \int_d^{d_0} \frac{\mathrm{d}d'}{\bar{t}v_1(d', d_0)} \,\mathrm{d}d_0 \tag{D.5}$$

Equation D.5 is very dynamic. Once the particle number distribution function of the feed $\bar{\psi}_0(d_0)$ and the rate of particle size change $v_1(d, d_0)$ are specified, the particle number distribution $\bar{\psi}(d)$ and consequently the particle number density function $f_{\mathrm{n}}(d)$ of the reacted particles (or $f_{\mathrm{m}}(d)$), the conversion and particle surface area can be calculated in a well stirred reactor. In other words, eq. D.5 is valid for all particle kinetics, even when particles shrink or grow (as in crystallization systems). In fact, the Population Balance Model was first developed to describe crystallization processes [5.32, 5.33].

D.2 Particle Size Distribution for Surface Reaction Control

If the particles react according to the shrinking core model for surface reaction control, then from eq. C.1 we have

$$v_1(d, d_0) = v_S = -d_0 k_S \tag{D.6}$$

where v_S is actually a constant quantity since the product $d_0 k_S$ is also a constant according to eq. C.2. Substituting and performing the integration of the exponential term in eq. D.5 we have

$$\int_d^{d_0} \frac{\mathrm{d}d'}{\bar{t}v_S} = -\frac{d_0 - d}{\bar{t}d_0 k_S}$$

and subsequently eq. D.5 becomes

$$\bar{\psi}(d) = \int_{d}^{d_{0,\max}} \frac{\bar{\psi}_0(d_0)}{\bar{t} d_0 k_S} e^{-\frac{d_0 - d}{\bar{t} k_S d_0}} \, \mathrm{d}d_0 \tag{D.7}$$

It can easily be seen that eq. D.7 is similar to eq. C.30 by recognizing that $f_{\mathrm{n}}(d)$ is defined by eq. C.18 (Appendix C). It follows from this similarity that the mass-PSD function will be identical to that given by eq. C.34. That is

$$f_{\mathrm{m}}(d) = \frac{d^3 \int_{d}^{d_{0,\max}} d_0^{-3} f_{\mathrm{m},0}(d_0) e^{-\frac{d_0 - d}{\bar{t} k_S d_0}} \, \mathrm{d}d_0}{\int_{0}^{d_{0,\max}} d^3 \int_{d}^{d_{0,\max}} d_0^{-3} f_{\mathrm{m},0}(d_0) e^{-\frac{d_0 - d}{\bar{t} k_S d_0}} \, \mathrm{d}d_0 \, \mathrm{d}d} \tag{D.8}$$

For different particle kinetics the same procedure can be followed. It is possible, however, that eq. D.5 might require a numerical rather than analytical integration. Furthermore, the inherent weakness of the macroscopic PBM is that eq. D.5 accounts only for the RTD function given by eq. 5.19 because of the "well mixed" assumption.

D.3 Particle Size Distribution for Gas Transfer Control

For the case that particles react according to the gas transfer control-SCM, then from equation 5.38 we have

$$v_1(d, d_0) = v_G = -\frac{1}{3} d_0 k_G (1 - k_G t)^{-\frac{2}{3}} \tag{D.9}$$

By solving eq. 5.38 for $(1 - k_G)$ and substituting in eq. D.9, the latter is written in a more simplified form as

$$v_G = -\frac{1}{3} \frac{d_0^3 k_G}{d^2} \tag{D.10}$$

Inspection of eq. 5.36 shows that the term $d_0^3 k_G$ is a constant. In a similar manner to the procedure outlined in the previous section, the exponential term in eq. D.5 becomes, upon integration

$$\int_{d}^{d_0} \frac{\mathrm{d}d'}{\bar{t} v_G} = -\frac{d_0^3 - d^3}{\bar{t} d_0^3 k_S}$$

Substitution in eq. D.5 results

$$\bar{\psi}(d) = \int_{d}^{d_{0,\mathrm{max}}} \frac{\bar{\psi}_0(d_0)d^2}{\bar{t}d_0^3 k_S} e^{-\frac{d_0^3-d^3}{\bar{t}d_0^3 k_S}} \,\mathrm{d}d_0 \tag{D.11}$$

On the basis of eq. D.1, the number-PSD function will be

$$f_{\mathrm{n}}(d) = \frac{\bar{\psi}(d)}{\bar{\eta}} = \frac{\bar{\psi}(d)}{\int_{0}^{d_{0,\mathrm{max}}} \bar{\psi}(d) \,\mathrm{d}d} \tag{D.12}$$

Furthermore, $f_{\mathrm{n}}(d)$ is transformed into the respective mass-PSD function according to eq. C.27. After appropriate simplifications we obtain

$$f_{\mathrm{m}}(d) = \frac{d^5 \int_{d}^{d_{0,\mathrm{max}}} \bar{\psi}_0(d_0) e^{-\frac{d_0^3-d^3}{\bar{t}d_0^3 k_S}} \,\mathrm{d}d_0}{\int_{0}^{d_{0,\mathrm{max}}} d^5 \int_{d}^{d_{0,\mathrm{max}}} \bar{\psi}_0(d_0) e^{-\frac{d_0^3-d^3}{\bar{t}d_0^3 k_S}} \,\mathrm{d}d_0 \,\mathrm{d}d} \tag{D.13}$$

Finally, expressing $\bar{\psi}_0(d_0)$ in terms of $f_{\mathrm{m},0}$ with the aid of eq. C.29, the mass-PSD of reacted particles becomes

$$f_{\mathrm{m}}(d) = \frac{d^5 \int_{d}^{d_{0,\mathrm{max}}} d_0^{-3} f_{\mathrm{m},0}(d_0) e^{-\frac{d_0^3-d^3}{\bar{t}d_0^3 k_S}} \,\mathrm{d}d_0}{\int_{0}^{d_{0,\mathrm{max}}} d^5 \int_{d}^{d_{0,\mathrm{max}}} d_0^{-3} f_{\mathrm{m},0}(d_0) e^{-\frac{d_0^3-d^3}{\bar{t}d_0^3 k_S}} \,\mathrm{d}d_0 \,\mathrm{d}d} \tag{D.14}$$

D.4 Surface Area and Conversion

From the definition of $\bar{\psi}(d)$ it becomes obvious that the total specific (i.e. per unit volume) surface area of a particle population is given by

$$\bar{s} = \int_{d_{\mathrm{min}}}^{d_{\mathrm{max}}} \pi d^2 \bar{\psi}(d) \,\mathrm{d}d \tag{D.15}$$

the total specific volume by

$$\bar{v} = \int_{d_{\mathrm{min}}}^{d_{\mathrm{max}}} \frac{\pi d^3}{6} \bar{\psi}(d) \,\mathrm{d}d \tag{D.16}$$

and the total specific mass by

$$\bar{m} = \int_{d_{\mathrm{min}}}^{d_{\mathrm{max}}} \frac{\pi d^3}{6} \rho \bar{\psi}(d) \,\mathrm{d}d \tag{D.17}$$

From the definition of the overall conversion $\bar{x}$ on the basis of mass rather than mole units, i.e.

$$\bar{x} = \frac{\bar{m}_0 - \bar{m}}{\bar{m}_0}$$

it follows that

$$\bar{x} = \frac{\displaystyle\int_{d_{0,\min}}^{d_{0,\max}} \tfrac{\pi d_0^3}{6} \rho \bar{\psi}_0(d_0)\, \mathrm{d}d_0 - \int_{d_{\min}}^{d_{0,\max}} \tfrac{\pi d^3}{6} \rho \bar{\psi}(d)\, \mathrm{d}d}{\displaystyle\int_{d_{0,\min}}^{d_{0,\max}} \tfrac{\pi d_0^3}{6} \rho \bar{\psi}_0(d_0)\, \mathrm{d}d_0} \tag{D.18}$$

Appendix E

General Flowchart of the Simulation Program(s)

The program flowchart for both Version 1 and 2 is shown in the pages that follow.

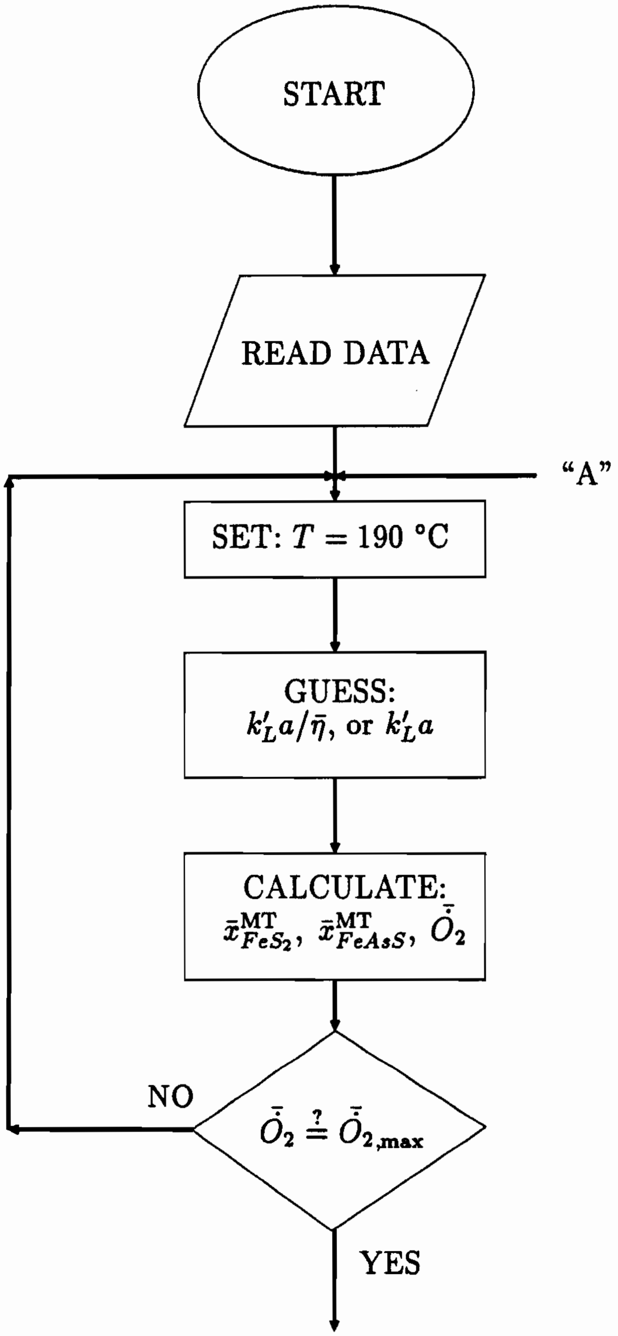
START
READ DATA
"A"
SET: $T = 190$ °C
GUESS:
$k'_L a/\bar{\eta}$, or $k'_L a$
CALCULATE:
$\bar{x}^{MT}_{FeS_2}$, $\bar{x}^{MT}_{FeAsS}$, $\bar{\dot{O}}_2$
NO
$\bar{\dot{O}}_2 \overset{?}{=} \bar{\dot{O}}_{2,\max}$
YES

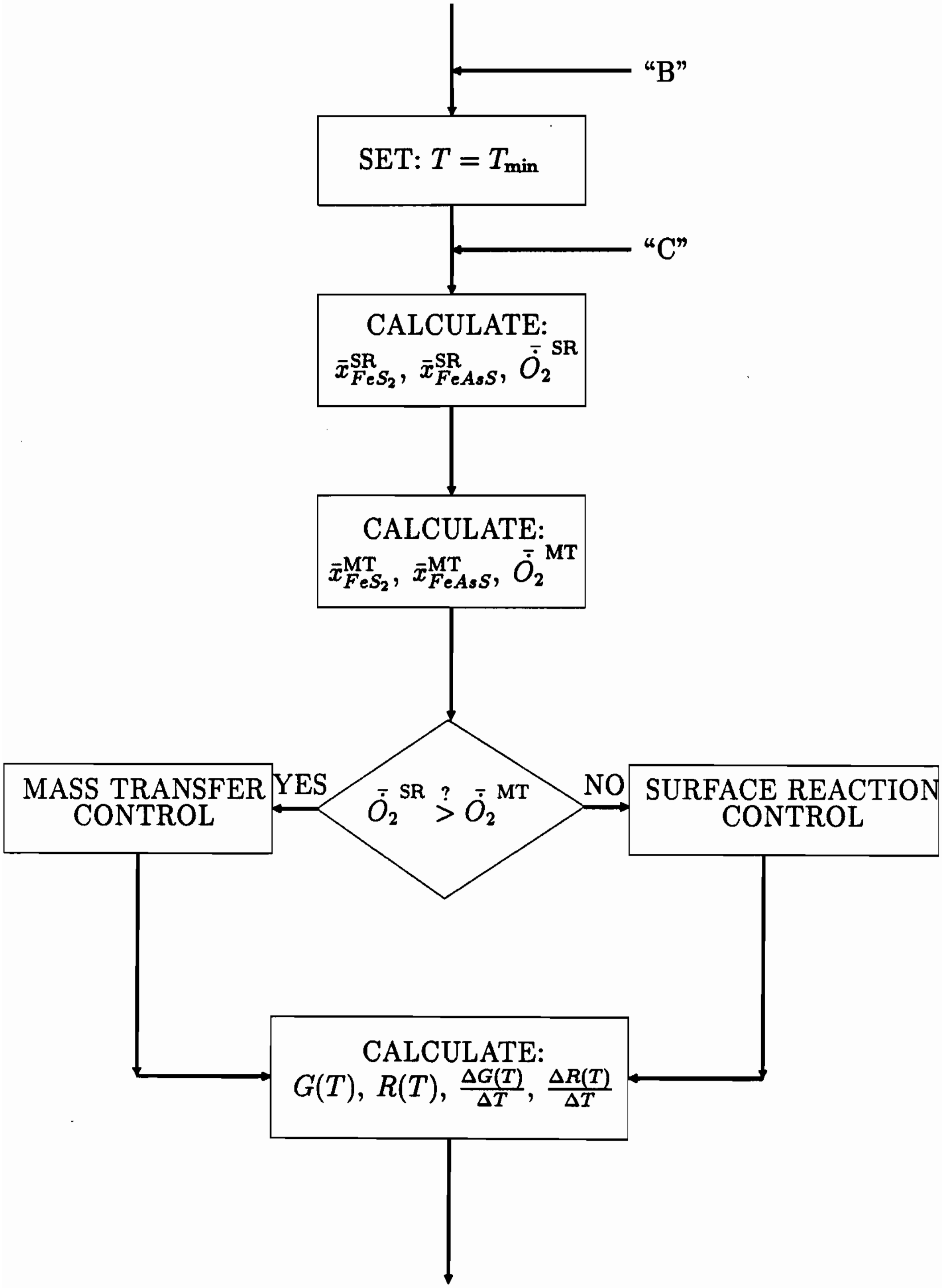
"B"
SET: $T = T_{\min}$
"C"
CALCULATE:
$\bar{x}^{SR}_{FeS_2}$, $\bar{x}^{SR}_{FeAsS}$, $\bar{\dot{O}}_2^{\ SR}$
CALCULATE:
$\bar{x}^{MT}_{FeS_2}$, $\bar{x}^{MT}_{FeAsS}$, $\bar{\dot{O}}_2^{\ MT}$
$\bar{\dot{O}}_2^{\ SR} \overset{?}{>} \bar{\dot{O}}_2^{\ MT}$
YES
NO
MASS TRANSFER CONTROL
SURFACE REACTION CONTROL
CALCULATE:
$G(T)$, $R(T)$, $\frac{\Delta G(T)}{\Delta T}$, $\frac{\Delta R(T)}{\Delta T}$

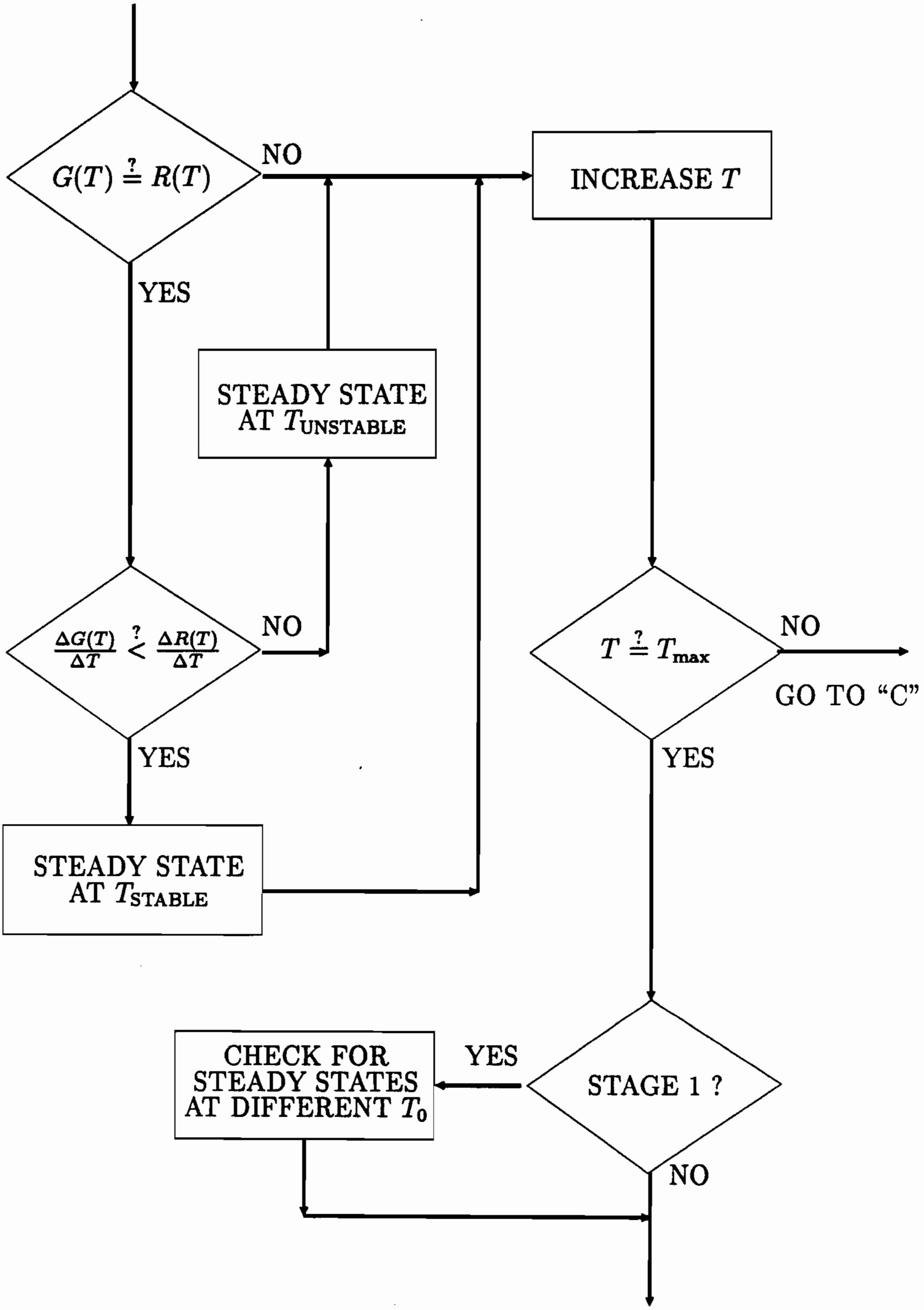

$G(T) \overset{?}{=} R(T)$
NO
INCREASE T
YES
STEADY STATE AT T_{UNSTABLE}
$\frac{\Delta G(T)}{\Delta T} \overset{?}{<} \frac{\Delta R(T)}{\Delta T}$
NO
$T \overset{?}{=} T_{\max}$
NO
GO TO "C"
YES
YES
STEADY STATE AT T_{STABLE}
CHECK FOR STEADY STATES AT DIFFERENT T_0
YES
STAGE 1 ?
NO

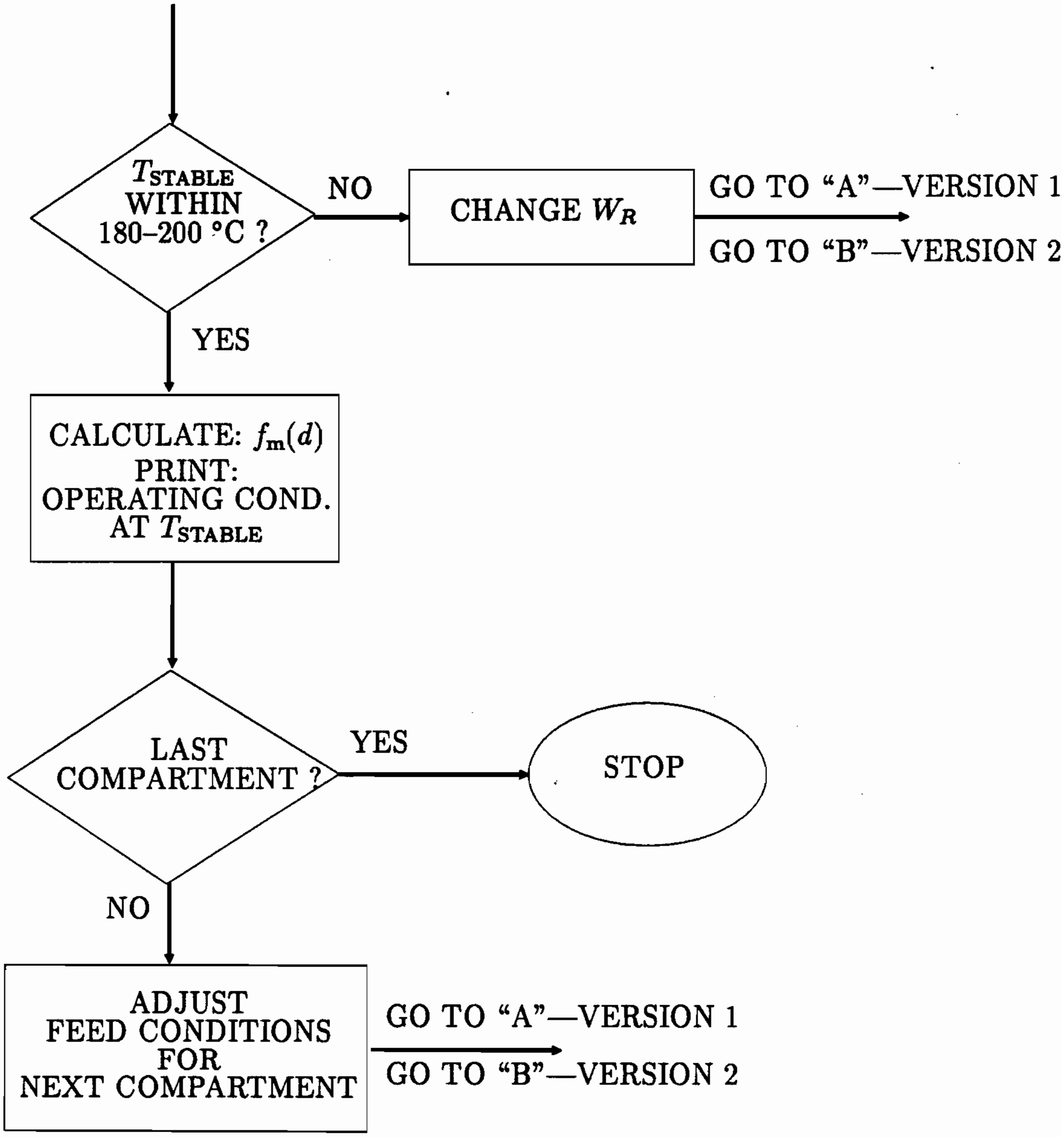

T_{STABLE} WITHIN 180–200 °C ?
NO
CHANGE W_R
GO TO “A”—VERSION 1
GO TO “B”—VERSION 2
YES
CALCULATE: $f_m(d)$
PRINT:
OPERATING COND.
AT T_{STABLE}
LAST COMPARTMENT ?
YES
STOP
NO
ADJUST FEED CONDITIONS FOR NEXT COMPARTMENT
GO TO “A”—VERSION 1
GO TO “B”—VERSION 2

Appendix F

Fitting Discrete Size Distribution Data to the Continuous Size Distribution Function

Two-parameter distributions are usually characterized by the mean μ and spread c. Such two-parameter PSD function is the one adopted in this work [5.7], which is given below

$$f(d_0) = \frac{\frac{\alpha d_0 - d_0^2}{\alpha d_0 - d_0^2 + \beta} \exp[-(\frac{d_0 - \mu}{c})^2]}{\int_0^{\alpha} \frac{\alpha d_0 - d_0^2}{\alpha d_0 - d_0^2 + \beta} \exp[-(\frac{d_0 - \mu}{c})^2] \, \mathrm{d}d_0} \tag{F.1}$$

This function describes the distribution of particles with sizes between 0 and a. The parameters μ and c can be calculated from discrete data, which are obtained experimentally (i.e. sizing an assembly of particles using a series of sieves).

If an entire size range of particles between $d_{\min}$ to $d_{\max}$ is divided into a series of n discrete sub-intervals, then the fraction in the ι interval (bounded by d_ι above and $d_{\iota+1}$ below) is given by:

$$f_\iota = \int_{d_{\iota+1}}^{d_\iota} f(d) \, \mathrm{d}d = F(d_\iota) - F(d_{\iota+1}) \qquad \iota = 1, 2, 3, ...n \tag{F.2}$$

where $f(d)$ is the particle size density function and $F(d)$ the cumulative particle size function. From the mean-value theorem of calculus the density function can be approximated by

$$f(d_\iota^*) \cong \frac{F(d_\iota) - F(d_{\iota+1})}{d_\iota - d_{\iota+1}} = \frac{f_\iota}{d_\iota - d_{\iota+1}} \tag{F.3}$$

where d_ι^* is an average value of d in the interval d_ι to $d_{\iota+1}$. The value of d_ι^* can be the arithmetic, geometric or harmonic average [5.17].

The mean of a particle population is determined from the density function using the defining equation

$$\mu = \int_{d_{\min}}^{d_{\max}} d f(d)\, \mathrm{d}d \tag{F.4}$$

Its corresponding approximation obtained from a set of f_ι values is

$$\hat{\mu} = \sum_{\iota=1}^{n} d_\iota^* f(d_\iota^*)\, \Delta d_\iota = \sum_{\iota=1}^{n} d_\iota^* f_\iota \tag{F.5}$$

The variance of sizes (around the mean) is given by

$$\sigma^2 = \int_{d_{\min}}^{d_{\max}} (d-\mu)^2 f(d)\, \mathrm{d}d \tag{F.6}$$

or approximated by

$$\hat{\sigma}^2 = \sum_{\iota=1}^{n} (d_\iota^* - \hat{\mu})^2 f(d_\iota^*)\, \Delta d_\iota = \sum_{\iota=1}^{n} (d_\iota^* - \hat{\mu})^2 f_\iota \tag{F.7}$$

Since the size density function given by eq. F.1 is a modified normal distribution, the spread c is equal to the standard deviation σ [5.7].

Application of the above formulae to the discrete size distribution data for the Olympias concentrate (which is the feed material for the simulation runs presented in this work) are shown in Table F.I. The second and third column of Table F.I refer to raw data [5.21], while the forth column is calculated from equation F.3. The arithmetic rather than the geometric mean particle size d_ι^*, was used to ensure a non zero value for the mean size which is bounded by 0 (i.e. the finest). It is noted that $F(d_\iota)$ values in column 3 refer to cumulative mass fraction passing through sieve ι. From equations F.5 and F.7 we finally obtain:

$$\hat{\mu} = 20.8 \quad \mu\mathrm{m}$$

$$\hat{\sigma}^2 = 266.05$$

Hence, $\mu = 20.8$ μm and $c = 16.3$. The latter values were rounded to 21 μm and 16.5 respectively before they were used in the simulation runs.

Table F.I: Discrete size distribution data (Olympias concentrate)

ι	d_ι μm	$F(d_\iota)$	$f(d_\iota^*)$ μm^{-1}	d_ι^* μm
1	100	1.000	$2.60 \cdot 10^{-4}$	94.0
2	88	0.997	$2.40 \cdot 10^{-4}$	75.5
3	63	0.991	$4.29 \cdot 10^{-3}$	56.0
4	49	0.931	$6.22 \cdot 10^{-3}$	44.5
5	40	0.875	$1.30 \cdot 10^{-2}$	35.0
6	30	0.745	$2.05 \cdot 10^{-2}$	25.0
7	20	0.540	$1.68 \cdot 10^{-2}$	15.0
8	10	0.372	$4.46 \cdot 10^{-2}$	7.5
9	5	0.149	$2.98 \cdot 10^{-2}$	2.5
10	0	0.000		